THERMO-MECHANICAL PROCESSING AND MECHANICAL BEHAVIOUR OF HIGH PHOSPHOROUS STEELS

Ph.D. THESIS

by

YASHWANT MEHTA

DEPARTMENT OF METALLURGICAL AND MATERIALS ENGINEERING
INDIAN INSTITUTE OF TECHNOLOGY ROORKEE
ROORKEE- 247 667 (INDIA)
JULY, 2017

THERMO-MECHANICAL PROCESSING AND MECHANICAL BEHAVIOUR OF HIGH PHOSPHOROUS STEELS

A THESIS

Submitted in partial fulfilment of the
requirements for the award of the degree

of

DOCTOR OF PHILOSOPHY

in

METALLURGICAL AND MATERIALS ENGINEERING

by

YASHWANT MEHTA

DEPARTMENT OF METALLURGICAL AND MATERIALS ENGINEERING
INDIAN INSTITUTE OF TECHNOLOGY ROORKEE
ROORKEE- 247 667 (INDIA)
JULY, 2017

INDIAN INSTITUTE OF TECHNOLOGY ROORKEE
ROORKEE

CANDIDATE'S DECLARATION

I hereby certify that the work which is being presented in the thesis entitled **"THERMO-MECHANICAL PROCESSING AND MECHANICAL BEHAVIOUR OF HIGH PHOSPHOROUS STEELS"** in partial fulfilment of the requirement for the award of the Degree of Doctor of Philosophy and submitted in the Department of Metallurgical and Materials Engineering of the Indian Institute of Technology Roorkee, Roorkee is an authentic record of my own work carried out during a period from July, 2012 to July, 2017 under the supervision of Dr. G.P. Chaudhari, Associate Professor, and Dr. V.V. Dabhade, Associate Professor, Department of Metallurgical and Materials Engineering, Indian Institute of Technology Roorkee, Roorkee.

The matter presented in this thesis has not been submitted by me for the award of any other degree of this or any other Institution.

(**YASHWANT MEHTA**)

This is to certify that the above statement made by the candidate is correct to the best of our knowledge.

(G.P.Chaudhari)
Supervisor

(V.V.Dabhade)
Supervisor

The Ph.D. Viva-Voce Examination of **Mr. Yashwant Mehta,** Research Scholar has been held on 31st January 2018.

Chairman, SRC **Signature of the External Examiner**

This is to certify that the student has made all the corrections in the thesis.

Signature of Supervisor(s) **Head of the Department**
Dated:

Abstract

Goods and services are produced to satisfy the needs of society. The useful life of the goods is shortened by corrosion. This fuels the quest for corrosion resistant products. One such product is archaeological iron like the Delhi iron pillar. The Delhi iron pillar has withstood corrosion for about 1600 years. Other ancient iron artefacts like Konark temple beams have withstood marine environment for long periods of time. These were made by iron produced by a sinter-forge technique using charcoal. Ancient iron relied on high phosphorous content for strength and corrosion resistance. The artefact developed a passive film in wet dry conditions, which protected it from further environmental damage. If high phosphorous steel is produced through the melt route using coke, it exhibits cold shortness. This brittle behaviour is caused due to grain boundary segregation of phosphorous. Therefore, if ductile and tough high phosphorous steels could be produced using the modern iron and steel making methods, the cost of corrosion to society could be reduced to a great extent.

The present work is an attempt towards the achievement of the aforesaid goal. The thesis is divided into six chapters. The first chapter contains the introduction. The second chapter contains the details of the literature survey. The third chapter contains the experimental details of the work done. The fourth chapter contains the results of the experiments and discussions related to the findings. The fifth chapter contains the summary of the work done and the conclusions. The sixth chapter deliberates upon the suggestions for future work.

In order to improve the ductility and toughness of high phosphorous a combination of alloying elements, heat treatment and thermo-mechanical processing can be used. The alloying elements can be chosen out of carbon, silicon, nickel, nitrogen, boron, and molybdenum. The heat treatment temperatures can be chosen from the (α+γ) region of the equilibrium phase diagram. Thermo-mechanical processing includes rolling and forging in the present context.

The alloying elements of carbon and nitrogen improve grain boundary cohesion by displacing phosphorous from the grain boundaries. Silicon reduces the ductile brittle transition temperature of high phosphorus steels. Heat treatment in the intercritical region of ferrite + austenite for long periods of time causes a partitioning of alloying elements between austenite and ferrite at high temperatures. The partitioning is retained at lower temperatures. Phosphorous is concentrated in the ferrite grain interiors and carbon and nitrogen are retained

near the grain boundaries. The partitioning of the alloying elements is more effective when the material is subjected to thermo-mechanical processing like forging or rolling. Grain refinement is an added advantage when the material is thermo-mechanically processed.

A set of high phosphorous steel compositions using the aforesaid alloying elements has been designed, melted and cast in the present endeavour. These compositions were subjected to dilatometry tests to ascertain the transformation temperatures. The knowledge of the transformation temperatures has been used to design heat treatments and thermo-mechanical processing schedules.

The metallographic studies of the steels have been conducted in order to understand the partitioning of alloying elements like phosphorous and carbon, etc., between the ferrite and austenite phases during the holding of the high phosphorous steels in the intercritical phase $(\alpha+\gamma)$ field. This understanding of the diffusion behaviour of phosphorous in the $(\alpha+\gamma)$ phase field has been used to improve the toughness of the high phosphorous steels by removing phosphorous from the grain boundaries. The results of the metallographic studies were used to design heat treatments for preparing samples for studies of mechanical properties and corrosion behaviour.

The mechanical properties of the high phosphorous steels have been studied in five sets. As cast, hot forged at 1150°C, hot forged at 1150°C and subsequently heat treated at 900°C for one hour, hot forged at 1150°C and subsequently heat treated at 900°C for six hours, and hot forged at 900°C and subsequently hot rolled at 900°C for one hour. Tensile, Charpy impact and Vicker's hardness tests have been conducted. The results were compared with the mechanical properties of plain carbon steel and the results obtained by other researchers who studied iron and steel compositions containing phosphorous contents higher than 0.04 wt.%. The best toughness was observed in the samples hot forged at 1150°C and subsequently heat treated at 900°C for six hours. This sample was also evaluated for corrosion behaviour amongst others.

The corrosion behaviour was studied using potentiodynamic polarization and electrochemical impedance spectroscopy. The samples chosen were annealed samples and that which was hot forged at 1150°C and subsequently heat treated at 900°C for six hours. The potentiodynamic polarization and electrochemical impedance spectroscopy studies revealed that the high phosphorous steels were able to withstand 0.1 wt. % chloride concentration in saturated

$Ca(OH)_2$ solution. Plain carbon steel could withstand only upto 0.06 wt. % chloride concentration in saturated $Ca(OH)_2$ solution.

The Gleeble 3800 thermo-mechanical simulator was used to subject high phosphorous steel samples to hot compression at temperatures of 750, 800, 850, 900, 950, 1000, and 1050°C and strain rates of 10, 1, 0.5, 0.1, 0.01, 0.001 s^{-1}. Grain size of high phosphorous steel samples subjected to hot compression at temperatures of 800, 850, 900, 950, and 1050°C and strain rates of 10, 1, 0.1, and 0.01 s^{-1} was found out. The results indicated that the grain size decreased with decrease in deformation temperature and increase in strain rates. Adiabatic rise in temperatures disturbed the trend.

Processing map (Murty and Rao) has been constructed for high phosphorous steel composition S1, using samples subjected to hot compression at temperatures of 750, 800, 850, 900, 950, 1000, and 1050°C and strain rates of 10, 1, 0.5, 0.1, 0.01, and 0.001 s^{-1}. The results have been validated by comparing them with electron microscopic studies. The safe processing windows for the steel have been found out.

ACKNOWLEDGEMENTS

First of all, I would like to thank the almighty, omnipresent and omniscient **AUM** for his benevolence. I would then like to express my sincere gratitude, deepest respect and heartiest thanks to my supervisors, Dr. G.P. Chaudhari Associate Professor and, Dr. V.V. Dabhade, Associate Professor, Department of Metallurgical and Materials Engineering (MMED), Indian Institute of Technology, Roorkee for their valuable and intellectual guidance, unwavering support and encouragement throughout the tenure of my research work. This thesis could not have attained its present form, both in content and presentation, without their active interest, timely help, painstaking efforts, direction and valuable guidance. The words prove to be insufficient to express my deep feelings and heartfelt thanks to my supervisors for their benevolence and un-hesitating guidance throughout my doctoral work.

I express my sincere gratitude to Dr. V. Pancholi, Associate Professor, MMED, IIT Roorkee (Chairman SRC) for his utmost co-operation, help and support throughout the course of my research work. I am highly obliged to the members of my SRC committee, Dr. Ujjwal Prakash, (Internal member), Professor, MMED and Dr. D.B. Karunakar (External member), Associate Professor, MIED, IIT, Roorkee for their invaluable suggestions and encouragements to pursue this work. I extend my deep sense of gratitude to all the faculty members of MMED who have directly or indirectly facilitated for the smooth progress of my research work.

I would like to express my sincere thanks to Mr. Rajendra Sharma and Mr. R. K. Sharma, technical staff, MMED for the help and support they extended during my doctoral work. I am also thankful to all the technical and administrative staff of the MMED, especially to Mr. S.M. Giri, Mr. Shakti Gupta, Mr. Naresh Kumar, Mr. Pradip, Mr Sanjay, Mr. Ashish and Mr. S. Sharma, who have rendered their help in all possible ways during the Ph.D. work.

I would like to thank all India council of technical education (AICTE), New Delhi for providing me the opportunity of doing Ph.D. through quality improvement program (QIP). I gratefully acknowledge QIP Centre, IIT Roorkee for providing me the complete support during entire work of PhD. I express my deep sense of gratitude to the Co-ordinator and co-cordinator, QIP Centre, for his co-operation. I express my sincere thanks to all the QIP staff members especially to Mr. Anil Kumar, and Mr. Rajeev.

I am highly obliged and express my sincere thanks to the Director, National Institute of Technology, Srinagar, Jammu and Kashmir for giving me an opportunity of doing Ph.D. through QIP program. I owe my sincere gratitude to Prof. (Dr.) R. Ambardar, Dr. D.M.A. Khan, and Dr. A. Rahman of Metallurgical and Materials Engineering department, NIT Srinagar for providing unstinting support to me.

I wish to thank my friends and student colleagues, Dr. Sunil K Rajput, Dr. Sanjeev Kumar, Dr. Brij Kishor, Dr. Sanjay Rathore, Dr. P. Nageshwar Rao, Dr. Kuldeep Saxena, Mr. Neeraj Srivastava, Mr. Sandan Sharma, and all the fellows who helped me directly or indirectly during the entire period of this work.

I wish to thank Shri A. Aggarwal, proprietor of 'M/S Vaishnav Steel Private Limited', Muzaffernagar, Uttar Pradesh, India, who provided the castings of the three high phosphorous steels used in this work. These steel ingots were provided free of charge for conducting the research work.

My family deserves special attention for their unflagging love and support throughout my life and this work would not have been possible without their support, never-ending patience and constant encouragement. I express my profound regards to my parents for their blessings and for being the main source of inspiration to succeed in my endeavors. I am indebted to my mother, Mrs. Kanti Mehta, for her care and love throughout my life. I would like to express my gratitude to my wife, Mrs. Anamika for her sacrifice, help and providing constant encouragement. I would like to thank my children Atharv and Shruti for bearing with my absence for long periods of time, with a smile. I would like to thank everyone who was important to the successful realization of thesis, as well as expressing my apology that I could not mention everyone personally. I would like to dedicate this thesis to **AUM** for giving courage, strength and patience to me to carry out my research work.

(Yashwant Mehta)

Contents

Page No.
Certificate i
Abstract ii
Acknowledgements v
Contents vii
List of Figures xii
List of Tables xix
Symbols xxi
Abbreviations xxii

Chapter 1

INTRODUCTION 1
1.1 General 1
1.2 Objectives of the study 2
1.3 Plan of work 3

Chapter 2

LITERATURE SURVEY 4
2.1 Iron phosphorous system 4
  2.1.1 Equilibrium phase diagram of the Fe-P system 4
  2.1.2 Studies on the microstructure of Fe-P alloys using optical microscope 7
  2.1.3 Transformations in the Fe-P System 10
    2.1.3.1 Partitioning of alloying elements during the formation and growth of γ-austenite from α-ferrite 11
    2.1.3.2 Partitioning of alloying elements during the formation and growth of α-ferrite from γ-austenite 11
    2.1.3.3 Kinetics of diffusion of phosphorous 11
  2.1.4 Use of Dilatometry to study transformations 12
  2.1.5 Effect of alloying elements in wrought Fe-P alloys 12
    2.1.5.1 Effect of carbon 12
    2.1.5.2 Effect of nitrogen 13

		2.1.5.3 Effect of boron	13
		2.1.5.4 Effect of sulfur	13
		2.1.5.5 Effect of nickel	14
		2.1.5.6 Effect of chromium	14
		2.1.5.7 Effect of manganese	14
		2.1.5.8 Effect of vanadium	14
		2.1.5.9 Effect of silicon	15
		2.1.5.10 Effect of molybdenum	15
		2.1.5.11 Effect of niobium	15
	2.1.6 Phosphorous alloying in iron		16
	2.1.7 Effect of phosphorous on the mechanical behaviour of steel		17
	2.1.8 Advantages of phosphorus in ingot metallurgy		20
2.2	Effect of phosphorous on corrosion resistance of iron and iron-carbon alloys		21
	2.2.1 Reinforcing bar		21
	2.2.2 Corrosion of reinforcement bars		22
		2.2.2.1 Breakdown of passive film and pitting corrosion	23
		2.2.2.2 Chloride threshold for depassivation of reinforcing steel embedded in concrete	23
		2.2.2.3 Stages of the process of corrosion of rebars	26
		2.2.2.4 Propagation of pits	26
		2.2.2.5 Nature of polarization and pitting potential	27
		2.2.2.6 Protection methods	27
	2.2.3 Evaluation of corrosion performance of rebars in simulated concrete pore solution		27
		2.2.3.1 Visual inspection and weight loss	28
		2.2.3.2 Open circuit potential	28
		2.2.3.3 Linear polarization resistance (LPR) and Tafel extrapolation method	28
		2.2.3.4 Chloride threshold determination using potentiodynamic polarization	29
		2.2.3.5 Electrochemical impedance spectroscopy (EIS)	29
	2.2.4 Corrosion of steel		31

	2.2.5 Hot compression	33
	2.2.5.1. Grain refinement	35
	2.2.5.2 Hot deformation of low carbon steels	36
	2.2.5.3 Processing windows	43
	2.2.6 Applications	45
	2.2.7 Research gap and formulation of the problem	46

Chapter 3

EXPERIMENTAL PROCEDURE		48
3.1	Ingot Metallurgy	48
	3.1.1 Materials	48
	3.1.2 Melting and casting	49
3.2	Forging	49
	3.2.1 Homogenization	49
	3.2.2 Forging	50
	3.2.3 Composition analysis	50
3.3	Heat Treatment	50
3.4	Microscopy	52
	3.4.1 Optical and scanning electron microscope	52
3.5	Characterization	54
	3.5.1 Phase transformation characterization	54
	3.5.2 Tensile and Charpy impact testing	55
	3.5.3 Hardness test	58
	3.5.4 Micro-hardness	59
3.6	Electrochemical testing	60
	3.6.1 Environments	60
	3.6.2 Electrochemical techniques	60
	3.6.2.1 Sample preparation	61
	3.6.2.2 Test cells and potentiostat	61
	3.6.2.3 Open circuit potential and linear polarization resistance	62
	3.6.2.4 Potentiodynamic polarization	62
	3.6.2.5 Electrochemical impedance spectroscopy	63
3.7	Thermo-mechanical simulation and grain refinement	65

	3.7.1 Hot compression	65
	3.7.2 Grain refinement	66
	3.7.3 Processing map	66

Chapter 4

RESULTS AND DISCUSSION		68
4.1	Phase transformation	68
4.2	Metallography	70
4.3	Mechanical properties	80
	4.3.1 Effect of hot rolling and heat treatment in the (α+γ) region of the phase diagram on mechanical properties: A comparison	90
	4.3.2 Hardness test	95
4.4	Corrosion behaviour	96
	4.4.1. Anodic polarization behavior	96
	4.4.2 OCP and LPR studies	98
	4.4.3 Electrochemical impedance spectroscopy	100
	4.4.3.1 Results of the EIS study on S3 steel heat treated at 900°C for 6 hours	127
	4.4.3.2 Growth and destruction of the passive layer	131
	4.4.4. SEM analysis of the pit	132
	4.4.5 Beneficial effect of phosphorous alloying	133
	4.4.6 Immersion test in 3.5 wt. % NaCl solution	135
4.5	Grain refinement	135
	4.5.1 True stress, true strain curves	136
	4.5.1.1 True stress, true strain curves of S1 steel	136
	4.5.1.2 True stress, true strain curves of S2 steel	138
	4.5.1.3 Effect of addition of silicon on flow behaviour of S1 steel	141
	4.5.1.4. True stress, true strain curves of S3 steel	144
	4.5.1.5 Effect of addition of Si, N, and Mn on flow behaviour of S2 steel	146
	4.5.2 Microstructural evolution	149
	4.5.3 Adiabatic rise, peak stress and Z values	157
4.6	Thermo-mechanical processing	159

	4.6.1 Phase transformation characterization		160
	4.6.2 Flow behaviour of S1 steel		160
	4.6.3 Microstructure of S1 steel		166
	4.6.4 Processing map		167
	4.6.5 Discussion		168
		4.6.5.1 Microstructure evolution and processing maps	168
Chapter 5			
SUMMARY AND CONCLUSIONS			172
Chapter 6			
SUGGESTIONS FOR FUTURE WORK			176
PUBLICATIONS			177
BIBLIOGRAPHY			178

List of Figures

S.No.	**List of Figures**	Page no.
2.1.1.	(a) Fe–P binary phase diagram and (b) high temperature gamma loop region of the Fe–P phase diagram	5
2.1.2.	High-temperature gamma loop region of Fe-P phase diagram by Vogel	5
2.1.3.	C-Fe-P computed isothermal sections at (a) 1100°C and (b) 1000°C (c) 900°C and (d) 800°C (e) P=0.1 wt.%	6, 7
2.1.2.1.	Microstructure of Fe-0.29P-0.03C-0.2Si-0.2Mn-0.14Cr alloy; (a) As cast; (b) hot forged; and etched with 2% nital solution	8
2.1.2.2.	Microstructure of Fe-0.28P-0.14C-0.18Si-0.2Mn-0.15Cr alloy; (c) As cast; (d) hot forged; and etched with 2% nital solution	9
2.1.2.3.	Microstructure of Fe-0.29P-0.23C-0.16Si-0.22Mn-0.16Cr alloy; (e) As cast; (f) hot forged; and etched with 2% nital solution	9
2.1.2.4.	Microstructure of Fe-0.281P-0.145C-0.182Si-0.206Mn-0.15Cr alloy heat treated at 800˚C for 30 min, normalized and etched with 2% nital solution	9
2.1.2.5.	Microstructure of Fe-0.11P-0.08C reinforcement bar steel etched with 2% nital solution	10
2.1.2.6.	Optical micrographs of Fe-0.3P-0.02C alloy after etching with 2% nital solution: showing prior austenite regions along the grain boundary	10
2.2.2.1.	Protection of iron against corrosion (Pourbaix diagram)	23
2.2.3.5	(a) Circuit; (b) Nyquist plot; (c) Bode plot	30
2.2.3.6	A schematic Nyquist plot for mild steel in alkaline solution	31
2.2.5.1.	Typical flow curves during hot and cold deformation	34
2.2.5.2	Evolution of the microstructure during (a) DRV (b) DRX	35
3.3.1.	Schematic diagram illustrating gamma loop of iron–phosphorus phase diagram with tie lines for the investigated temperatures	52
3.4.1.1.	Leica DMI 5000M inverted optical microscope at Metallography laboratory	53
3.4.1.2.	Zeiss EVO18® LaB6 filament SEM at SEM laboratory	54
3.5.1.1.	Gleeble® 3800 at thermo-mechanical simulator laboratory	55

3.5.2.1.	A typical cylindrical tensile sample	56
3.5.2.2.	Charpy impact test specimen as per ASTM standard A-370	57
3.5.2.3.	H-25K tensile testing machine (Capacity 25 kN)	57
3.5.2.4.	Veb Werkstoffprufmaschinen impact test machine	58
3.5.3.1.	FIE Vickers hardness tester	59
3.5.4.1.	Walter UHL micro-hardness tester VMH 104 Auto	60
3.6.2.1.	Digital pH meter - pH 510 of Eutech instruments.	61
3.6.2.2.1.	Flat cell - Ametek, USA	63
3.6.2.2.2.	EG&G PARSTAT 273A Potentiostat (Ametek, USA)	64
3.6.2.2.3.	Gamry 1000 Interface potentiostat	64
3.6.2.2.4.	Bio-Logic SP-200 Potentiostat	65
4.1.1.	Results of the CCT test conducted on the steel using a thermo-mechanical simulator (GLEEBLE 3800$^{\circledR}$); points of inflection correspond to the Ar_1 and Ar_3 temperatures (a) S1 steel; (b) S2 steel; (c) S3 steel	69, 70
4.2.1.	Optical micrographs of the steel samples etched with 2% nital solution	71
4.2.2.	Optical micrographs of the steel samples etched with 2 % nital solution at higher magnifications	72
4.2.3.	Microstructure of S3 steel heated at 865°C for 24 h, water quenched, and etched with Oberhoffer’s reagent	72
4.2.4.	Optical micrographs of S3 steel specimens held at 865°C for different times and etched with Oberhoffer's reagent	74
4.2.5.	Optical micrographs of S3 steel specimens held at 830°C & 900°C for different times and etched with Oberhoffer's reagent	75
4.2.6.	Optical micrographs of S3 steel specimens held at 805°C for different times and etched with Oberhoffer's reagent	76
4.2.7.	Optical micrographs of S3 steel specimens held at 865°C for 24 h, water quenched, reheated and held at 750°C for different times and etched with Oberhoffer's reagent	77
4.2.8.	SEM photo of S3 steel sample held at 865°C for 24 h, and water quenched, etched with Oberhoffer's reagent, displaying X-ray area mapping results for phosphorous.	78
4.2.9.	Phase diagrams calculated using commercial thermodynamic software (Thermocalc^{TM} database TCFE7) for Fe-P system with other elements as	79

	present in S3 steel	
4.3.1.	Microstructures of S1, S2, and S3 steels in X1, X2 and X3 conditions; etched with 2 % nital solution	80
4.3.2.	SEM images of the tensile test samples of S1, S2, and S3 steels in X1, X2 and X3 conditions	81
4.3.3.	(a) SEM images of the fractured impact test samples of S1, S2, and S3 steels in X1, X2 and X3 conditions	82
	(b) SEM images of the fractured impact test samples of S1, S2, and S3 steels in X1, X2 and X3 conditions at higher magnification	83
4.3.4.	Surface morphology and EDS quantification: (a) as cast S1X1; (b) impact test sample of S1X2; (c) tensile test sample of S2X2; (d) different areas on S3X3	84
4.3.5.	(a) Engineering stress-strain curves of as cast high phosphorous steels	85
	(b) Engineering stress-strain curves of hot forged (1150°C) high phosphorous steels	85
	(c) Engineering stress-strain curves of high phosphorous steels, hot forged and then heat treated at 900°C for 6 h	86
4.3.1.1.	Optical micrographs of the tensile test samples of hot forged and heat treated (at 900°C for 1 h) high phosphorous steels etched with 2% nital solution	90
4.3.1.2.	SEM images of the tensile test samples of hot forged and heat treated (at 900°C for 1 h) high phosphorous steels	91
4.3.1.3.	SEM images of the fractured impact test samples of the hot forged and heat treated (at 900°C for 1 h) high phosphorous steels	91
4.3.1.4.	The microstructures of the three high phosphorous steels hot forged and hot rolled at 900°C and etched with 2 % nital solution	91
4.3.1.5.	SEM images of the tensile test samples of the steels hot forged and hot rolled at 900°C	92
4.3.1.6.	SEM images of the fractured impact test samples of the steels hot forged and hot rolled at 900°C	92
4.3.1.7.	(a) Engineering stress-strain curves of high phosphorous steels: hot forged and heat treated at 900°C for 1 h	93
	(b) Engineering stress-strain curves of high phosphorous steels: hot forged	93

	and hot rolled at 900°C.	
4.4.1.	Potentiodynamic polarization curves of S2, S2, S3 and S4 steels obtained in saturated $Ca(OH)_2$ solution having various chloride concentrations	97
4.4.2.	Variation of the OCP and i_{corr} for S1, S2, S3 and S4 steel samples exposed to saturated $Ca(OH)_2$ solution containing various chloride concentrations	99, 100
4.4.3.1.	Nyquist plots of S1 steel in saturated $Ca(OH)_2$ solution (a) without Cl^-; (b) with 0.05 wt. % Cl^-; (c) with 0.1 wt. % Cl^-	101, 102
4.4.3.2.	Nyquist plots of S2 steel in saturated $Ca(OH)_2$ solution (a) without Cl^-; (b) with 0.05 wt. % Cl^-; (c) with 0.1 wt. % Cl^-	102, 103
4.4.3.3.	Nyquist plots of S3 steel in saturated $Ca(OH)_2$ solution (a) without Cl^-; (b) with 0.05 wt. % Cl^-; (c) with 0.1 wt. % Cl^-	104, 105
4.4.3.4.	Nyquist plots of S4 steel in saturated $Ca(OH)_2$ solution (a) without Cl^-; (b) with 0.05 wt. % Cl^-; (c) with 0.1 wt. % Cl^-	105, 106
4.4.3.5.	Bode magnitude plots of S1 steel in saturated $Ca(OH)_2$ solution (a) without Cl^-; (b) with 0.05 wt. % Cl^-; (c) with 0.1 wt. % Cl^-	107, 108
4.4.3.6.	Bode magnitude plots of S2 steel in saturated $Ca(OH)_2$ solution (a) without Cl^-; (b) with 0.05 wt. % Cl^-; (c) with 0.1 wt. % Cl^-	109, 110
4.4.3.7.	Bode magnitude plots of S3 steel in saturated $Ca(OH)_2$ solution (a) without Cl^-; (b) with 0.05 wt. % Cl^-; (c) with 0.1 wt. % Cl^-	110, 111
4.4.3.8.	Bode magnitude plots of S4 steel in saturated $Ca(OH)_2$ solution (a) without Cl^-; (b) with 0.05 wt. % Cl^-; (c) with 0.1 wt. % Cl^-	112, 113
4.4.3.9.	Bode phase plots of S1 steel in saturated $Ca(OH)_2$ solution (a) without Cl^-; (b) with 0.05 wt. % Cl^-; (c) with 0.1 wt. % Cl^-	114, 115
4.4.3.10.	Bode phase plots of S2 steel in saturated $Ca(OH)_2$ solution (a) without Cl^-; (b) with 0.05 wt. % Cl^-; (c) with 0.1 wt. % Cl^-	116, 117
4.4.3.11.	Bode phase plots of S3 steel in saturated $Ca(OH)_2$ solution (a) without Cl^-; (b) with 0.05 wt. % Cl^-; (c) with 0.1 wt. % Cl^-	117, 118
4.4.3.12.	Bode phase plots of S4 steel in saturated $Ca(OH)_2$ solution (a) without Cl^-; (b) with 0.05 wt. % Cl^-; (c) with 0.1 wt. % Cl^-	119, 120
4.4.3.13.	Nyquist plot showing the second time constant in the high frequency region for S3 steel immersed in saturated $Ca(OH)_2$ solution containing 0.1% wt. % Cl^- for 5 h	122
4.4.3.14.	Equivalent circuit for the steels used in this work	122

4.4.3.15.	The variation of (a) R_p, (b) Y_0, and (c) α of the passive film with respect to time of immersion of S3 and S4 steels in saturated $Ca(OH)_2$ solution containing 0.1 wt. % Cl^-	126
4.4.3.1.1.	Variation of (a) OCP and (b) i_{corr} for S3 steel heat treated at 900°C for 6 h exposed to saturated $Ca(OH)_2$ solution containing 0.1 wt. % Cl^-	127
4.4.3.1.2.	(a) Nyquist plots of S3 steel heat treated at 900°C for 6 h after immersion in saturated $Ca(OH)_2$ solution with 0.1 wt. % Cl^-	128
	(b) High frequency portion of Nyquist plots of S3 steel heat treated at 900°C for 6 h after immersion in saturated $Ca(OH)_2$ solution with 0.1 wt. % Cl^- for 5 h	128
4.4.3.1.3.	Bode magnitude plots of S3 steel heat treated at 900°C for 6 h in saturated $Ca(OH)_2$ solution with 0.1 wt. % Cl^-	129
4.4.3.1.4.	Bode phase plots of S3 steel heat treated at 900°C for 6 h in saturated $Ca(OH)_2$ solution with 0.1 wt. % Cl^-.	130
4.4.3.1.5.	The variation of (a) R_p, (b) Y_0, and (c) α of the passive film with respect to time of immersion of S3 steel heat treated at 900°C for 6 h in saturated $Ca(OH)_2$ solution containing 0.1% wt. % Cl^-	131
4.4.3.2.1.	Schematic displaying the formation, growth and degradation of the passive film on the steel surface in saturated $Ca(OH)_2$ solution. In first condition the solution is without Cl^- or with Cl^- present in amounts lower than the threshold amount; (a) start of immersion; (b) passive layer grows with time. In second condition the solution contains Cl^- ions more than the threshold amount; (c) same as (a); (d) de-passivated steel	132
4.4.4.	The SEM-EDS study of surface morphology of S3 steel after potentiodynamic polarization testing in ($Ca(OH)_2$ + 0.14 wt. % Cl^-) solution, and elemental distribution at the corroded area	134
4.5.1.1.	True stress, true strain curves of S1 steel obtained under various deformation temperatures and strain rate of (a) 10 s^{-1}; (b) 1 s^{-1}; (c) 0.1 s^{-1}; (d) 0.01 s^{-1}	136-138
4.5.1.2.	True stress, true strain curves of S2 steel obtained under various deformation temperatures and strain rate of (a) 10 s^{-1}; (b) 1 s^{-1}; (c) 0.1 s^{-1}; (d) 0.01 s^{-1}	139-140
4.5.1.3.	The effect of alloy chemistry on the true stress, true strain curves of S1	142-

	and S2 steels at (a) 950°C and $0.01s^{-1}$; (b) 900°C and $0.01s^{-1}$; (c) 850°C and $0.01s^{-1}$; (d) 800°C and $0.01s^{-1}$	143
4.5.1.4.	True stress, true strain curves of S3 steel obtained under various deformation temperatures and strain rates of (a) 10 s^{-1}; (b) 1 s^{-1}; (c) 0.1 s^{-1}; (d) 0.01 s^{-1}	144-146
4.5.1.5.	The effect of alloy chemistry on the true stress, true strain curves of S2 and S3 steels at (a) 900°C and $0.1s^{-1}$; (b) 850°C and $0.1s^{-1}$; (c) 900°C and $0.01s^{-1}$; (d) 850°C and $0.01s^{-1}$	147-149
4.5.2.1.	Evolution of the microstructure and ferrite grain refinement at different deformation temperatures and strain rates of S1 steel	150
4.5.2.2.	SEM micrograph showing pearlite grains in S1 steel at 850°C and $0.01s^{-1}$	152
4.5.2.3.	Evolution of the microstructure and ferrite grain refinement at different deformation temperatures and strain rates of S2 steel	153
4.5.2.4.	Evolution of the microstructure and ferrite grain refinement at different deformation temperatures and strain rates of S3 steel	154
4.5.2.5.	Effect of various deformation temperatures and strain rates on the ferrite grain size of (a) S1 steel; (b) S2 steel; (c) S3 steel	155, 156
4.5.2.6.	(a) Microstructure of S2 steel compressed at 750°C and 1 s^{-1}; (b) Corresponding true stress, true strain curve	156
4.5.3.1.	Peak stress corrected for adiabatic rise in temperature for S1, S2 and S3 steels	158
4.6.2.	True stress, true strain curves of S1 steel corrected and uncorrected for deformation heating for different strain rates, at (a) 1050°C; (b) 1000°C; (c) 950°C; (d) 900°C; (e) 850°C; (f) 800°C; (g) 750°C	161-164
4.6.2.	(h) True stress, true strain curves of S1 steel corrected and uncorrected for deformation heating at 10 s^{-1} and different temperatures	164
4.6.3.1.	Light optical micrograph of S1 steel specimen, hot forged at 1150°C, etched with 2% nital solution	166
4.6.3.2.	Microstructures of specimens of S1 steel after hot compression at different temperatures and strain rates	167
4.6.5.1.	EBSD grain boundary map of S1 steel specimen hot forged at 900°C. Grain boundaries are dark (black) and the sub grain boundaries are light	169

	(green).	
4.6.5.2.	Processing map of S1 steel as a function of temperature and strain rate for the true strain of 0.6, constructed using modified DMM of Murty and Rao	170
4.6.5.3.	SEM micrographs of S1 steel after hot compression (a) with strain rate of 0.001 s^{-1}and 850°C; (b) with strain rate of 10 s^{-1}and 918°C	170

List of Tables

S.No.	List of Tables	Page no.
2.1.8.1	Effect of phosphorous on the tensile and notch-impact properties of high-purity iron and iron-carbon alloys	18
2.2.2.2	Chloride thresholds for rebars found using potentiodynamic, and open circuit potential tests	25
2.2.4.1	Corrosion rate reported by Hudson and Stanners using weight loss method	32
2.2.4.2	The corrosion properties of phosphoric irons in neutral/marine environment pH 6.8	32
2.2.5.2	Review of thermo-mechanical processing of low carbon steels	37
3.2.1	Average chemical composition (wt.%) of the steels used in the present work	50
3.3.1	Details of heat treatments conducted on high phosphorous steel specimens	51
3.5.3	Details of differently processed steel specimens used for characterization	56
4.1.1	Transformation temperatures of the 3 high phosphorous steels determined by dilatometry studies conducted in a thermo-mechanical simulator	68
4.2.1	Calculations of free energies of ferrite-austenite transformation using commercial thermodynamic software	76
4.2.2	Estimates of diffusion distances of phosphorus in S3 steel specimens held at 865°C for 24 h, water quenched, reheated and held at 750°C for different times	78
4.3.1	Change in grain size due to heat treatment of hot forged steels	81
4.3.2	Mechanical properties of S1, S2, and S3 steels in X1, X2 and X3 conditions	87
4.3.3	Comparison of experimental results with values reported for similar steels in references	89
4.3.4	Mechanical properties of the steels, hot forged and subsequently heat treated at 900°C for 1 h	94
4.3.5	Mechanical properties of steels hot forged and hot rolled at 900°C	94
4.3.6	Vickers hardness results of the three prepared high phosphorous steels in different processing conditions	95
4.4.1.1	Pitting nucleation resistance $R=\lvert ZCP-E_{pit}\rvert$ in mV for high phosphorous steels and mild steel specimens in saturated calcium hydroxide solution, with	98

	and without chloride	
4.4.3.1	Polarization resistance (R_p) in $\Omega.\text{cm}^2$ as a function of time in saturated $Ca(OH)_2$ solution with or without chloride obtained from EIS spectra modelling	124
4.4.3.2	Constant phase element (Y_0) in $\mu S \cdot s^a/cm^2$ as a function of time in saturated $Ca(OH)_2$ solution with or without chloride obtained from EIS spectra modelling	124
4.4.3.3	CPE exponent (α) as a function of time in saturated $Ca(OH)_2$ solution with or without chloride obtained from EIS spectra modelling	125
4.4.6.1	Rate of uniform corrosion obtained using immersion test	135
4.5.3.1	Maximum increment in temperature during hot compression of S1, S2 and S3 steels	157
4.5.3.2	Peak stress corrected for adiabatic rise in temperature for S1, S2 and S3 steels	157
4.5.3.3	Z values for the steels at 1, 0.1 and 0.01 s^{-1} and at 800, and 1050°C.	159
4.6.1	Maximum increment in temperature during compression of S1 steel	165
4.6.2	Flow stress at a true strain of 0.6 corrected for adiabatic rise in temperature for S1 steel	165

SYMBOLS

1.	Ar_3	Temperature at which, during cooling, transformation of the austenite into ferrite starts
2.	Ar_1	Temperature at which, during cooling, transformation of the austenite into ferrite + cementite ends
3.	D_0	Frequency factor for diffusion
4.	C	Capacitance
5.	Y_0	Constant phase element
6.	R	Resistance in corrosion section
		Universal gas constant in sinh law
7.	f	Frequency
8.	Z	Impedance
9.	i_{corr}	Corrosion current density
10.	σ	Flow stress
11.	σ_{p}	Peak flow stress
12.	ε	True strain
13.	$\dot{\varepsilon}$	Strain rate
14.	P	Power given to visco-plastic material
15.	G	Power dissipated by plastic work
16.	J	Power dissipated by microstructural changes
17.	D	Power dissipation function
18.	η	Power dissipation efficiency
19.	κ	Instability parameter proposed by Murty and Rao
20.	Z	Zener - Hollomon parameter in constitutive equations
		Impedance in electrochemical impedance spectroscopy
21.	m	Strain rate sensitivity
22.	A	Material constant
23.	Q	Activation energy
24.	α	Material constant in sinh law, stress multiplier = 0.012
		Constant phase element exponent in equivalent circuit for corrosion
		Ferrite phase
25.	γ	Austenite phase
26.	n	Stress exponent in power or sinh law
		Strain hardening exponent in mechanical properties

ABBREVIATIONS

Fig.	Figure
SEM	Scanning electron microscope
EDS	Energy dispersive spectroscopy
CCT	Continuous cooling transformation
IGF	Inter granular fracture
DBTT	Ductile brittle transition temperature
SCE	Saturated calomel electrode
SHE	Standard hydrogen electrode
OCP	Open circuit potential
ZCP	Zero current potential
LPR	Linear polarization resistance
EIS	Electrochemical impedance spectroscopy
CPE	Constant phase element
DMM	Dynamic materials model
DRV	Dynamic recovery
DRX	Dynamic recrystallization
SIDT	Strain induced dynamic transformation
SIT	Strain induced transformation
SFE	Stacking fault energy

Chapter 1

INTRODUCTION

1.1 GENERAL

Corrosion has gained considerable concern over the past many years as it causes premature failure of the metals and alloys being used in various structural and mechanical applications. The economic loss due to corrosion is estimated to be about 3% of GDP of developed nations like USA (Hays, 2016). Industrial plants, machinery, structural reinforcements, shipping, railways, etc., use iron and steel in one form or the other. Thus, corrosion of iron and steel is a major problem and of particular interest.

Ancient Indian artefacts like the Delhi iron pillar, Dhar iron pillar and Konark temple iron hooks and beams, etc., have withstood atmospheric corrosion for hundreds of years. The atmospheric conditions in India vary considerably from dry desert conditions to wet coastal conditions. The corrosion resistance of these artefacts is attributed to the presence of high phosphorous content in the metal. The ancient Indian iron making technique was essentially a sinter forge technique in which good quality iron ore was reduced using charcoal and the resulting lump was forged to squeeze out the slag. The product thus obtained had lower sulphur content than modern iron and steel which uses coke in its manufacturing. When iron and steel containing high phosphorous is manufactured in the modern furnaces via the melt route, the material suffers from low toughness. The problem is aggravated further if both carbon and phosphorous contents are high in the metal. It is for this very reason that the modern steelmaking industry has been prompted to remove phosphorous during production itself. If tough high phosphorous steel could be manufactured corrosion related losses would be mitigated.

In order to eliminate the cold shortness of iron and steel containing high phosphorous content, the researchers tried to remove phosphorous from the grain boundaries. This was accomplished by employing alloying addition of any one of these elements - C, N, B, and Si. Subsequently, the material was subjected to a heat treatment in the (α+γ) region so that the alloying elements could be partitioned between the prior phases of ferrite and austenite. The austenite phase is formed at the grain boundaries of ferrite during the intercritical heat treatment. On cooling, the partitioning at higher temperatures is retained at room temperature, thereby ensuring that phosphorous is not located at the grain boundaries of the ferrite grains.

This improves the ductility and toughness of the material. Although limited success has been achieved in improving the ductility and toughness, further improvements are required to come close to the toughness levels of plain carbon steels. Unless those levels are achieved high phosphorous steels will never be used by designers.

In the present work, an attempt has been made to improve the toughness of low carbon steels containing 0.13 wt. % phosphorous which is much higher than that recommended for modern steels *i.e.*, <0.04 wt. %. The goal here is to design tough and corrosion resistant steels for use as structural reinforcements. The alloying elements such as carbon, silicon and nitrogen were chosen to push phosphorous away from the grain boundaries. In order to further improve the partitioning of phosphorous and other alloying elements between the grain boundaries and grain interiors, a few thermo-mechanical treatments like hot forging and hot rolling, and heat treatments at intercritical temperatures have been used. Using a combination of hot forging and subsequent heat treatments at intercritical temperatures, toughness levels comparable to plain carbon steel have been achieved.

Corrosion resistance of the prepared high phosphorous steels have also been evaluated and found to be comparable to plain carbon steels. The strain rates and temperatures leading to the smallest grains have been identified by utilizing a thermo-mechanical simulator. The processing window for one high phosphorous steel has been found out.

1.2 OBJECTIVES OF THE STUDY

The overall aim of the proposed research was to improve the ductility and toughness of iron-phosphorous alloys by alloying them with small amounts of C, Si & N and employing intercritical heat treatment. In general, the objectives of the present work can be summarized as follows:

1. To design and prepare high phosphorous steels having good mechanical properties and corrosion resistance.
2. To develop high phosphorous steels with refined microstructure using thermo-mechanical processing.
3. To understand the underlying mechanisms of microstructural evolution during thermo-mechanical processing of high phosphorous steels.

4. To determine suitable thermo-mechanical processing parameters using deformation processing maps.

1.3 PLAN OF WORK

Based on the objectives of the study, the following work plan was chalked out:

a. Procurement of various materials necessary to carry out the study.
b. Melting and casting of the proposed high phosphorous steels.
c. Understanding the transformation temperatures of the high phosphorous steels by dilatometry.
d. Forging and rolling of the high phosphorous steels.
e. Heat treatment of the high phosphorous steels.
f. Metallographic study of the high phosphorous steels.
g. Evaluation of mechanical properties (Tensile, impact and hardness) of the high phosphorous steels.
h. Evaluation of corrosion properties (OCP, LPR, potentiodynamic polarization and EIS) of the high phosphorous steels.
i. Correlation of thermo-mechanical processing parameters of the high phosphorous steels with grain refinement and microstructure. Determination of the grain sizes.
j. Determining the safe hot working zones of one high phosphorous steel using deformation processing maps.

Chapter 2

LITERATURE SURVEY

2.1 IRON PHOSPHOROUS SYSTEM

The overall aim is to develop tough and corrosion resistant high phosphorous steels. Tough high phosphorous steels can be developed by utilizing alloying elements and working or heat treating within the (α+γ) phase region of the phase diagram. Since the alloying of phosphorous in steels and the ferrite-austenite duplex phase field is of interest here, the phase relationships in the Fe-P system need to be studied.

2.1.1 Equilibrium Phase Diagram of the Fe-P System

The phase diagram of the Fe-P system is presented in Fig. 2.1.1. This was ascertained by Kubaschewski after taking into consideration the findings of previous researchers like Vogel, Haughton, and Doan *et al*. (O. Kubaschewski, 1982). The equilibrium phase diagram is indicated by solid lines. Solid solubility is 4.52 atom % at 1048 ºC (Fig. 2.1.1a). The eutectic point is at 16.9 atom % P. Vogel reported that alpha-iron can assimilate 1.2 atom % phosphorous at room temperature (R. Vogel, 1929). Modern steelmakers restrict the phosphorous content to less than 0.04 wt. %. Archaeological iron artefacts have higher contents (0.05-0.5 wt. % P) of phosphorous (McDonnell, 1989). Ancient Indian (Piccardo et al., 2004) and European irons (Stewart et al., 2000a) possessed higher phosphorous content.

Vogel established the high temperature gamma loop of the Fe-P phase diagram for low phosphorous Fe-P alloys (R. Vogel, 1929). This high temperature loop (Fig. 2.1.2) has been favoured by some researchers over that established by Kubaschewski (Sahoo and Balasubramaniam, 2007a). The intercritical region is sandwiched between the ferrite and austenite phase fields in the temperature range 910°C to 1400°C. The maximum solid solubility of phosphorous in the (α+γ) region at about 1150°C is 0.57 wt. % which is lower than that reported by Kubaschewski. It can be concluded from the phase diagram that phosphorous is a stabilizer of α-ferrite.

Another attempt to establish the Fe-P phase diagram by taking into account all the findings of the previous authors and thermodynamic software has been made by Okamoto (Okamoto, 1990). He reports that the solid solubility of phosphorous in α-ferrite is 2.8 wt. % at 1048 ºC. The eutectic point is at 10.2 wt. % P.

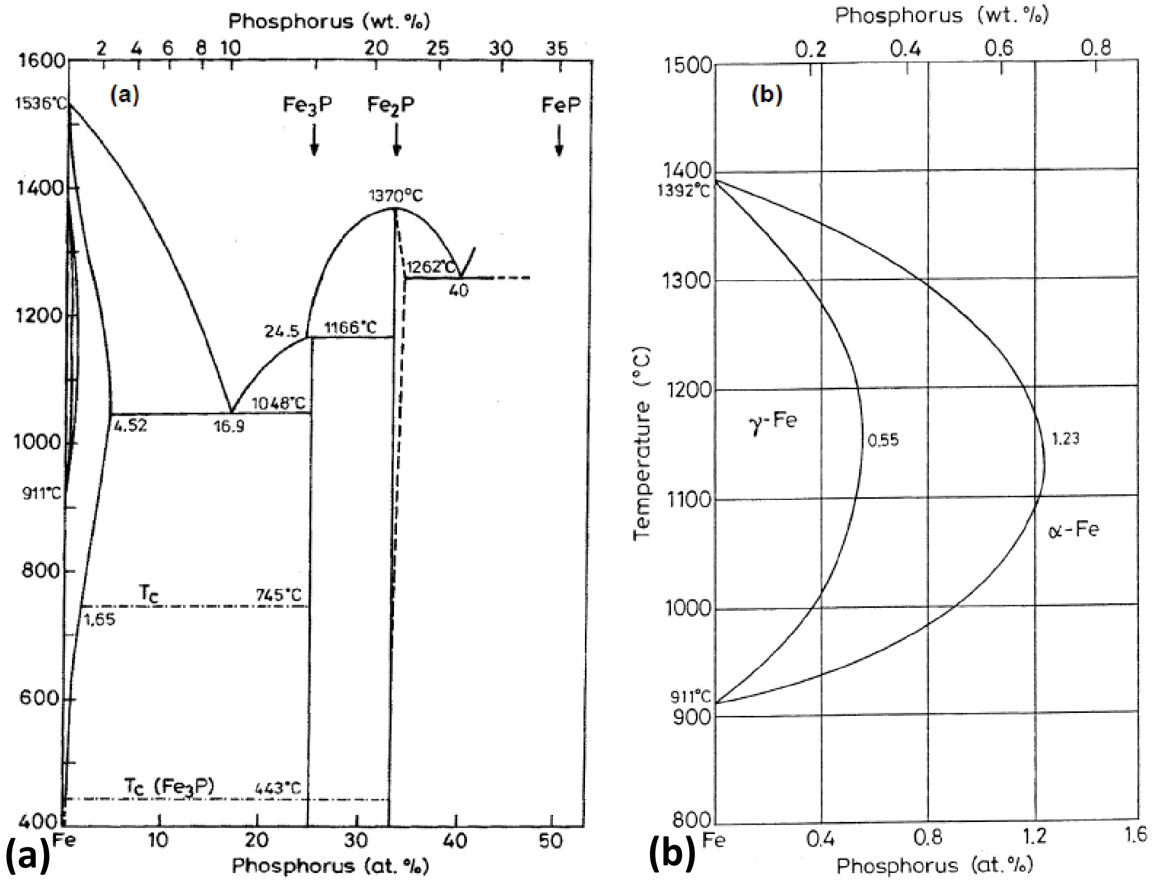

Fig. 2.1.1. (a) Fe-P binary phase diagram and (b) high temperature gamma loop region of the Fe-P phase diagram (O. Kubaschewski, 1982)

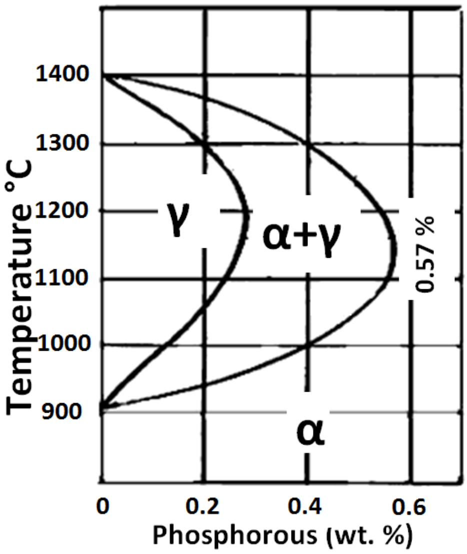

Fig. 2.1.2. High-temperature gamma loop region of Fe-P phase diagram by Vogel (R. Vogel, 1929)

The Fe-P-C ternary system has been studied by Shim *et al.* (Jae-Hyeok et al., 2000), and V.Raghavan (Raghavan, 2004). A few ternary sections are displayed as Fig. 2.1.3. The α+γ region expands at the expense of γ region as the temperature is lowered from 1100 to 800°C. According to the Fig. 2.1.3e an Fe-P-C alloy having 0.1 wt. % phosphorous and 0.05 wt. % carbon is situated in the (α+γ) region at a temperature of 800°C. Thermocalc^{TM} database can also be used for drawing phase diagrams of high phosphorous steels and studying solidification behaviour (Awe et al., 2017).

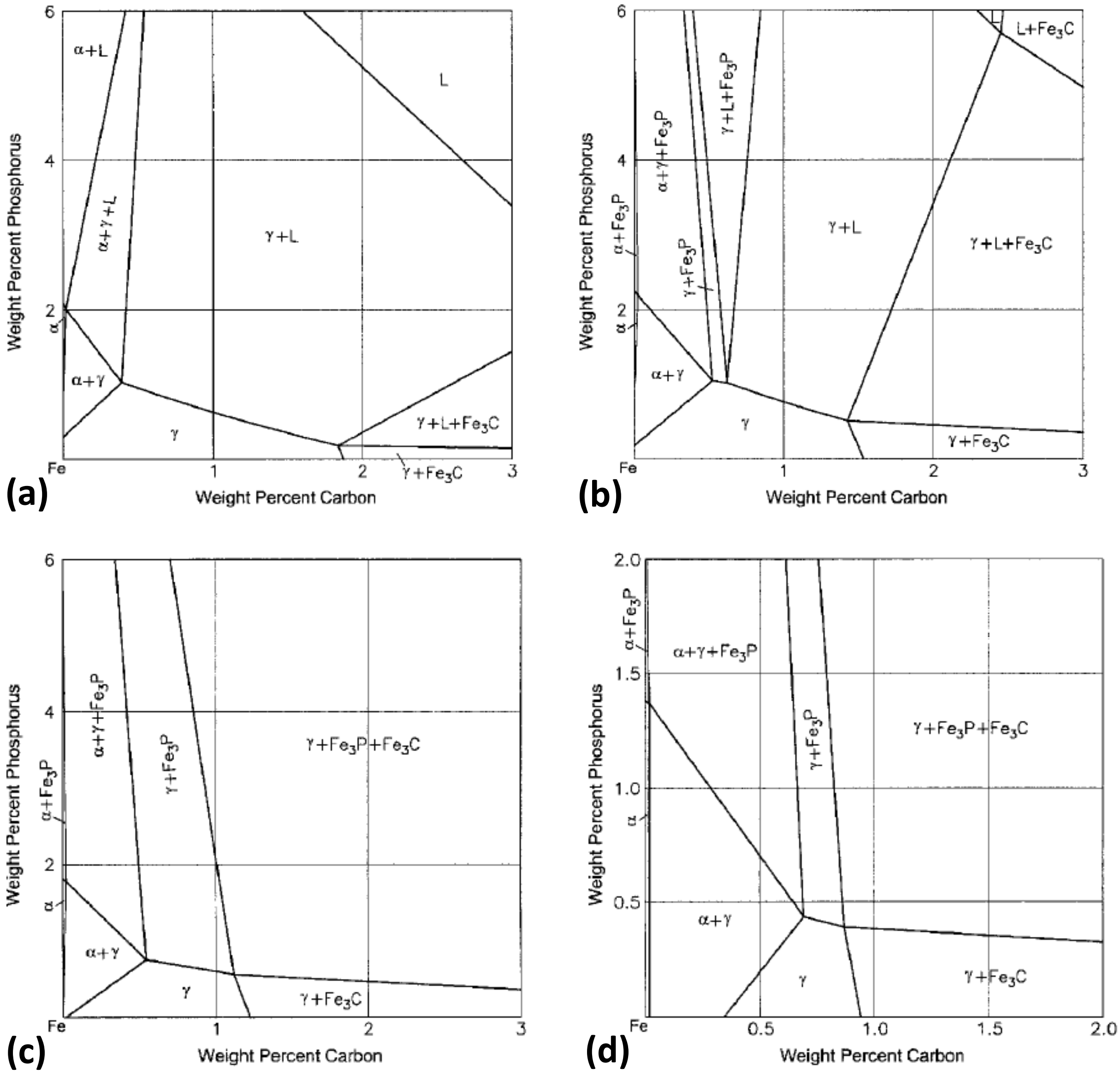

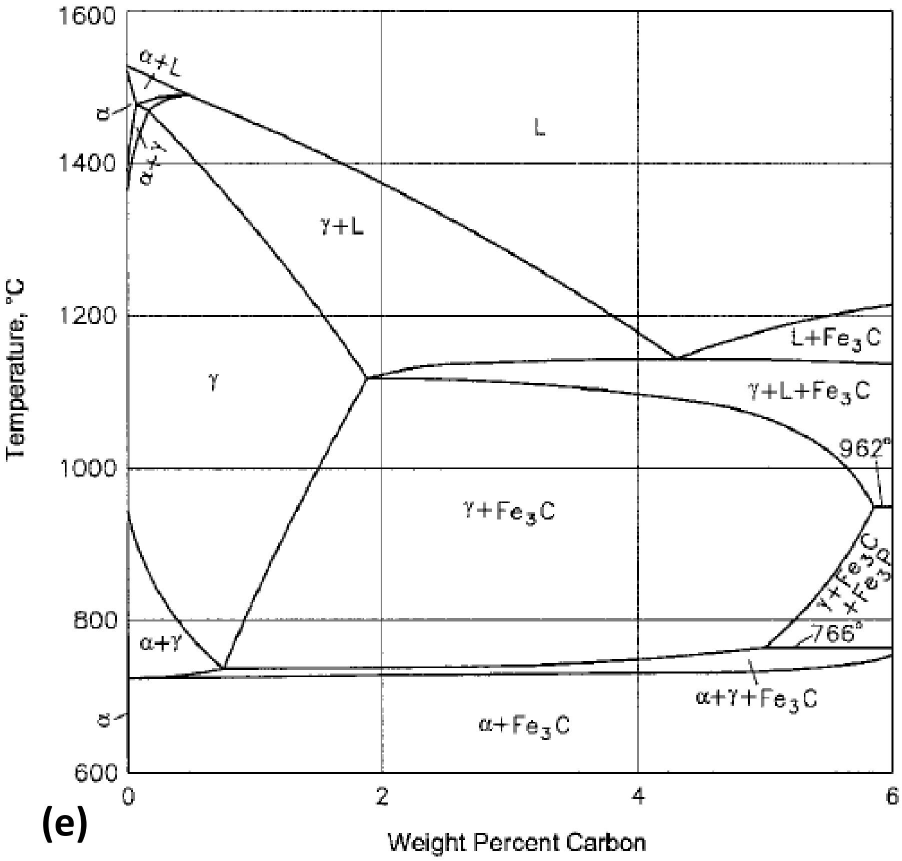

Fig. 2.1.3. C-Fe-P computed isothermal sections at (a) 1100°C and (b) 1000°C (c) 900°C and (d) 800°C (e) P=0.1 wt. %

2.1.2 Studies on the Microstructure of Fe-P Alloys using Optical Microscope

The phases in single phase alloys are identified on the basis of the contrast created between the grain interiors and the grain boundaries. Such contrast is brought about by etching the surface with an etching reagent. Stewart *et al.*, Sahoo and other researchers have used a special etching reagent for the metallographic study of Fe-P alloys (O. Kubaschewski, 1982), (R. Vogel, 1929), (Sahoo and Balasubramaniam, 2007b; Stewart et al., 2000a, 2000b). This special etching reagent was used to differentiate and delineate the ferrite and prior austenite phases of the high phosphorous alloys. The etchant is known as the Oberhoffer's reagent and is traditionally used to display microstructural inhomogeneity of phosphorous in iron. The reagent consists of 500 mL H_2O + 30 g $FeCl_3$ + 0.5 g $SnCl_2$ +1 g $CuCl_2$ + 500 mL C_2H_5OH + 50 mL HNO_3 (Stewart et al., 2000a). Copper (II) in Oberhoffer's reagent is precipitated first on low phosphorus regions (Stewart et al., 2000b). Hence, optical observation after etching shows that the high phosphorus areas (*e.g.,* ferrite) appear light while those low in phosphorus (*e.g.,* prior austenite) appear dark due to the precipitated copper.

Stewart *et al*. conducted metallography studies of Fe-P alloys containing 0.1, 0.2, & 0.38 phosphorous. A few specimens were held in the (α+γ) region and then air-cooled or water quenched. Inhomogeneity in phosphorous content was present in these samples at high temperatures and the same was maintained after cooling down to room temperatures too. The prior austenite grains of higher temperatures which transformed to ferrite at room temperatures appeared dark due to the deposition of copper. Similarly, the prior ferrite grains appeared bright on being etched with Oberhoffer's reagent.

Nital solution can also be used for studying Fe-P alloys. It attacks the low phosphorous areas preferentially. This creates a surface relief in the low phosphorous regions on the etched surface of the alloy. The revealed regions were austenite when held at higher temperatures in the (α+γ) region. The term used to delineate such a condition is 'ghost' structure or ghosting (Fig. 2.1.2.6) (Stead, 1915). The contrast produced by nital solution is possible due to the distinct phase boundaries between prior austenite and prior ferrite.

With increasing phosphorus content more ferrite has been formed with finer grains (Li et al., 2006). Phosphorus promotes Cu_2S precipitation in α-Fe instead of in γ-Fe and changes the morphology of Cu_2S from plate-like to spherical. The Cu_2S sizes are smaller than those in low phosphorus steel (Liu et al., 2005). In contrast to the straight dislocation segments in the 0.15C steel, tangled and curved dislocations are observed in the phosphorus steel in both the as-rolled and annealed conditions. A high dislocation density of about two times higher than that in the 0.15C steel is revealed in the 0.15C-0.1P steel (Yin et al., 2003) .

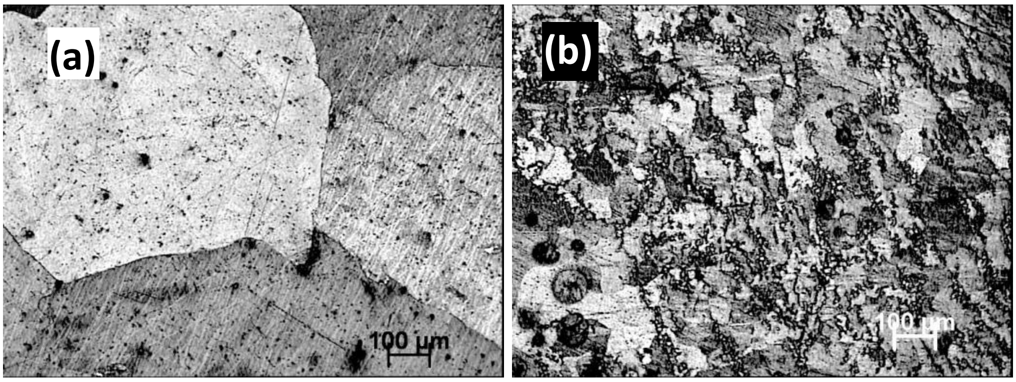

Fig. 2.1.2.1. Microstructure of Fe-0.29P-0.03C-0.2Si-0.2Mn-0.14Cr alloy; (a) As cast; (b) hot forged; and etched with 2% nital solution (Mehta and Mishra, 2011)

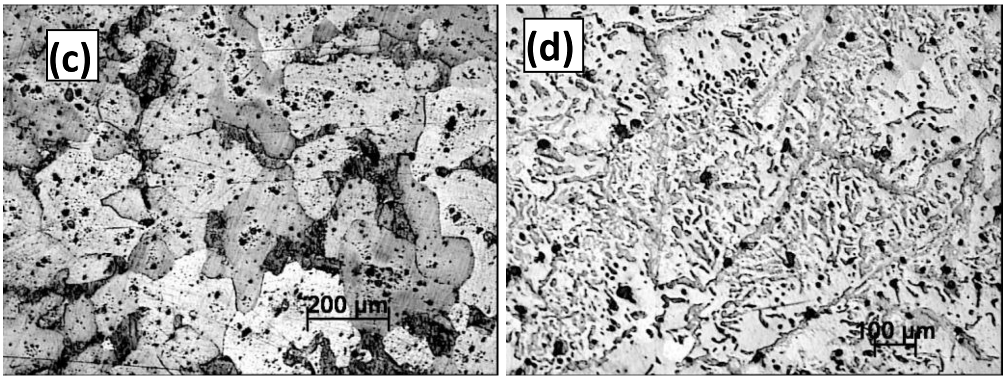

Fig. 2.1.2.2. Microstructure of Fe-0.28P-0.14C-0.18Si-0.2Mn-0.15Cr alloy; (c) As cast; (d) hot forged; and etched with 2% nital solution (Mehta and Mishra, 2011)

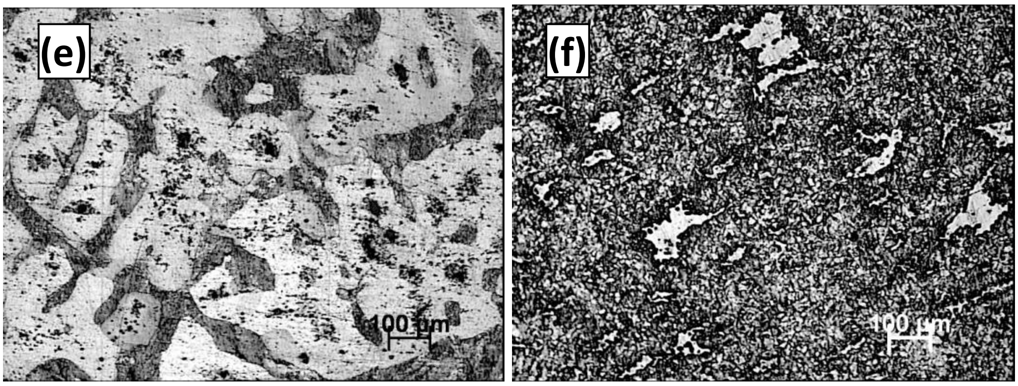

Fig. 2.1.2.3. Microstructure of Fe-0.29P-0.23C-0.16Si-0.22Mn-0.16Cr alloy; (e) As cast; (f) hot forged; and etched with 2% nital solution (Mehta and Mishra, 2011)

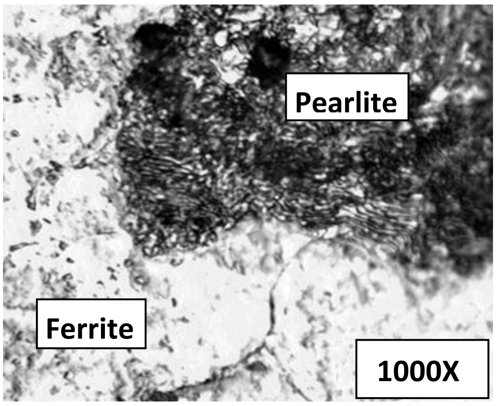

Fig. 2.1.2.4. Microstructure of Fe-0.281P-0.145C-0.182Si-0.206Mn-0.15Cr alloy heat treated at 800˚C for 30 min, normalized and etched with 2% nital solution (Mehta et al., 2010)

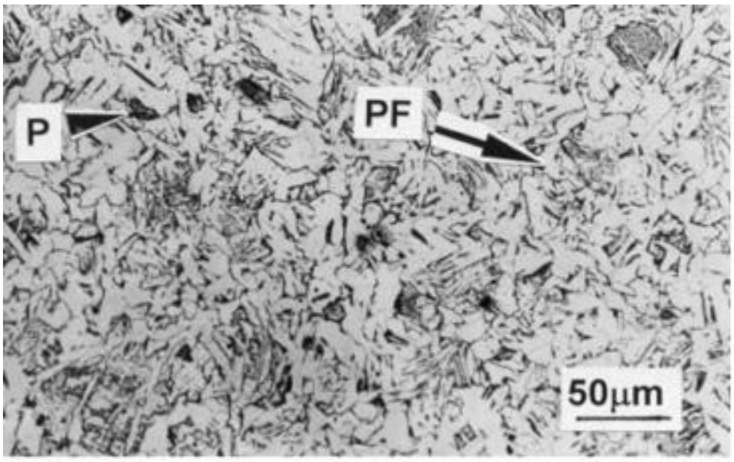

Fig. 2.1.2.5. Microstructure of Fe-0.11P-0.08C reinforcement bar steel etched with 2% nital solution (PF = polygonal ferrite; P = pearlite/carbide) (Panigrahi, 2010a)

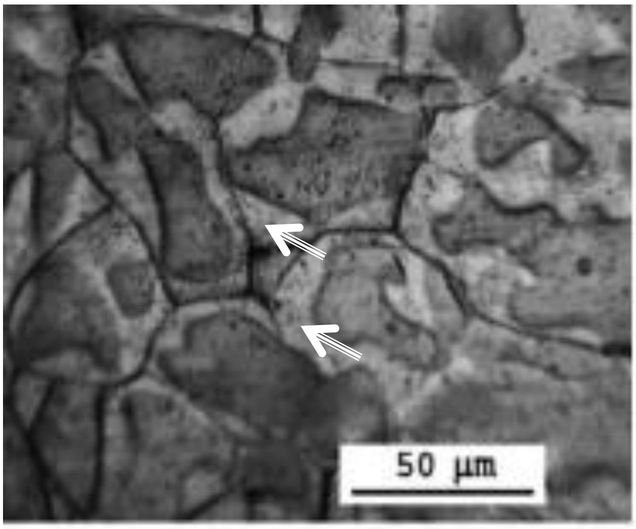

Fig. 2.1.2.6. Optical micrographs of Fe-0.3P-0.02C alloy after etching with nital solution, showing prior austenite regions (indicated by arrows) along the grain boundary (Sahoo and Balasubramaniam, 2007a)

Figures 2.1.2.1 to 2.1.2.5 show the microstructures of low carbon and high phosphorous alloys. Pearlite and ferrite are the most common phases found in them. Fig. 2.1.2.6 shows a typical example of ghosting microstructure. This microstructure is obtained as a result of variation in the concentration of phosphorous in the material.

2.1.3 Transformations in the Fe-P System

Phosphorous can be removed from the grain boundaries of ferrite if it is displaced away by carbon. This partitioning of alloying elements requires an understanding of the phase transformations and the time required to bring about a partitioning to improve toughness. The phase morphology during nucleation and growth of ferrite phase transformed from austenite during cooling, and austenite phase transformed from ferrite during heating has been studied by earlier authors (R. Vogel, 1929) (Stewart et al., 2000a) and is given below.

2.1.3.1 Partitioning of alloying elements during the formation and growth of γ-austenite from α-ferrite

The partitioning of alloying elements during the formation and growth of γ-austenite from α-ferrite in Fe-0.2P alloys was studied by Stewart *et al.* (Stewart et al., 2000a). They heated the specimens at 972°C for various time periods. Austenite nucleated and grew from the ferrite grain boundaries as needles and allotriomorphs. Austenite spheroidized and coarsened with time and an equilibrium dual phase microstructure was developed fully after 24 h. Phosphorous diffused into ferrite grains and carbon diffused into austenite grains. Similarly, the transformation of Fe-0.1P was also studied at 935°C for times upto 24 h. Another study was conducted on Fe-0.11P at 950°C upto 24 h and Fe-0.32P and Fe-0.49P at 1100°C for times upto 12 h (Sahoo and Balasubramaniam, 2007b). It was found that the phase fractions were in better agreement with the high temperature loop of Vogel (R. Vogel, 1929).

2.1.3.2 Partitioning of alloying elements during the formation and growth of α-ferrite from γ-austenite

The partitioning of alloying elements during the formation and growth of α-ferrite from γ-austenite was studied by Stewart *et al.* in Fe-0.2P alloys. The specimen was initially austenitized at 1100°C for 10 min and then held at 940°C in the (α+γ) region for varying times upto 4 h before rapid cooling to room temperature. Ferrite allotriomorphs grew at the grain boundaries of austenite and thickened with increasing time. Phosphorous diffused into ferrite grains and out of austenite grains creating the basis of a contrast revealed by Oberhoffer's reagent. A dual phase microstructure was observed at longer times.

2.1.3.3 Kinetics of diffusion of phosphorous

The partitioning of phosphorous between ferrite and austenite at high temperatures does not manifest on cooling itself. The alloy should be held or worked in the ferrite-austenite duplex phase region for longer periods of time. The transformation from austenite to ferrite was slower than the opposite transformation (Rocquet and Jegaden, 1951). Phosphorous is a substitutional element (Pickering F.B., 1978). The rate of diffusion of phosphorous in austenite is lower than that in ferrite (Stead, 1915). The phosphorous inhomogeneity created by holding in the dual phase region was removed by heat treating at 900°C for 4 to 24 h (Stewart et al., 2000a). Short period of heat treatment in dual phase region partitions phosphorous between the prior phases of austenite and ferrite (Stewart et al., 2000a). This helps in reducing grain boundary segregation of phosphorous. The frequency factor D_0 for the diffusion of phosphorous in ferrite is $7.1\text{X}10^{-3}$ cm^2s^{-1} for the temperature range 700 - 850°C, and 2.9 cm^2s^{-1} for the temperature range 860 - 900°C. The activation energy Q for the diffusion of phosphorous in ferrite is 167.36 kJ/mol for the temperature range 700 - 850°C, and 230.12 kJ/mol for the temperature range 860 - 900°C (Askill, 1970).

2.1.4 Use of Dilatometry to study transformations

The transformation of BCC ferrite to FCC austenite is accompanied by a change in volume. This happens due to the fact that atoms are more closely packed in an FCC lattice as compared to a BCC lattice. The dilatometer uses the relative change in length of the specimen to determine the transformation temperature of phase transformations in steel. While cooling the austenitized specimen Ar_1 ($\alpha+\gamma\rightarrow\alpha$) and Ar_3 ($\gamma\rightarrow\alpha+\gamma$) temperatures can be found by determining the temperature where the linear thermal expansion deviates from linearity (Prado et al., 1990). Rocquet *et al.* (Rocquet and Jegaden, 1951), and Sahoo and Balasubramaniam (Sahoo et al., 2008) have used dilatometry to study Fe-P alloys.

2.1.5 Effect of alloying elements in wrought Fe-P alloys

The brittleness of phosphorus-containing wrought steel arises due to grain boundary segregation of phosphorus. The presence of a small amount of alloying elements (C, N, B, etc.) displaces phosphorus from the grain boundaries. This improves grain boundary cohesion and enhances ductility and toughness of the material. Nickel reduces the ductile brittle transition temperature by solution softening effect in Fe-P alloys. Silicon reduces DBTT and susceptibility to intergranular failure of Fe-P alloys. Molybdenum and Niobium improve toughness in steels containing phosphorous.

2.1.5.1 Effect of carbon

The presence of a small amount of carbon at the grain boundaries displaces phosphorus from those areas by a site competition effect (Suzuki et al., 1985)(H Erhart and Grabke, 1981). Therefore, by a judicious use of carbon in high phosphorous steels, required ductility can be obtained. Grain boundary segregation of carbon is determined by the concentration of dissolved carbon alone, and not by the total carbon (Hansel and Grabke, 1986). The tendency of grain boundary segregation of carbon is higher because its segregation free energy ΔG (−72 kJ/mol at 773 K) is much more negative than that of phosphorus (−49 kJ/mol at 773 K) (Hansel and Grabke, 1986).

2.1.5.2 Effect of nitrogen

The grain boundary concentration of phosphorus decreases when the bulk content of nitrogen increases. At the same time the nitrogen concentration at the grain boundary increases. Nitrogen (0.05 wt. %) can expel phosphorus (0.17 wt. %) from the grain boundary sites. This affects the fracture mode and decreases the percentage of inter granular fracture, hence decreasing embrittlement (H. Erhart and Grabke, 1981).

2.1.5.3 Effect of boron

The effect of boron on the segregation of phosphorus at the grain boundaries in a high-purity Fe-0.2 wt. % P alloy has been studied by Auger electron spectroscopy (AES). The segregation of phosphorus decreases with the increased segregation of boron. Phosphorus atoms are displaced by boron atoms at the grain boundaries. The effect of boron on the phosphorus-induced intergranular fracture (IGF) has been examined with impact testing. The fracture surfaces have been studied with scanning electron microscopy (SEM). Addition of 12.5 wt. ppm boron completely prevents the IGF induced by the segregation of phosphorus and decreases the ductile-brittle transition temperature (DBTT) by about 170 K when quenched from 800°C. The aforesaid suppression of the IGF due to the addition of boron is caused by two mechanisms:

a) Increased grain boundary cohesion of iron is caused by the segregated boron.
b) Decrease in the segregation of phosphorus is caused by the segregation of boron.

The former has been found to be more effective in suppressing the IGF (Liu et al., 1992).

2.1.5.4 Effect of sulfur

Segregation of phosphorus and sulfur to grain boundaries of ultra-low carbon steel (IF-steel) was investigated by Auger electron spectroscopy (AES) and scanning electron microscopy (SEM). The segregation kinetics of both phosphorus and sulfur while holding at 600°C has the characteristics of non-equilibrium segregation. Phosphorus and sulfur segregate competitively at the grain boundaries of iron. This competition appears to be a thermodynamic effect. Generally, an increase in the activity of one element in solid solution increases its concentration at the grain boundary which in turn decreases the concentration of the other element at the grain boundary (Briant, 1988)(Zhang et al., 2000).

2.1.5.5 Effect of nickel

The degree of phosphorus segregation and the grain size are independent of the bulk nickel concentration (0.23-0.95 wt. %). A decrease in susceptibility to intergranular fracture and hence ductile to brittle transition temperature is observed only when the solution-softening effect of nickel is present (Saito et al., 1988). The addition of nickel to Fe-P alloys decreases the ductile brittle transition temperature as determined by Charpy impact test. The decrease in DBTT means a decrease in the susceptibility of the alloys to IGF.

2.1.5.6 Effect of chromium

Chromium reduces intergranular fracture in Fe-P alloys containing carbon within its solubility limit, and enhances intergranular fracture in alloys containing carbon above its solubility limit (Liu et al., 1994). Chromium is believed to improve grain boundary cohesion by segregating to grain boundaries and/or by reducing the deleterious effect of phosphorus, owing to the attractive interaction between the segregated chromium and phosphorus (Liu et al., 1994).

2.1.5.7 Effect of manganese

Mn decreases the activity and solubility of carbon. This decreases the effect of carbon which competes with phosphorous for the sites at the grain boundaries. The grain boundary segregation of phosphorous increases with increasing manganese content, in alloys containing manganese and carbon. Mn itself segregates to the grain boundaries and this may also cause a certain embrittlement. The diffusivity of phosphorous is accelerated by manganese as an alloying element in ferrite. Phosphorous can thus, diffuse faster to the grain boundaries in high manganese steels during cooling in the critical temperature range of 600 to 400°C after tempering (Hennesen et al., 1987).

2.1.5.8 Effect of vanadium

The influence of vanadium on grain boundary segregation of phosphorus has been studied in iron and iron-carbon alloys by means of fracture experiments in a scanning Auger microprobe. It is found that the principal determining factor in the scavenging or retardation of migration of phosphorus to the grain boundaries is whether vanadium is present in the combined form (say, carbide) or is available in solid solution form. When vanadium is present in solid solution form, grain boundary segregation of phosphorus is low due to the chemical interaction of vanadium and phosphorus. However, as carbon is increasingly introduced into the alloy, vanadium now preferentially reacts with carbon in view of higher interaction for carbon as compared to phosphorus. A consequence of this is the increase in the grain boundary concentration of phosphorus (Misra, 1991).

2.1.5.9 Effect of silicon

The grain boundary segregation of solutes has been investigated in high purity Fe-Si-P alloys. Solutes were dissolved, and the specimens were heat-treated within the alpha phase region. The segregation of P was reduced by the addition of Si, and vice versa. Addition of 0.5 wt. % Si reduced the ductile-brittle transition temperature as determined by small scale Charpy impact test by approx. 100 K, and the fracture mode changed from intergranular to transgranular (Liu et al., 1989).

2.1.5.10 Effect of molybdenum

The effect of molybdenum could be that of co-segregation with carbon; causing carbon-induced enhancement of cohesion which would offset the embrittling effect of phosphorous (Menyhard and McMahon, 1989). Molybdenum prevents the diffusion transfer of phosphorus in the bulk of the ferrite grains and slows down the enrichment of the former austenite grain boundaries in phosphorus thus inhibiting reversible temper brittleness (Gruzin and Mural, 1969). For a given amount of P grain boundary segregation the grain boundary strength increases with increasing Mo or W grain boundary segregation and decreases with increasing Mn grain boundary segregation (Lee et al., 1984).

2.1.5.11 Effect of niobium

During the coiling stage of the thermo-mechanical processing of Ti-stabilized interstitial-free steels, P segregates to the ferrite grain boundaries. The addition of Nb decreased the segregation of P in the as-coiled condition. Presence of Nb on the ferrite grain boundaries is believed to increase the grain boundary cohesion (Rege et al., 2000).

Thus, carbon, nitrogen, boron, sulfur and vanadium reduce grain boundary segregation of phosphorous. Nickel and molybdenum too reduce the brittleness. Manganese (> 0.2 wt. %) should be avoided in phosphorous steels.

2.1.6 Phosphorous Alloying in Iron

Although some researchers have highlighted the problematic aspects of phosphorous alloyed in iron others have pointed out the positive effects attributable to it.

Stead (Stead, 1915) reported that many prominent metallurgists viewed phosphorous as a treacherous impurity since it causes marked work-hardening and hence brittleness in steel during cold working (Abiko et al., 1982). Phosphorous segregates to the grain boundaries of iron and causes brittleness (Stewart et al., 2000c), (Hansel and Grabke, 1986; Inman and Tipler, 1958), (Menyhard, 1992). Phosphorous segregates to the grain boundaries and reduces grain boundary cohesion thus causing intergranular failure (Hansel and Grabke, 1986), (Inman and Tipler, 1958), (Menyhard, 1992). Due to this phosphorous content is usually controlled to 0.04 wt. % in contemporary steels (Boyer and Gall, 1990)(Gouthama and Balasubramaniam, 2003). Archaeological phosphoric irons generally contain 0.05-0.5 wt. % P (McDonnell, 1989)(Gouthama and Balasubramaniam, 2003). Phosphorous in irons reduces ductility during prolonged exposure of steel in the temperature range 250-600°C (Briant and Banerji, 1982), (Horn and Ritchie, 1978), (Capus and Meyer, 1963), (Capus and Meyer, 1960), (Briant and Banerji, 1982), (Briant and Banerji, 1979). Phosphorous increases the ductile to brittle transition temperature of steel (Goodway and Fisher, 1988), (Capus and Meyer, 1963). Phosphorous increases the flow stress promoting cleavage fracture (Yu-Qing and McMahon, 1987).

Other researchers have highlighted the benefits of alloying iron with phosphorous. Phosphorous does not render the iron ‘hot short’ or brittle at high temperatures (Gouthama and Balasubramaniam, 2003). Phosphorous has a marked solid solution strengthening effect in ferrite which is of the same order as the interstitial elements, carbon and nitrogen (Allen, 1963), (Clarke and McIvor, 1989). Hopkins *et al.* (Hopkins and Tipler, 1958) found that the tensile properties and ductile brittle transition temperature of Fe-P alloys containing small amount of carbon (0.05 wt. % C) were similar to that of Fe-0.15 wt. % C alloys. The presence of carbon improves grain boundary cohesion (Abiko et al., 1982). The presence of small amount of carbon displaces phosphorous from grain boundaries by site competition effect (De Avillez and Rios, 1983; Hansel and Grabke, 1986; Menyhard, 1992), (Stewart et al., 2000c). Therefore, required ductility and toughness can be obtained by proper selection of the carbon content in phosphoric irons and by suitable soaking at high temperature of the $(\alpha+\gamma)$ dual phase region in the Fe-P phase diagram (Suzuki et al., 1985), (Gouthama and

Balasubramaniam, 2003). The alloy design of ductile Fe-P alloys calls for avoiding P segregation to the grain boundaries by precipitating austenite allotriomorphs, by utilizing a critical amount of carbon to segregate carbon or precipitate carbide at grain boundaries and by precipitating some of the P in solid solution in the form of fine coherent phosphide precipitates (Gouthama and Balasubramaniam, 2003).

Thus, phosphorous increases strength and ductile brittle transition temperature while decreasing the ductility of iron. Addition of carbon, nitrogen, boron, silicon, etc as alloying additions and heat treatment in the dual phase region improve its ductility and toughness. This is brought about by removing phosphorous from the grain boundaries.

2.1.7 Effect of Phosphorous on the Mechanical Behaviour of Steel

If low alloy steel containing phosphorous is heated in the temperature range of 300 to 450 ºC, there is loss in toughness which is called temper embrittlement. This can be avoided by cooling the specimen quickly in the range 300-450 ºC. Phosphorous, arsenic, antimony or tin segregate to the grain boundaries and reduce the cohesive energy leading to temper embrittlement in steel (Mulford et al., 1976; Woodfine, 1953a, 1953b)(ISO 898-1, 2013). Above certain concentrations molybdenum, vanadium and tungsten cause embrittlement in steel (Guttmann, 1980). Phosphorous promotes cold shortness or brittleness during cold working (Goodway and Fisher, 1988). Addition of 0.01 wt. % phosphorous raises the ductile to brittle transformation temperature by 7°C (Rinebolt and Harris, 1951). In case the DBTT falls above the cold working temperature, the steel shall become brittle.

The atomic radius of phosphorous is 0.11 nm and that of iron is 0.124 nm. Thus, when phosphorous atom substitutes an iron atom in the lattice distortion of the lattice, it causes an increase in strength and decrease in ductility. Thus, phosphorous causes solid solution strengthening in iron which is the largest observed for substitutional solutes (Spitzig, 1972), (W. A. Spitzig and Sober, 1977; W.A. Spitzig and Sober, 1977), (Spitzig, 1974). The addition of 0.05 to 0.1 wt. % P causes an increase in yield strength of low carbon steel by 40-50% without affecting the transition temperature (Spitzig, 1972). Low carbon phosphoric iron (0.15 wt. % P) was used to produce music wire in musical instruments in ancient times (Goodway, 1993), (Goodway and Fisher, 1988). Automobile steel sheets containing about 0.01 wt. % carbon have been strengthened by using ~0.1 wt. % P (Hu, 1976)(Hu, 1979).

The toughness of steel is determined by Charpy impact test. Addition of either carbon or phosphorous to iron increases the ductile to brittle transition temperature. The addition of manganese lowers it and thus counteracts the effect of carbon. Manganese should be three times the concentration of carbon in mild steel in order to attain satisfactory notch toughness (Rinebolt and Harris, 1951). Hopkins *et al.* found that phosphorous weakened the grain boundaries and that this could be remedied by adding 0.05 wt. % carbon (Hopkins and Tipler, 1958). Other researchers found that optimum carbon concentration for achieving ductile failures was 0.01 wt. % (Abiko et al., 1982), (Suzuki et al., 1985). The harmful effect of TiN particles and MnS inclusions on impact toughness and ductile brittle transition temperature (DBTT) can be remedied by refining the grain size and restricting the intensity of low-angle boundaries (Modak et al., 2016).

Stewart *et al.* found that a specimen of Fe-0.37P alloy heated in the ferritic region failed in a fully brittle manner and another specimen of Fe-0.37P alloy heated in the dual phase region failed in a ductile manner. The improvement in ductility was ascribed to the formation of austenite at the grain boundaries of ferrite. The grain boundary segregation of phosphorous in austenite decreases since the solubility of phosphorous is low in austenite. Conversely, carbon being an austenite stabilizer gets concentrated at the grain boundary. The effect of phosphorous on the tensile and notch-impact properties of high-purity iron and iron-carbon alloys is listed in Table 2.1.8.1.

Table 2.1.8.1: Effect of phosphorous on the tensile and notch-impact properties of high-purity iron and iron-carbon alloys

Material	YS, MPa	UTS, MPa	El, %	DBTT, °C	Heat Treatment	Ref.
Fe-0.12C-0.087P-0.4Mn -0.015N	323	432	26	-70	950°C, Air cool	(Josefsson, 1954)
Sample size for Impact test 10x10x55mm						
Fe	103	241	56	-10	950°C, Air cool	(Hopkins and Tipler, 1958)
Fe-0.05P	110	255	55	-13		
Fe-0.1P	124	262	45	20		
Fe-0.15P	152	290	43	60		
Fe-0.3P	207	345	42	155		
Fe -0.05C	124	262	54	70		
Fe-0.05C-0.05P	152	296	52	50		

Fe-0.05C-0.1P	180	324	50	63		
Fe-0.05C-0.15P	207	345	46	78		
Fe-0.15C	152	303	50	67		
Fe-0.15C-0.05P	180	331	38	48		
Fe-0.15C-0.1P	193	359	44	51		
Fe-0.15C-0.15P	207	386	44	59		
Fe-0.05P-0.15C-0.5Mn	193	359	44	40		
Compression strength		Sample size for Impact test 5x10x55 mm				
Fe-0.05P	220	-	-	-38	Heats treated in evacuated vycor capsules; brine quench.	(Spitzig, 1972)
Fe-0.1P	240	-	-	-38		
Fe-0.2P	265	-	-	14		
Fe-0.6P	400	-	-	186		
Sample size for Impact test 5x10x55 mm						
0.1C, 1.0 Mn	210	460	-	-25	Normalized at 925°C for 1.2 h.	(W. A. Spitzig and Sober, 1977)
0.1C, 1.0 Mn-0.05P	230	485	-	-16		
0.1C, 1.0 Mn-0.1 P	280	525	-	20		
0.1C, 1.0 Mn-0.2 P	310	610	-	60		
Sample size for Impact test 4x4x55 mm						
Fe-0.2P	450	-	-	95	Quenched at 1373 K and annealed at 973 K	(Saito et al., 1988)
Fe-0.2P-0.25Ni	430	-	-	84		
Fe-0.2P-0.5Ni	410	-	-	75		
Fe-0.2P-1Ni	400	-	-	60		
Fe-0.006P-0.5 Si-1.3 Mn-0.18 C	500	900	26	-	Intercritical anneal for 1-7.5 min, hold at 673-723 K for 1-5 min	(Chen et al., 1989)
Fe-0.07P-0.5 Si-1.5 Mn-0.12 C	450	740	35	-		
Fe-0.2P-0.5 Si-1.5 Mn-0.14 C	475	645	27	-		
Sample size for Impact test 4x4x55 mm						
Fe-0.2P	355	-	-	147	Quench to 273 K after annealing at 1073 K for 1 h	(Liu et al., 1994)
Fe-0.2P-1Cr	356	-	-	127		
Fe-0.2P-2Cr	380	-	-	115		
Fe-0.2P-0.016C	-	-	-	-42		
Fe-0.2P-2Cr-0.016C	-	-	-	-43		

Fe-0.1 P-0.013C	200	340	45	-	Heat at 1100°C for 4 days; water quench.	(Stewart et al., 2000c)
Fe-0.2 P-0.004C	210	360	47	-		
Fe-0.37 P-0.003C	250	400	43	-		
Fe-0.38 P-0.01C	253	405	44	-		
Sample size for Impact test 5x10x55mm						
Fe-0.17C-0.093P-0.99Mn-0.017S	-	-	-	4	TMT	(Panigrahi and Jain, 2002)
Fe-0.14C-0.092P-0.93Mn-0.029S	605	698	19	1		
Fe-0.077C-0.11P-0.59Mn-0.023S	428	539	25	-20		(Panigrahi, 2010a)
Fe-0.11P-0.028C	325	425	35	-	Soak at 1150°C in (α+γ); forge	(Sahoo and Balasubramaniam, 2007a)
Fe-0.32P-0.026C	440	575	26	-		
Fe-0.49P-0.022C	550	580	4	-		
Fe-0.3P-0.03C-0.2Si-0.2Mn	468	593	25	-	Hot forged twice, 1150°C	(Mehta and Mishra, 2011)
Fe-0.3P-0.15C-0.2Si-0.2Mn	471	618	24	-		
Fe-0.3P-0.24C-0.2Si-0.2Mn	520	706	25	-		
Fe-0.15C-0.15P-0.2Cu-0.1Mn	315	460	20	-		(ASTM A242-04, 2001)

The fracture surface of the 0.1 wt. % P annealed alloy is totally transgranular. Fracture initiates at the weakened grain boundaries, however, when the boundary is inherently bending, for instance due to lamellae of cementite, the fracture occurs along the planes of cementite. At the carbide-matrix interface the phosphorus concentration is about half that at the grain boundary (Yendrzhievsky and Klimkin, 1994). Therefore, an optimum amount of carbon should be added to the alloy to ensure that the amount of carbide is low enough to avoid crack propagation along the cementite planes.

2.1.8 Advantages of Phosphorus in Ingot Metallurgy

Phosphorus is a very effective alloying element in ingot iron because of its following features:

1. It improves corrosion resistance of steel in coastal regions (Kreyser and Eckermann, 1992).
2. Effectively strengthens ferrite phase (next only to carbon and nitrogen) by substitutional solid solution strengthening mechanism (Renavikar, 2003).
3. P also segregates to the ferrite grain boundaries and hence brings about strengthening by grain boundary hardening (Renavikar, 2003).
4. It improves wear resistance (Svidunovich et al., 1989) (Sharma et al., 2015).
5. P imparts the highest increase in yield stress per unit wt. pct. added compared to other substitutional solutes in steel (Gladman, 1997) (Spitzig, 1972).
6. Increase in P increased the fatigue limit of pure iron (Islam et al., 2011).
7. The spot weldability of re-phosphorized steels is comparable with that of carbon steels, albeit up to 0.1 wt. % P (Sawhill and Baker, 1980).

Hadfield opines that phosphorous has no disastrous effect on the toughness of red-hot metal when the content does not exceed 0.15 per cent but phosphoritic metal should be finished at a lower temperature than pure steel, in order to prevent the formation of a crystalline structure during the cooling (Hadfield, 1889), (Fidler, 1907).

2.2 EFFECT OF PHOSPHOROUS ON CORROSION RESISTANCE OF IRON AND IRON-CARBON ALLOYS

2.2.1 Reinforcing Bar

Concrete is reinforced by using reinforcing steel bars or rebars. These are popular in the construction of bridges, dams, high-rises, fly-overs, etc. There are three main types of rebar used in the construction industry (Chilton and Roberts, 1980; Harrison, 1977; Martinez et al., 1995; Panigrahi and Jain, 2002). These include cold twisted deformed rebars, hot rolled rebars and thermo-mechanically treated rebars. The strength of cold twisted rebar depends on carbon content due to which higher strength bars had problems with ductility and weldability (Harrison, 1977). Vanadium (≤0.24 wt. %) and/or Niobium (≤ 0.23 wt. %) are used as alloying elements to strengthen and toughen hot rolled rebars (Chilton and Roberts, 1980; Martinez et al., 1995). Thermo-mechanical treatment of the rebar involves online quenching and self-tempering of the rebar during hot rolling. During quenching the temperature of the outer region of the rod falls below the Ms (<400°C) temperature and martensite is formed. This martensite is tempered by the heat trapped inside the ferrite-pearlite core. Thus, the microstructure of the bar consists of tempered martensite, bainite, ferrite and pearlite producing an optimum combination of strength and toughness (Kundu et al., 2004; Panigrahi and Jain, 2002).

2.2.2 Corrosion of Reinforcement Bars

Corrosion of rebar causes deterioration of reinforced concrete structures. Corrosion can be either due to carbonation or presence of chloride ions. Chloride ions could be present either in the raw materials or the service environment. Corrosion renders structures unsafe (Cramer et al., 2002). Generally, the rebar is in a passive state inside the concrete since the pH level in the micro-pores of concrete is high. The micro-pores contain a concentrated aqueous solution of ions in hydrated cement paste. Concrete pores are always moist, except when dried in an oven (Bertolini et al., 2004).

The passivity of iron rebar in concrete can be understood using the Pourbaix diagram of Fe-H_2O system shown in Fig. 2.2.2.1 (Pourbaix and Zoubov, 1966). The pourbaix diagram clearly shows that iron corrodes to form ferrous ions when pH is below 5. When pH is between 5 and 9 iron is passivated at higher potentials by precipitation of $Fe_2O_3.nH_2O$. For pH between 9 and 13 the formation of Fe_3O_4 and Fe_2O_3 passivates iron. Fe_3O_4 converts to Fe_2O_3 or $Fe(OH)_3$ later.

The reactions involved in passivation are

$$3Fe + 4H_2O \rightarrow Fe_3O_4 + 8H^+ + 8e^- \tag{2.2.2.1}$$

$$2Fe_3O_4 + H_2O \rightarrow 3Fe_2O_3 + 2H^+ + 2e^- \tag{2.2.2.2}$$

$$2Fe + 3H_2O \rightarrow \gamma\text{-}Fe_2O_3 + 6H^+ + 6e^- \tag{2.2.2.3}$$

The most likely cathodic reaction in an oxygen starved micro-pore inside concrete could be:

$$2H_2O + O_2 + 4e^- \rightarrow 4OH^- \tag{2.2.2.4}$$

The passive film on iron should consist of the substrate Fe_3O_4 and/or the provider of passivity γ-Fe_2O_3 (Bardwell et al., 1988; Kruger and Calvert, 1967; Ord and DeSmet, 1966). The passive film formed on iron in concrete pore solution is a form of hydrated Fe_2O_3 *i.e.*, FeOOH which is an oxyhydroxide (Oranowska and Szklarska-Smialowska, 1981), (Zakroczymski et al., 1985).

2.2.2.1 Breakdown of passive film and pitting corrosion

Reinforcing steel can be corroded by chloride ion contamination in aggregate or water (Bertolini et al., 2004), de-icing salts (Hara et al., 2005; Jang et al., 1998; Katayamaa et al., 2004), and marine environments (Alvarez and Galvele, 1984; Hoar, 1967; Janik-Czachor et al., 1975; Trejo and Monteiro, 2005). Once the passive film is corroded the rebar starts corroding. The reactions involved are:

$Fe(s) \rightarrow Fe^{2+} (aq) + 2e^{-}$ (2.2.2.5)

$Fe^{2+} + 2H_2O \rightarrow Fe(OH)_2 + 2H^{+}$ (2.2.2.6)

The H^{+} ions raise the pH and give rise to pitting (Pourbaix, 1974) (Brown, 1970).

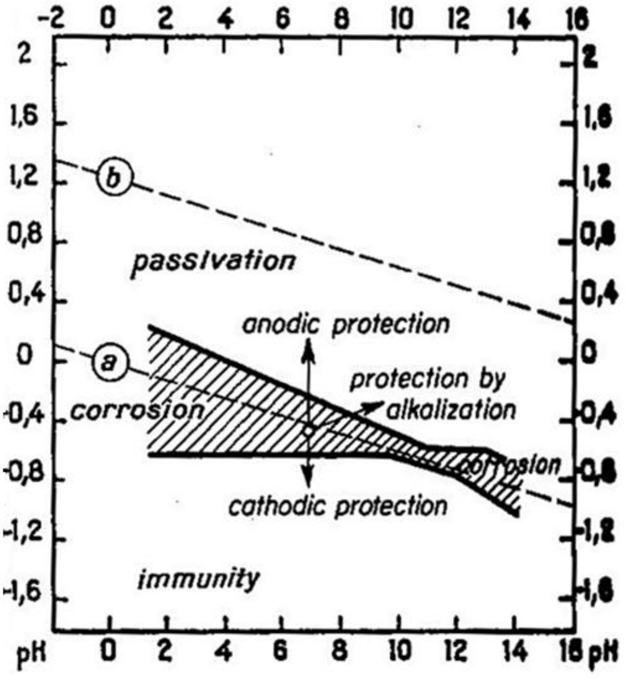

Fig. 2.2.2.1. Protection of iron against corrosion (Pourbaix diagram)

2.2.2.2 Chloride threshold for depassivation of reinforcing steel embedded in concrete

A critical amount of chloride concentration is needed to initiate pitting corrosion in reinforcing steels embedded in concrete. The value of this threshold concentration depends on various factors like smoothness of the steel surface, moisture content inside the concrete micro pores, prevailing temperature, environmental conditions, etc (Alvarez and Galvele, 1984) (Goñi and Andrade, 1990) (Gouda, 1970) (Guilbaud et al., 1994) (Hausmann, 1967) (Mammoliti et al., 1996) (Moreno et al., 2004) (Vrable and Wilde, 1980).

A few of these factors are listed as follows:

a. Ingredients of cement: Cements with higher tri-calcium aluminate content will be able to bind more chloride since chlorides react with these ingredients (Bertolini et al., 2004) (Arya and Xu, 1995; Rasheeduzzafar et al., 1990). Thus, lower tri-calcium aluminate is detrimental for rebar corrosion.

b. Silica fumes, fly ash and blast furnace slag: Silica fumes, fly ash and ground blast furnace slag are added to cement to refine the pore size of the concrete. This improves the resistance to ingress of chloride or sulphate ions (Kayyali and Haque, 1995; Thomas, 1996).

c. Water-cement ratio: If one increases the water cement ratio, the porosity and hence permeability of concrete increases (Baweja et al., 1999). This allows greater penetration of chloride ion and oxygen (Jaegermann, 1990; Kobayashi and Shuttoh, 1991).

d. Relative humidity and exposure temperature: Increasing temperatures raise the rates of reaction and thus the threshold chloride concentration is lowered (Hussain et al., 1995). In case of dry concrete, rise in temperatures reduce the solubility of oxygen and hence the rate of corrosion (López et al., 1993).

e. Availability of moisture and oxygen: Moisture is necessary for providing the electrolyte for corrosion. Oxygen and water provide hydroxyl ions which are required to form iron hydroxides. Without oxygen, the rate of corrosion reaction will decrease and this shall increase the threshold chloride concentration (Andrade et al., 1990).

f. Effect of surface finish: Polished rebar surfaces show lower corrosion rates as compared to as-received rebars in alkaline electrolytes (Mammoliti et al., 1996).

g. Effect of composition of rebar: Addition of alloying elements like V, Cu, Nb, Cr, Ni, Ti, and Mo in the range of 0.01 to 5 wt. % is used to improve the corrosion resistance of iron (Shimada and Sakakibara, 1989; Yoshimura, 1991).

h. Admixture: Admixtures are added to the mass of concrete before mixing either to reduce the amount of water requirement or to accelerate the rate of development of early strength in the concrete or retard the setting time of concrete (O'Neill and Hill, 2008). Admixtures containing chlorides like $CaCl_2$ accelerate corrosion.

i. Impurities in raw materials: The threshold chloride concentration required to initiate pitting depends on the chloride concentration in the mixing water and aggregates used in concrete (O'Neill and Hill, 2008).

The chloride thresholds for rebars found using potentiodynamic, and open circuit potential tests are displayed in Table 2.2.2.2.

Table 2.2.2.2: Chloride thresholds for rebars found using potentiodynamic, and open circuit potential tests

Electrolyte	**Method of Testing**	**Pitting potential E_{SCE}(mV)**	**Threshold chloride, M**	**Threshold chloride, $[Cl^-]/[OH^-]$**	**Ref.**
$Ca(OH)_2$ (12.5 pH), NaCl	Measurement of OCP	-50 to -230		0.5-1.08	(Hausmann, 1967)
$Ca(OH)_2$ (12.5 pH) + NaCl	Potentiodynamic	-175, -275, -350, -600	0.5, 1, 3, 6		(Vrable and Wilde, 1980)
$Ca(OH)_2$ + KOH (12 to 13.2 pH), NaCl, $CaCl_2$	Potentiodynamic, LPR	-150 to -300	0.1, 0.5, 0.75, 1 N	0.25-0.8	(Goñi and Andrade, 1990)
$Ca(OH)_2$ (12.5 pH)	Cyclic Potentiodynamic	+450 to -250, +500 to -100	1-5% in solution, 3-7% in solution		(Mammoliti et al., 1996)
$Ca(OH)_2$ (12.5 pH), 0-0.2 % NaCl	Potentiodynamic	0 to +800 (SHE)	0.02 wt. % chloride in solution	0.178 for 0% and 0.89 for 0.1% Cl^-	(Moreno et al., 2004)
$Ca(OH)_2$ (12.5 pH), 0-0.14 wt. % NaCl	Potentiodynamic	0 to +700	0.1 wt. % Cl^- in solution for Fe-P alloy		(Sahoo and Balasubramaniam, 2008)

2.2.2.3 Stages in the process of corrosion of rebars

Corrosion can be uniform or localized. Localized corrosion is generally caused by anions like chloride, etc. Initiation of corrosion takes place when the chloride content at the surface of the rebar reaches a critical level. Subsequently, the pit grows.

Model for pitting of rebars:

One group of authors suggests that chloride ion penetrates the passive film before nucleation of pits (Hoar et al., 1965; Hong et al., 1996; Rosenfeld and Marshakov, 1964). Another group proposed that pits nucleate after the mechanical breakdown of passive film due to stress and then propagate due to chloride ions (Hoar, 1949). A third group of authors proposed that aggressive anions adsorb on the passive film forming soluble metal complexes using the cations in the oxide film at a constant anodic electrode potential until the metal is exposed and pitting due to chloride ions starts (Ameer et al., 2004) (Betova et al., 2002) (Bockris et al., 1961) (Bockris et al., 1971) (Bojinov et al., 1999) (Dallek and Foley, 1976) (Foroulis and Thubrikar, 1975) (Hoar and Jacob, 1967) (Nagayama and Cohen, 1962) (Szklarska-Smialowska, 2002).

Smialowska (Szklarska-Smialowska, 2002) concluded that chloride ion is adsorbed on iron hydroxide and an electron injected into the metal surface. This injection of electrons increases with increasing anodic polarization voltage. At a certain voltage maximum number of electrons would be ejected into the passive film and a high local current is created by Zener mechanism which causes heat leading to expansion of the metal at the metal-film interface. The passive film breaks down as a result and pits are formed (Szklarska-Smialowska, 2002).

2.2.2.4 Propagation of pits

Corrosion by pitting involves initiation and propagation. The propagation of pits involves the reaction of iron with chloride ions to form ferrous chloride. The ferrous chloride may be hydrolysed to form ferrous hydroxide and hydrochloric acid. Hydrochloric acid can dissociate and supply chloride ions. Hydroxyl ions may also be liberated due to the cathodic reaction of oxygen. Thus, chloride ions migrate from the bulk to the pit creating a low pH condition. These ions are also recycled within the pit. Some chlorine is also obtained by the breakdown of chloro-aluminate complexes from concrete.

2.2.2.5 Nature of polarization and pitting potential

Threshold chloride concentration is related to a polarized potential known as the pitting potential. Polarized potentials are different for various threshold chloride concentrations. At the pitting potential the corrosion current increases drastically. Similarly a dramatic increase in corrosion current is observed in the trans-passive region attributed to oxidative dissolution of metal. The increase in current density for iron and carbon steel at high and positive anodic potentials is due to oxygen evolution and not trans-passive dissolution (Bertolini et al., 2004) (Moreno et al., 2004) (Pourbaix and Zoubov, 1966). The Fe-H_2O pourbaix diagram shows that iron remains passive at high potentials and pH. Increase in the chloride concentration causes an increase in the corrosion current density in the transpassive region due to pitting corrosion (Moreno et al., 2004). As the chloride concentration increases the pitting potential decreases.

2.2.2.6 Protection methods

The quality of concrete can be improved by optimizing water-cement ratio, proper mixing and curing of concrete, and keeping the concrete surface free of water. This will ensure protection of rebars. Nitrite based anodic inhibitors are also used to protect the rebars (Ngala et al., 2002). Organic inhibitors adsorb on the rebar and inhibit both anodic and cathodic processes (Nmai, 2004; Nmai et al., 1992). Epoxy coating has also been used successfully for protecting rebars (Darwin and Scantlebury, 2002; Weyers and Cady, 1987). Zinc coating provide sacrificial protection to rebars (ASTM A767, 2015). Alloying additions of copper, chromium, nickel, niobium, vanadium, titanium, etc in small amounts provide corrosion resistance (Shimada and Sakakibara, 1989; Yoshimura, 1991).

2.2.3 Evaluation of Corrosion Performance of Rebars in Simulated Concrete Pore Solution

Since inserting electrodes into concrete is tough and diffusion of ions in concrete is slow giving rise to different pH and ionic composition of the electrolyte near the surface of the rebar, the determination of polarization curves and hence corrosion rates is difficult. Therefore, these are determined indirectly, using solutions simulating the concrete pore solution.

2.2.3.1 Visual inspection and weight loss

Sahoo *et al.* studied the corrosion of phosphoric irons containing 0.11, 0.32, and 0.49 wt. % phosphorous using visual inspection. They used saturated $Ca(OH)_2$ solution with 3.5 wt. % NaCl for immersing the samples for 300 days and reported that corrosion was initiated on the 60th, 90th, 125th, and 300th day for mild steel, and the samples having 0.11, 0.32, and 0.49 wt. % phosphorous, respectively (Sahoo and Balasubramaniam, 2008).

The rust on the corroded samples can be removed; the weight loss measured and the rate of corrosion calculated using the following formula.

$$mpy = \frac{534 \times W(mg)}{D(gm/cc) \times A(sq.inch) \times T(hours)} \qquad (2.2.3.1)$$

W is the weight loss, D is the density of the specimen, A is the area of the specimen, and T is the exposure time.

2.2.3.2 Open circuit potential

Sahoo and Balasubrahmaniam studied the corrosion of phosphoric irons containing 0.11, 0.32, and 0.49 wt. % phosphorous using OCP. They used saturated $Ca(OH)_2$ solution with varying amounts of NaCl for immersing the samples and recording the OCP for a week. They found that the OCP increased and corrosion rate decreased for the phosphoric irons with time (Sahoo and Balasubramaniam, 2008). The E_{corr} decreased with increase in immersion time in $Ca(OH)_2$ solutions containing chloride ions (Moreno et al., 2004). In general, deaerated solutions presented lower I_{corr} values than the corresponding aerated ones (Garces et al., 2005).

2.2.3.3 Linear polarization resistance (LPR) and Tafel extrapolation method

Polarization methods are much faster experimental techniques as compared to weight loss estimation. Tafel extrapolation method (Singh et al., 2016) and LPR are two polarization methods useful in determining corrosion rates. The rate of corrosion can be determined by directly measuring LPR using as-received or polished steel samples in simulated concrete pore solutions containing various chloride ion concentrations (Garces et al., 2005; Hope and Ip, 1987; Lambert et al., 1991; Moreno et al., 2004).

2.2.3.4 Chloride threshold determination using potentiodynamic polarization curves

Potentiodynamic polarization method is useful in determining the threshold solution concentration for pitting. Potentiodynamic polarization curves are obtained for rebars in as-received condition in simulated concrete pore solutions containing various chloride ion concentrations (ASTM G5 14, 2011). The increase in current in carbon steel is due to pitting corrosion in pore solution containing chlorides. The pitting potential decreases with an increase in chloride ion concentration (Sahoo and Balasubramaniam, 2008).

Sahoo and Balasubrahmaniam found that the threshold chloride concentration for pitting corrosion of phosphoric irons containing 0.11, 0.32, and 0.49 wt. % phosphorous in saturated $Ca(OH)_2$ solution with varying amounts of NaCl was 0.1 wt. % chloride (Sahoo and Balasubramaniam, 2008).

2.2.3.5 Electrochemical impedance spectroscopy (EIS)

The polarization resistance of a specimen is measured using EIS. EIS data can be displayed as Bode magnitude, Bode phase and Nyquist plots (Walter, 1986) (Tiwari et al., 2012, 2011). The data provides information about the nature of the passive film which grows on the surface of the specimen. Increasing immersion time of the specimen in concrete pore solution containing chloride ions increases the capacitive part which indicates the formation and thickening of a passive film (Poupard et al., 2004). Decreasing capacitive part indicates corrosion.

Saremi and Mahallati studied the EIS plots of mild steel in concrete pore solution having various chloride concentrations (Saremi, M., 2002). They observed that mild steel found a threshold at $[Cl^-]/[OH^-] = 0.6$ beyond which pitting would occur.

Sahoo and Balasubrahmaniam studied the corrosion of phosphoric irons containing 0.11, 0.32, and 0.49 wt. % phosphorous in saturated $Ca(OH)_2$ solution with varying amounts of NaCl using EIS. They found that the pitting damage occurred after 0.1 wt. % chloride ion concentration in simulated concrete pore solution (Sahoo and Balasubramaniam, 2008).

Upon dipping a metal in a solution, the metal ions enter the solution and in time an electrical double layer is formed at the metal-solution interface. The current at the metal electrolyte interface can be modelled as a capacitance as $C=q/V$. Here, q represents the charge in the double layer upon dissolution of the metal. V is the potential at which the sample corrodes freely (Sahoo and Balasubramaniam, 2008). If the passive film grows and becomes more protective with time then the micro-pores present on the film will grow smaller with time and metal dissolution will decrease. This implies that the capacitance associated with the double layer will decrease since:

$$C = \frac{1}{2\pi f R} \tag{2.2.3.5.1}$$

Here f is the frequency and R is the resistance. Capacitance can also be related to the film thickness as follows:

$$C = \frac{\varepsilon \varepsilon_0}{d} \tag{2.2.3.5.2}$$

where d is the thickness of the film, ε_0 is the vaccum permittivity and ε is the dielectric constant of the film (Keddam et al., 1987).

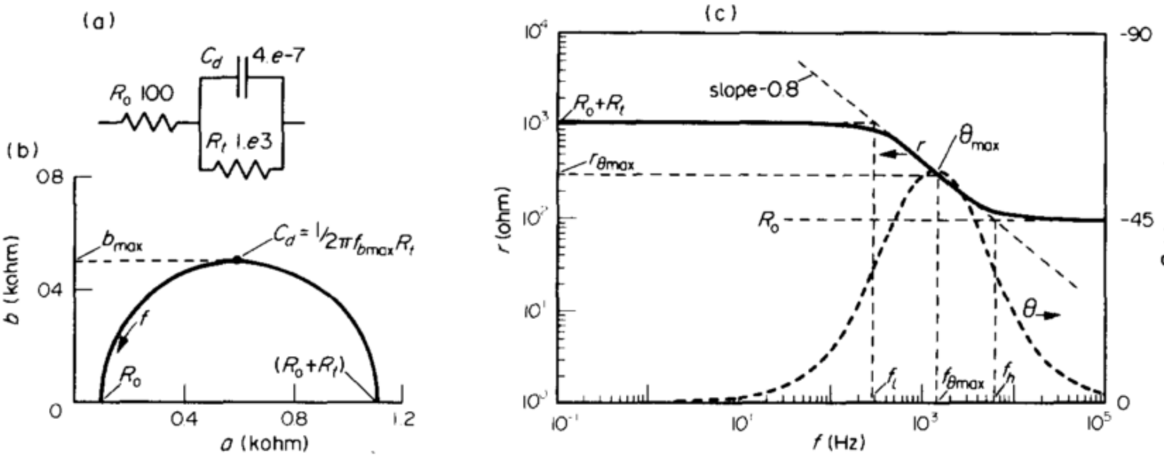

Fig. 2.2.3.5. (a) Circuit; (b) Nyquist plot; (c) Bode plot (Walter, 1986)

By measuring the high and low break point frequencies of the Bode magnitude plots, capacitance can be calculated. These frequencies are found where the two frequency independent horizontal parts intersect with the central straight line portion having negative slope (Walter, 1986) (Fig. 2.2.3.5). The low and high frequencies can be located at the 45° phase angle too. The capacitance corresponding to high (f_h) and low (f_l) frequencies can be calculated as follows:

$$C_h = \frac{1}{2\pi f_h R_0} \tag{2.2.3.5.3}$$

$$C_l = \frac{1}{2\pi f_l (R_0 + R_t)} \tag{2.2.3.5.4}$$

Where R_0 is the solution resistance and R_t is the polarization resistance. A schematic Nyquist plot for mild steel in alkaline solution (Saremi, M., 2002) is displayed in Fig. 2.2.3.6. There are two time constants in the plot. The high frequency arc is associated with the OH^- ion adsorption on the surface of the steel. The other arc is associated with the passive film and charge transfer resistance.

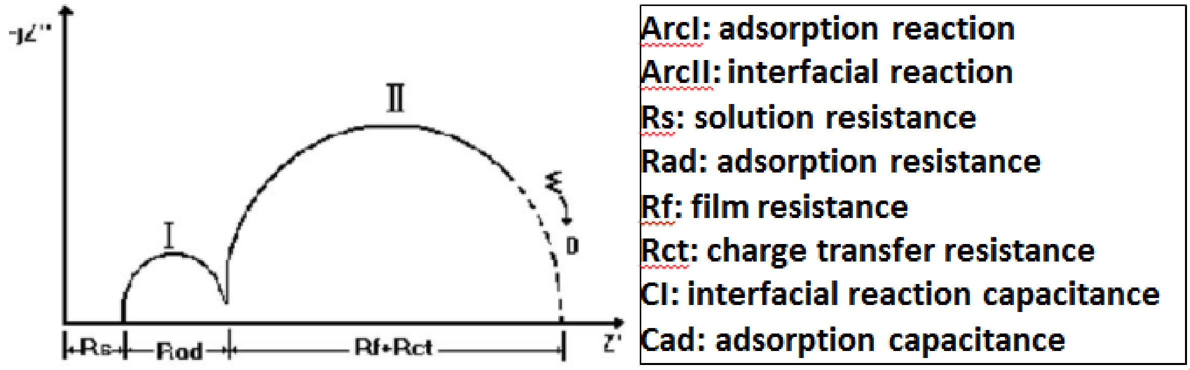

Fig. 2.2.3.6. A schematic Nyquist plot for mild steel in alkaline solution

2.2.4 Corrosion of Steel

Iron or steel tend to corrode when exposed to the environment (Fontana, 1987)(Silvermann and Puyear, 1987). Corrosion depends on pH, concentration of the electrolyte, velocity of the fluid, temperature and oxidizing power of the solution (Kelly, 1965; Lorbeer and Lorenz, 1980; Stern, 1955). The rate of corrosion depends on the hydrogen ion concentration of the solution (Silvermann and Puyear, 1987), (Lorbeer and Lorenz, 1980). This dependence can also be understood using the pourbaix diagram for Fe-H_2O system (Pourbaix and Zoubov, 1966). The environment is considered strongly acidic for pH<5, near neutral or marine for 5<pH<9 and strongly basic for pH>9 (Silvermann and Puyear, 1987). The oxides or hydroxide layer of the metal in near neutral solution (5<pH<9) tend to remain on the surface. The corrosion rates of different steel samples tested in sea water at Emsworth (a small town in Hampshire on the south coast of England, near the border of West Sussex), using weight loss method are presented in Table 2.2.4.1. Increasing the chromium content above 2.5 wt. % reduces the corrosion rate to very low levels. The lowest corrosion index (1 mpy) was reported for Cr-Al steel (Hudson and Stanners, 1955). Ni and Mo also reduce corrosion rate but to a lesser extent than Cr.

Table 2.2.4.1: Corrosion rate reported by Hudson and Stanners using weight loss method (Hudson and Stanners, 1955)

Steel specification	wt. % of C/Cu/Cr/Mo/Ni/Al	Duration of immersion	Average corrosion rate (mpy)
Carbon steel ,	0.1C	2 yr and 5 yr	2.6
Carbon steel	0.4 C	Same	3.1
Cr-Cu steel	1Cr-0.5Cu	Same	2.3
Cr-Cu steel	2Cr-0.05Cu	Same	1.8
Cr-Cu steel	2.4Cr-0.5Cu	Same	1.5
Cr-Al steel	2.6Cr-0.1Cu	Same	1.2
Cr-Al steel	2.6Cr-1.4 Cu	Same	1.0
Cr-Mo-Ni steel	0.8 Cr-0.5Mo-3Ni	Same	2.2
Cr-Mo-Ni steel	3.1 Cr-0.4Mo-0.1Ni	Same	1.2

Gadadhar Sahoo and R. Balasubrahmaniam (Gadadhar and Balasubramaniam, 2008) studied the corrosion properties of phosphoric irons. They investigated the corrosion properties of the phosphoric irons in marine environment (Table 2.2.4.2). These phosphoric irons were manufactured using the ingot metallurgy route.

Table 2.2.4.2: The corrosion properties of phosphoric irons in neutral/marine environment pH 6.8 (Gadadhar and Balasubramaniam, 2008)

Sample	P wt. %	C wt. %	Fe	I_{corr} (µA)	Corrosion Rate (mpy)
1	0.11	0.02	Balance	19	9
2	0.32	0.02	Balance	13	6
3	0.49	0.02	Balance	13	6

In the case of 3.5 wt. % NaCl solution, the diffusion-controlled oxygen reduction reaction is the dominant reaction at E_{corr} (Flitt and Schweinsberg, 2005). The corrosion rate of pure iron is 12 mpy as obtained by the Tafel extrapolation method after 24 h of immersion in unstirred, air saturated 3.5 wt. % NaCl solution (McCafferty, 2005).

Potentiodynamic polarization curves exhibited stable passive behaviour of phosphoric irons, when compared to normal steel. The threshold chloride for initiation of pitting in simulated concrete pore solution was estimated to be 0.1 wt. % Cl^- for phosphoric iron while that for mild steel it was 0.06 wt. %. EIS studies indicated that the nature of the passive film improved and passive film thickened with increasing time of immersion in case of phosphoric irons (Sahoo and Balasubramaniam, 2008).

The surfaces of rusts formed on cast strips containing high phosphorous contents (0.15 wt. % P and 0.26 wt. % P) were more homogeneous and compact than that on the 0.08 wt. % P strip; and average thickness of rust layer of the former was less than 60% of that of the latter after 120 dry and wet cycles. The P enrichment (compact and steady phosphate) at the interface between rust layer and substrate for strips containing high phosphorous contents, was responsible for the improvement of weathering resistance by resisting corrosive agents from further penetrating the substrate (Zhou et al., 2009). In acid sulphate or sulphide solutions, phosphorus increases the hydrogen activity, which is later decreased due to scale formation. Phosphorus lowers the iron dissolution reaction but the corrosion rate is increased (Riecke et al., 1987). According to the ternary Fe-P-O phase diagram, the critical P concentration required for the formation of a protective phosphate layer in steel should be greater than 0.24 wt. % (Liu et al., 2010).

The passive range in hot nitrate solutions is short for high phosphorous concentrations, since the activation potential (Flade-Potential) is higher for high phosphorus content. It is 250 mV (SHE) for pure iron and 880 mV (SHE) for Fe-1P. The current densities in the passive range increase with increasing phosphorus content of the alloy; the passive current density is $5x10^{-4}$ mA cm^{-2} for pure iron and $2x10^{-1}$ mA cm^{-2} for Fe-1P (Küpper et al., 1981).

2.2.5 Hot Compression

Hot compression test is carried out at high temperatures using a thermo-mechanical simulator. It is generally used to determine the parameters for safe hot forming of the material. Thermo-mechanical simulator can be effectively utilized for simulating a wide range of metallurgical processes, leading to improvement in processing of difficult to process steels, process optimization, as well as improvement in the product quality (Kumar, 2015).

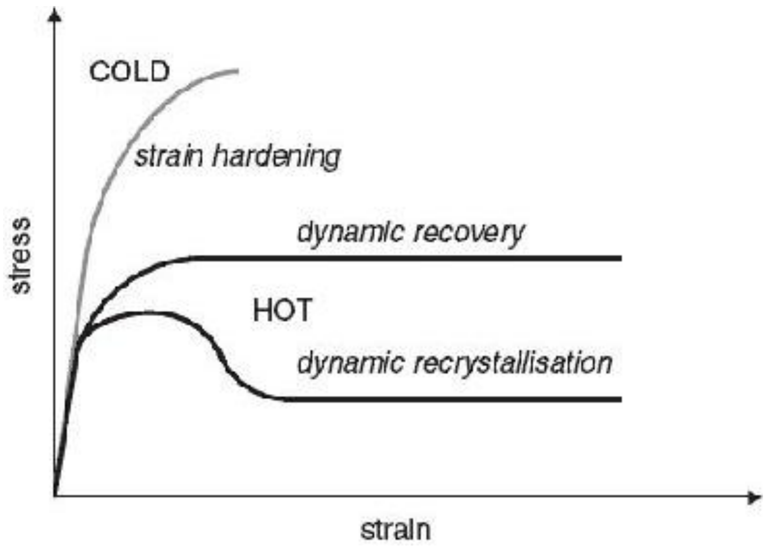

Fig. 2.2.5.1. Typical flow curves during hot and cold deformation

During cold deformation the curve shows strain hardening. During hot deformation, the shape of the true stress-true strain curve can display either dynamic recovery (DRV) or dynamic recrystallization (DRX) (Fig. 2.2.5.1). The flow stress saturates after an initial period of work hardening in a typical dynamic recovery curve. DRV is more prevalent in high stacking fault energy (SFE) metals like aluminium and low carbon ferritic steel, etc (Verlinden et al., 2007). DRX (Cho et al., 2001; Wang et al., 2012) is accompanied by one or multiple broad peaks. During DRV, the original grains are progressively strained yet the sub-structure re-adjusts continuously to the increasing strain and the remains equi-axed (Fig. 2.2.5.2.a). During DRX of low SFE metals like copper and austenitic stainless steels, DRV is slow resulting in an increase in stored energy. At a critical strain dynamically recrystallized grains are formed at the original grain boundaries. This is called a necklace structure. Further deformation causes more nuclei to form new recrystallized grains. The new grains are also subjected to deformation on further straining. Then a dynamic equilibrium between hardening due to high dislocation density and softening due to DRX is established at the plateau of the curve (Fig. 2.2.5.2.b). The microstructure here consists of a dynamic mixture of grains having various dislocation densities (Verlinden et al., 2007).

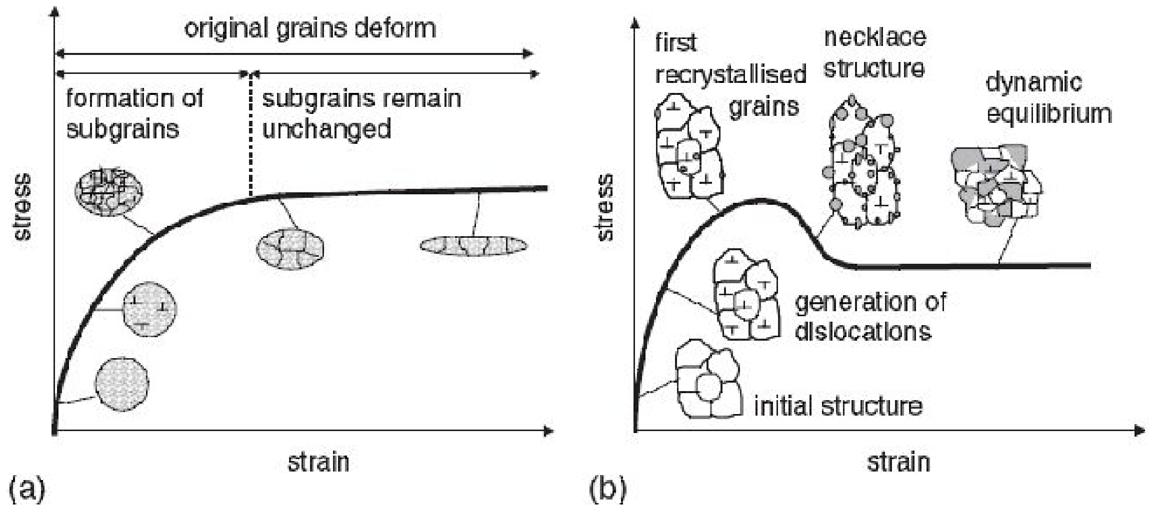

Fig. 2.2.5.2. Evolution of the microstructure during (a) DRV (b) DRX (Verlinden et al., 2007)

2.2.5.1. Grain refinement

Thermo-mechanical processing has been employed for producing plates and sheets with optimized mechanical properties (Sankaran et al., 2005, 2003). Research in low carbon steels and low alloy steels is driven by the desire to improve yield strength and toughness. Improved yield strength and toughness are obtained in fine grained ferrite which is prepared by using thermo-mechanical controlled processing routes. Controlled rolling is used to produce steels with yield strength as high as 600 MPa at low costs (Hurley and Hodgson, 2001). Fine grain sized steels can be produced by using three mechanisms: (a) strain induced transformation (SIT), (b) transformation from dynamically recrystallized austenite, and (c) dynamic recrystallization of ferrite (Hodgson et al., 1999). Several metallographic studies have confirmed the achievement of fine ferrite via strain induced transformation in plain carbon steels (Santos et al., 2003)(Han and Yue, 2003)(Huang and Froyen, 2002)(Hong et al., 2003) and micro-alloyed steels (Eghbali and Abdollah-zadeh, 2006)(Eghbali and Abdollah-zadeh, 2005a)(Chakrabarti et al., 2013) (Eghbali and Abdollah-zadeh, 2005b). These researchers have hot worked the steel just above the Ar_3 temperature and in the (α+γ) phase field to obtain fine grain size.

In order to enhance the ductility of high phosphorous steels further by reducing the grain size one must find the thermo-mechanical parameters like strain rate and deformation temperature, which shall allow the achievement of fine grain size (Stumpf, 2004, 2003) by holding and working in the (α+γ) phase field. Although a few researchers have worked on hot compression studies of high phosphorous steels, studies on grain refinement of high phosphorous steels are scarce (Kim et al., 2005).

2.2.5.2 Hot deformation of low carbon steels

Many studies have been carried out on hot deformation of low carbon steels in a wide range of temperatures and strain rates. Fe-0.06 wt. % C steel was tested at strain rates of 0.1, 1, and 8 s^{-1} by hot deformation in the temperature range of 900°C to 1100°C to a total strain of 0.8 (Rao et al., 1996). It was observed that the hot deformation behaviour in the austenitic phase field followed a hyperbolic sine relationship. Huang *et al.* conducted hot compression tests on a 0.16 % C steel at deformation temperatures in the range 520°C to 900°C, with true strain upto 0.8 and a constant strain rate of 1 s^{-1} (Huang and Froyen, 2002).

Isolated studies have been conducted on interstitial free steels having phosphorous and boron as alloying elements with limited objectives. For example, Kim *et al.* studied a Ti-Nb interstitial free steel and found that the effect of phosphorous on dynamic recrystallization was less than that of boron (Kim et al., 2005). A comprehensive study on high phosphorous steels has not been taken up as yet. A review of thermo-mechanical processing of low carbon steels is presented in Table 2.2.5.2.

Table 2.2.5.2: Review of thermo-mechanical processing of low carbon steels

S. No.	Material (wt. %)	Experiment	Findings	Ref.
1.	Fe-0.16C-1.5Mn-1.2Si steel and Fe-0.16C-1.5Mn-1.2Si-0.11V-0.077 Nb steel	All the specimens were reheated to 1100°C for 2 min and cooled at a rate of 1°C s^{-1} to the deformation temperature, compressed and water quenched	-Deformation induced ferrite transformation was influenced by austenite grain size, amount of strain and strain rate, and the grain size of about 2 µm could be produced by heavy deformation of 80%. At least reduction of 50% per pass was required to induce deformation induced ferrite transformation. -Ferrite growth occurred during the intercritical isothermal holding after deformation. -Micro-alloying such as Nb, V was effective for suppressing the ferrite growth.	(Hong and Lee, 2002)
2.	Fe-0.06C-0.59Mn steel	Specimens heated at 1250°C, soaking time 15 min. The heat treated specimen was rolled in single pass up to reduction of 30% at roll speed of 24 m/min and 780°C and air cooled to room temp.	-Ultra fine equiaxed grains of size 1 µm were produced. -Refinement was due to strain induced transformation from austenite to ferrite. -Yield strength was increased by 100%.	(Hodgson et al., 1999)
3.	Fe-0.15C-1.1Mn -0.25Si steel	Hot rolling in the intercritical region.	-Ultra fine ferrite grains (about 1 µm) in steels are obtained through hot rolling in the intercritical region, under condition of strain-induced transformation from austenite to ferrite.	(Han and Yue, 2003)
4.	Fe-0.45C-0.28Si -0.96Cr-0.63Mn -0.19Mo steel	Specimen compressed at deformation temperature from 850 to 1150°C and strain rates from 0.01-50s^{-1} and different deformation degrees	The deformation resistance increases with the decreasing temperature of deformation and increases with the increase of strain rates for a given deformation temperature.	(Lin and Liu, 2009)

5.	Fe-0.16C-0.20Si -0.61Mn steel	Various deformation temperatures using different strain rates and total true strains.	Ferrite grain size of 3-5µm was achieved. -The strain assisted austenite to ferrite transformation and austenite recovery are responsible for the softening. -The strain-assisted austenite to ferrite transformation should preferentially be considered in obtaining the equiaxed, homogeneous and ultrafine ferrite because it occurs more easily than the dynamic recrystallization of ferrite. Decreasing the recovery rate of ferrite and increasing the defect concentration in austenite are beneficial to the formation of the ultrafine ferrite.	(Huang and Froyen, 2002)
6.	Fe-0.09C-1.68Mn -0.22Si-0.27Mo steel; Fe-0.11C -1.68Mn-0.22Si steel	-heated to 1250°C for 900 s and air-cooled to the rolling temperature which was just above the Ar_3 (800°C) followed by air cooling. - heated to 1250°C for 900 s and air-cooled to the rolling temperature which was just below the Ar_3 (675°C) followed by air cooling.	- The equiaxed ultra-fine ferrite is formed due to strain induced transformation and fine-scale (0.05-0.2µm) spherical carbide particles were distributed throughout the microstructure.	(Hurley and Hodgson, 2001)
7.	Fe-0.0031 C-0.0018 N-0.012Si-0.15Mn -0.010P-0.005S -0.049Ti-0.0001 B-0.054 Al steel	-The specimens were heated to 1123 K at a heating rate of 20 Ks^{-1}, held for 30s, and then compressed at the same temperature at various strain rates in the range of $10^{-3}s^{-1}$ to $10s^{-1}$.	- Dynamic recrystallization can occur also in ferrite where it has been generally considered that recovery is an only restoration process during hot deformation.	(Tsuji et al., 1997)
8.	Fe-0.0016C-0.1Si -0.3Mn steel	Specimens were heated at 10 K s^{-1} to their specified temperature, and then plane strain compressed in a single stroke after holding at the temperature for 10 s. The compressive deformation was carried out at strain rates of $1s^{-1}$ and $0.01s^{-1}$, respectively and water quenched.	Deformation at lower temperatures and higher strain rates (high Z) results in dynamic recovery and at higher temperatures and lower strain rates (low Z), dynamic recrystallization in ferrite prevails. Dynamic recrystallization is confirmed in the temperature range of 723-823 K and at a strain rate of 0.01 s^{-1}.	(Murty et al., 2005b)

9.	Fe-0.15C steel; Fe-0.2C steel; Fe-0.3C steel	Reheat at 100 K above Ae_3 for 3 min. followed by air cooling to 1133 K or 1143 K, one step deformation pass upto total true strain of 0.3 at strain rate of $10s^{-1}$ in order to obtain fully recrystallized austenite followed by cooling to 823 K using the maximum admissible cooling rate. After a 2 min holding period at 823 K, the large strain warm deformation was applied in four-pass plane strain compression (each of ε=0.4) process with an interpass time of 0.5s at strain rate of $10s^{-1}$. Subsequently, an annealing treatment of 2 h at 823 K was applied.	-The ultrafine ferrite grains (1.1-1.4 μm) and homogeneously distributed fine cementite particles were produced by large strain warm deformation (ε = 1.6) and subsequent annealing (823 K, 2h) of plain C steel. - The increase in the carbon content was observed to be beneficial for the enhancement of the work hardening rate.	(Song et al., 2005)
10.	Fe-0.15C-0.16Si -0.56Mn-0.012P -0.028S steel	Specimen is heated up to 900°C soaked for 5min, cooled to temperature in the range of 550-850°C at the rate of 15°C s^{-1}, immediately deformed, reheated up to 750°C, kept for at least 5min, and finally cooled in air.	Ferrite grain size of 7.5 μm has been produced. -The yield strength of the plates is 325-385 MPa, tensile strength is 465-525 MPa and elongation is 27-36%.	(Jian-wen et al., 2006)
11.	Fe-0.16C-0.26Si -1.5Mn-0.03Ti steel	Sample heated at 900°C for 10min., followed by air cooling to 750°C (Ar_3 temp. is 735°C and the austenite grain size was 50μm) followed by shear rolling and reduction ratios of 30, 40, 50 and 60%. The rolled specimens were cooled at various cooling rates.	-The fine grained ferrite less than 2μm in size were produced by the asymmetric rolling. Fine cementite particles are dispersed at the ferrite grain boundaries. -The grain size of the ferrite decreases with increasing effective rolling strain and also with increasing cooling rate after rolling.	(Lee and Lee, 2010)
12	Fe-0.06C-0.27Mn -0.02Si steel	The compression tests were performed at constant strain rates of 0.1, 1 and $8s^{-1}$ to a strain of 0.8 at constant temp. 900, 1000, and 1100°C. The specimen is heated to 1200°C at a heating rate of 2.6°C s^{-1}, held at that temperature for 2 min, cooled at a rate of 2°C s^{-1} to the test temp., held for 30s before compressing followed by	-Depending on the temperature and strain rate conditions during deformation, the material exhibited strain hardening, dynamic recovery, and static and dynamic recrystallization behaviour. -A constitutive equation has been developed with which strain hardening, dynamic recovery and	(Rao et al., 1996)

		water quenching	dynamic recrystallization, temperature dependence can be satisfactorily described covering a wide range of strain rates. - The entire flow stress data can be well represented using a hyperbolic-sine relationship, and a constitutive equation reflecting strain, strain-rate and temperature contributions to flow stress has been obtained for the plain low carbon steel.	
13	Fe-0.15C-0.15Si -1.10Mn steel	Specimen heated to 900°C at a heating rate of 10°Cs^{-1}, and held for 10 min. Then cooled at a cooling rate of 5°Cs^{-1} to the deformation temp., ranging from 875°C to 700°C, and deformed immediately by compression to various amounts of deformation at two different strain rates of 0.01 s^{-1} and 1 s^{-1} before ice-brine quenching.	-The observed flow softening behaviour of the steel during its hot-deformation at temperature lower than critical temperature within γ+α phase under low strain rate condition was due to deformation-induced massive transformation of austenite-to-ferrite transformation instead of conventional strain-induced transformation. The unusual behaviour was strongly dependent on the strain rate of deformation below critical temperature T_C (780°C). A significant flow softening behaviour was observed for low strain rate of 0.01 s^{-1}. -The observed critical temperature T_C (780°C) was significantly higher than T_0 (730°C) temperature and this was because the γ+α phase-equilibrium was largely shifted toward higher temperature because of the development of unequal deformation-induced stresses in two phases because of the yield stress difference.	(Chung et al., 2010)
14.	Fe-0.04C-0.78Mn -0.25Si steel	Compression was performed at temperature range of 850-1150°C and strain rate of 0.001-1 s^{-1} followed by water quench.	- The flow curves at temperatures higher than 950°C show DRX while at lower temp., the flow curves show work hardening without any DRX. - The linear dependence of flow stress on	(Momeni et al., 2011)

			temperature changes to a non-linear one at about 950°C. This temperature is introduced as the recrystallization-stop temperature of the alloy. - The apparent activation energy for DRX is determined as 377 kJ/mol.	
15.	Fe-0.27C-0.2Si -0.3Mn-1.5Cr -0.35Mo-3.7Ni -0.1V-0.007N steel	Heated for 10 min at 1200°C and then cooled down to deformation temperature. Hot compression was performed at temperature range of 850-1150°C and at strain rates of 0.001-1 s^{-1}	-Dynamic recovery in austenite occurs very sluggishly due to its low stacking fault energy (SFE). -DRX actually originates from the local bulging of grain boundaries that is initiated at a critical strain (ε_c) 0.6-0.8 times the peak strain (ε_p). - At temp., higher than 1000°C, DRX was found responsible for flow softening, whereas at lower temp., the flow curves were associated with work hardening without DRX. - The value of apparent activation energy found using hyperbolic sine function was 437 kJ/mol. - The stress relaxation tests at low temperatures confirmed the possibility of dynamic precipitation. The lowest times for the start and finish of precipitation were respectively as 10 and 1000 s and were obtained at 900°C. -The solubility products of VC, VN and Mo_2C were calculated using the alloy contents and it was concluded that a combination of V and Mo could cause dynamic precipitation of carbonitrides.	(Mirzaee et al., 2012)
16.	Fe-0.15C-1.5Mn -0.4Si steel	Specimens heated at different temperatures (900, 1050, and 1200°C) for 1 min followed by cooling at the rate of 2°C s^{-1} to the desired deformation temp. and then deformed in	- Strain-induced dynamic transformation (SIDT) can be used for grain refinement in low carbon steels. About 2 μm ferrite grains are obtained through dynamic transformation in the	(Choi et al., 2003)

		compression at constant strain rates of either 1 or 0.1 s^{-1} immediately followed by ice-brine quenching	temperature range between Ae_3 and Ae_1. - The main contributions of SIDT to the grain refinement are very rapid and concurrent nucleation and random orientation distribution of ferrite grains due to the deformation. - The fraction of SIDT ferrite increases with the increase of strain. - softening mechanisms of strained austenite, SIDT and dynamic recrystallization (DRX) compete with each other - Under Ae_3 temperature where the critical strain for SIDT is smaller than that of DRX, SIDT is predominant softening mechanism.	
17.	Fe-0.156C -1.36Mn -0.249Si steel	true stress−strain curves under different deformation temperatures 850, 950, 1050 and 1150°C with strain rates of 0.01, 0.1, 1 and 10 s^{-1} are obtained	The constitutive model for flow stress of Q345E steel under elevated temperature is established by utilizing Arrhenius equation and the modified Zener-Hollomon parameter considering the compensation of both strain and strain rate, which can accurately predict the flow stress under different deformation conditions during the hot compression process.	(Dong-sheng et al., 2017)
18.	Fe-0.43 C-0.27 Si -0.21Mn steel	Each specimen was heated with heating rate of 5°Cs^{-1} up to austenitization temperature of 1100°C and soaked for 2 min and followed by cooling with 1°Cs^{-1} to deformation temperatures ranging from 800–1050°C with an interval of 50°C. The compression tests were performed at four constant strain rates *i.e.*, 0.01, 0.1, 1 and 10 s^{-1} upto total true strain of 0.7.	The apparent activation energy of hot deformation using sinh type law is found to be 368 kJ/mol at a true strain of 0.6. The value of stress exponent n is 5.4 using sinh type equations, which suggests that the mechanism of hot deformation is dislocation glide controlled by dislocation climb. High values of m and η at low strain rates, and moderate to high temperatures (950-1050°C) result from DRX of austenite.	(Kumar et al., 2017)

2.2.5.3 Processing windows

Processing maps are drawn in the Cartesian space having temperature as abscissa and strain rate as the ordinate at a given strain. Processing maps have been drawn for magnesium (Wang et al., 2007), aluminium (Wang et al., 2008) and steels (Rastegari et al., 2016), etc. Processing maps were developed first by Ashby (Ashby, 1972) and later by Prasad *et al.* (Prasad et al., 1984). The latter's maps are based on the dynamic materials model (DMM) and consist of two superimposed maps *i.e.,* power dissipation efficiency and instability maps. High dissipation efficiency and no instability represent good workability. Prasad *et al.* (Prasad, 1996; Prasad et al., 1984) assumed that the material does not store energy. Murthy and Rao (Murty et al., 2005a, 2003, 2002; Murty and Rao, 1998) modified the determination of energy efficiency and instability parameters.

Power P given to a viscoplastic material during plastic deformation is the product of stress and strain rate. Prasad assumed that this power P can be divided into G and J. G is the power dissipated in plastic work and J is the power dissipated in microstructural changes. This division can be expressed as (Chakravartty et al., 1995; Murty et al., 2005a)

$$P_{T,\varepsilon} = G + J = \sigma\dot{\varepsilon} = \int_0^{\dot{\varepsilon}} \sigma d\dot{\varepsilon} + \int_0^{\sigma} \dot{\varepsilon} d\sigma \qquad (2.2.5.1)$$

σ is the flow stress and $\dot{\varepsilon}$ is the strain rate. Based on this consideration, two parameters are described *i.e.,* ξ and η. η is the efficiency of power dissipation. ξ is the instability parameter. η is the ratio of J and the maximum possible J.

$$\eta = \frac{J}{J_{\max}} = \frac{2J}{P} = \frac{2m}{m+1} \qquad (2.2.5.2)$$

The values of η, strain rate sensitivity m, and stress exponent n are high when diffusion controlled phenomenon such as recrystallization, recovery and phase transformations occur (Rajput et al., 2013). Murthy and Rao proposed a modified DMM to avoid the use of m while calculating η. The resulting model was found to be good for multiphase materials. In this method (Murty et al., 2003) efficiency of power dissipation η is proposed as

$$\eta = \frac{2(P-G)}{P} \qquad (2.2.5.3)$$

with

$$\eta = \frac{2(\sigma\dot{\varepsilon} - ((\sigma\dot{\varepsilon}/(m+1)_{\dot{\varepsilon}=\dot{\varepsilon}_{\min}}) + {}_{\dot{\varepsilon}_{\min}}\int^{\dot{\varepsilon}} \sigma d\dot{\varepsilon})}{\sigma\dot{\varepsilon}} \qquad (2.2.5.4)$$

$\dot{\varepsilon}_{\min}$ is the minimum strain rate tested and *m* is the strain rate sensitivity for the lowest strain rate. *m* is defined in (Prasad et al., 1984) as

$$m = \left[\frac{\partial \ln \sigma}{\partial \ln \dot{\varepsilon}}\right]_{\varepsilon,T} \qquad (2.2.5.5)$$

Flow instabilities can be related to flow concentrations. Ziegler's (Murty and Rao, 1998) approach assumes that instability occurs when

$$\frac{\partial D}{\partial \dot{\varepsilon}} < \frac{D}{\dot{\varepsilon}} \qquad (2.2.5.6)$$

D is the power dissipation function. Thus, the calculation of the flow instability depends on the formulation of *D*. *D=P* implies that total power is dissipated and then instabilities occur when m<0 according to Montheillet *et al.* (Montheillet et al., 1996). Whereas, *D=J* assumes that power is dissipated by microstructural changes alone and by using it different instability parameters can be calculated. Prasad *et al.* (Prasad et al., 1984) proposed the following instability parameter.

$$\xi(\dot{\varepsilon}) = \frac{\partial \ln(m/(m+1))}{\partial \ln \dot{\varepsilon}} + m < 0 \qquad (2.2.5.7)$$

Murthy and Rao (Murty et al., 2003) proposed the following instability parameter κ

$$\kappa = \frac{2m}{\eta} - 1 < 0 \qquad (2.2.5.8)$$

Strain rate, temperature, and steady state flow stresses are interdependent. They obey kinetic equations too. The Zener-Holloman parameter, *Z* at different deformation parameters correlates well with the constitutive equations which are given below (Rajput et al., 2014). The power creep law is used for low stresses (Eq. 2.2.5.9); the exponential law equation for high stresses (Eq. 2.2.5.10). For a wide range of stresses the universal constitutive equation proposed by Sellars and Tegart (Sellars and McTegart, 1966) is used (Eq. 2.2.5.11). Equation

2.2.5.11 reduces to (Eq. 2.2.5.9) when $\alpha\sigma$<0.8 and (Eq. 2.2.5.10) when $\alpha\sigma$>1.2 (Zhang et al., 2013).

$$Z_p = A_p \sigma^{np} = \dot{\varepsilon} \exp(\frac{Q_p}{RT}) \qquad (2.2.5.9)$$

$$Z_E = A_E \exp(\beta\sigma) = \dot{\varepsilon} \exp(\frac{Q_E}{RT}) \qquad (2.2.5.10)$$

$$Z = A[\sinh(\alpha\sigma)]^n = \dot{\varepsilon} \exp(\frac{Q}{RT}) \qquad (2.2.5.11)$$

R is the gas constant and Q is the apparent activation energy. A, α, β and n are material constants and the subscripts P and E are related to power and exponential laws, respectively. The activation energy is determined using the Arrhenius plot. It is assumed that microstructures do not change. Q is the apparent activation energy. The stress exponent n obtained according to sinh type law is generally lower than that corresponding to the power law (Mcqueen et al., 1995). The value of constant α was taken as equal to 0.012 as found for similar steels when using the sinh type equation (McQueen, 2002).

2.2.6 Applications

Phosphorous is being used to improve the desirable properties of automobile steel sheets. The resistance spot-welding characteristics of plain-carbon steel was compared with those of rephosphorized steel containing 0.04 percent to 0.12 percent of phosphorus and adequate weld button size, strength and toughness were obtained over a practical range of welding conditions (Sawhill and Baker, 1980). Addition of up to about 0.1 percent P to low-C, low Mn steels greatly improves their deep-drawing properties (*i.e.*, higher r_m and lower Δr values) (Hu, 1976) (Spitzig et al., 1978). Additions of phosphorus up to 0.05 percent increase the strength of iron and steel by about 24 MPa with no significant effect on toughness (Spitzig, 1972; W.A. Spitzig and Sober, 1977). To gain additional strengthening, static-strain-aging treatments can be applied to low C, low Mn, silicon steels containing about 0.05 percent P, and increases in strength of about 15 percent obtained with no appreciable changes in r_m values (Spitzig et al., 1978). Reasonably good ductility (13% uniform elongation) remains after the strain-aging treatment. Dynamic-strain aging treatments on iron-phosphorus alloys (Spitzig and Sober, 1975) can produce greater increases in strength (with no appreciable decreases in subsequent uniform elongation) than static-strain-aging treatments.

The addition of phosphorous to CMnSiAl TRIP steel compositions resulted in the formation of a higher amount of retained austenite which did not decompose at longer austempering times; as compared to the non P-alloyed TRIP steel. Si and P were found to have a synergetic effect on the tensile strength. Addition of 0.14 wt. % of Si resulted in an increase in tensile strength of 60MPa which is five times larger than the Si solid solution strengthening effect in ferrite reported in literature, namely 80 MPa per wt. % Si (Barbé et al., 2006). Compared to the ultimate tensile strengths of all individual alloys, phosphorus added alloys exhibited increasingly better fatigue limit (as the phosphorous content increased), under cyclic loading conditions at room temperature in air (Islam et al., 2011).

P is being used as an alloying element in weathering steels. "Weathering" steel forms a protective layer on its surface under the influence of the weather. The corrosion-retarding effect of the protective layer is produced by the particular distribution and concentration of alloying elements (Cu, Si, P, Ni, etc) in it. The steel is allowed to rust in order to form the 'protective' coating (Yamashita et al., 1994). Weathering steel 09CuPTiRe is widely adopted for manufacturing rolling stock in China (Chunling et al., 2004). More than 50% of steel bridges in America are made of weathering steel (Kihira and Kimura, 2011). About 33% of the steel bridges in Japan are made from unpainted weathering steel, (Kihira and Kimura, 2011) and its share is increasing.

2.2.7 Research Gap and Formulation of the Problem

In cast steels, phosphorus is treated as an impurity because it exhibits strong segregation during solidification. Phosphorous forms fine Fe_3P inclusions at the grain boundaries during cooling from the melting temperatures and thereby results in embrittlement of the steel. The permissible amount for phosphorus in modern steels, therefore, is less than 0.05 wt. %. However, the beneficial effect of phosphorous in conferring corrosion resistance to steel is attested by several archaeological iron structures in India, one famous example being the Delhi Iron Pillar which is more than 1600 years old. The iron of the pillar contains an average amount of 0.25 wt. % phosphorous (Wranglen, 1970).

Phosphorus is a very effective alloying element in iron and steel because of its following features:

- Effectively strengthens ferrite phase (next only to carbon and nitrogen).
- Promotes corrosion resistance by forming a passive film.
- Improves wear resistance.

However, in spite of the versatility of phosphorous as an alloying element, its full scope is not yet developed. The aforesaid reasons are strong enough to underline the need to establish phosphorus as an important and effective alloying element and widen its applicability by way of appropriate alloy design.

The alloy design in the present investigation is based on the following concepts:

i. That a small amount of carbon (~0.01 wt. %) should be added to Fe-P alloys to reduce grain boundary segregation of phosphorous (Suzuki et al., 1985).
ii. That nitrogen can expel phosphorous from the grain boundary sites and decrease the percentage of intergranular fracture (H. Erhart and Grabke, 1981).
iii. That adding 0.5 wt. % Si reduced the ductile-brittle transition temperature by approximately 100 K, and the fracture mode became transgranular (Liu et al., 1989).
iv. That silicon bearing ultra-fine grained weathering steel exhibits excellent corrosion resistance compared with carbon steel in the wet/dry cyclic corrosion test by promoting the formation of goethite having smaller particle size (Gomez, Mejia et al., 2012; T. Nishimura, 2008; Toshiyasu Nishimura, 2008).
v. That nitrogen suppresses the pitting susceptibility of iron and steel and favours repassivation of pits which are formed by widening the potential range where repassivation occurs and reducing the size of the repassivated pits (Grabke, 1996).

In view of the above facts, it becomes interesting to study the combined effect of adding C, Si and N on the strength, ductility, toughness and corrosion resistance of Fe-P steels as no literature was found on this area of research.

In view of the observations, the present investigation is aimed at the following objectives:

- To design and prepare high phosphorous steels having good mechanical properties and corrosion resistance.
- To develop high phosphorous steels with refined microstructure using thermo-mechanical processing.
- To understand the underlying mechanisms of microstructural evolution during thermo-mechanical processing of high phosphorous steels.
- To establish suitable thermo-mechanical processing parameters by using deformation processing maps.

Chapter 3

EXPERIMENTAL PROCEDURE

This chapter describes the detailed experimental procedures adopted in the present investigation. The overall aim is to develop high phosphorous steels with fine grain size having good mechanical properties and improved corrosion resistance. The high phosphorous steel shall be used as concrete reinforcement rebar.

3.1 INGOT METALLURGY

3.1.1 Materials

The materials used in the present work are:

1. Three high phosphorous steels having different compositions (S1, S2 and S3)
2. Plain carbon steel (S4)

S4 was procured from the open market as rods of 13 mm diameter. The high phosphorous steels were produced by casting at Vaishnav Steel Private Limited at Muzaffernagar, Uttar Pradesh, India.

The materials used for castings of high phosphorous steels were:

1. Ferro-phosphorous alloy 2 kg
2. Low carbon iron scrap, 300 kg
3. Ferro-Silicon 1.5 kg
4. Aluminium shots
5. Nitrided Manganese

Three ingots weighing 30 kg each were cast in sand moulds. They contained approximately 0.13 wt. % phosphorous (all the percentages mentioned in the thesis are in weight percentages). This was accomplished by adding calculated amounts of ferro-phosphorous alloy to the induction furnace during melting.

The ferro-phosphorous mother alloy contained 22 wt. % phosphorous. Therefore, 1 kg of ferro-phosphorous contains 220 g of phosphorous. 5 wt. % weight loss of phosphorous occurs due to oxidation during melting. Therefore, the yield of 1 kg ferro-phosphorous will become 0.21 kg. Further, to obtain 1 kg 0.13 wt. % phosphorous steel we need 0.0013 kg phosphorous. Thus, we need 300 x 0.0013=0.39 kg phosphorous to make 300 kg steel (the capacity of the induction furnace). Which implies that 0.39/0.21 =1.86 kg ferro-phosphorous should be added to the melt.

The ferro-silicon mother alloy contained 70 wt. % silicon. Therefore, 1 kg of ferro-silicon contains 700 g of silicon. 5 % weight loss of silicon occurs due to oxidation during melting. Therefore, the yield of 1 kg ferro-silicon will become 0.665 kg. Further, to obtain 1 kg 0.26 wt. % silicon steel we need 0.0026 kg silicon. Thus, we need 300 x 0.0026=0.78 kg silicon to make 300 kg steel. Which implies that 0.78/0.665 =1.17 kg ferro- silicon should be added to the melt.

Similarly, calculated amount of nitrided manganese (7 wt. % nitrogen) was also added to the melt to obtain the desired concentration of nitrogen.

3.1.2 Melting and Casting

300 kg of low carbon iron scrap was melted in an induction furnace of 300 kg capacity. A small amount of flux was added to the melt to form a layer of slag. Calculated amounts of ferro-phosphorous and ferro-silicon were added to the melt and allowed to dissolve. A part of the melt was transferred into the ladle after adding some amount of aluminium shots for de-oxidation. The contents of the ladle were then poured into the previously prepared sand mould. The second casting was obtained after adding calculated amounts of ferro-silicon. The third casting was obtained after adding both ferro-silicon and nitrided manganese. The castings were opened on the third day. The risers and runners were cut off and cleaning and grinding operations performed. The size of the casting was 200 mm x 400 mm x 400 mm.

3.2 FORGING

3.2.1 Homogenization

The castings were cut vertically and perpendicular to the bottom of the casting into slices of 72 mm x 32 mm x 41 mm. These slices were homogenized at 1000°C for 24 h and then processed to obtain samples for further studies.

3.2.2 Forging

Pieces with dimensions of about 72 mm x 32 mm x 41 mm were cut the casting. These were subjected to hot upset forging at about 900°C. The thickness was reduced from 41 mm to about 16 mm. Then sections of 1.6 cm × 1.6 cm × 15 cm were cut off. These were again hot forged at 1150°C to produce round and square bars of about 1.2 cm diameter or side respectively. A few 16 mm thick samples were reduced to 12 mm by hot rolling at 900°C.

3.2.3 Composition Analysis

The chemical compositions of the cast samples were analysed by MAGELLAN optical emission spectrometer at Vaishnav Steel Private Limited, Muzaffernagar. The plain carbon steel was determined using Thermo-Jarrell Ash spark emission spectroscope at the department of metallurgical and materials engineering at the Indian Institute of Technology-Roorkee. Testing was conducted twice for obtaining the compositions. The composition of each element was obtained by averaging the two values obtained. The compositions of all samples are provided in Table 3.2.1.

Table 3.2.1: Average chemical composition (wt. %) of the steels used in the present work

Steel	P	C	Si	Mn	Cr	Al	Cu	N	S	Fe
S1	0.13	0.05	0.26	0.2	0.13	0.003	0.023	0.004	0.016	Balance
S2	0.13	0.05	0.39	0.2	0.14	0.023	0.024	0.004	0.015	Balance
S3	0.13	0.05	0.48	0.46	0.18	0.033	0.026	0.015	0.014	Balance
S4	0.02	0.09	0.07	0.32	0.03	0.004	0.02	0.002	0.017	Balance

3.3 HEAT TREATMENT

All the heat treatments were carried out in a muffle furnace (Scientific systems, New Delhi) having silicon carbide rods for heating. The forged bars (1.2 mm diameter/side) were held at 900°C for 1 h and 6 h to produce a set of tensile test and charpy impact energy test samples.

Microstructures were developed by subjecting the samples to various heat treatments. The details of the heat treatments are summarized in Table 3.3.1. Pieces of 1cm x 1cm x 1cm were cut from large homogenized slices to prepare the specimens. The S1, S2 and S3 steel specimens were heat treated in the dual phase region of the Fe-P phase diagram (Fig. 2.1.2) at 900°C for 1 h. Subsequently, different sets of these samples were prepared by varying the cooling rate. The samples were cooled in the furnace, air and water. Yet another set was cut out of the original castings to obtain as cast specimens. Another set was cut out of rods hot forged at 1150°C. A set was also obtained from rods made by hot forging and hot rolling at 900°C.

Table 3.3.1: Details of heat treatments conducted on high phosphorous steel specimens

Sample name	**Composition**	**Heating Rate**	**Heat Temperature**	**Soak Time**	**Cooling Rate**
As cast	S1, S2, S3	-	-	-	-
Water quench	S1, S2, S3	5°C/min	900°C	1 h	Water quench
Furnace cool	S1, S2, S3	5°C/min	900°C	1 h	Furnace cool
Air cool	S1, S2, S3	5°C/min	900°C	1 h	Air cool
Hot forged	S1, S2, S3	5°C/min	1150°C	-	Air cool
Hot forged, hot rolled	S1, S2, S3	5°C/min	900°C	-	Air cool
Growth of austenite in ferrite matrix	S3	5°C/min	830°C	4 h	Water quench
		5°C/min	865°C	20 min, 1 h, 4 h and 24 h	Water quench
		5°C/min	900°C	20 min and 1 h	Water quench
Growth of ferrite in austenite matrix	S3	5°C/min	1000°C, 30 min. Transfer to 805°C	30 min, 1 h, 4 h and 24 h.	Water quench
Homogenization of phosphorous	S3	5°C/min	865°C, 24 h, WQ. Re-heat to 750°C	20 min, 1 h, 4 h and 24 h	Water quench
Note: Homogenization of the casting was carried out at 1000°C for 24 h.					

In order to study the ferrite to austenite and austenite to ferrite transformation the samples of S3 steel were prepared. A separate slice of the casting of S3 steel was hot forged to obtain a rod with a square cross section 1.2 cm x 1.2 cm. The rod was cut to obtain samples of an approximate size: 1.2 cm x 1.2 cm x 1.2 cm. The ferrite to austenite transformation was studied in the duplex phase region by heat treating a set of S3 steel samples at different temperatures for different time intervals, namely 900°C for 20 min and 1 h, 865°C for 20 min, 1, 4 and 24 h and 830°C for 4 h (Table 3.3.1, Fig. 3.3.1). All the samples were then water quenched to retain the microstructural condition at the holding temperature. 865°C is situated in the middle of the ferrite-austenite duplex phase region for S3 steel. The austenite to ferrite transformation was studied by heating a set of S3 steel samples and holding them at 1,000°C for 1 h to achieve fully austenitic microstructure. Then the sample was transferred to another furnace and held at 805°C for 30 min, 1, 4 and 24 h to allow transformation of austenite to ferrite. Subsequently, the samples were water quenched. The transformation of austenite to ferrite of S3 steel starts at 805°C. Another set of S3 steel samples was heat treated at 865°C for 24 h and then water quenched. Phosphorous diffuses into ferrite regions from austenite regions in these specimens. These samples were re-heated to 750°C and held there for 20 min, 1, 4 and 24 h in order to study the homogenization of phosphorous with time. The phase diagram of S3 steel was drawn using Thermocalc^{TM} database TCFE7. Samples (15mm x 15 mm x 6 mm) were sliced from the casting and heat treated at 1000°C for 2 h and furnace cooled for conducting corrosion studies. The preparation of samples for dilatometry has been discussed in section 3.5.

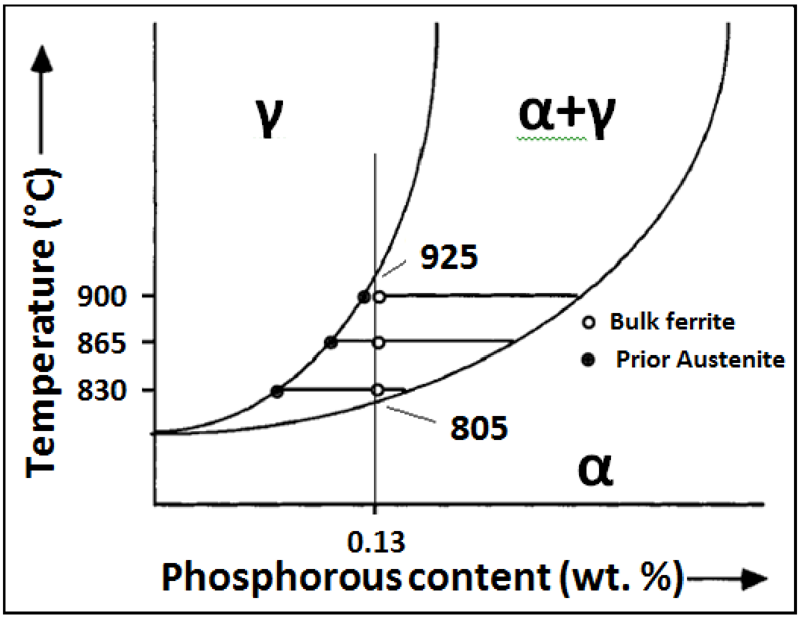

Fig. 3.3.1. Schematic diagram illustrating gamma loop of iron-phosphorus phase diagram with tie lines for the investigated temperatures (adapted from Vogel) (R. Vogel, 1929)

3.4 MICROSCOPY

3.4.1 Optical and Scanning Electron Microscope

As received cast samples and those prepared by heat treatment and forging were ground using emery paper 320, 800, 1200, 1500 and 2000 grit. Then the ground sample was polished on velvet using 1 micron and 0.024 micron alumina powder. The polished samples were cleaned with acetone and etched with 2 % nital solution (2 % HNO_3 in ethanol) reagent for optical microscopy using Leica DMI 5000M inverted optical microscope (Fig. 3.4.1.1). Nital solution attacks the low phosphorous areas and creates a relief effect called 'ghosting' (Stewart et al., 2000a). A few samples were etched with Oberhoffer's reagent. Oberhoffer's reagent reveals the dual phase microstructure by depositing copper on the low phosphorous region. As a result of this action, low phosphorous areas appear dark. Oberhoffer’s reagent was prepared by mixing 500 mL H_2O + 30 g $FeCl_3$ + 0.5 g $SnCl_2$ +1 g $CuCl_2$ + 500 mL C_2H_5OH + 50 mL HNO_3 (Stewart et al., 2000b).

A scanning electron microscope (Fig. 3.4.1.2) was used to study the segregation and distribution of phosphorous on the polished surface of cast steel. S3 steel sample held at 865°C for 24 h and then water quenched was prepared for x-ray mapping analysis by electron microscopy using a scanning electron microscope in order to confirm the de-segregation of phosphorous obtained due to holding the sample in the ferrite-austenite duplex phase region for longer times. Further, the fracture surface of the tensile test samples (hot forged) and impact test samples (hot forged) were studied for ductile or brittle characteristics using Zeiss EVO18 scanning electron microscope in SE mode. Elemental distribution at corroded area of an S3 steel sample, after potentiodynamic polarization testing in saturated $Ca(OH)_2$ solution (pH = 12.5) with 0.14 wt. % chloride, was also understood.

Fig. 3.4.1.1. Leica DMI 5000M inverted optical microscope at Metallography laboratory

Fig. 3.4.1.2. Zeiss EVO18® LaB6 filament SEM at SEM laboratory

3.5 CHARACTERIZATION

3.5.1 Phase Transformation Characterization

The Ar_3 and Ar_1 temperatures were determined from continuous cooling transformation (CCT) curves obtained using the Gleeble® 3800 machine (Fig. 3.5.1.1). A CCT test was conducted to find out the transformation temperatures by dilation of cylindrical samples of 85 mm length and 10 mm diameter during cooling at the rate of 1°C s^{-1}. These samples were machined out of the 12 mm hot forged bars. The temperature was controlled by a K-type thermocouple spot welded to the sample. The specimen was heated in Gleeble® 3800 to 1050°C with heating rate of 5°C s^{-1} followed by soaking at 1050°C for 10 s. Then the specimen was brought down to room temperature at a cooling rate of 1°C s^{-1}. The first and second deviation points in the CCT curve during cooling correspond to the Ar_3 and Ar_1 temperatures respectively.

Fig. 3.5.1.1. Gleeble® 3800 at thermo-mechanical simulator laboratory

3.5.2 Tensile and Charpy Impact Testing

Five sets of cylindrical tensile samples having a gauge diameter of 5 mm and charpy V notch impact specimens having size 10 mm x 10 mm x 55 mm were prepared according to ASTM standard A-370 (ASTM A370, 2014) (Fig. 3.5.2.1) (Fig. 3.5.2.2). Five sets of samples were prepared. The first set was prepared to study the mechanical properties of the compositions in the as cast condition. The second set was prepared by hot forging the compositions at about 1150°C. These hot forged bars were held at 900°C for 6 h to produce the third set of samples. The heat treated samples were subsequently air cooled. It was expected that the heat treatment in the ferrite-austenite duplex phase region would cause site competition between phosphorous and carbon and nitrogen (Fig. 3.3.1). This would lead to a reduction in intergranular embrittlement and improvement in ductility. The 900°C temperature was selected after dilatometric studies. Although complete partitioning of phosphorous and carbon into ferrite and austenite regions can be achieved in about 24 h at 935°C for a Fe-0.1P alloy (Stewart et al., 2000a), a 6 h heat treatment was chosen to minimize the increase in the grain size and its likely ill effect on toughness. The details of differently processed steel specimens used for characterization are shown in Table 3.5.3. The fourth set was prepared by heat treating the hot forged bars at 900°C for 1 h and air cooled to room temperature. The fifth set was prepared by hot forging and hot rolling at 900°C. First, approximately 41 mm thick slices were subjected to hot forging at 900°C to reduce their size to approximately 16 mm thick rods. Subsequently, the hot forged pieces were hot rolled at 900°C to obtain a thickness of about 13 mm and subsequently air cooled to room temperatures. Later, tensile and impact test specimens were prepared out of these hot rolled bars and their mechanical properties were found out.

While testing the specimen, two marks were made within the uniform section A using a permanent marker. The distance between these two gauge marks is called the gauge length G. Several values of the diameter are taken and an average D1 is used to calculate the area of cross-section. The tensile samples were tested at 6.6 x 10^{-4} s^{-1}; using a Hounsfield tensile testing machine (25 kN) (Fig. 3.5.2.3). Load versus extension data was collected from the computer interface attached to the tension test machine. The final gauge length and the final diameter were measured carefully after failure, using a digital Vernier Calliper. Yield stress, ultimate tensile stress and percentage elongation was obtained from the engineering stress versus engineering strain curve. The strain hardening exponent was found out from the plastic region of the true stress strain curve upto maximum stress using the software of the machine. The impact specimens were tested using a Veb Werkstoffprufmaschinen machine (Fig. 3.5.2.4) at room temperature.

Table 3.5.3: Details of differently processed steel specimens used for characterization

X1	**X2**	**X3**	**X4**	**X5**
As cast	Hot forge at 1150°C, air cool	X2 held at 900°C for 6 h, air cool	X2 held at 900°C for 1 h, air cool	Hot forge and hot roll at 900°C, air cool

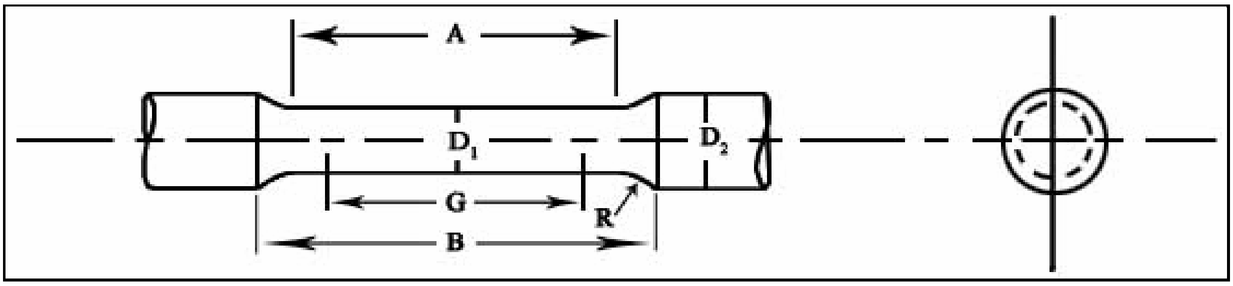

Fig. 3.5.2.1. A typical cylindrical tensile sample: A is the gauge section, G is the gauge length, D1 is the gauge diameter; An example of the dimensions D1, D2, B and R for the above tensile sample as per ASTM standard A-370 is: A = 20 mm, B = 28 mm, D1 = 4 mm, D2 = 8 mm and R = 4 mm

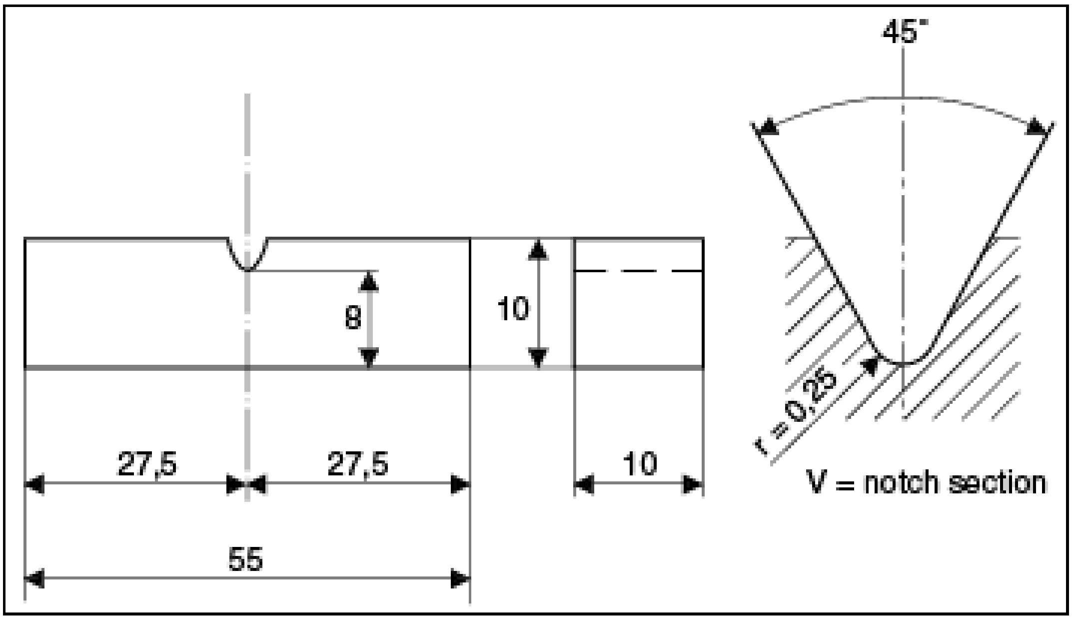

Fig. 3.5.2.2. Charpy impact test specimen as per ASTM standard A-370

Fig. 3.5.2.3. H-25K tensile testing machine (Capacity 25 kN)

Fig. 3.5.2.4. Veb Werkstoffprufmaschinen impact test machine

3.5.3 Hardness Test

Vickers hardness tests were conducted at the central portion of the polished faces of the prepared high phosphorous steels samples in different processing conditions using 10 kgf load and 15 seconds dwell time. Fig. 3.5.3.1 shows the instrument.

Fig. 3.5.3.1. FIE Vickers hardness tester

3.5.4 Micro-hardness

Micro-hardness measurements were performed to confirm the presence of ferrite-carbide mixture or martensite obtained after quenching from 750°C and above respectively in the hot compression samples using Walter UHL micro-hardness tester VMH 104 Auto (Fig. 3.5.4.1). Vickers indenter was used at 10 g load.

Fig. 3.5.4.1. Walter UHL micro-hardness tester VMH 104 Auto

3.6 ELECTROCHEMICAL TESTING

3.6.1 Environments

The corrosion behaviour of the steels was studied in saturated $Ca(OH)_2$ solution which is also called concrete pore solution (Bertolini et al., 2004). The effect of chloride ion on depassivation of the steels was studied in concrete pore solution without and with 0.05 wt. %, 0.1 wt. % and 0.14 wt. % sodium chloride.

3.6.2 Electrochemical Techniques

Different electrochemical techniques were used to understand the corrosion behaviour of the steels in aqueous solution. Linear polarization resistance (LPR), potentiodynamic polarization, electrochemical impedance spectroscopy (EIS) and open circuit potential (OCP) measurements were used in the study (Saremi, M., 2002)(Sahoo and Balasubramaniam, 2008). The LPR method was used to determine the resistance to polarization. The potentiodynamic polarization method was used to determine the pitting nucleation resistance. The EIS method was used to determine the resistance and capacitance associated with the passive layer. The solutions were prepared using single or double (for S3X3) distilled water and a calibrated digital pH meter (pH 510 of Eutech instruments) (Fig. 3.6.2.1) was used to measure the pH (12.5) of the solution.

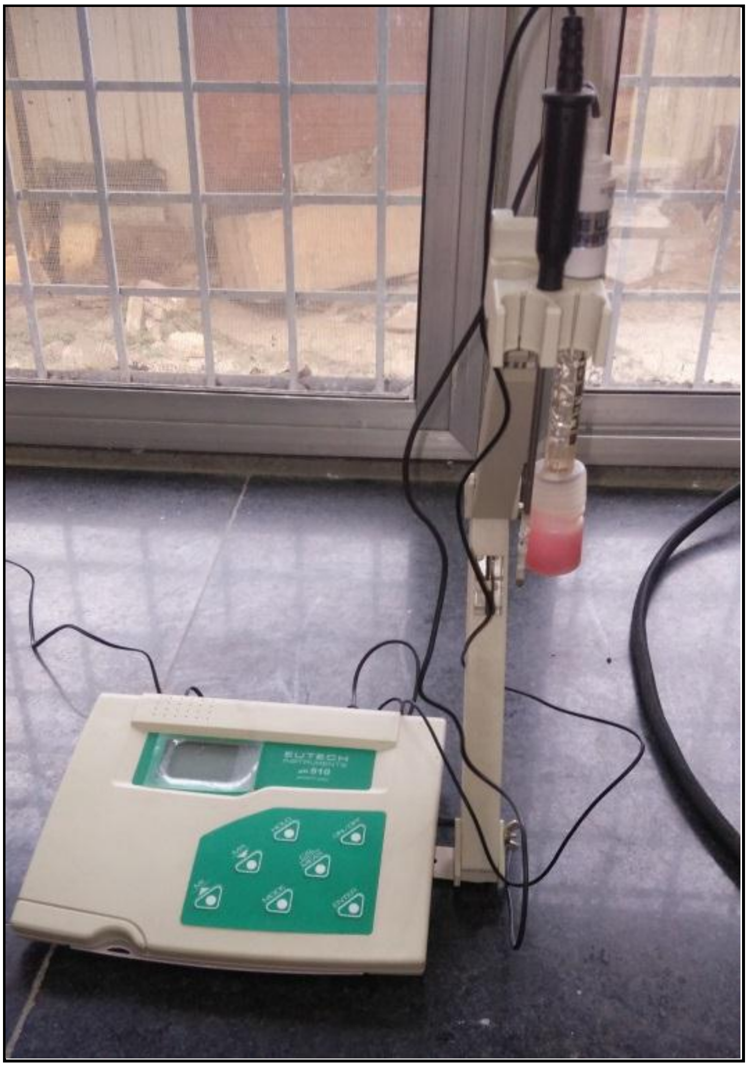

Fig. 3.6.2.1. Digital pH meter - pH 510 of Eutech instruments

3.6.2.1 Sample preparation

The surfaces of the furnace cooled samples (15mm x15 mm x 8 mm) were finished with emery paper (upto 800 grit) and degreased with acetone. Different samples of the same rod were prepared for conducting reproducible experiments.

3.6.2.2 Test cells and potentiostat

The samples were mounted on a standard flat cell (Ametek USA) having a platinum counter electrode (Fig. 3.6.2.2.1) for conducting potentiodynamic polarization, linear polarization resistance and electrochemical impedance spectroscopy studies. A saturated calomel electrode (SCE) was used in all the experiments. Potentiodynamic polarization studies were conducted using an EG&G PARSTAT 273A Potentiostat (Ametek, USA) (Fig. 3.6.2.2.2). The EIS and LPR experiments were conducted using Gamry 1000 Interface (Fig. 3.6.2.2.3)

3.6.2.3 Open circuit potential and linear polarization resistance

The OCP and LPR experiments were conducted using Gamry 1000 Interface (Fig. 3.6.2.2.3) at time intervals of 15 min, 5 h and 21 h. These experiments were conducted in saturated $Ca(OH)_2$ solution without chloride and with 0.05 and 0.1 wt % Cl^-. The LPR scan was conducted from -20mV to +20 mV w.r.t. the OCP at a scan rate of 0.125 mV s^{-1}. The LPR or R_p was measured from the slope of the potential vs current density curve at i=0 using Gamry Echem analyst software. The linear region of the plot was selected and the polarization resistance fit method was used to obtain the R_p. The linear portion should be selected carefully. Usually, it is between ±5 and ±10 mV (Oldham and Mansfeld, 1971)(Mansfeld, 2005)(Mansfeld, 1974).

The instantaneous corrosion rate of the specimens was obtained from the measured LPR using the Stern-Geary equation (Alonso et al., 2000)(Jone, 1992) as shown below:

$$i_{corr} = \frac{1}{2.303} \times \frac{\beta_a \beta_c}{R_p \times (\beta_a + \beta_c)} = \frac{B}{R_p} \qquad (3.6.2.3)$$

In the above equation, β_a, β_c are the anodic and cathodic tafel slopes respectively, R_p is the polarization resistance and B is a function of the tafel slopes. Duplicate tests were conducted in each solution.

3.6.2.4 Potentiodynamic polarization

Potentiodynamic polarization studies were conducted using an EG&G PARSTAT 273A Potentiostat (Ametek, USA) (Fig. 3.6.2.2.2) at a scan rate of 0.75 mVs^{-1} in saturated $Ca(OH)_2$ solution without chloride and with 0.05, 0.1, 0.14 wt. % Cl^-. The open circuit potential was stabilized for 1 h before conducting the experiment. All the experiments were repeated three times. The chloride pitting potential and the pitting nucleation resistance was found out for each chloride concentration. The difference between the OCP and the pitting potential is called the pitting nucleation resistance *R* (Bethencourt et al., 1998).

3.6.2.5 Electrochemical impedance spectroscopy

The EIS experiments were conducted using Gamry 1000 Interface (Fig. 3.6.2.2.3) at time intervals of 15 min, 5h and 21h. These experiments were conducted in saturated $Ca(OH)_2$ solution without chloride and with 0.05 and 0.1 wt. % Cl^-. In the EIS tests, impedance response was scanned by applying a sinusoidal potential perturbation of 10 mV at the open circuit potentials with frequency sweep from 100 kHz to 10 mHz using the GAMRY Interface 1000 potentiostat (Fig. 3.6.2.2.3). The EIS data was analysed by fitting with equivalent circuits using GAMRY EChem analyst software. The EIS tests of S3X3 steel have been done using double distilled water and Bio-Logic SP 200 and the analysis of the plots are done using its Zfit software (Fig. 3.6.2.2.4). The frequency sweep in this case was from 7 MHz to 5 mHz. The time intervals were 5, 15, 25, 40, 65 h. These experiments were conducted in saturated $Ca(OH)_2$ solution with 0.1 wt. % Cl^-.

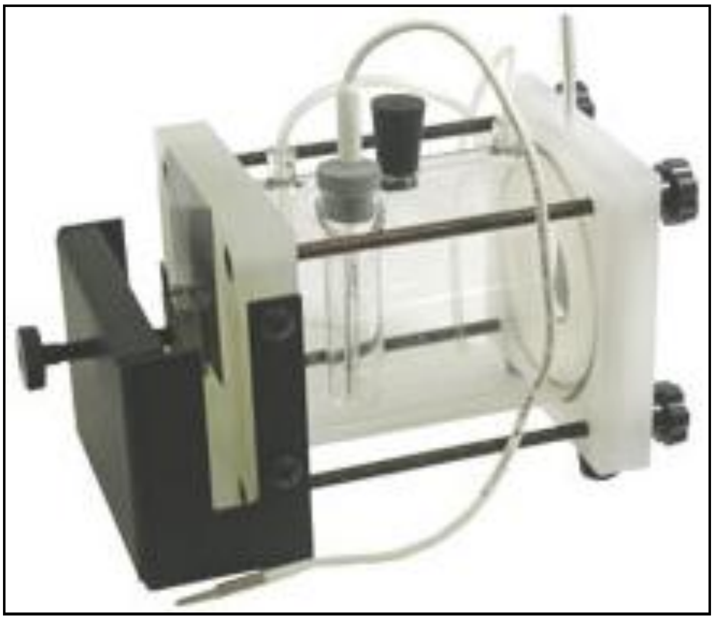

Fig. 3.6.2.2.1. Flat cell - Ametek, USA

Fig. 3.6.2.2.2. EG&G PARSTAT 273A Potentiostat (Ametek, USA)

Fig. 3.6.2.2.3. Gamry Interface 1000 Potentiostat

Fig. 3.6.2.2.4. Bio-Logic SP-200 Potentiostat

3.7 THERMO-MECHANICAL SIMULATION AND GRAIN REFINEMENT

3.7.1 Hot Compression

Hot compression tests were conducted on samples of S1, S2, and S3 steels with the help of a Gleeble® 3800 thermo-mechanical simulator (Fig. 3.5.1.1) under vacuum (pressure of 1 Pa). The dimensions of the cylindrical specimen were 15 mm length and 10 mm diameter. The specimens were machined out of the 12 mm hot forged bars. In order to control the temperature during the experiment, a K-type thermocouple was spot welded to the sample. A nickel based lubricant and a graphite foil were used between the sample and the ISO-T anvil to achieve reduction in both, the temperature gradient and the friction. All the specimens were heated upto the austenitization temperature of 1050°C at 5°C s^{-1} and soaked for 10 s. They were then cooled down to corresponding compression test temperature in the range of 750-1050°C, at increments of 50°C at the rate of 1°C s^{-1}. The specimens were deformed at constant strain rates of 0.001, 0.01, 0.1, 0.5, 1 and 10 s^{-1}; up to a total logarithmic deformation of 0.69. Finally, in-situ water quenching was employed to freeze the microstructure and avoid any meta-dynamic or static phenomena that could occur after hot deformation. Barrelling coefficient was calculated for the compressed samples. $B = l_0 d_0^2 / l_f d_f^2$, where, l_f is the average length of deformed test piece and d_f is the average diameter of deformed test piece.

The values of flow stress at compressive strain of 0.6 were obtained from the flow curves corresponding to the specific temperature and strain rate and used for calculations. The flow stress data obtained at higher strain rates (10, 1, 0.5, 0.1, and 0.01 s^{-1}) was corrected for adiabatic temperature rise using linear interpolation between ln (σ) and $1/T$ (T is in K) at constant strain and strain rate (Goetz and Semiatin, 2001). The corrected flow data was utilized to obtain different parameters like efficiency of power dissipation η and instability parameter κ using equations (2.2.5.4) and (2.2.5.8), respectively. The processing maps were made with the help of Origin 7.5 software.

3.7.2 Grain Refinement

The grain size of the samples prepared at various strain rates and temperatures were found out using ASTM E112-13 line intercept method. The grain refinement results were also correlated with the Zener-Hollomon parameter (Z) values.

3.7.3 Processing Map

Processing map for 0.6 true strain is plotted based on the modified dynamic materials model proposed by Murty and Rao (Murty et al., 2003). The iso-efficiency (η) lines are shown in the plot of log $\dot{\varepsilon}$ versus T. The instability parameter (κ) domains which are shown as shaded area, is superimposed.

Thus, the experimental procedure has been designed to:

- design and prepare steels having high phosphorous
- study the diffusion of phosphorous during the growth of γ grains in α matrix and vice versa
- heat treat and hot work the steels in the (α+γ) region and study the mechanical properties

- study the corrosion behaviour of the high phosphorous steels, especially that having the best impact properties
- study the effect of hot deformation temperatures and strain rates on the microstructures and grain sizes of the high phosphorous steels
- identify the safe processing window

The results obtained during the experiments and the discussions regarding the findings are presented in the next chapter.

Chapter 4

RESULTS AND DISCUSSION

This chapter is divided into five major sections. The first section describes the phase transformation studies and the microstructural aspects of the as cast, hot forged and heat-treated samples. The second section discusses the mechanical properties of the samples. Chloride induced depassivation of the samples in saturated $Ca(OH)_2$ solution is elaborated upon in the third section. The fourth section is devoted to the microstructural evolution and ferrite grain refinement of the steels. The fifth section delves into the determination of the safe hot working domains for S1 steel.

The phase transformation studies were conducted to understand the partitioning of phosphorous and carbon during the growth of austenite grains from ferrite phase and vice versa. Since phosphorous is a ferrite stabilizer and carbon is an austenite stabilizer, they will move in opposite directions during high temperature holding or working in the intercritical phase field of (α+γ). This will create the desirable effect of removing phosphorous away from the grain boundaries and result in improved toughness.

4.1 PHASE TRANSFORMATION

Dilatometry studies were conducted using a thermo-mechanical simulator (GLEEBLE 3800®) and the results are reported in Fig. 4.1.1 and Table 4.1.1. S2 steel with higher silicon shows a higher Ar_1 transformation temperature when compared with S1 steel. Silicon is a ferrite stabilizer and therefore, causes the Ar_1 temperature to increase (Durand-Charre, 2004). S3 steel contains higher nitrogen than S2 steel, and hence shows lower Ar_1 and Ar_3 temperatures. Nitrogen being an austenite stabilizer should expand the gamma phase field and hence cause the transformation temperatures to fall (Durand-Charre, 2004).

Table 4.1.1: Transformation temperatures of the 3 high phosphorous steels determined by dilatometry studies conducted in a thermo-mechanical simulator (GLEEBLE 3800®)

Transformation temperature	**S1 steel**	**S2 steel**	**S3 steel**
Ar_1 (°C)	**790**	**813**	**805**
Ar_3 (°C)	**965**	**941**	**925**

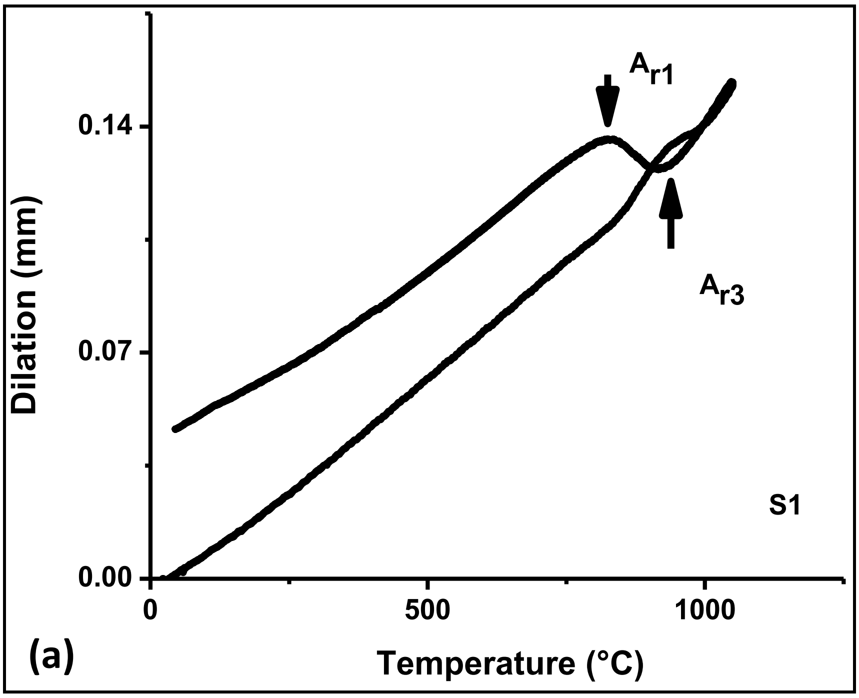

Fig. 4.1.1. (a) Results of the CCT test conducted on the S1 steel using a thermo-mechanical simulator (GLEEBLE 3800®); points of inflection correspond to the Ar_1 and Ar_3 temperatures

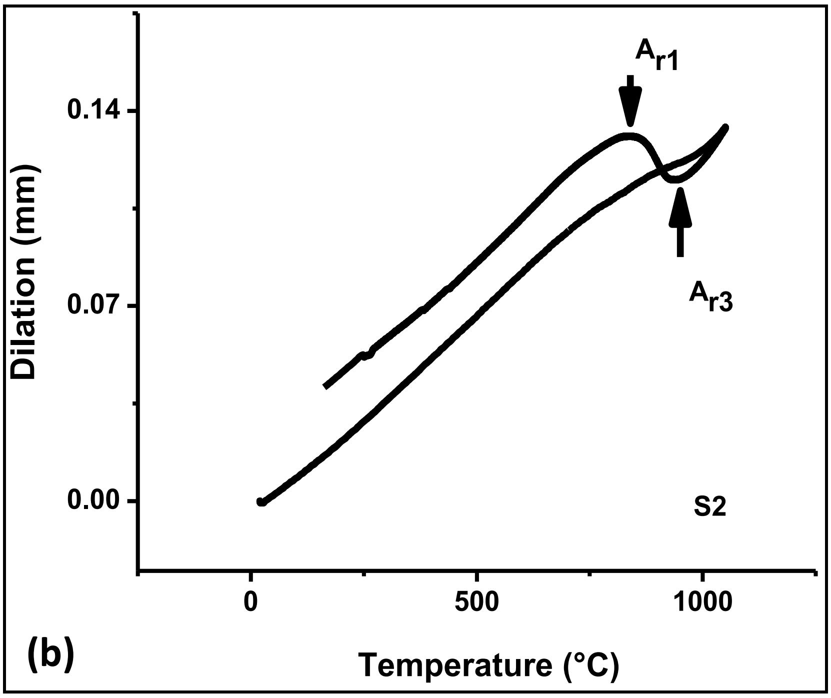

Fig. 4.1.1. (b) Results of the CCT test conducted on the S2 steel using a thermo-mechanical simulator (GLEEBLE 3800®); points of inflection correspond to the Ar_1 and Ar_3 temperatures

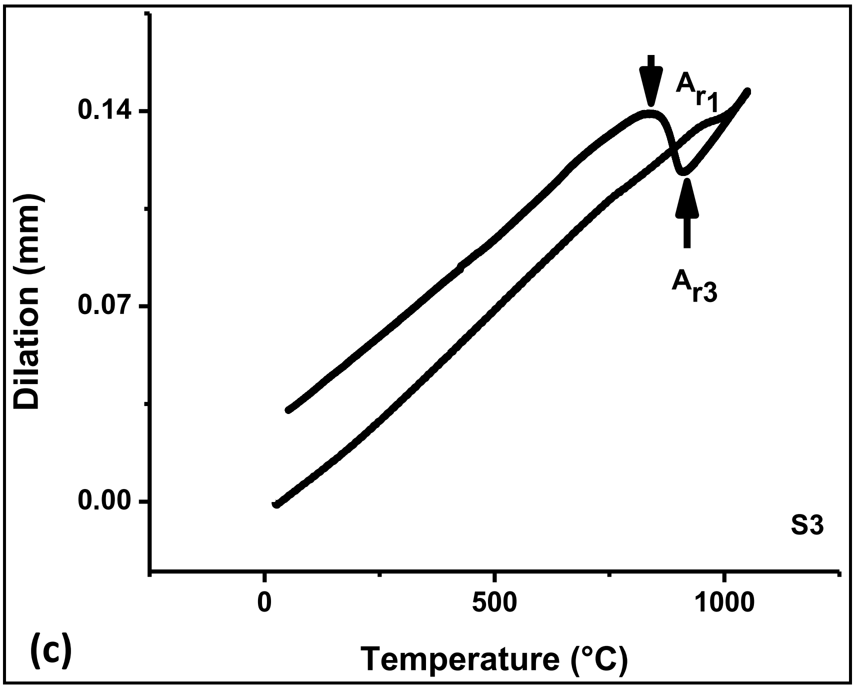

Fig. 4.1.1. (c) Results of the CCT test conducted on the S3 steel using a thermo-mechanical simulator (GLEEBLE 3800®); points of inflection correspond to the Ar_1 and Ar_3 temperatures

4.2 METALLOGRAPHY

The specimens of S1, S2 and S3 steels were heat treated at 900°C for 1 h and subsequently, the samples were subjected to furnace cooling, air cooling and water quenching to obtain three sets. As cast steels and hot forged steels were used to obtain another 2 sets. Micrographs of these sets are shown in Fig. 4.2.1. Pearlite grains can be seen in all the three compositions in the as cast condition, and this is shown in Fig. 4.2.2a. All the three compositions show ghosting features typical of high phosphorous steels in the hot rolled condition. The micrograph of hot forged S2 is shown in Fig. 4.2.2b. It is reported that phosphoric irons show a watery, shimmering, ghosting microstructure when etched with nital solution (Stead, 1915) (Sahoo and Balasubramaniam, 2007a) (Sahoo and Balasubramaniam, 2007b) (Stewart et al., 2000b) (Stewart et al., 2000a). This ghosting is not visible in specimens hot forged at 1150°C and cooled in air. Thus, the partitioning of phosphorous between ferrite and austenite is not produced by itself on cooling after the transformation at higher temperatures.

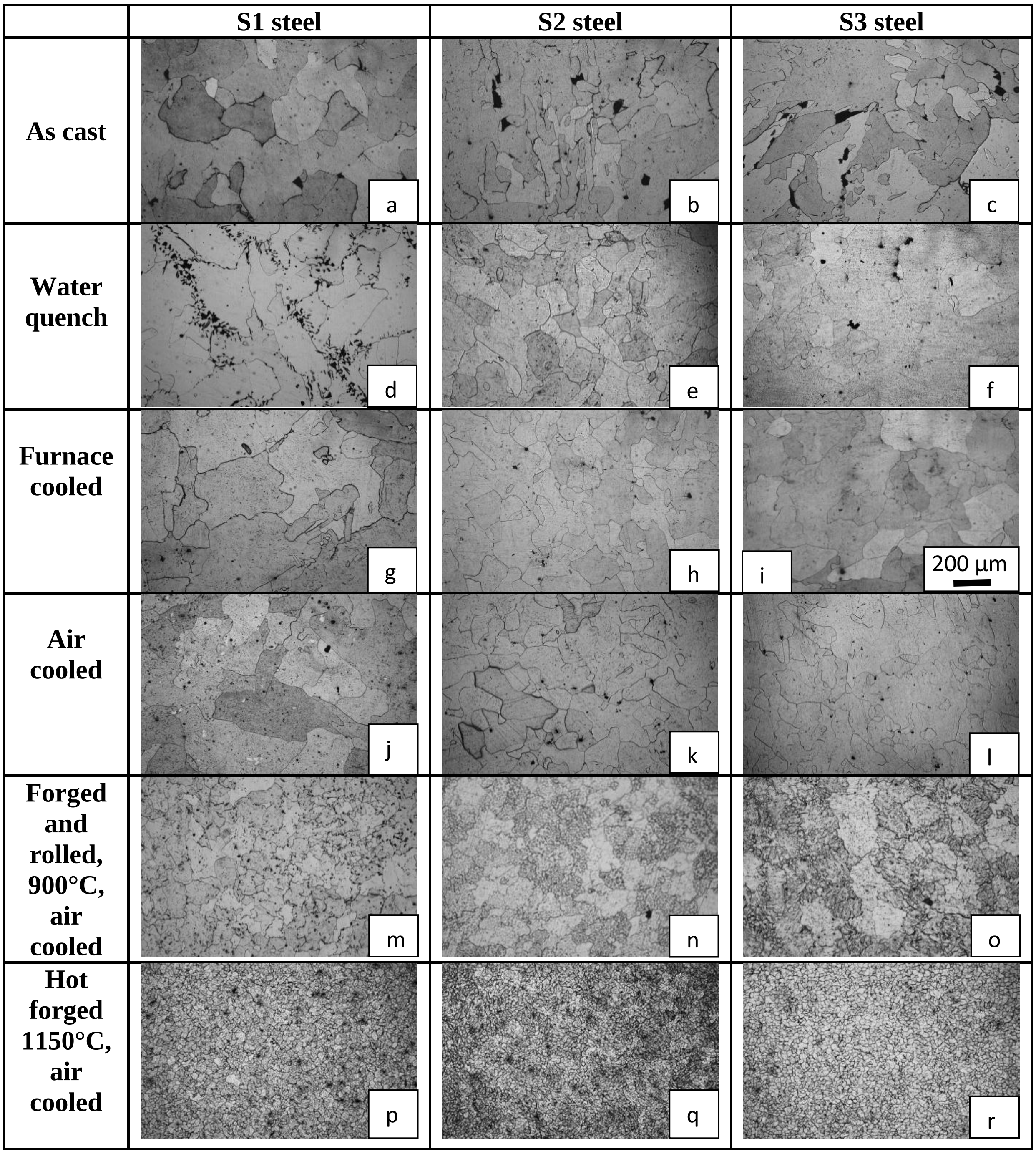

Fig. 4.2.1. Optical micrographs of the steel samples etched with 2 % nital solution

Etching action of Oberhoffer’s reagent: Copper is precipitated first on low phosphorus regions (Stewart et al., 2000b). Hence, optical observation after etching shows that the high phosphorus areas (*e.g.,* ferrite) appear light while those low in phosphorus (*e.g.,* prior austenite) appear dark (Fig. 4.2.3).

S1 steel, As cast	**S2 steel, hot forge and hot roll at 900°C, air cool**
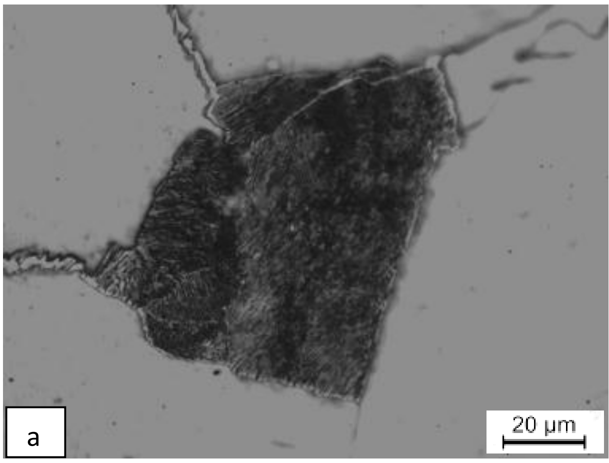	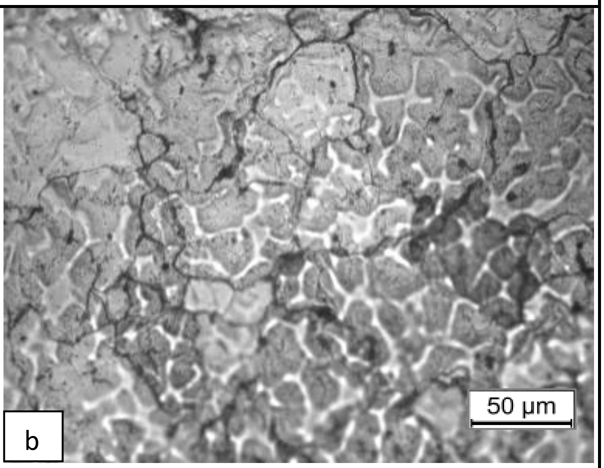

Fig. 4.2.2. Optical micrographs of the steel samples etched with 2 % nital solution at higher magnifications

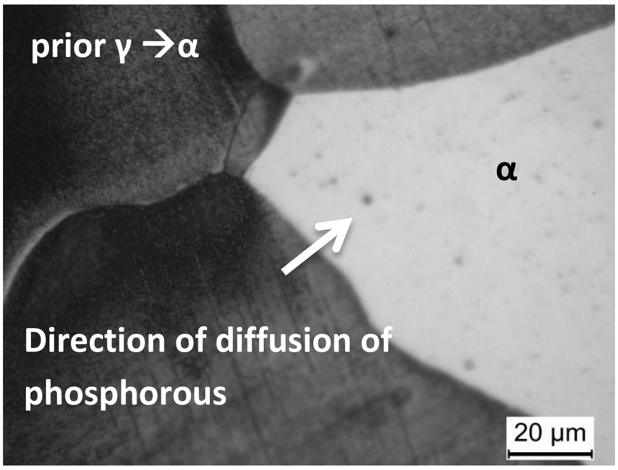

Fig. 4.2.3. Microstructure of S3 steel heated at 865°C for 24 h, water quenched, and etched with Oberhoffer's reagent

In order to understand the partitioning of phosphorous between prior phases of α and γ during the growth of austenite grains in a ferritic matrix, the samples were heated to 865°C and held at that temperature for 20 min, 1 h, 4 h and 24 h. 865°C was chosen as it is situated at the middle of the (α+γ) phase field of S3 steel. Since the sample has been heat treated in the (α+γ) phase field for a given amount of time, alpha and gamma phases were formed at that temperature. Austenite was formed by a diffusion controlled nucleation and growth mechanism at the expense of ferrite. The dark coloured austenite grains start to form as allotriomorphs at the grain boundaries of the ferrite grains when the steel was held for 20 min at the afore-mentioned temperature. The white and light grey portions**,** *i.e.,* bulk ferrite grains**,** are rich in phosphorous. As the time of holding progresses, the grains of austenite keep growing progressively at the expense of ferrite. Prolonged heating caused competitive coarsening and spheroidization of the phases as they approached equilibrium. The partitioning of phosphorous between the ferrite regions and the austenite regions continues up to 24 h. The largest grains are observed at 24 h of holding time since a duplex phase microstructure is well developed after 24 h. There is no evidence of a concentration gradient as revealed by the Oberhoffer's reagent at this stage suggesting that equilibrium has been attained. The prior gamma phase was transformed to low phosphorous and high carbon ferrite on quenching which was done to preserve the state of the material at that temperature. Copper deposition renders the low phosphorous region red. The contrast is enhanced to obtain the micrographs. *The drawback is that on some occasions scratch lines are also highlighted*. Thus, the low phosphorous and high carbon prior austenite transformed to ferrite on quenching shows dark contrast and high phosphorous and low carbon duplex phase ferrite shows light contrast in the micrographs (Fig. 4.2.4). The austenite morphology conformed to the Dube classification system and included allotriomorphs, idiomorphs and sawtooth (Dube et al., 1958). Observing at higher magnification reveals that the initial austenite formed had needle type morphology since it showed either spherical or oblong shapes in the micrographs. The austenite grains showed lower phosphorous than the bulk ferrite. But the austenite grains were encircled by a thin region of high phosphorous ferrite which etched white and was formed due to the diffusing out of phosphorous during the formation of austenite. This light coloured 'halo' kept increasing in thickness at longer holding times. As equilibrium is approached both the contrasts become more and more distinct (Fig. 4.2.4f). The free energy of ferrite-austenite transformation for S3 steel composition at 865°C was calculated to be -54.5 kJ/mol, using commercial thermodynamic software (Thermocalc^{TM} database TCFE7) (Table 4.2.1).

Similar results were obtained on studying the samples heat treated at 900°C for 20 min, 1 h and at 830°C for 4 h (Fig. 4.2.5a-f). The austenite grains formed at 900°C in 20 min were thick allotriomorphs and idiomorphs since the driving force is higher at higher temperatures. There exists a gradient of concentration of phosphorous in the ferrite region. The contrast between ferrite and austenite grains grows larger when the sample is held at 900°C for 1 h. The contrasts of prior austenite and ferrite are quite distinct for the specimen held for 4 h at 830°C although some areas show a gradient of phosphorous concentration. The free energy of ferrite-austenite transformation for S3 steel at 830°C and 900°C was calculated to be -51.9 and -57.1 kJ/mol respectively, using commercial thermodynamic software (Thermocalc^{TM} database TCFE7) (Table 4.2.1).

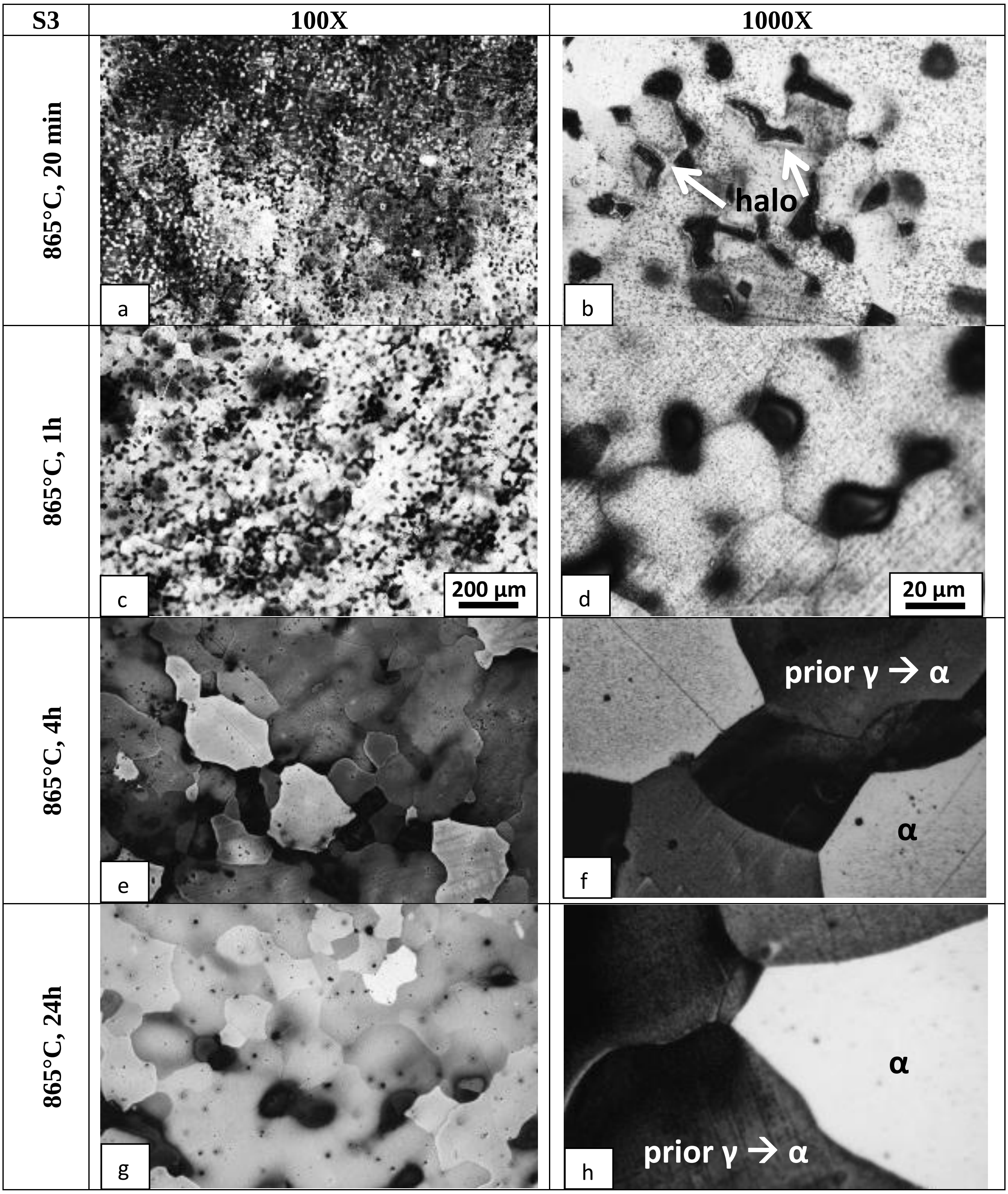

Fig. 4.2.4. Optical micrographs of S3 steel specimens held at 865°C for different times and etched with Oberhoffer's reagent

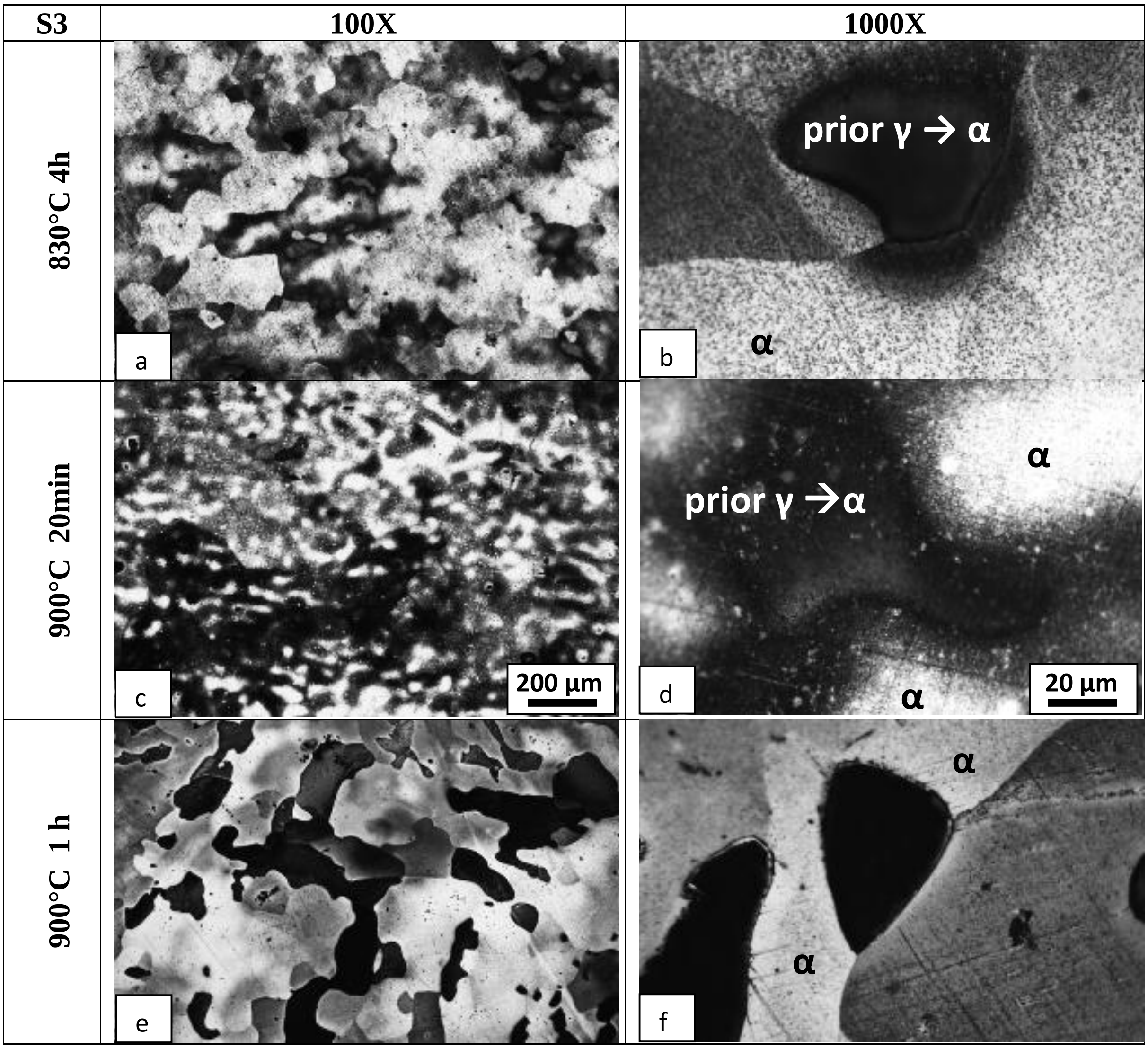

Fig. 4.2.5. Optical micrographs of S3 steel specimens held at 830°C and 900°C for different times and etched with Oberhoffer's reagent

The partitioning of phosphorous between prior phases of α and γ during the growth of ferrite grains in an austenitic matrix was studied by preparing another set of samples. The samples were heated to 1000°C for 30 min in order to austenitize the samples fully. Then they were transferred to another furnace held at 805°C and held for 30 min, 1 h, 4 h and 24 h at that temperature. The ferrite grains nucleate at the austenite grain boundaries and are etched bright and white by the Oberhoffer's reagent. Phosphorous diffuses towards the ferrite grains and hence the region surrounding the ferrite grains is depleted in phosphorous. Such a region etches darker than the phosphorous rich ferrite. Both allotriomorphic, idiomorphic and sawtooth ferrite can be observed as described in the Dube classification system (Dube et al., 1958). The ferrite islands have blunt tips. At longer soak times the ferrite grains form a network. The size of the ferrite grains increase at the expense of the austenite phase till equilibrium is reached and is signified by the distinction of the two grain contrasts to a maximum (Fig. 4.2.6a-d). In the present case, partitioning of phosphorous between prior phases of ferrite and austenite at 805°C was not completed even after 24 hours. The free energy of ferrite-austenite transformation for S3 steel at 805°C was calculated to be -50.1 kJ/mol, using commercial thermodynamic software (Thermocalc^{TM} database TCFE7) (Table 4.2.1).

Table 4.2.1: Calculations of free energies of ferrite-austenite transformation using commercial thermodynamic software (Thermocalc^{TM} database TCFE7)

Temperature (°C)	**Free energy of ferrite-austenite transformation for S3 steel (kJ/mol)**
805	-50.1
830	-51.9
865	-54.5
900	-57.1

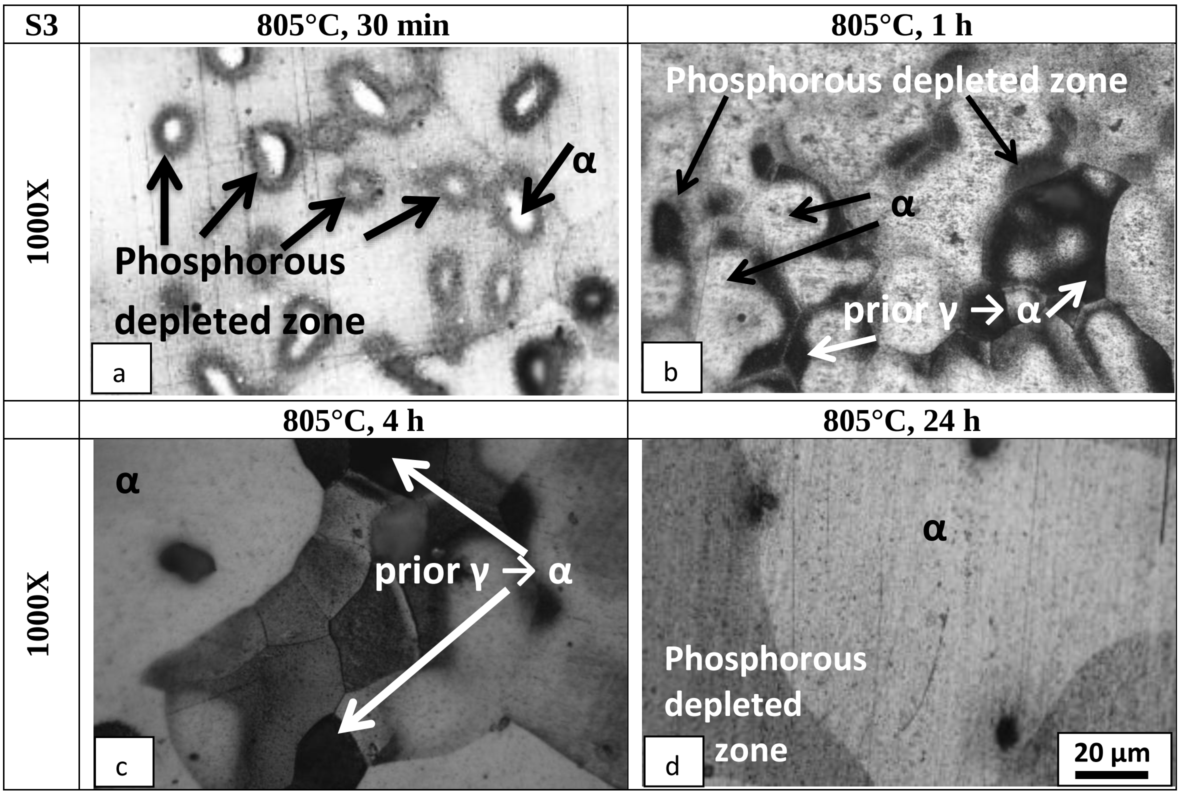

Fig. 4.2.6. Optical micrographs of S3 steel specimens held at 805°C for different times and etched with Oberhoffer's reagent

In order to understand the time of heat treatment required for homogenization of phosphorous, samples were soaked at 865°C for 24 h, water quenched and then re-heated at 750°C for 20 min, 1 h, 4 h and 24 h. The samples showed that the contrast decreased but remained even in the sample heated for 24 h (Fig. 4.2.7a-d). The rate of diffusion of phosphorous in austenite is less than that in ferrite. The kinetics of diffusion controlled austenite-ferrite reaction in the dual phase region is slower than the reverse reaction (Rocquet and Jegaden, 1951). Further, an estimate of diffusion distances √ (*Dt*) was made using values of activation energy and diffusion coefficient quoted in Askill (Askill, 1970) for the temperature range 700-850°C (Table 4.2.2). The diffusion distance calculated for 24 h at 750°C is 13.1 μm. This is less than that (18.8-46.2 μm) required for redistributing phosphorous evenly as reported by Stewart *et al.* (Stewart et al., 2000a). Therefore, the temperature should be increased to above the ferrite-austenite duplex phase region for achieving quicker removal of inhomogeneity of phosphorous in ferrite (Stewart et al., 2000c). It should be recognized that the difusion distance is not a straight line distance. It has been calculated to compare with the diffusion distances required to homogenize phosphorous.

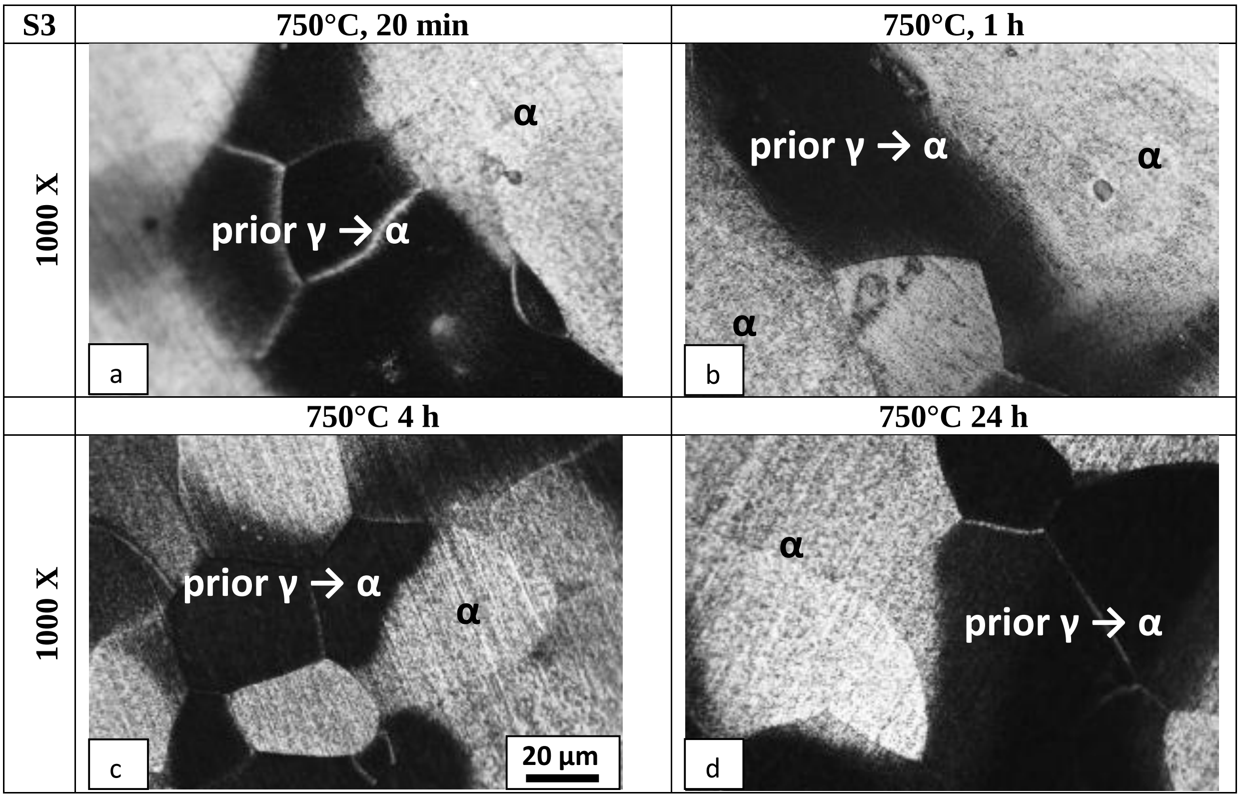

Fig. 4.2.7. Optical micrographs of S3 steel specimens held at 865°C for 24 h, water quenched, reheated and held at 750°C for different times and etched with Oberhoffer's reagent

Table 4.2.2: Estimates of diffusion distances of phosphorus in S3 steel specimens held at 865°C for 24 h, water quenched, reheated and held at 750°C for different times

Length of heat treatment	**Estimates of diffusion distances $\sqrt{(Dt)}$ in µm**
20 min	1.55
1 h	2.7
4 h	5.2
24 h	13.1

X-ray area mapping analysis was conducted on a S3 steel sample held at 865°C for 24 h and etched with Oberhoffer's reagent in order to confirm the removal of phosphorous (Fig. 4.2.8) using an SEM. The results of the EDS analysis are qualitative and confirm that dark contrast regions have lower phosphorous concentrations than lighter regions *i.e.*, ferrite.

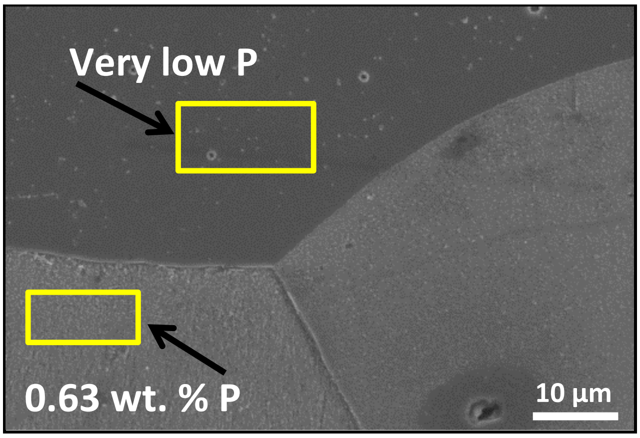

Fig. 4.2.8. SEM photo of S3 steel sample held at 865°C for 24 h, and water quenched, etched with Oberhoffer's reagent, displaying X-ray area mapping results for phosphorous

The volume fraction of austenite was calculated by drawing a tie line at 865°C in the ferrite-austenite duplex phase region of the phase diagram calculated using a commercial thermodynamic software (Thermocalc^{TM} database TCFE7) for Fe-P system with other elements as present in S3 steel and finding the phase fractions for 0.13 wt. % P. The ferrite-austenite duplex phase region of the calculated phase diagram (Fig. 4.2.9) was larger and expanded as compared to the binary Fe-P phase diagram (Fig. 3.3.1) due to the influence of the austenite stabilizers such as carbon and nitrogen. The austenite volume fraction was calculated to be 89.9 wt. %.

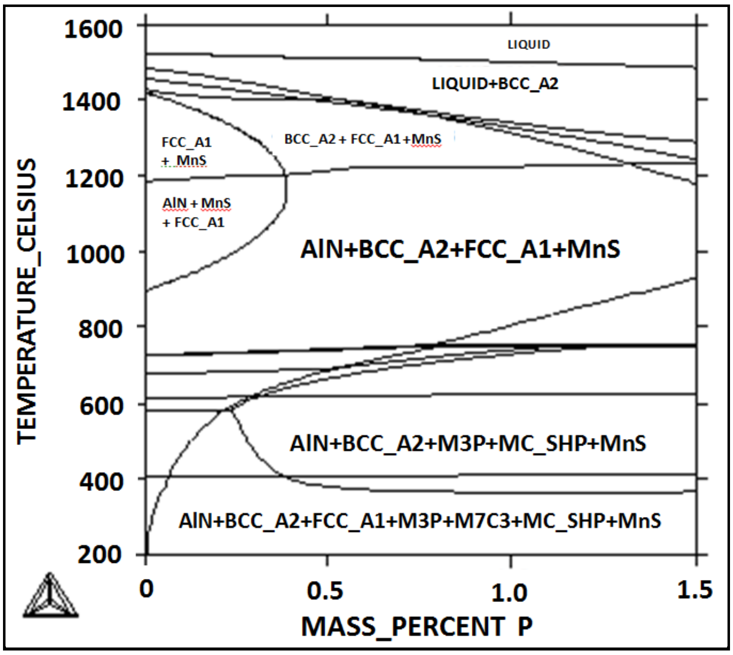

Fig. 4.2.9. Phase diagrams calculated using commercial thermodynamic software (Thermocalc^{TM} database TCFE7) for Fe-P system with other elements as present in S3 steel

The temperatures of 877.5, 877 and 865°C fall in the middle of the (α+γ) regions of S1, S2 and S3 steels. 865°C was chosen for metallographic study of S3 steel. It was understood from the metallographic studies that phosphorous could be diffused into the ferrite grains and away from the austenite grains by holding the S3 steel specimens at 865°C between 4 and 24 h. The magnitude of variation of phosphorous content became negligible on holding S3 steel specimens at 865°C for a time interval between 4 h and 24 h. An estimate of diffusion distances $\sqrt{}$ (Dt) was made using values of activation energy and diffusion coefficient quoted in Askill (Askill, 1970) for the temperature range 860-900°C. The value was estimated to be 10.2 and 25.1 μm for S3 steel specimens held at 865°C for 4 and 24 h. S3 steel specimens should be held at 900°C for a time period between 1.9 to 11.6 h to allow the phosphorous to travel the same diffusion distances and reach similar equilibrium distribution of phosphorous between austenite and ferrite. This is lower than that required at 865°C. Stewart *et al.* (Stewart et al., 2000a) found that the amount of inhomogeneity in phosphorus content within Fe-0.2P steel held at 900°C and 4 h was very low as revealed by Oberhoffer's reagent and that the variation was nil at 24h. At 24h, the grain sizes are very large. Accordingly, a temperature had to be chosen to heat treat or hot work, all the three high phosphorous steels to bring about the desired removal of phosphorous from the grain boundaries of the steels, resulting in improved toughness. Therefore, keeping the above discussion in mind, a temperature of 900°C and holding times of 1 and 6 h were chosen for the study on mechanical properties of the high phosphorous steels and their comparison with earlier work.

4.3 MECHANICAL PROPERTIES

The toughness of high phosphorous steels can be improved by removing phosphorous from the grain boundaries by utilizing alloying elements and heat treatment and hot working in the (α+γ) phase field (Gouthama and Balasubramaniam, 2003; Sahoo and Balasubramaniam, 2007a). Accordingly, the S1, S2 and S3 steels are forged and heat treated or hot rolled at 900°C for various times and the mechanical properties are studied in this section. The microstructures of cast, hot forged and hot forged and heat treated samples are studied using optical microscope (Fig. 4.3.1a-i). The cast specimens show pearlite and coarse ferrite grains. Fine grain size is obtained owing to the hot forging treatment. There is no apparent influence of the composition of the phosphorous steels on the grain size. The grains of the forged and heat treated samples are larger than the hot forged samples (Table 4.3.1).

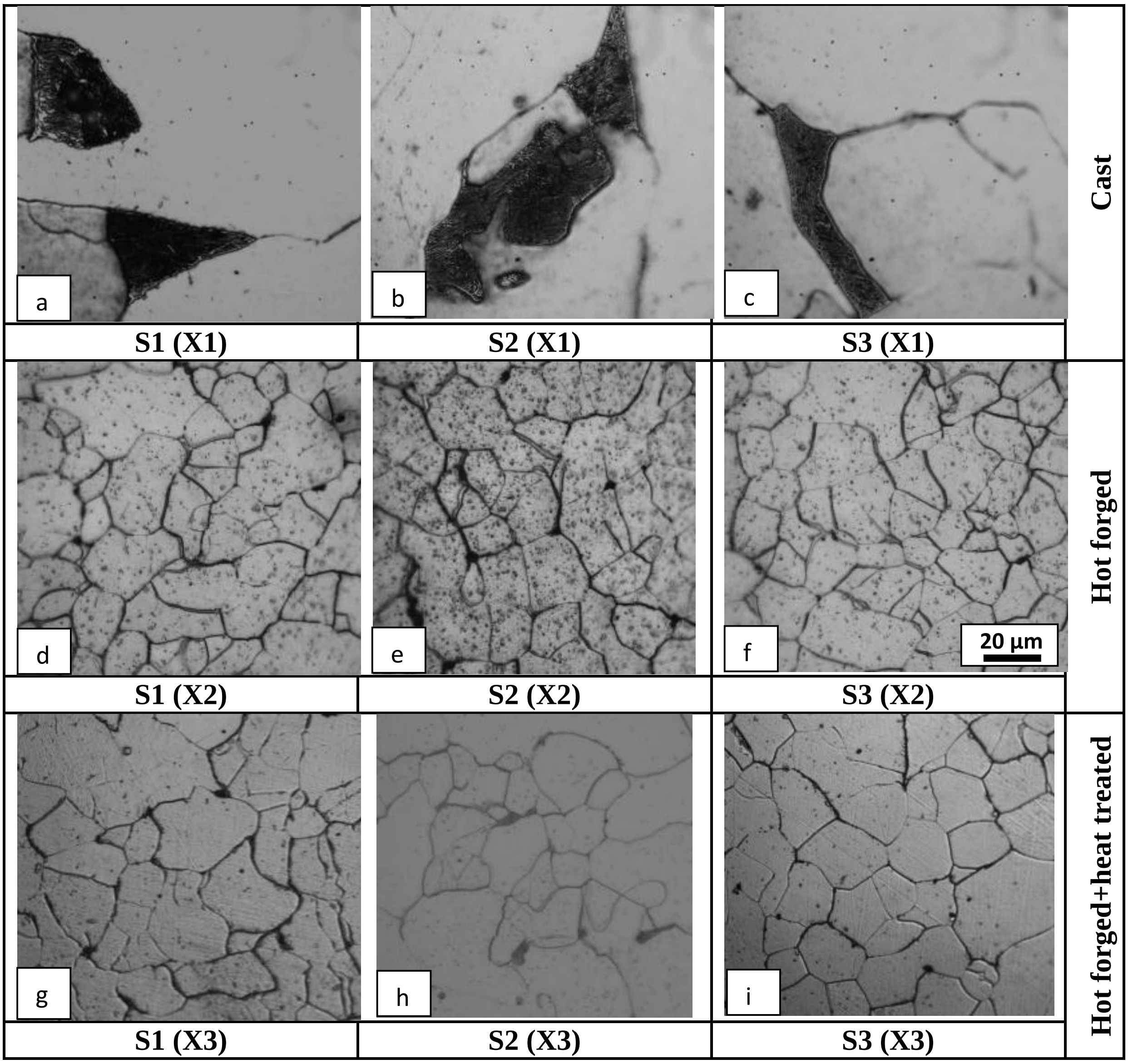

S1 (X1) S2 (X1) S3 (X1)

S1 (X2) S2 (X2) S3 (X2)

S1 (X3) S2 (X3) S3 (X3)

Fig. 4.3.1. Microstructures of S1, S2, and S3 steels in X1, X2 and X3 conditions; etched with 2 % nital solution

Table 4.3.1: Change in grain size due to heat treatment of hot forged steels

Specimen	Field 1	Field 2	Mean (µm)	Specimen	Field 1	Field 2	Mean (µm)
S1X2	16.4	15.7	16.1	**S1X3**	31	27.7	29.4
S2X2	12.1	17.9	15	**S2X3**	41.5	39.8	40.7
S3X2	16.4	15.3	15.9	**S3X3**	19.3	22.5	20.9

The fracture surfaces of the uniaxial tensile test samples of S1, S2 and S3 steels were studied in the cast, hot forged and hot forged and heat treated condition using SEM. The images of the cast specimens show brittle behaviour. The images of the hot forged, and hot forged plus heat treated specimens show ductile behaviour in the form of conical equiaxed dimples (Fig. 4.3.2a-i). S2X2 has the smallest dimples indicating a lower tendency for localized deformation.

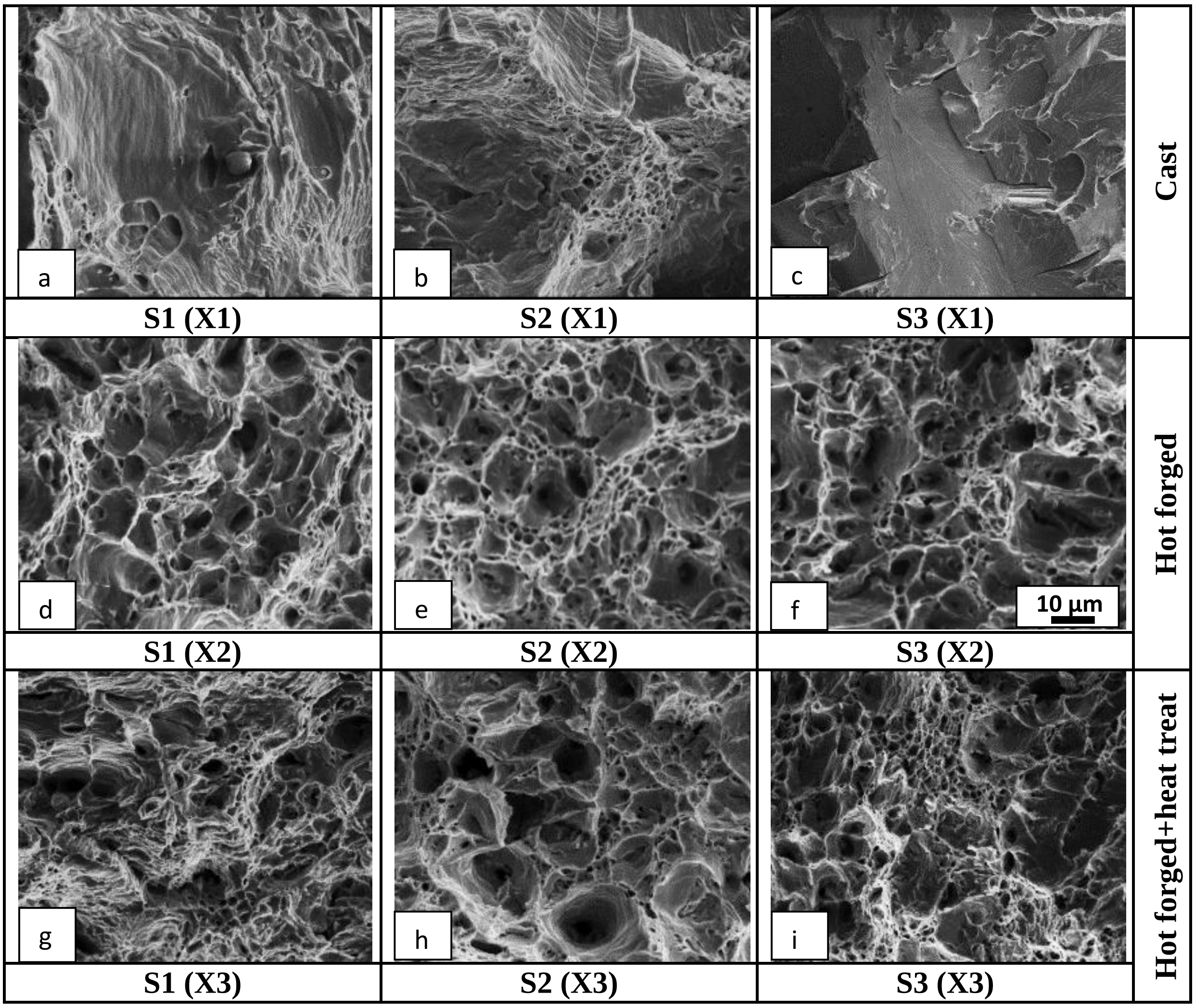

S1 (X1) **S2 (X1)** **S3 (X1)**

S1 (X2) **S2 (X2)** **S3 (X2)**

S1 (X3) **S2 (X3)** **S3 (X3)**

Fig. 4.3.2. SEM images of the tensile test samples of S1, S2, and S3 steels in X1, X2 and X3 conditions

The fracture surfaces of the Charpy V-notch impact test specimens of the hot forged and subsequently heat treated steels show more than 70% shear fracture appearance (Fig. 4.3.3.a, i-ix) calculated as per ASTM standards (ASTM E 23-12c, 2013). The twisted edges bear testimony to ductile mode of fracture. The fracture surfaces of the cast samples display brittle failure.

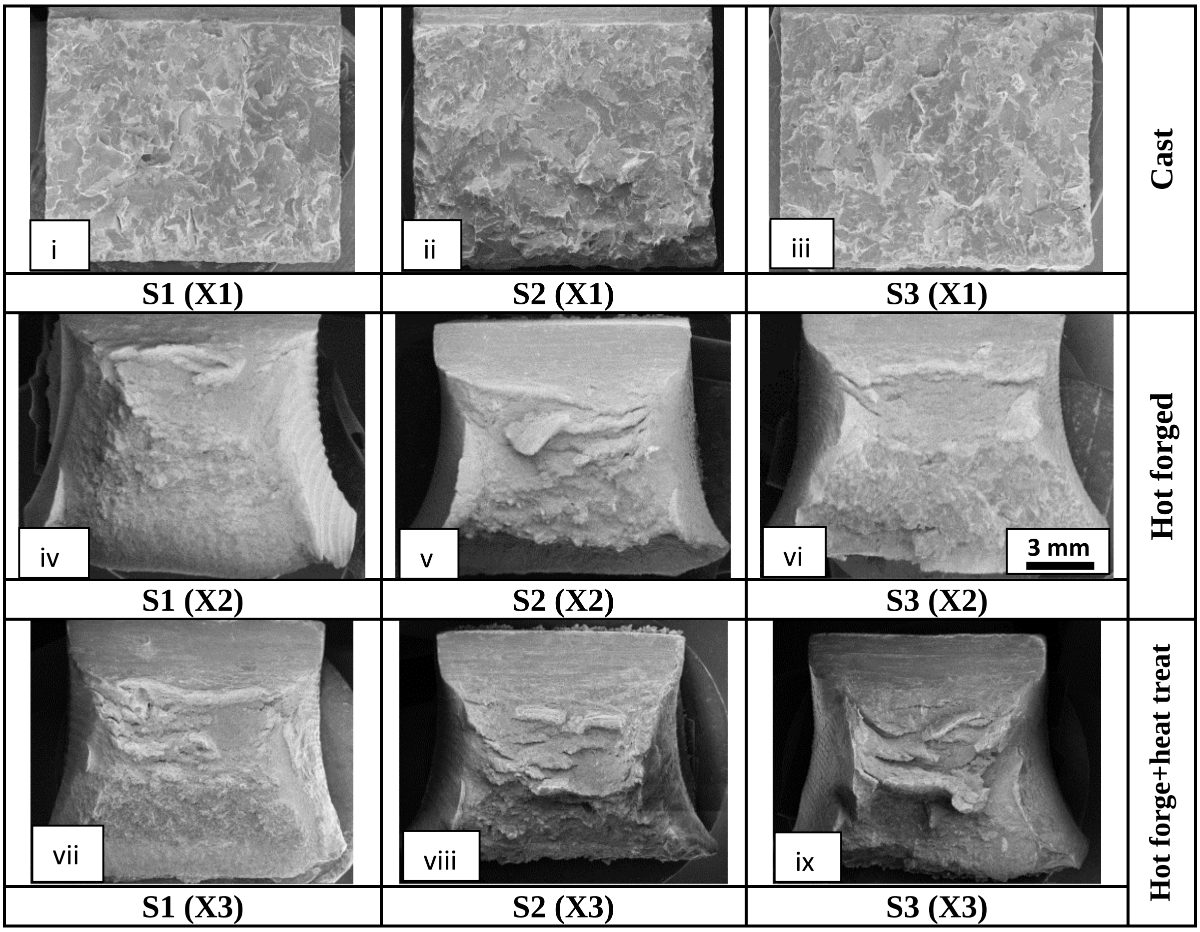

Fig. 4.3.3a. SEM images of the fractured impact test samples of S1, S2, and S3 steels in X1, X2 and X3 conditions

The fracture surfaces of the impact test samples of S1, S2 and S3 steels were also studied in the cast, hot forged, and hot forged plus heat treated condition using SEM. The images of the cast specimens show brittle behaviour. The images of the hot forged, and hot forged plus heat treated specimens show parabolic dimples signifying ductile behaviour (Callister and Rethwisch, 2014) under shear loading (Fig. 4.3.3b, i-ix).

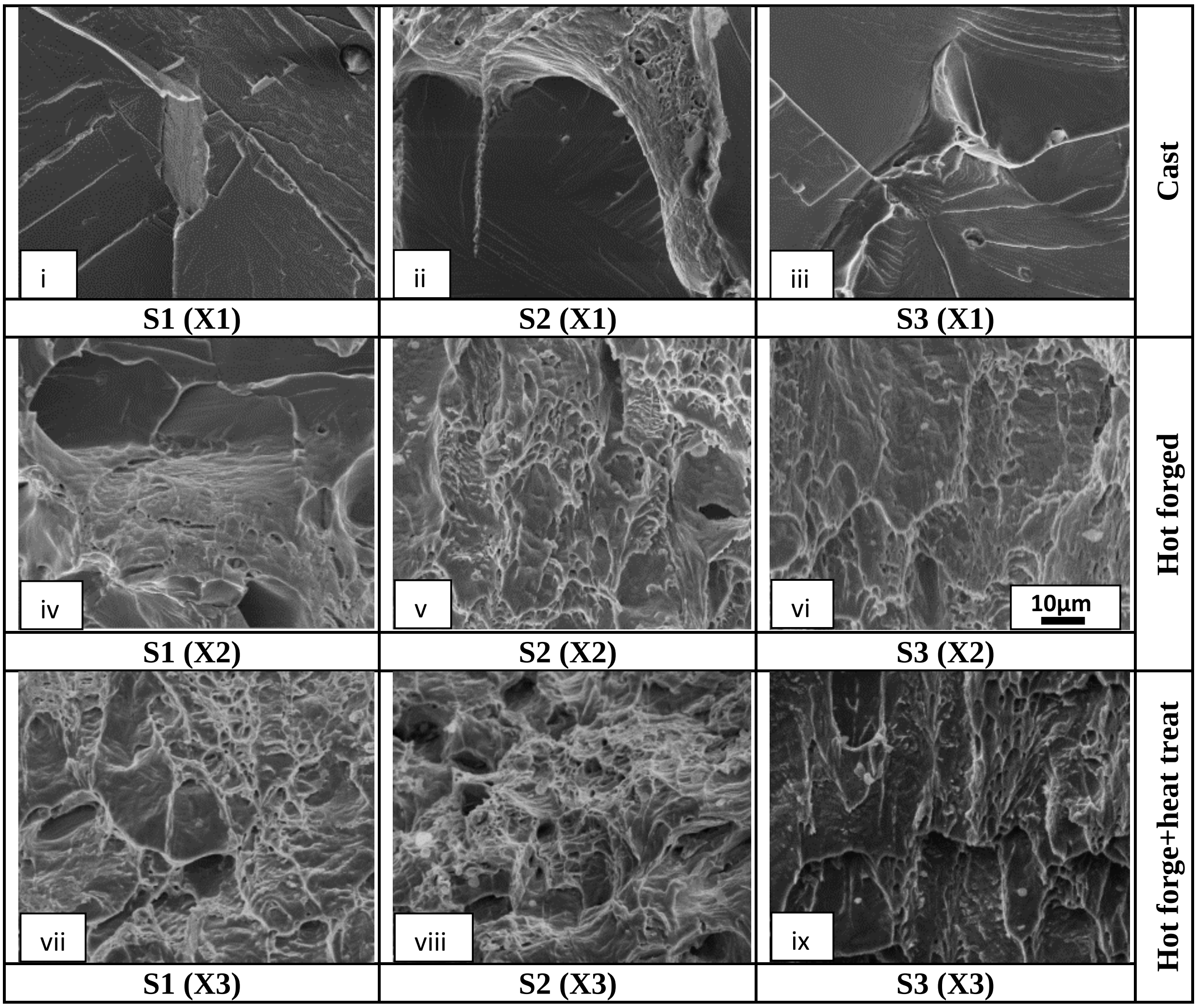

Fig. 4.3.3b. SEM images of the fractured impact test samples of S1, S2, and S3 steels in X1, X2 and X3 conditions at higher magnification

The SEM-EDS studies reveal that phosphorous segregation is present in the cast sample of S1 steel (Fig. 4.3.4a). Particles having high concentration of phosphorous and iron are detected near the grain boundaries. This segregation can be remedied by suitable alloying and application of thermo-mechanical processing like hot forging, hot rolling and ferrite-austenite duplex phase heat treatments (Sahoo and Balasubramaniam, 2007a). The surface of the fractured impact test sample of forged S1 steel and that of the tensile test sample of forged S2 steel, show that disc shaped or spherical features contain high amounts of Al, O, Mn and S. This means that the fracture is facilitated by MnS and Al_2O_3 inclusions (Fig. 4.3.4 b, c). The heat treated sample of S3 steel shows that the grain boundary contains significant amounts of carbon and no phosphorous while the grain interior contains substantial amounts of phosphorous and no carbon (Fig. 4.3.4 d). This implies that the combination of the alloy design scheme, and the ferrite-austenite duplex phase heat treatment has caused phosphorous to move away from the grain boundaries and into the grain interior.

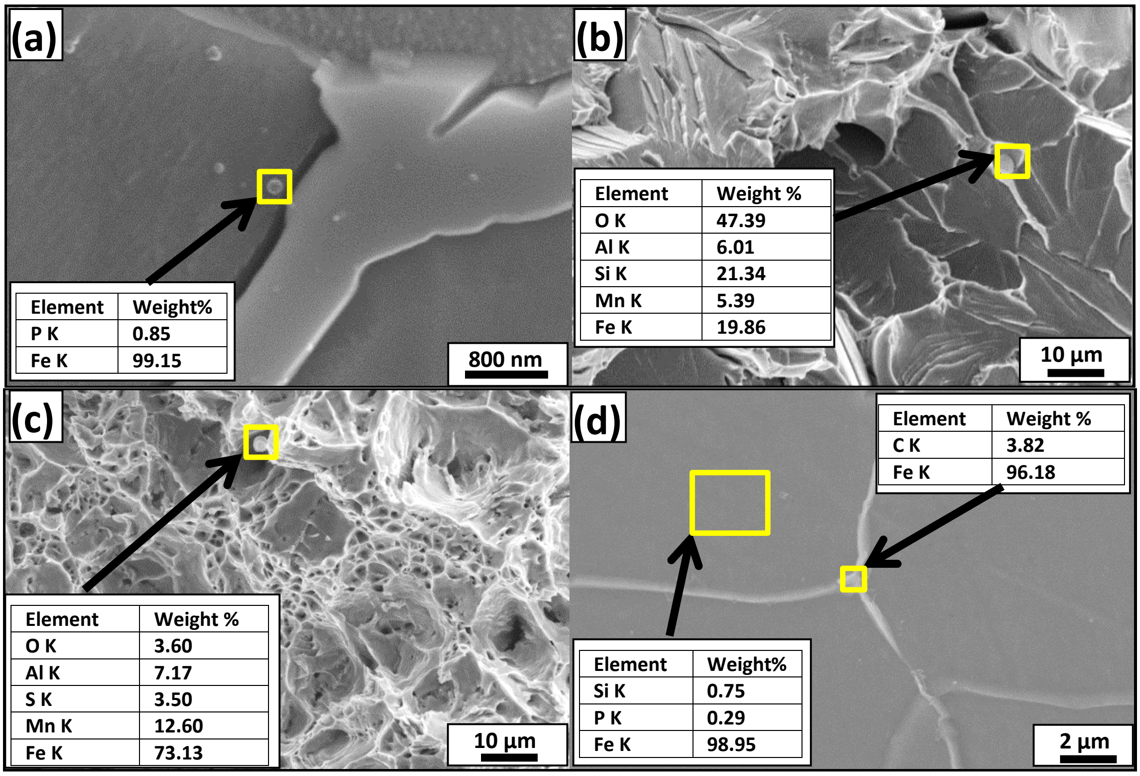

(a)

Element	Weight%
P K	0.85
Fe K	99.15

(b)

Element	Weight %
O K	47.39
Al K	6.01
Si K	21.34
Mn K	5.39
Fe K	19.86

(c)

Element	Weight %
O K	3.60
Al K	7.17
S K	3.50
Mn K	12.60
Fe K	73.13

(d)

Element	Weight %
C K	3.82
Fe K	96.18

Element	Weight%
Si K	0.75
P K	0.29
Fe K	98.95

Fig. 4.3.4. Surface morphology and EDS quantification: (a) as cast S1X1; (b) impact test sample of S1X2; (c) tensile test sample of S2X2; (d) different areas on S3X3

The typical stress strain curves for the tensile tests of the steels in X1, X2 and X3 conditions are shown in Fig. 4.3.5 a, b and c. The cast samples do not show yield point phenomenon as is observed in the case of dual phase steels (Tyagi et al., 2004). The hot forged samples show prominent yield point phenomenon. The hot forged and heat treated samples show a subdued yield point phenomenon as compared to the plots of the hot forged samples except in the case of S2X3. The hot forged and heat treated sample plots display higher elongation and lower strength than the hot forged sample plots. Thus, the heat treatment in the (α+γ) region helps in improving ductility.

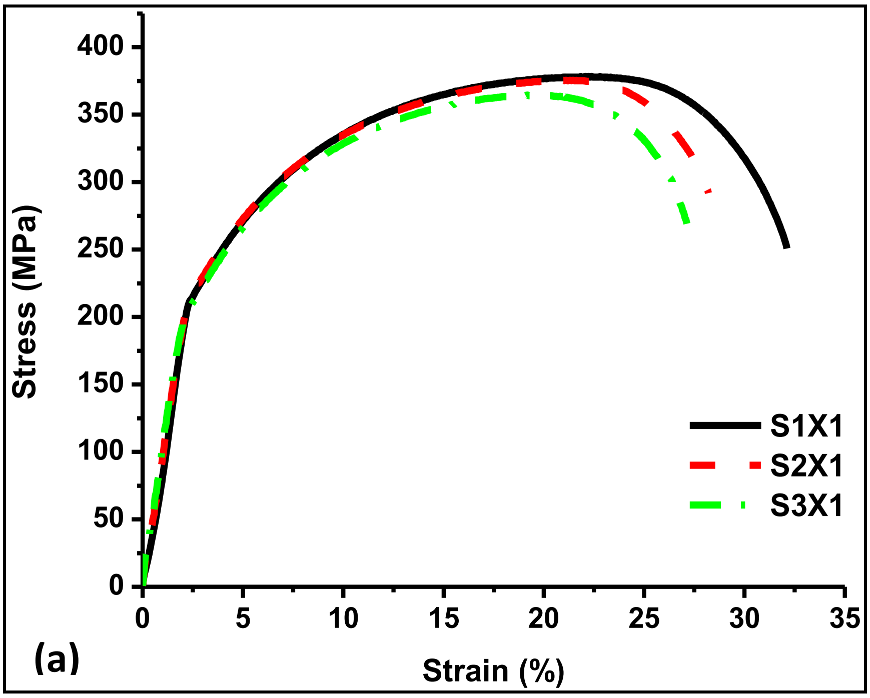

Fig. 4.3.5. (a) Engineering stress-strain curves of as cast high phosphorous steels

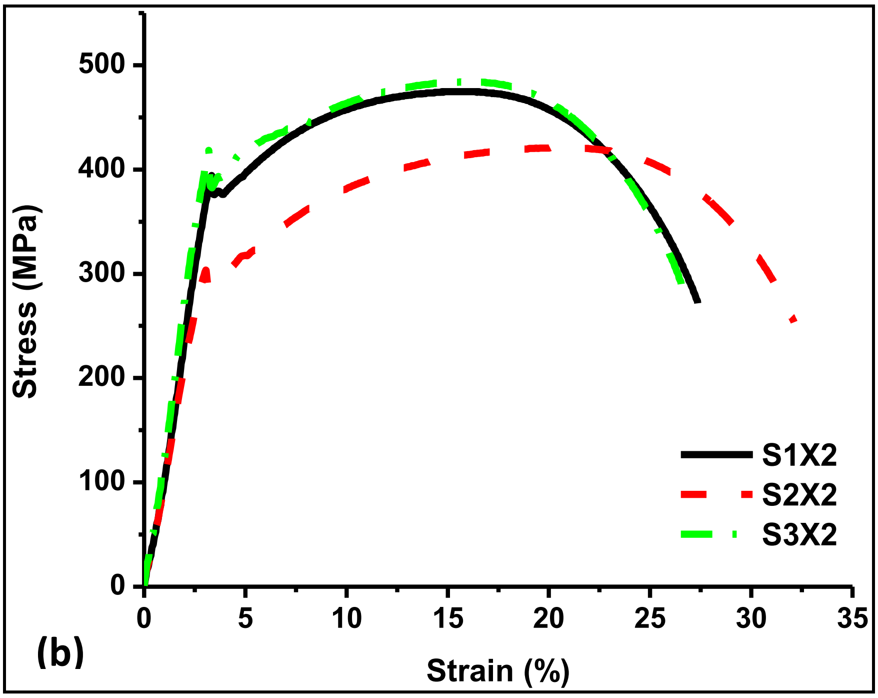

Fig. 4.3.5. (b) Engineering stress-strain curves of hot forged (1150°C) high phosphorous steels

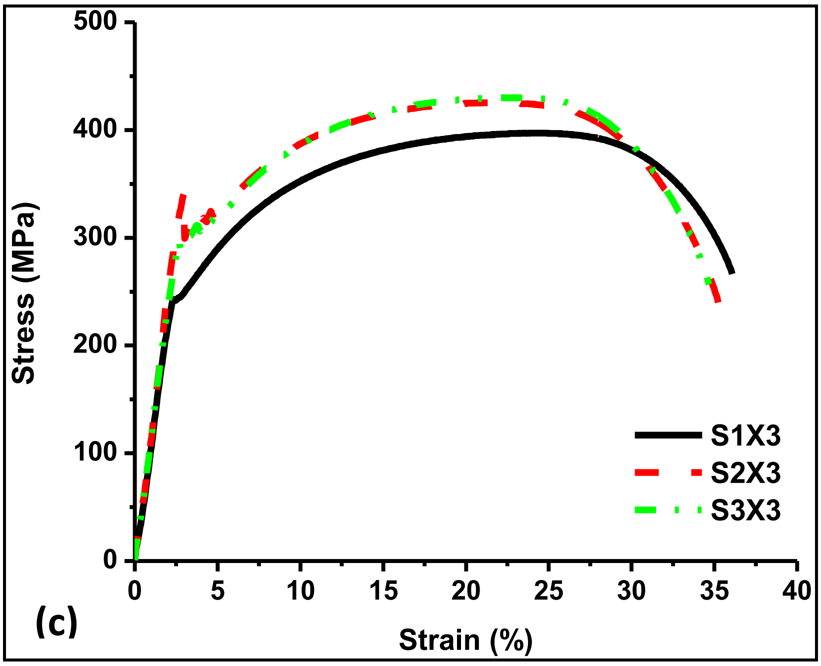

Fig. 4.3.5. (c) Engineering stress-strain curves of high phosphorous steels, hot forged and then heat treated at 900°C for 6 h

The mechanical properties of the steels prepared in this study are shown in Table 4.3.2. The cast specimens showed poor values for impact toughness. The hot forged specimens show much better mechanical properties as compared to the as cast samples. The yield strength (YS) and ultimate tensile strength (UTS) of S1X2 and S3X2 steels decreases on heat treatment due to the increase in grain size and the effect of intercritical heat treatment. The YS and UTS of S2X2 do not decrease even though grain size increases. Silicon tends to lower the stacking fault energy of austenite (Bhadeshia and Honeycombe R W K, 2006). This means that the cross-slip and climb of dislocations will be more difficult, leading to higher yield stress. Silicon being a ferrite stabilizer raises the critical temperatures and reduces the width of the (α+γ) phase field. This would reduce the formation of austenite grains around the ferrite grains at 900°C in the case of S2X3. This could reduce the removal of carbon from the ferrite grain interiors by diffusion into the austenite grains. Thus, the resulting microstructure shows high yield stress even after heat treatment in the (α+γ) phase field. The scatter in toughness values of X2 condition is reduced after heat treatment. The YS and UTS of S1X2 compare well with the Fe-0.11P steel studied by Sahoo (Sahoo and Balasubramaniam, 2007a). The UTS values of S1X3 are similar to those reported by Hopkins (Hopkins and Tipler, 1958). The UTS values of the hot forged, and hot forged plus heat treated steels are above 400 MPa (Table 4.3.2) which are similar to those found by Davies (Davies, 1979) and Stewart and co-workers (Stewart et al., 2000c). The total percentage elongation is above 33 % and the % reduction in area is above 46 % for the steels studied in hot forged and heat treated condition

(Table 4.3.2) which compare well with Panigrahi *et al.* (Panigrahi et al., 2009), and Stewart *et al.* (Stewart et al., 2000c). The Impact energy values of the forged and heat treated steels are above 200 J (Table 4.3.2) which is better than the half width charpy values recorded by Panigrahi (Panigrahi, 2010b), Panigrahi and Jain (Panigrahi and Jain, 2002) and Spitzig and Sober (W. A. Spitzig and Sober, 1977) and the full width energy value of 118±7.8 J recorded for Fe-0.09C-0.37Si-0.42Mn- 0.15P- 0.37Cr- 0.35Cu- 0.31Ni-0.03Al steel by Sahoo *et al.* (Sahoo et al., 2015). The scatter in the impact values is reduced by the heat treatment. Toughness of the hot forged and heat treated samples is found to be better than the hot forged samples. The strain hardening exponent (*n*) of these steels varies between 0.3-0.38 (Table 4.3.2) which is similar to that found by Hu (Hu, 1976) and Davies (Davies, 1979). The ductility of the material is higher in deformation processing operations like wire drawing and deep drawing of sheets for higher strain hardening exponents (Dieter, 1988; Gouthama and Balasubramaniam, 2003; Hu, 1976). The UTS/YS ratios of all the steels are equal to or above 1.25 which meets the requirements of ASTM A 706 (ASTM A706, 2016). The UTS values of forged S3 steel are very close to the requirements of the standard for concrete reinforcement (Indian Standard 1786, 2008).

Table 4.3.2: Mechanical properties of S1, S2, and S3 steels in X1, X2 and X3 conditions

Specimen processing condition	**YS (MPa)**	**UTS (MPa)**	**UTS/ YS ratio**	**El (%)**	**Reduction in area (%)**	**Strain hardening exponent (n)**	**Impact energy (J)**
S4	407.1 ±1.3	478.7 ±2.3	1.18	19.4 ±2.0	63.2 ±3.6	0.27 ±0.01	222.2 ±2.7
S1 X1	210.6 ±12.9	368.3 ±3.6	1.75	33.2 ±1.7	55.5 ±3.2	0.38 ±0.01	7.5 ±0.3
S1 X2	311.3 ±18.9	423.8 ±12.4	1.37	31.6 ±5.1	63.7 ±8.3	0.31 ±0.02	174.3 ±22.6
S1 X3	241.5 ±11.6	394.6 ±11.4	1.64	37.3 ±1.9	47 ±1.4	0.34 ±0.01	196 ±13.6
S2 X1	220.8 ±8.5	379.6 ±4.2	1.72	32.8 ±4.5	54.3 ±3.2	0.38 ±0.01	8.8 ±0.7
S2 X2	325 ±21.3	424.2 ±4.1	1.32	28.5 ±3.9	68.7 ±1.5	0.32 ±0.03	264.3 ±11.8
S2 X3	327.4 ±21.2	434.6 ±8.4	1.33	34.9 ±0.9	48.1 ±4.2	0.32 ±0.01	279.4 ±16.5
S3 X1	203.6 ±3.9	357.4 ±6	1.75	21.8 ±4.6	29.7 18.7	0.38 ±0.01	8.1 ±0.3
S3 X2	375.6 ±5.4	465.1 ±4.9	1.24	30.5 ±1.1	68.4 ±3.7	0.3 ±0.01	247.3 ±29.3
S3 X3	297 ±9.1	424.9 ±8.6	1.43	33.4 ±2.5	46.2 ±2.7	0.34 ±0.01	284.5 ±11.4

The yield strength of hot forged S1 steel and S3 steel falls by about 20 % on heat treatment while the grain size increases by 81 % for S1 steel and 31 % for S3 steel (Table 4.3.1 and 4.3.2). Similarly the UTS values of hot forged S1 steel and S3 steel fall by about 7 % and 9 % respectively on heat treatment. The heat treatment causes the interstitial elements like C and N to displace the phosphorous atoms from the grain boundary sites to the grain interior giving rise to the softening of the S1 and S3 steels (Allen, 1963) (Hopkins and Tipler, 1958)(H. Erhart and Grabke, 1981). The experimental results are compared with the referenced values in Table 4.3.3.

The steels which are hot forged and subsequently heat treated for 6 h in the ferrite-austenite duplex phase region offer the best impact properties. This is expected as the heat treatment causes the interstitial elements like C and N to displace the phosphorous atoms from the grain boundary sites to the grain interior (Allen, 1963) (Hopkins and Tipler, 1958)(H. Erhart and Grabke, 1981). Experiments have shown that C and N are not as detrimental to the grain boundary cohesion as is phosphorous (Suzuki et al., 1985) (Hopkins and Tipler, 1958)(H. Erhart and Grabke, 1981). Further, carbides act as sites of initiation of fracture in high phosphorous steels (Suzuki et al., 1985). Silicon which promotes the formation of graphite when present above 1 wt. % is not carbide former and dissolves in ferrite (Callister and Rethwisch, 2014)(Avner, 1997)(Bain, 1939)(Ghasemi et al., 2016). Hence, toughness is improved by reducing the amount of carbides and displacing P away from the grain boundaries by intercritical heat treatment or working. Accordingly, S3 steel in X3 condition shows the best impact toughness.

Table 4.3.3: Comparison of experimental results with values reported for similar steels in references

Specimen processing condition	**Property**	**Value for experimental steel**	**Value for reference steel**	**Composition of reference steel**	**Ref.**
S1X2	UTS (MPa)	423.8	425	Fe-0.11P-0.03C	(Sahoo and Balasubramaniam, 2007a)
S1X3		394.6	345	Fe-0.15P-0.05C	(Hopkins and Tipler, 1958)
S2 X3		434.6	400-500	Fe-0.1P	(Davies, 1979)
S3 X3		424.9	340	Fe-0.1P	(Stewart et al., 2000c)
S2 X3	El (%)	34.9	20	Fe-0.14C-0.11P-0.75Mn-0.33Cu	(Panigrahi et al., 2009)
S3 X3		33.4	45	Fe-0.1P	(Stewart et al., 2000c)
S2 X3, S3 X3	Impact toughness (J)	279.4 J	90 J (half width)	Fe-0.08C-0.11P-0.6Mn -0.03Si	(Panigrahi, 2010b)
		284.5 J	35 J (half width)	Fe-0.14C-0.9Mn-0.1P-0.3Cu	(Panigrahi and Jain, 2002)
		279.4 J	67 J (half width)	Fe-0.1P-0.1C-1Mn	(W. A. Spitzig and Sober, 1977)
		284.5 J	118 J	Fe-0.09C-0.37Si- 0.42Mn-0.15P- 0.37Cr-0.35Cu- 0.31Ni-0.03Al	(Sahoo et al., 2015)
S1X2, S2X2, S3X2	*n*	0.3-0.38	~0.3	Fe-0.12P-0.01C	(Hu, 1976)
			0.28-0.31	Fe-0.1P	(Davies, 1979)
S1X2, S2X2, S3X2	UTS/YS	>1.25	>1.25	Fe-C	(ASTM A706, 2016)
S3X2	UTS	465.1	485	Fe-0.3C-0.06P	(Indian Standard 1786, 2008)

Therefore, the intercritical heat treatment of the high phosphorous steels is able to remove phosphorous from the grain boundaries and improve toughness. The phosphorous is displaced into the grain interiors where it provides solution strengthening. The presence of carbon at the grain boundaries is beneficial for grain boundary cohesion.

4.3.1 Effect of Hot Rolling and Heat Treatment in the (α+γ) Region of the Phase Diagram on Mechanical Properties: A Comparison

The microstructures of the hot forged and heat treated (at 900°C for 1 h and subsequently normalized; X4) specimens are shown in Fig. 4.3.1.1. The microstructures reveal the formation of prior austenite grains at the grain boundaries of ferrite grains. These austenite grains are small and transform to ferrite on cooling to lower temperatures.

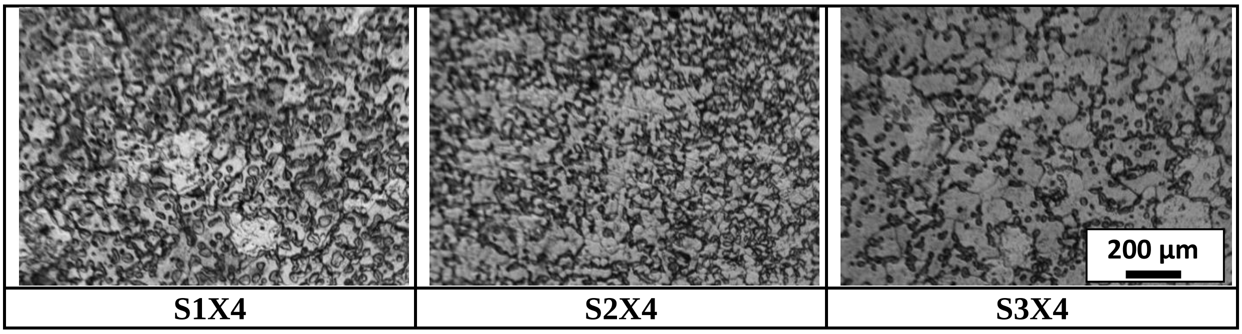

S1X4 **S2X4** **S3X4**

Fig. 4.3.1.1. Optical micrographs of the tensile test samples of hot forged and heat treated (at 900°C for 1 h) high phosphorous steels etched with 2% nital solution

The SEM micrographs of the fracture surfaces of the tensile test samples prepared from hot forged and heat treated (at 900°C for 1 h) high phosphorous steels show dimples which confirms ductile fracture (Fig. 4.3.1.2). The shape of the dimples is conical, elliptical and spherical which is characteristic of uniaxial tensile loading. Elongated dimples are formed when the propensity for localization of deformation is high. All the three samples show a mix of small and large dimples. In S3X4 a line feature suggests cleavage along with ductile dimples. Similarly, the SEM photographs of the fracture surfaces of the Charpy impact test samples prepared from hot forged and heat treated (at 900°C for 1 h) high phosphorous steels display dimples suggesting ductile fracture (Fig. 4.3.1.3). The shape of the dimples is parabolic which is characteristic of fracture resulting from shear loading (Callister and Rethwisch, 2014). The size of dimples in S2X4 is smaller as compared to the other two. This indicates that the localization of flow is lower in S2X4 sample. The impact toughness of S2X4 is the best amongst the three high phosphorous steels in X4 condition (Table 4.3.4).

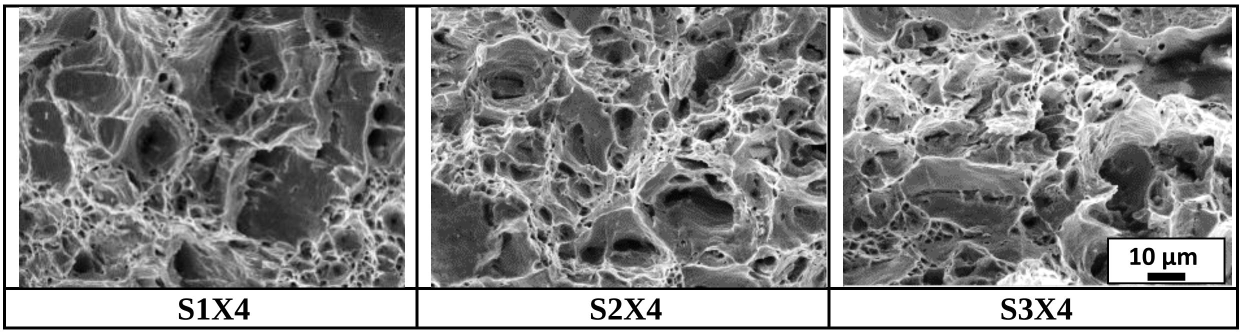

S1X4	S2X4	S3X4

Fig. 4.3.1.2. SEM images of the tensile test samples of hot forged and heat treated (at 900°C for 1 h) high phosphorous steels

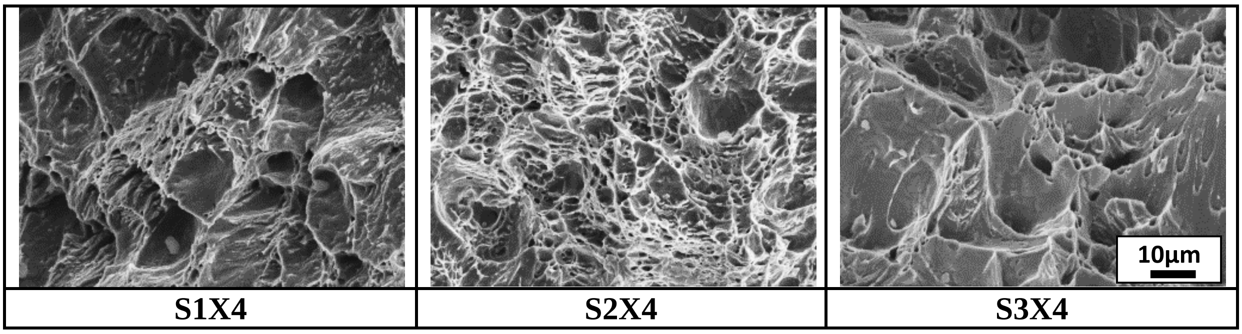

S1X4	S2X4	S3X4

Fig. 4.3.1.3. SEM images of the fractured impact test samples of the hot forged and heat treated (at 900°C for 1 h) high phosphorous steels

The microstructures of the hot forged and hot rolled (at 900°C and subsequently normalized) high phosphorous steels are shown in Fig. 4.3.1.4. They show ghosting patterns typical of high phosphorous steels and formation of prior austenite grains at the grain boundaries of ferrite grains. These patterns signify that the distribution of phosphorous is non-uniform between the grain interiors and the grain boundaries.

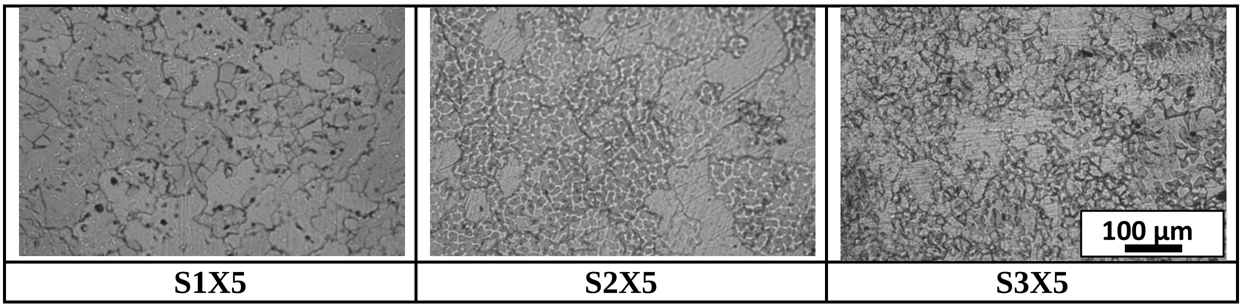

S1X5	S2X5	S3X5

Fig. 4.3.1.4. The microstructures of the three high phosphorous steels hot forged and hot rolled at 900°C and etched with 2 % nital solution.

The SEM images of the fracture surfaces of the tensile test specimen of the three high phosphorous steels, after hot forging and hot rolling at 900°C are shown in Fig. 4.3.1.5. Presence of spherical, conical and elliptical dimples indicates predominantly ductile failure attributed to uniaxial loading. These ductile failures are initiated by nucleation of voids at second phase particles like sulphides and oxides. The voids form either by cracking of the particles, or by decohesion of the particle/matrix interfaces (Bhadeshia and Honeycombe R W K, 2006). The SEM images of the fracture surfaces of the impact test specimens of the three high phosphorous steels after hot forging and hot rolling at 900°C are shown in Fig. 4.3.1.6. Parabolic shaped dimples show extensive plastic deformation before failure due to shear loading. The presence of dimples points towards predominantly ductile failure.

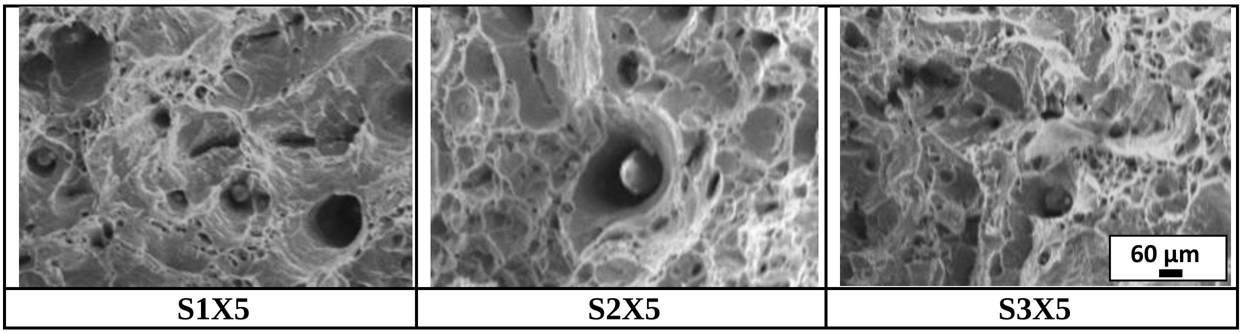

S1X5	**S2X5**	**S3X5**

Fig. 4.3.1.5. SEM images of the tensile test samples of the steels hot forged and hot rolled at 900°C

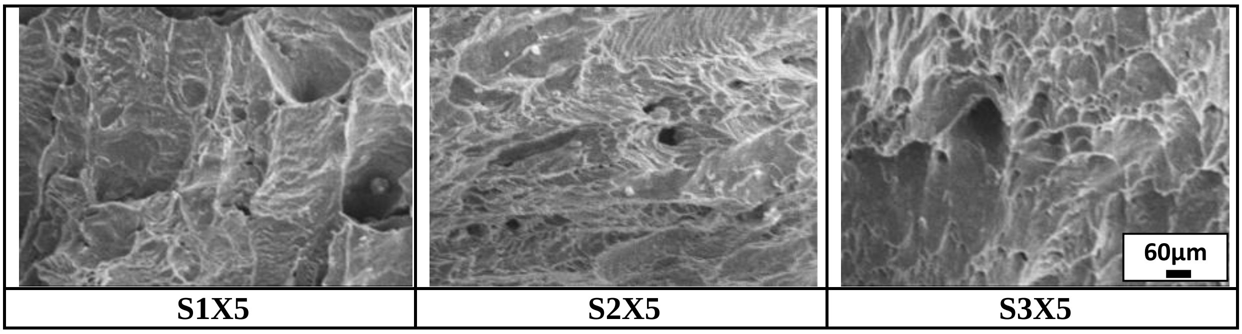

S1X5	**S2X5**	**S3X5**

Fig. 4.3.1.6. SEM images of the fractured impact test samples of the steels hot forged and hot rolled at 900°C

Fig. 4.3.1.7 displays the engineering stress-strain curves of high phosphorous steels in the conditions of (a) hot forged and heat treated at 900°C for 1 h and (b) hot forged and subsequently hot rolled at 900°C. Both the sets of specimens were normalized to room temperature. The hot rolled steels show a clear trend of a decrease in strength with an increase in alloying elements. Yield point phenomenon is prominent in S2 steel (Fig. 4.3.1.7.b).

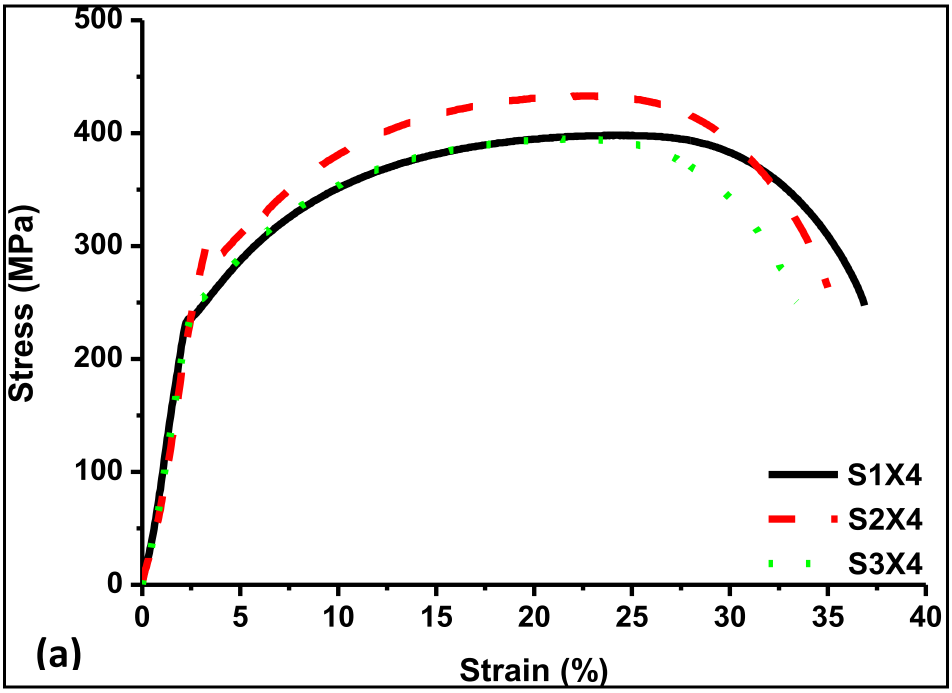

Fig. 4.3.1.7. (a) Engineering stress-strain curves of high phosphorous steels: hot forged and heat treated at 900°C for 1 h

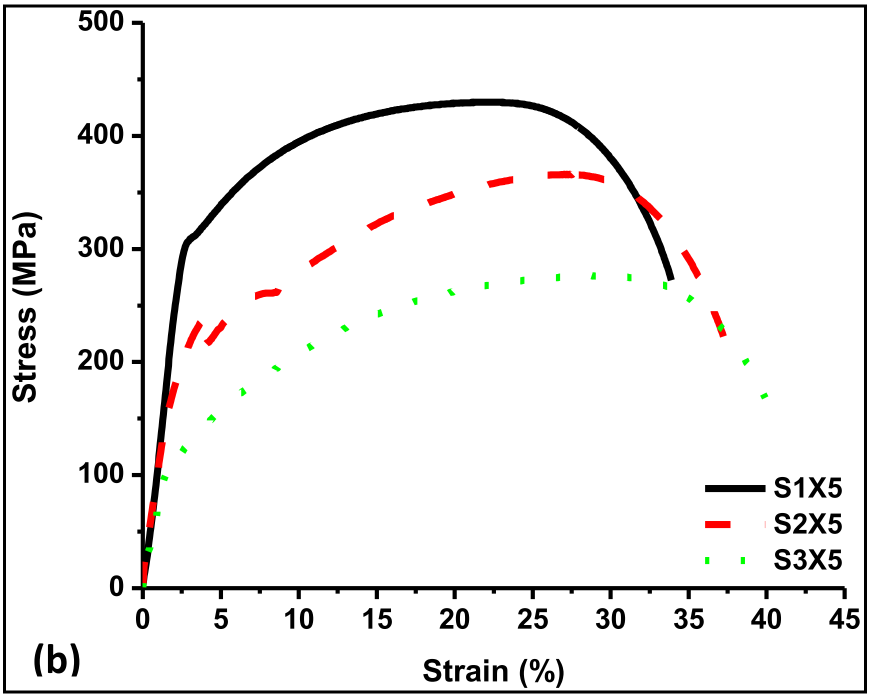

Fig. 4.3.1.7. (b) Engineering stress-strain curves of high phosphorous steels: hot forged and hot rolled at 900°C

The mechanical properties of these steels which were hot forged and subsequently heat treated for 1 h at 900°C are shown in Table 4.3.4. The properties for X4 condition are near those observed for X3 condition. The toughness values are much better for X3 condition (6h heat treatment) as compared to the 1 h heat treatment of X4 condition, in the case of S2 and S3 steels. The YS and UTS of S3 steel are better in X3 condition as compared to those recorded in X4 condition. This implies that a 6 h heat treatment gives better properties than a 1 h heat treatment. The strength of the high phosphorous steels is near 400 MPa and the elongation exceeds 33% in X4 condition. The impact values are comparable with those of the plain carbon steel. The strength and toughness values for S2 steel are found to be better than those recorded for S1 steel and S3 steel although the scatter in toughness readings is more pronounced for S2 steel.

Table 4.3.4: Mechanical properties of the steels, hot forged and subsequently heat treated at 900°C for 1 h

Specimen	**YS (MPa)**	**UTS (MPa)**	**Elongation (%)**	**Impact energy (J)**
S1(X4)	229.8±8.3	392.5±10.6	35.3±2.6	205.1±9.9
S2(X4)	327.5±26.7	421.7±9.8	34.6±0.8	239.2±16.9
S3(X4)	258.6±19.2	396.6±13.8	33.6±1.5	233.1±5.7

Table 4.3.5: Mechanical properties of steels hot forged and hot rolled at 900°C

Specimen	**YS (MPa)**	**UTS (MPa)**	**Elongation (%)**	**Impact energy (J)**
S1(X5)	319.5±12.6	444.7±12.8	30.2±5.8	181.2±9.1
S2(X5)	244.5±6.8	388.1±20.7	36.5±2.2	194.5±9.7
S3(X5)	137.7±17.8	292.7±18.8	35.3±3.1	205.1±13.2

The mechanical properties of these steels which were hot forged and subsequently hot rolled at 900°C (X5) are shown in Table 4.3.5. The elongation of these steels exceeds 30%. The hot rolled specimens indicate a decreasing trend in the strength values from S1 steel to S3 steel. The toughness improves from S1 steel to S3 steel. In the heat treated samples no such trend can be observed. Overall, it appears to be possible that the removal of phosphorous from the grain boundaries and the resulting softening is better achieved by the dynamic recrystallization occurring during hot rolling than by heat treatment in the (α+γ) region for short times such as 1 h.

4.3.2 Hardness Test

The Vickers hardness values (10 kgf load and 15 seconds dwell time) of the three prepared high phosphorous steels in different processing conditions were found out and are reported in Table 4.3.6:

Table 4.3.6: Vickers hardness results of the three prepared high phosphorous steels in different processing conditions

Specimen	**S1 steel**	**S2 steel**	**S3 steel**	**Trend**
X1	150	145	142	Decreasing
X2	170	167	178	-
X4	154	160	159	-
X5	142	161	134	-
Water quench	167	142	170	-
Annealed	120	127	126	-
Normalized	142	133	147	-

A clear decreasing trend was found in the X1 (as cast condition) samples alone. But this trend did not match with the trend in the tensile strength values of the high phosphorous steels. The other conditions did not show a clear trend. The hot forged steels (X2) show a higher hardness than the as cast (X1) samples. This correlates well with the higher UTS for X2 condition as compared to X1 condition. The X3 samples which were heat treated at intercritical temperatures show lower hardness than the hot forged samples (X2). This shows that the material softened on heat treatment. The water quenched samples show a higher hardness than the normalized samples. The normalized samples are harder than the annealed samples. Generally the hot rolled samples (X5) shows lower hardness than the heat treated samples (X4) indicating that hot rolling is preferable over heat treatment for softening the material.

Thus, it can be concluded that the toughness of high phosphorous steels can be improved by heat treating the specimens in the (α+γ) region of the phase diagram. The same effect is also possible by hot working in the (α+γ) region of the phase diagram. The latter has been found to be more effective in softening the high phosphorous steels.

4.4 CORROSION BEHAVIOUR

Now the corrosion behaviour of the high phosphorous steels in saturated $Ca(OH)_2$ solution without/with chloride ions is studied and compared to the plain carbon steels. Occurrence of passivity of steel is controlled by the pH value of the solution and not by the cation (Oranowska and Szklarska-Smialowska, 1981). Earlier work has shown that results of electro-chemical tests conducted in saturated $Ca(OH)_2$ are similar to those obtained in concrete (Génin et al., 2002). Therefore, saturated $Ca(OH)_2$ solution with pH 12.5 was chosen (Oranowska and Szklarska-Smialowska, 1981) to simulate concrete pore solution which has a pH between 9 and 14 depending on carbonation, type of cement, etc.

The toughness of the high phosphorous steels designed and prepared in this work have been found to be comparable to that of plain carbon steel. The next step is to compare the corrosion behaviour of these steels with carbon steel in an environment similar to that encountered by rebars when embedded in concrete. The corrosion resistance of steel is best in the annealed condition. So initially the high phosphorous steels were studied in annealed condition in saturated $Ca(OH)_2$ solution without/with chloride ions in various concentrations. Later, the steel with the best toughness (S3X3) was studied in a similar way.

4.4.1 Anodic Polarization Behavior

Fig. 4.4.1 shows the anodic polarization curves of the processed steel samples tested in saturated $Ca(OH)_2$ solution containing various Cl^- ion concentrations (in weight %). All the samples exhibit passive behaviour in this solution. This conforms to the Fe-water E_h-pH diagram of 298.15 K. The range of passivity decreases as the Cl^- content increases beyond a threshold value. In all the curves for all the samples immersed in solution with 0.05 wt. % Cl^- and without chloride, current density increases at about 650 mV_{SCE} which is attributable to O_2 evolution and is dependent on pH. Beyond a critical chloride concentration, the corrosion current registered a drastic increase during the experiment preceding the oxygen evolution. In the presence of Cl^- ions, the pitting potential became more negative towards the active side. For each steel composition, the pitting or passive film breakdown occurred when the chloride concentration exceeded a critical amount. The threshold value of Cl^- ion concentration for the initiation of pitting is determined as 0.1 wt. % Cl^- for S1, S2 and S3 steels while it was 0.06 wt. % Cl^- for the S4 steel. At these concentrations the pitting potential of the steel samples was lower than the oxygen evolution potential. Tests were also carried out in solutions containing 0.14 wt. Cl^- in order to confirm the lower pitting potential of the steels. Other researchers have reported threshold values of 0.05 wt. % Cl^- for AISI 1010 steel (Moreno et al., 2004), 0.06 wt. % Cl^- for Fe-0.15C steel and 0.1 wt. % Cl^- for Fe-0.11P steel (Sahoo and Balasubramaniam, 2008). Thus, S1, S2 and S3 steels are more resistant to pitting than S4 steel as their threshold chloride is found to be higher in this work.

The pitting nucleation or generation resistance (R) can be defined as the difference between the zero current or corrosion potential (ZCP) and the pitting nucleation potential (E_{pit}) or the passive film breakdown potential (Bethencourt et al., 1998, 1997). These values were estimated from the potentiodynamic polarization curves and tabulated in Table 4.4.1.1. The pitting generation resistance decreased with an increase in chloride concentration in general. The pitting nucleation resistance of high phosphorous steels was significantly higher than that obtained for mild steel, especially above 0.06 wt. % chloride concentration. The mild steel specimen showed a drastic decrease in the pitting resistance beyond 0.06 wt. % chloride concentration. The corrosion potential and hence the pitting resistance value did not follow any particular trend.

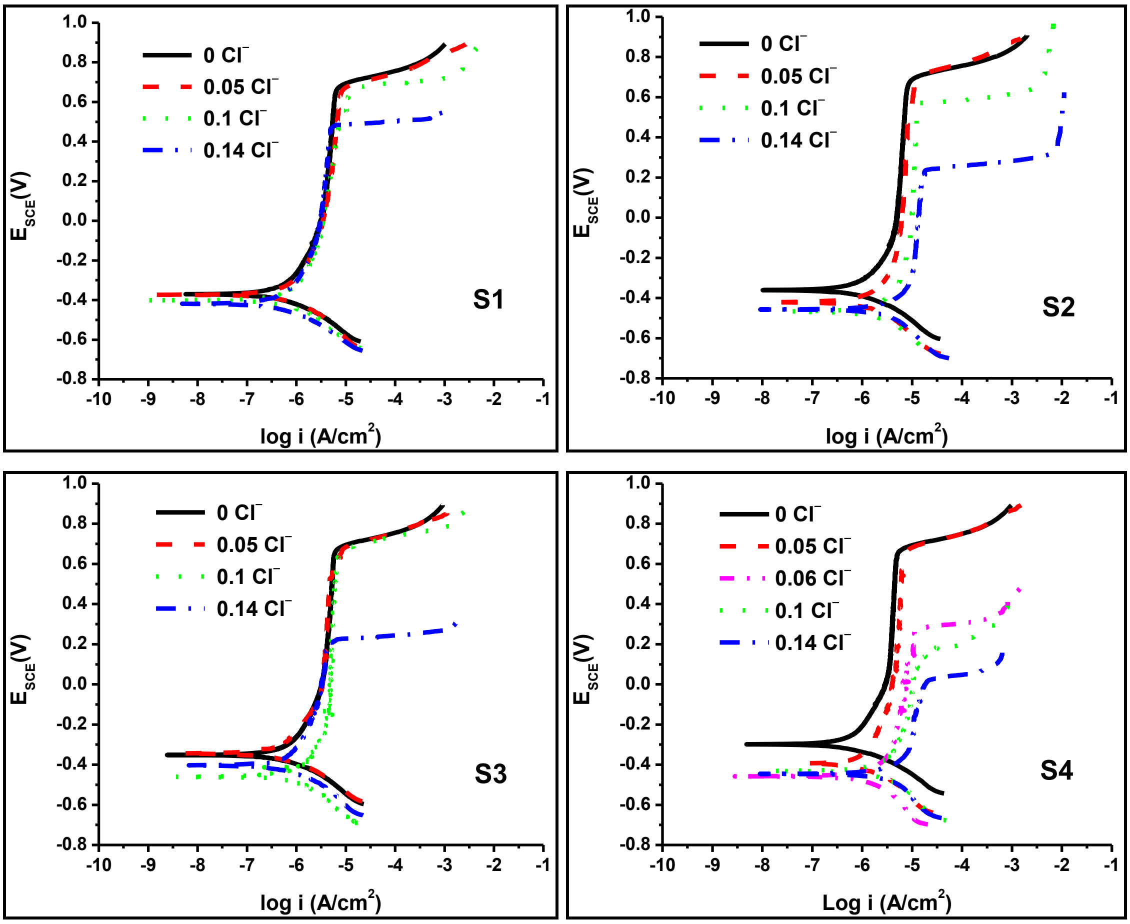

Fig. 4.4.1. Potentiodynamic polarization curves of S2, S2, S3 and S4 steels obtained in saturated $Ca(OH)_2$ solution having various chloride concentrations

Table 4.4.1.1: Pitting nucleation resistance R=│ZCP-E_{pit}│in mV for high phosphorous steels and mild steel specimens in saturated calcium hydroxide solution, with and without chloride

Sample	**0.0 Cl^-**	**0.05 Cl^-**	**0.06 Cl^-**	**0.1 Cl^-**	**0.14 Cl^-**
S1	1070	1062	-	1075	901
S2	1064	1135	-	1036	720
S3	1032	1024	-	1128	627
S4	979	1072	736	624	476

4.4.2 OCP and LPR Studies

For all steel samples, the open circuit potential and the linear polarization resistance were recorded after 15 min, 5 h and 21 h. The LPR values were used to calculate i_{corr} using Eq. 3.6.2.3. Fig. 4.4.2 shows the variation of the OCP and i_{corr} for the samples S1, S2, S3 and S4 steels exposed to aerated saturated solution of $Ca(OH)_2$ containing various chloride concentrations. The OCP of S3 steel shifted towards noble direction while the i_{corr} values decreased with time of dipping in all solutions. Similar trends were observed in the case of S1 and S2 steels too. This trend implies that with increasing immersion time the steel became nobler (MacDougall and Graham, 1995). It has been reported that as the anodic curve shifts to lesser current densities, the E_{corr} increases and i_{corr} decreases (Kelly et al., 2003). In the case of S4 steel immersed in solutions containing 0.05 wt. % and 0.1 wt. % Cl^-, there is an overall decline in OCP with the immersion time which suggests increased corrosion. The i_{corr} values of S4 steel did not show a corresponding overall increase. The OCP values indicate that the critical chloride concentration for initiation of pitting could be 0.05 wt. % and is probably lower than that of the high phosphorous steel samples.

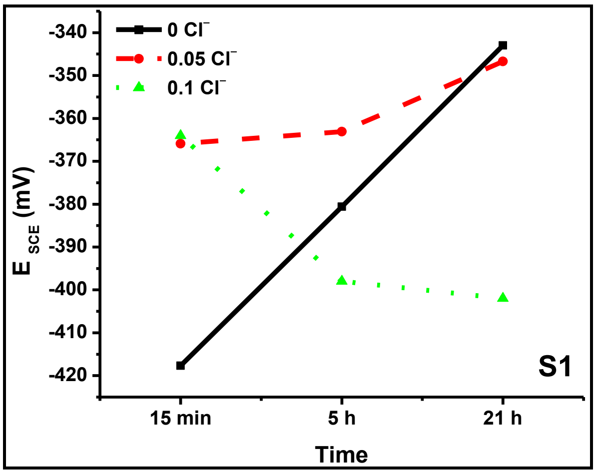
0 Cl⁻
0.05 Cl⁻
0.1 Cl⁻
E_{SCE} (mV)
-340
-350
-360
-370
-380
-390
-400
-410
-420
15 min
5 h
21 h
Time
S1

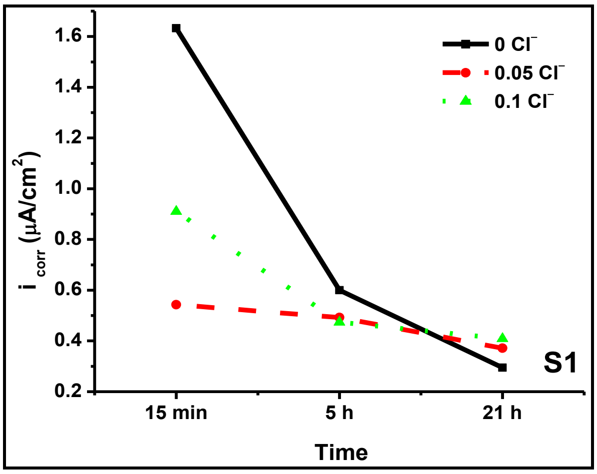
0 Cl⁻
0.05 Cl⁻
0.1 Cl⁻
i_{corr} ($\mu A/cm^2$)
1.6
1.4
1.2
1.0
0.8
0.6
0.4
0.2
15 min
5 h
21 h
Time
S1

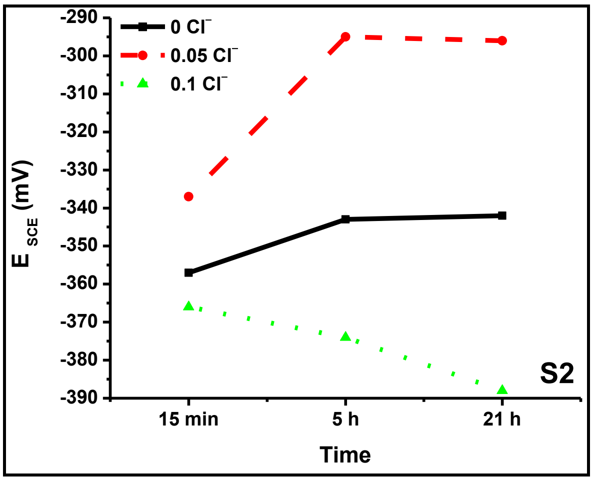
0 Cl⁻
0.05 Cl⁻
0.1 Cl⁻
E_{SCE} (mV)
-290
-300
-310
-320
-330
-340
-350
-360
-370
-380
-390
15 min
5 h
21 h
Time
S2

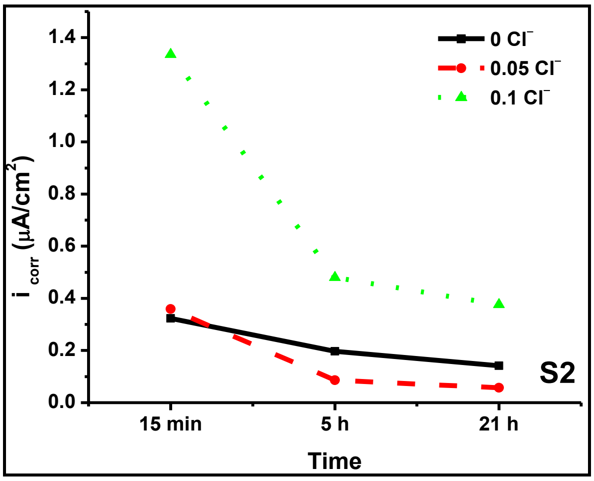
0 Cl⁻
0.05 Cl⁻
0.1 Cl⁻
i_{corr} ($\mu A/cm^2$)
1.4
1.2
1.0
0.8
0.6
0.4
0.2
0.0
15 min
5 h
21 h
Time
S2

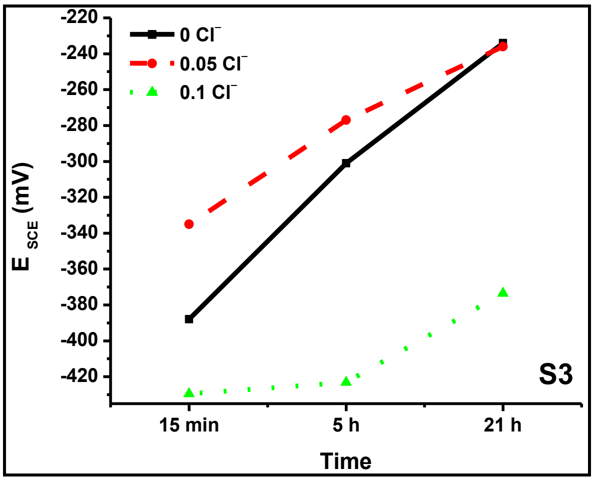
0 Cl⁻
0.05 Cl⁻
0.1 Cl⁻
E_{SCE} (mV)
-220
-240
-260
-280
-300
-320
-340
-360
-380
-400
-420
15 min
5 h
21 h
Time
S3

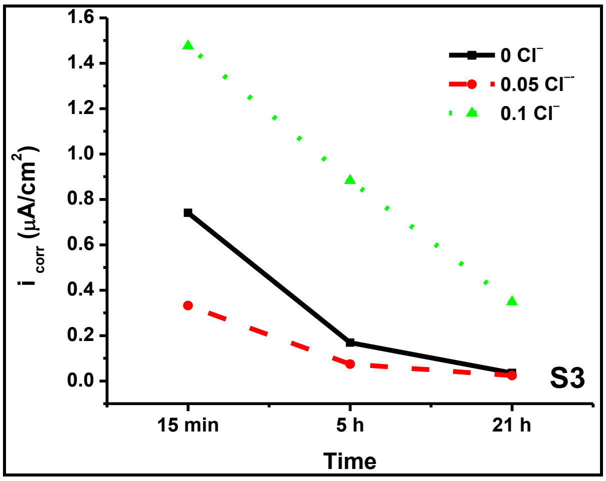
0 Cl⁻
0.05 Cl⁻
0.1 Cl⁻
i_{corr} ($\mu A/cm^2$)
1.6
1.4
1.2
1.0
0.8
0.6
0.4
0.2
0.0
15 min
5 h
21 h
Time
S3

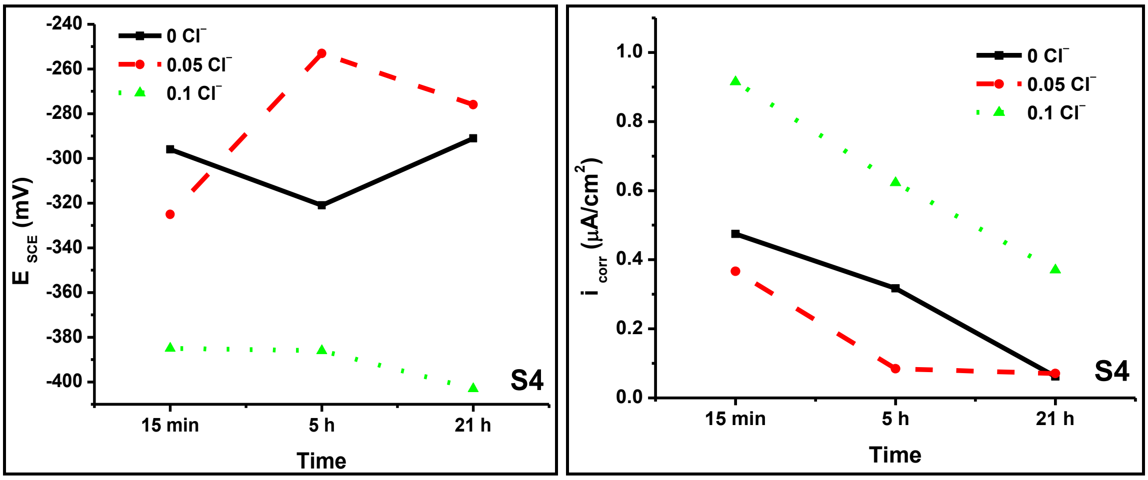

Fig. 4.4.2. Variation of the OCP and i_{corr} for S1, S2, S3 and S4 steel samples exposed to saturated $Ca(OH)_2$ solution containing various chloride concentrations

4.4.3 Electrochemical Impedance Spectroscopy

Fig. 4.4.3.1 to Fig. 4.4.3.12 shows the Nyquist, Bode magnitude and Bode phase plots of S1, S2, S3 and S4 steels in saturated solution of $Ca(OH)_2$ containing 0.1 wt. % Cl^- at different times of immersion. For S1, S2 and S3 steels, the impedance escalated with time in all solutions. The impedance responses of S1, S2 and S3 steels in saturated solution of $Ca(OH)_2$ without chloride and that having 0.05 wt. % Cl^- were similar to those obtained in solution having 0.1 wt. % Cl^-. This variation in response was also found similar to that of S4 steel in $Ca(OH)_2$ solution containing zero and 0.05 wt. % chloride. A different impedance response was recorded for S4 steel in $Ca(OH)_2$ solution with 0.1 wt. % chloride concentration.

The Nyquist plot of S1 steel (Fig. 4.4.3.1.) immersed in saturated $Ca(OH)_2$ solution for 21 h without chloride shows a real impedance of 93.1 $k\Omega.cm^2$. Real impedance for the same steel immersed in saturated $Ca(OH)_2$ solution with 0.05 wt. % chloride concentration for 21 h drops to 73.2 $k\Omega.cm^2$. The real impedance further drops to 52.5 $k\Omega.cm^2$ on immersion in saturated $Ca(OH)_2$ solution with 0.1 wt. % chloride concentration for 21 h. Therefore, the increase in chloride concentration lowers the real impedance values.

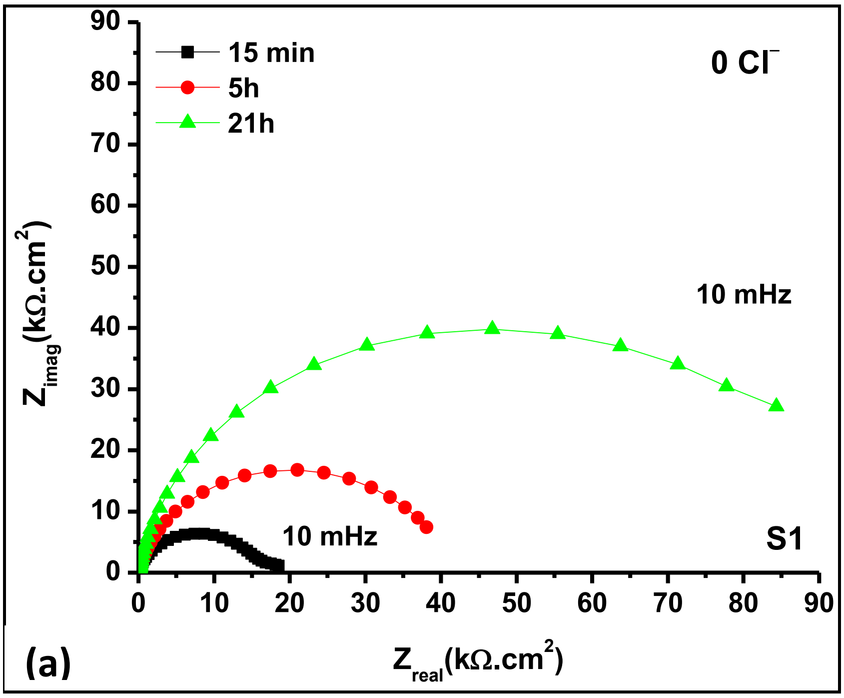

Fig. 4.4.3.1. (a) Nyquist plots of S1 steel in saturated $Ca(OH)_2$ solution without Cl^-

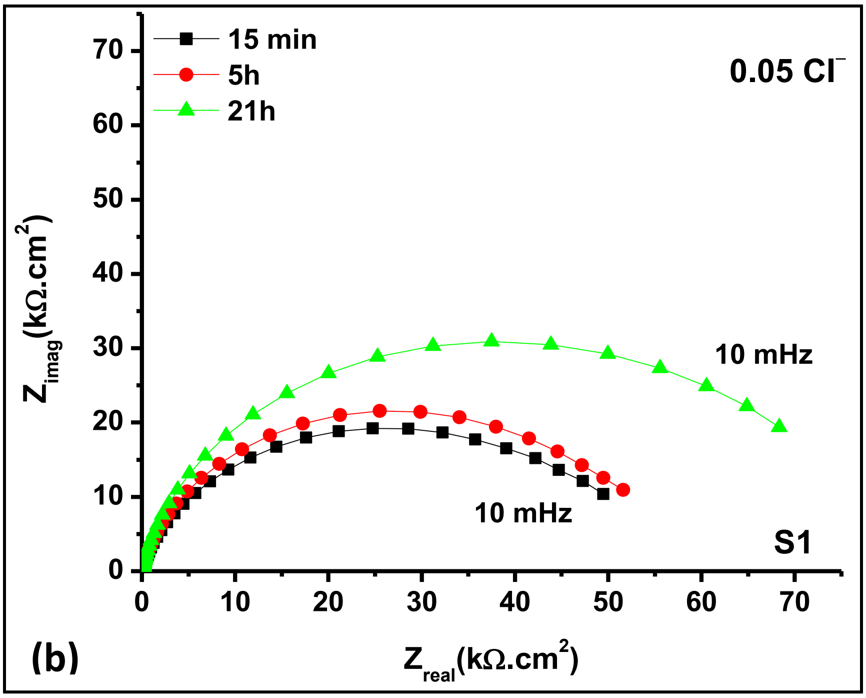

Fig. 4.4.3.1. (b) Nyquist plots of S1 steel in saturated $Ca(OH)_2$ solution with 0.05 wt. % Cl^-

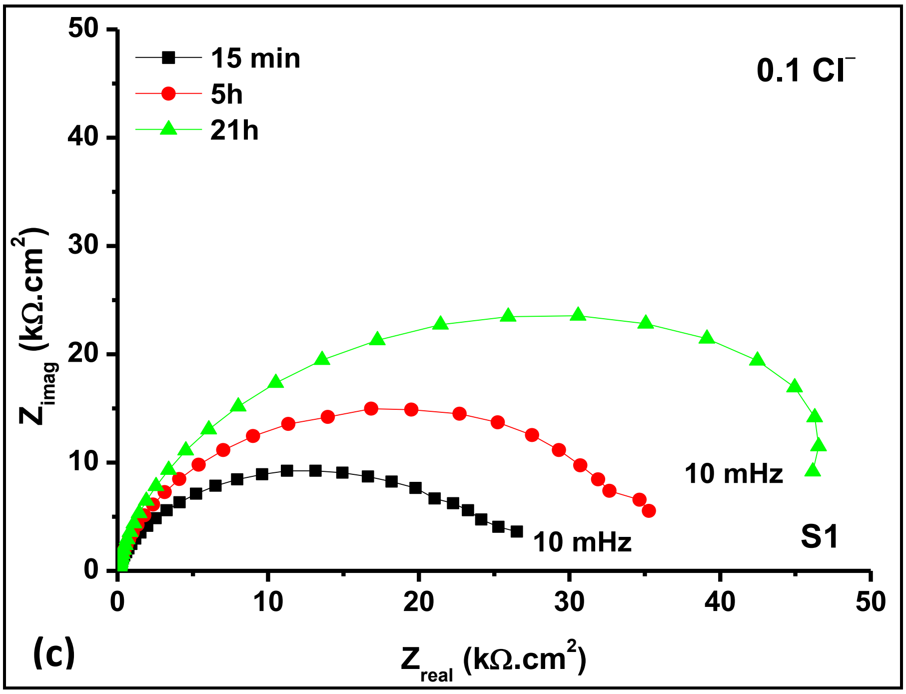

Fig. 4.4.3.1. (c) Nyquist plots of S1 steel in saturated $Ca(OH)_2$ solution with 0.1 wt. % Cl^-

The Nyquist plot of S2 steel (Fig. 4.4.3.2.) immersed in saturated $Ca(OH)_2$ solution for 21 h without chloride shows a real impedance of 119 kΩ.cm^2. The real impedance drops to 47.8 kΩ.cm^2 on immersion in saturated $Ca(OH)_2$ solution with 0.1 wt. % chloride concentration for 21 h. Therefore, the increase in chloride concentration depresses the real impedance values.

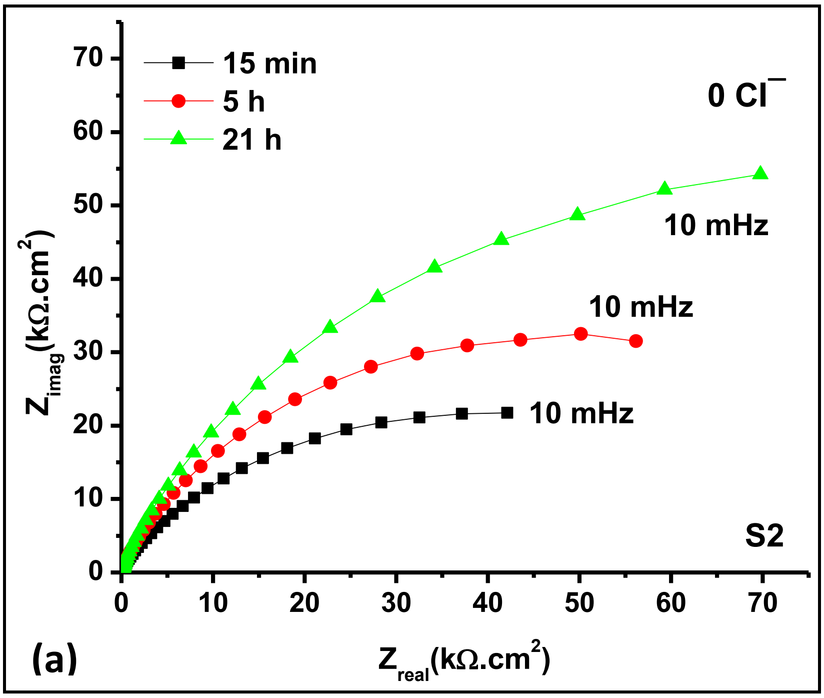

Fig. 4.4.3.2. (a) Nyquist plots of S2 steel in saturated $Ca(OH)_2$ solution without Cl^-

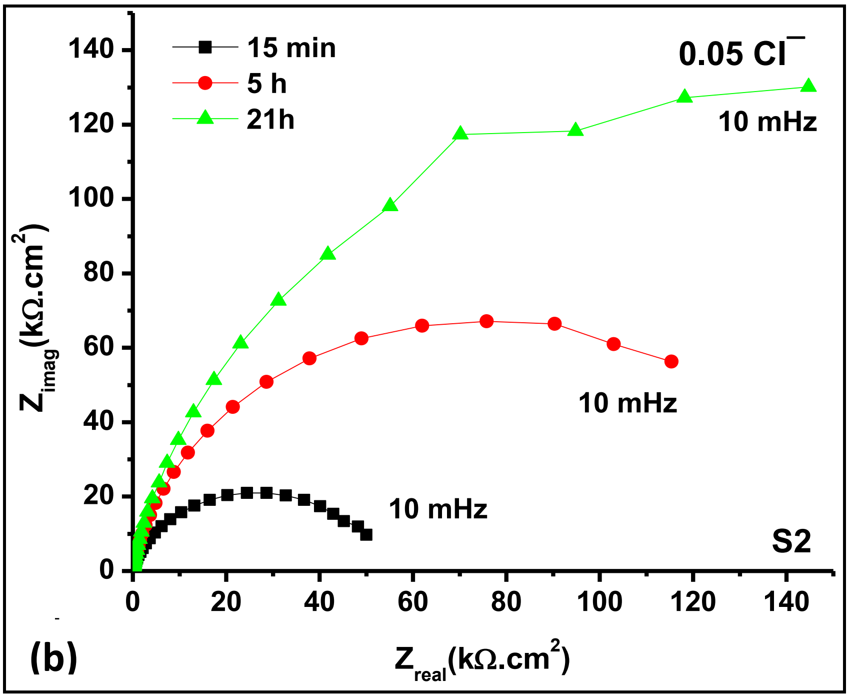

Fig. 4.4.3.2. (b) Nyquist plots of S2 steel in saturated $Ca(OH)_2$ solution with 0.05 wt. % Cl^-

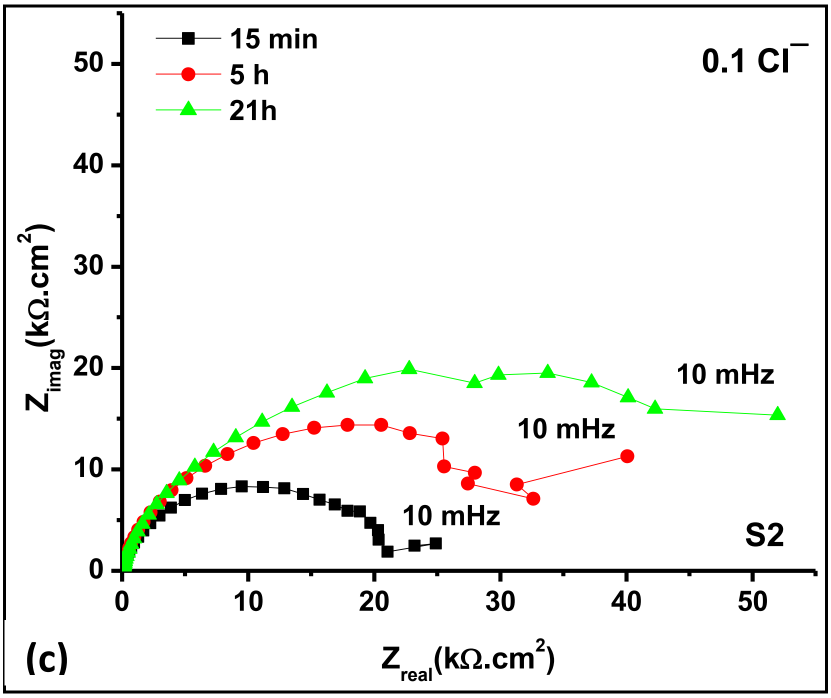

Fig. 4.4.3.2. (c) Nyquist plots of S2 steel in saturated $Ca(OH)_2$ solution with 0.1 wt. % Cl^-

The Nyquist plot of S3 steel (Fig. 4.4.3.3.) immersed in saturated $Ca(OH)_2$ solution for 21 h without chloride shows a real impedance of 490 kΩ.cm^2. The real impedance drops to 45.5 kΩ.cm^2 on immersion in saturated $Ca(OH)_2$ solution with 0.1 wt. % chloride concentration for 21 h. Therefore, increasing chloride concentration decreases the real impedance values.

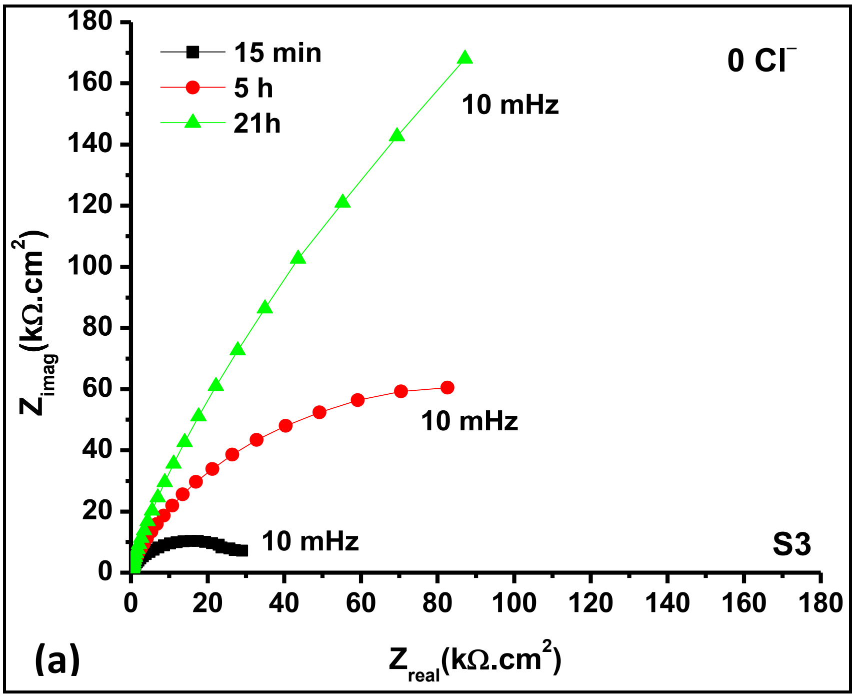

Fig. 4.4.3.3. (a) Nyquist plots of S3 steel in saturated $Ca(OH)_2$ solution without Cl^-

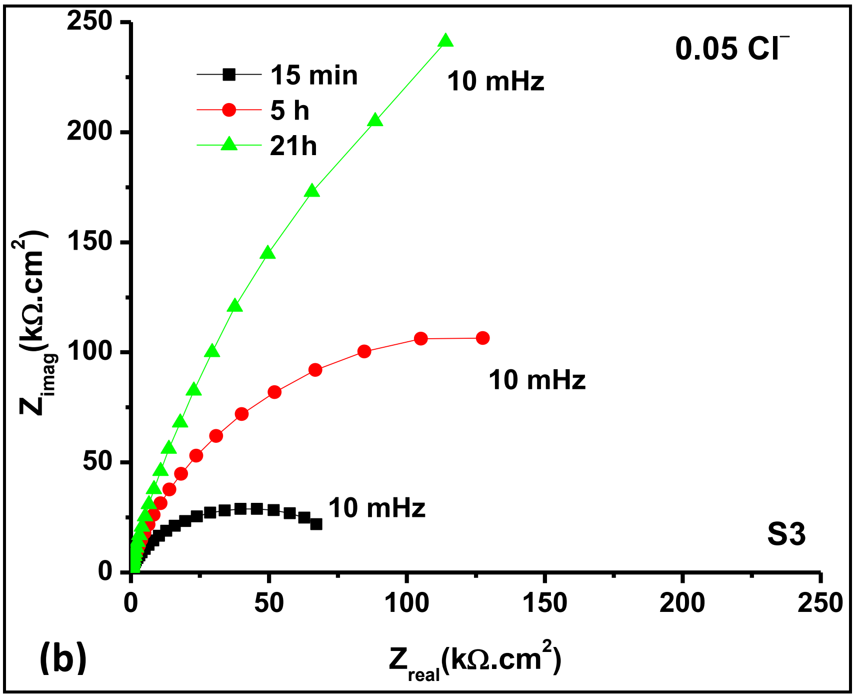

Fig. 4.4.3.3. (b) Nyquist plots of S3 steel in saturated $Ca(OH)_2$ solution with 0.05 wt. % Cl^-

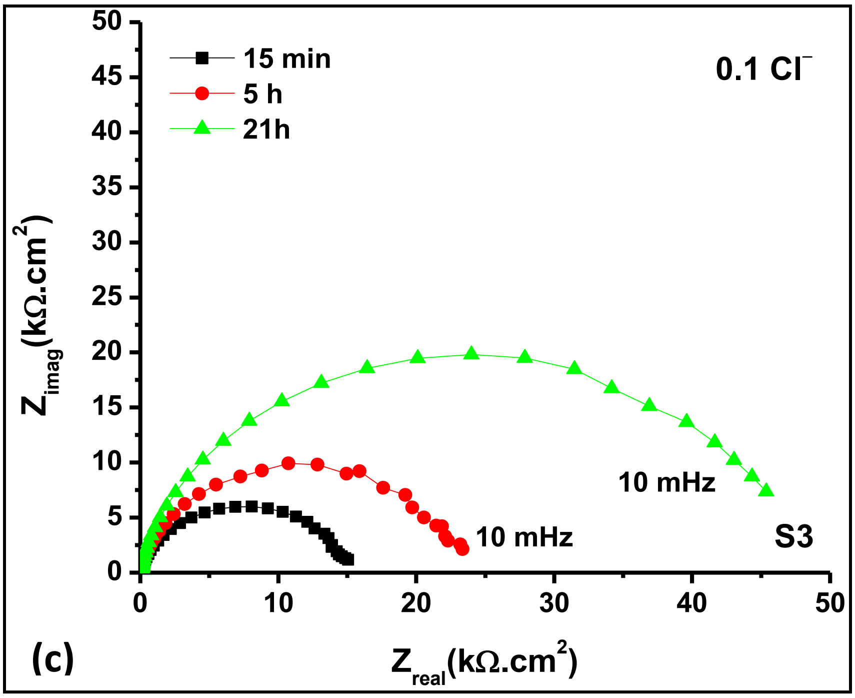

Fig. 4.4.3.3. (c) Nyquist plots of S3 steel in saturated $Ca(OH)_2$ solution with 0.1 wt. % Cl^-

The Nyquist plot of S4 steel (Fig. 4.4.3.4.) immersed in saturated $Ca(OH)_2$ solution for 21 h without chloride shows a real impedance of 425 kΩ.cm^2. Real impedance for the same steel immersed in saturated $Ca(OH)_2$ solution with 0.05 wt. % chloride concentration for 21 h drops to 235 kΩ.cm^2. The real impedance further drops to 32.8 kΩ.cm^2 on immersion in saturated $Ca(OH)_2$ solution with 0.1 wt. % chloride concentration for 21 h. Therefore, the real impedance values are lowered with increase in chloride concentration.

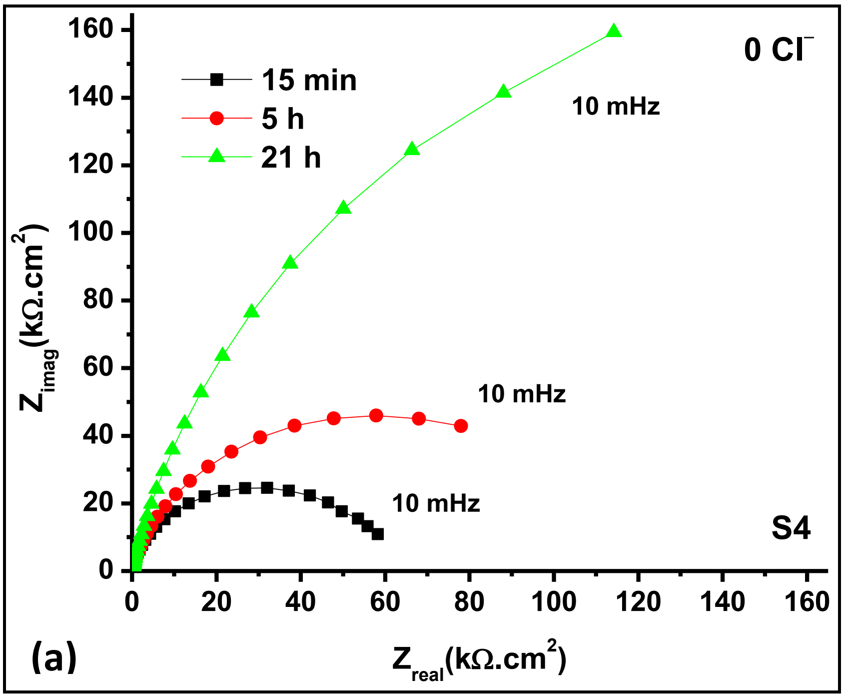

Fig. 4.4.3.4. (a) Nyquist plots of S4 steel in saturated $Ca(OH)_2$ solution without Cl^-

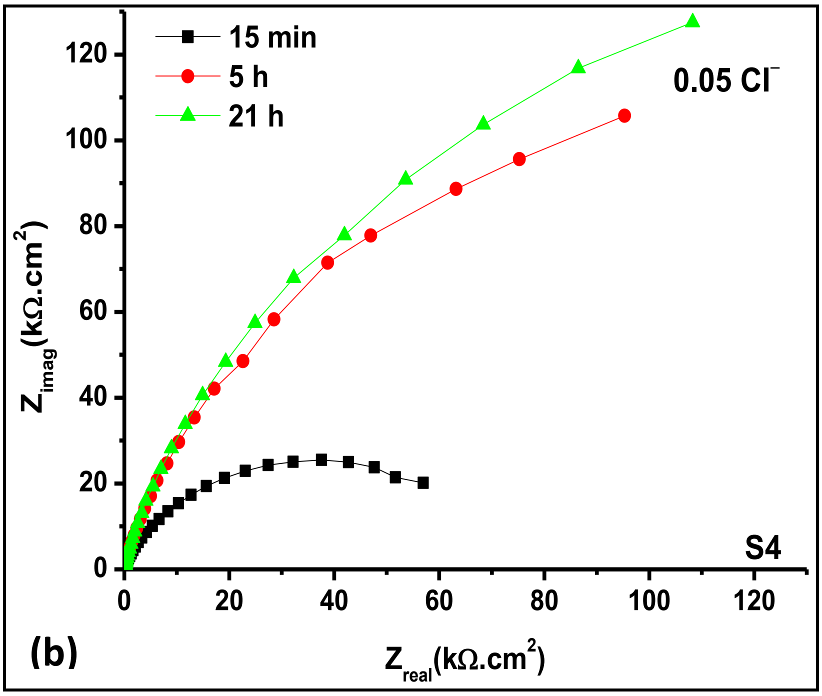

Fig. 4.4.3.4. (b) Nyquist plots of S4 steel in saturated $Ca(OH)_2$ solution with 0.05 wt. % Cl^-

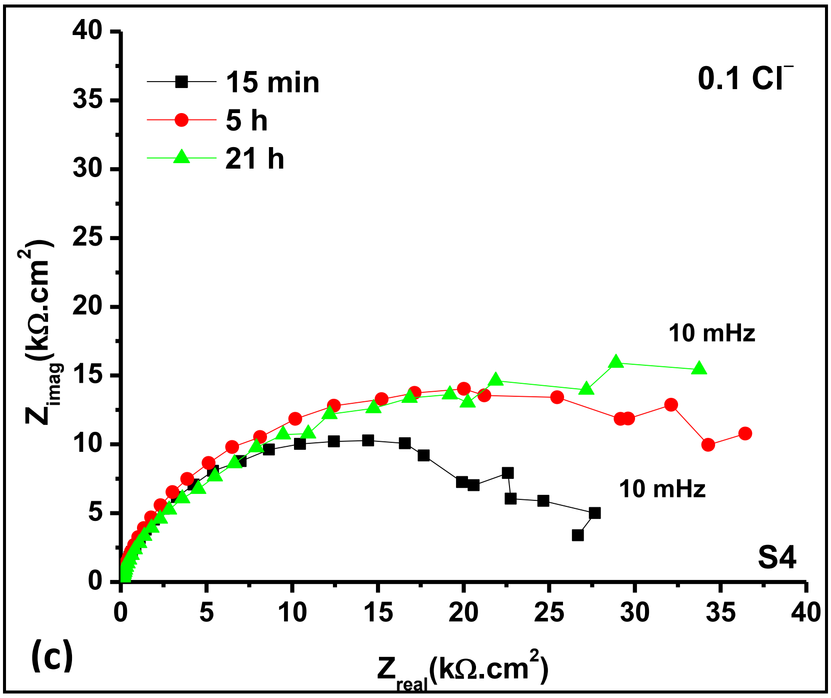

Fig. 4.4.3.4. (c) Nyquist plots of S4 steel in saturated $Ca(OH)_2$ solution with 0.1 wt. % Cl^-

A capacitive loop of depressed semicircles is seen in the Nyquist plots of S3 steel (Fig. 4.4.3.3c). Further, with increase in immersion time the capacitive part increases. Again, with escalation in immersion time, the polarization resistance or the real impedance increases. Opposite trend is seen in the Nyquist plot of S4 steel (Fig. 4.4.3.4c) *i.e.*, as the time of immersion increases there is a decline in the polarization resistance and capacitive component. The capacitive part increased and therefore, capacitance decreased with time of immersion for S1, S2 and S3 steels (Fig. 4.4.3.1 to Fig. 4.4.3.3). A decrease in capacitance as observed in the case of S1, S2 and S3 steels implies that a thicker and more protective passive layer is formed with increasing time of immersion. However, the capacitance increased and capacitive part decreased with immersion time, due to an increased double layer charge owing to corrosion of S4 steel in ($Ca(OH)_2$ + 0.1 Cl^-) solution (Fig. 4.4.3.4c). Real impedance decreased with immersion time indicating breakdown of passive film. Thus, S1, S2 and S3 steels can withstand 0.1 Cl^- whereas mild steel cannot.

The Bode magnitude plot of S1 steel immersed in saturated $Ca(OH)_2$ solution for various times is shown in Fig. 4.4.3.5. It shows that the straight line portion with a slope of −1 decreases in length as the concentration of chloride increases. Therefore, the increase in chloride concentration affects the passive film adversely.

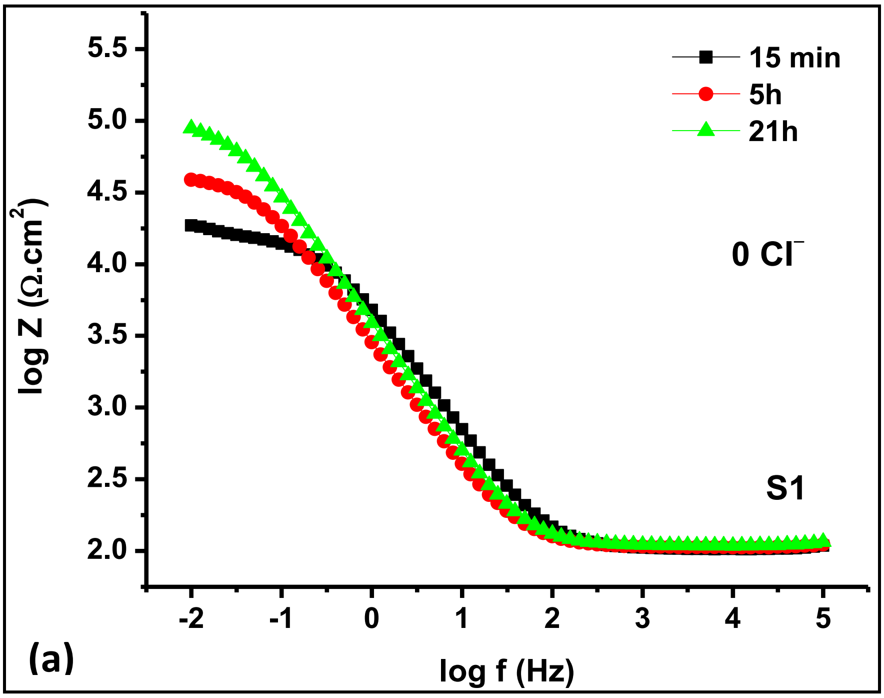

Fig. 4.4.3.5. (a) Bode magnitude plots of S1 steel in saturated $Ca(OH)_2$ solution without Cl^-

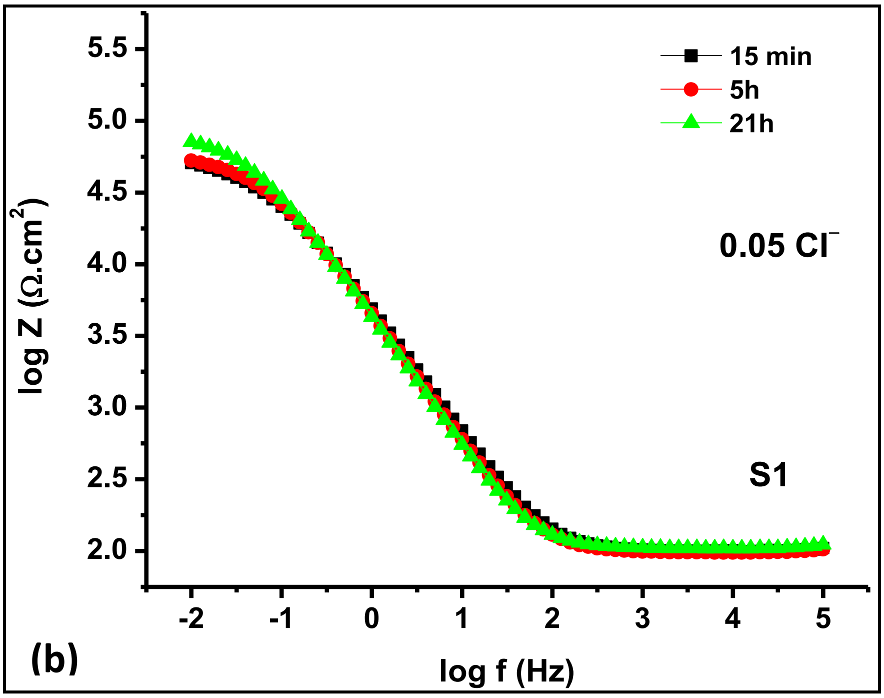

Fig. 4.4.3.5. (b) Bode magnitude plots of S1 steel in saturated $Ca(OH)_2$ solution with 0.05 wt. % Cl^-

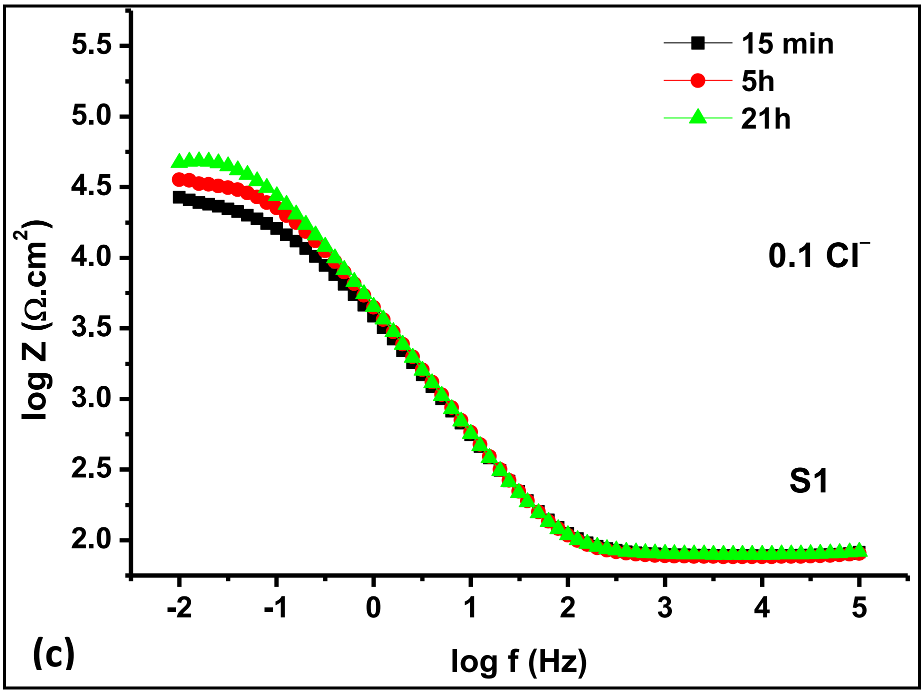

Fig. 4.4.3.5. (c) Bode magnitude plots of S1 steel in saturated $Ca(OH)_2$ solution with 0.1 wt. % Cl^-

The Bode magnitude plot of S2 steel (Fig. 4.4.3.6.) immersed in saturated $Ca(OH)_2$ solution for 21 h shows that the straight line portion with a slope of −1 decreases in length as the concentration of chloride increases from 0 to 0.1 wt. %. Therefore, the increase in chloride concentration weakens the passive film.

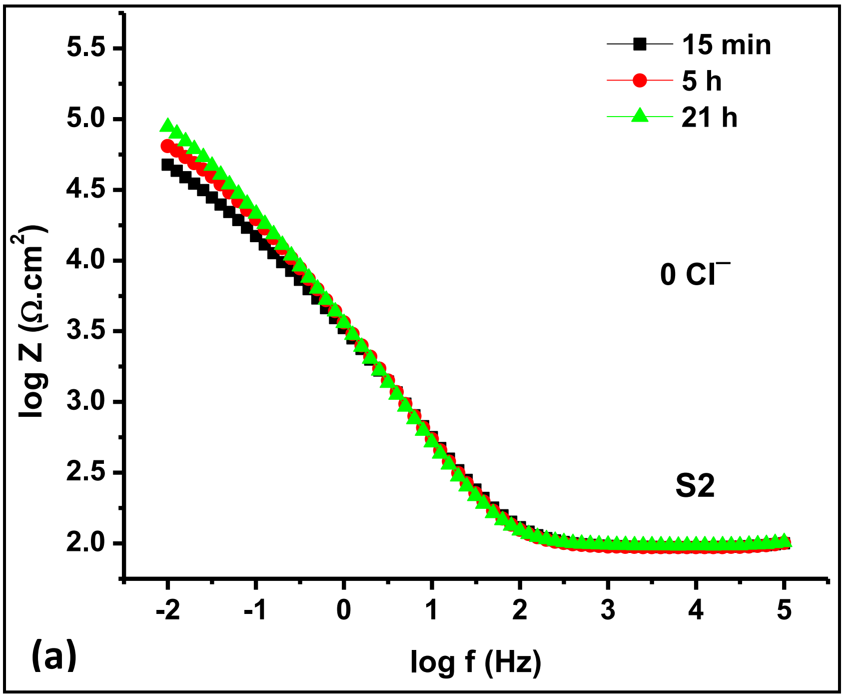

Fig. 4.4.3.6. (a) Bode magnitude plots of S2 steel in saturated $Ca(OH)_2$ solution without Cl^-

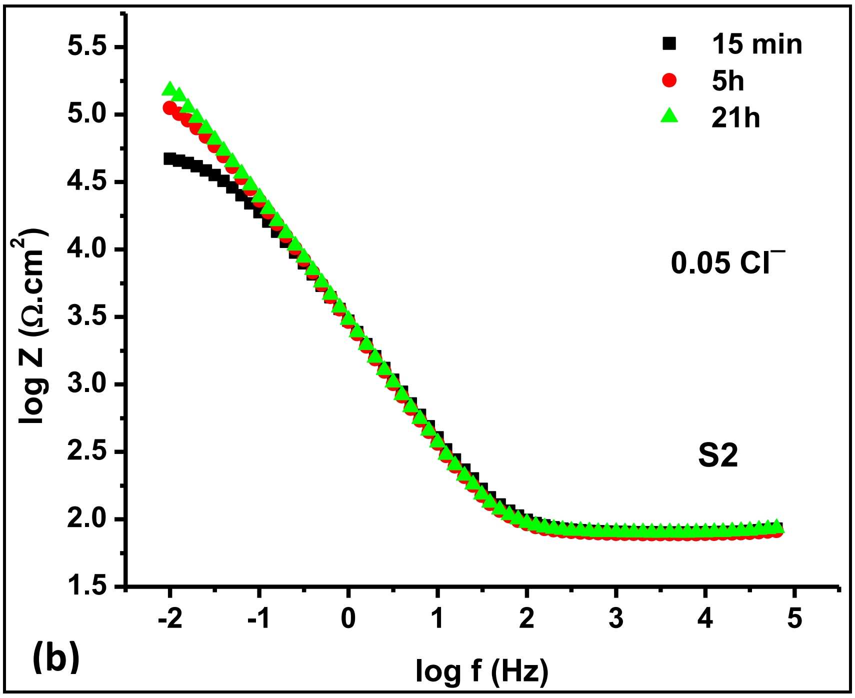

Fig. 4.4.3.6. (b) Bode magnitude plots of S2 steel in saturated $Ca(OH)_2$ solution with 0.05 wt. % Cl^-

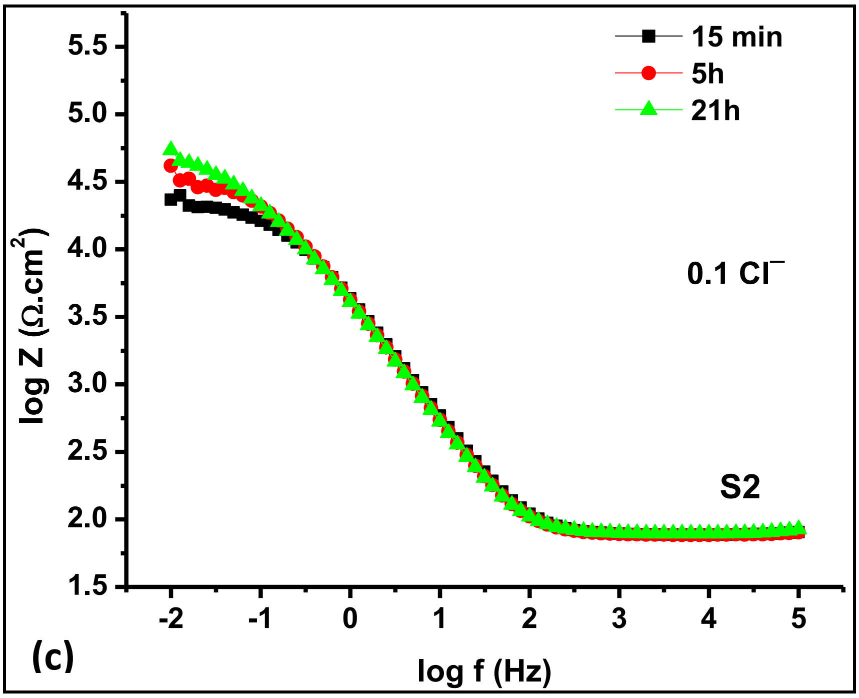

Fig. 4.4.3.6. (c) Bode magnitude plots of S2 steel in saturated $Ca(OH)_2$ solution with 0.1 wt. % Cl^-

The Bode magnitude plot of S3 steel (Fig. 4.4.3.7.) immersed in saturated $Ca(OH)_2$ solution for 21 h shows that the straight line portion with a slope of −1 decreases in length as the concentration of chloride increases from 0 to 0.1 wt. %. Therefore, the increase in chloride concentration reduces the protective ability of the passive film.

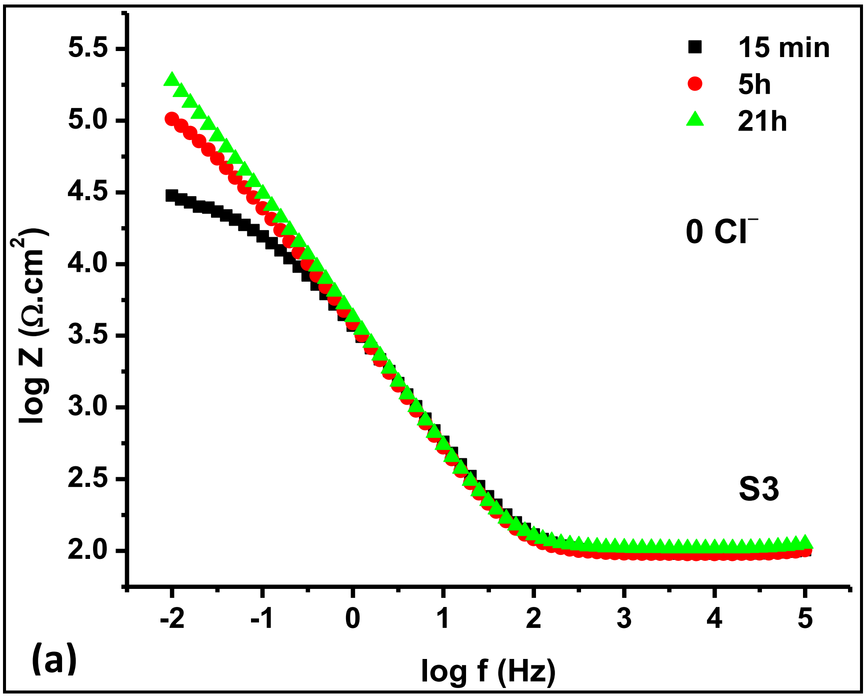

Fig. 4.4.3.7. (a) Bode magnitude plots of S3 steel in saturated $Ca(OH)_2$ solution without Cl^-

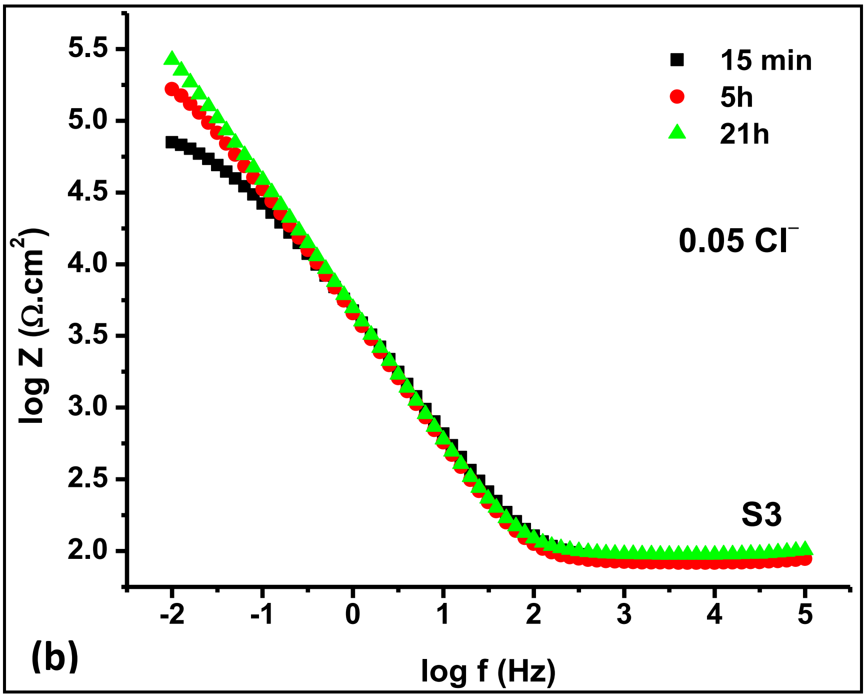

Fig. 4.4.3.7. (b) Bode magnitude plots of S3 steel in saturated $Ca(OH)_2$ solution with 0.05 wt. % Cl^-

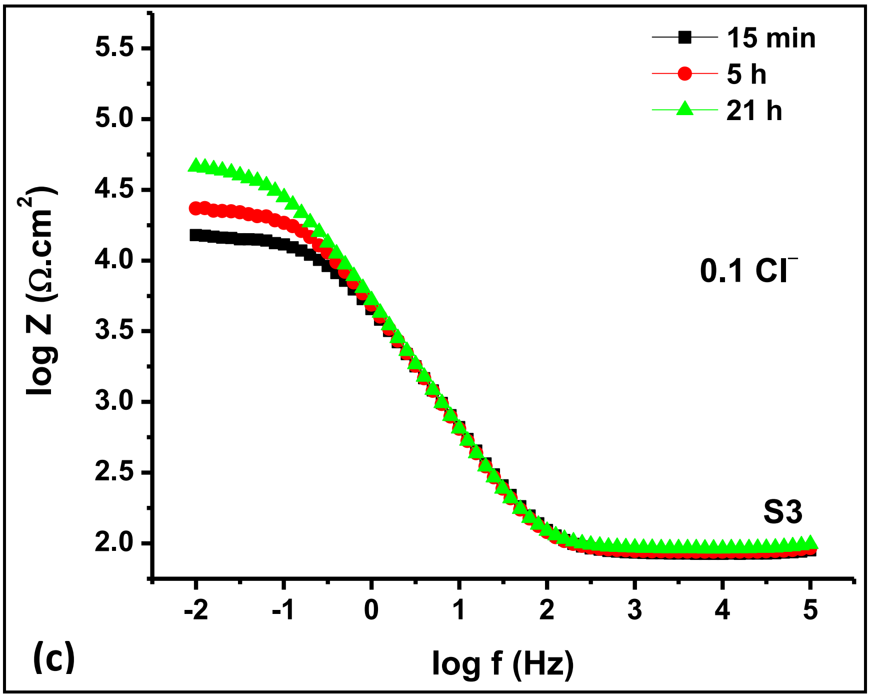

Fig. 4.4.3.7. (c) Bode magnitude plots of S3 steel in saturated $Ca(OH)_2$ solution with 0.1 wt. % Cl^-

The Bode magnitude plot of S4 steel (Fig. 4.4.3.8.) immersed in saturated $Ca(OH)_2$ solution for various times shows that the straight line portion with a slope of −1 decreases in length as the concentration of chloride increases from 0 to 0.1 wt. %. Therefore, the increase in chloride concentration affects the passive film adversely.

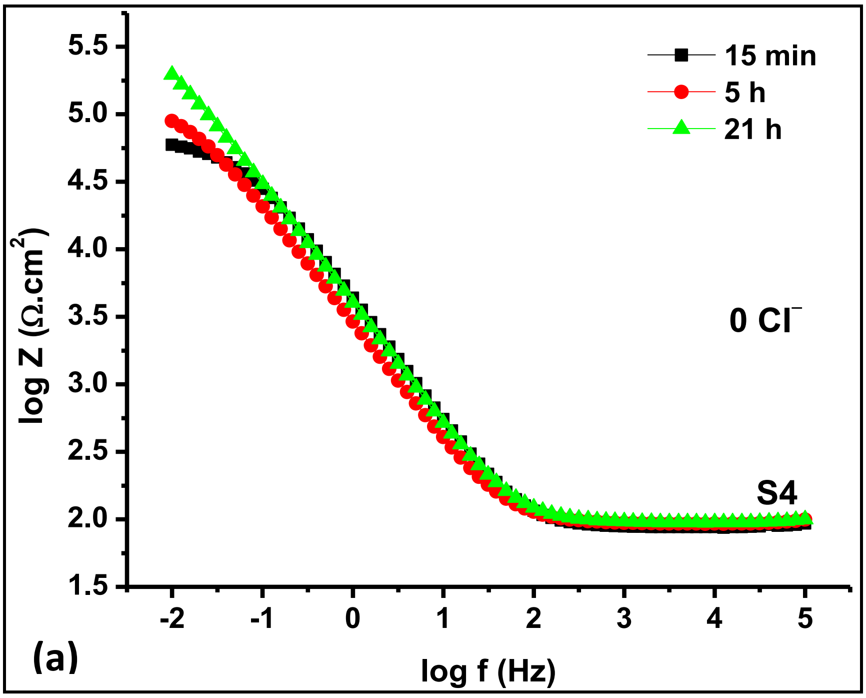

Fig. 4.4.3.8. (a) Bode magnitude plots of S4 steel in saturated $Ca(OH)_2$ solution without Cl^-

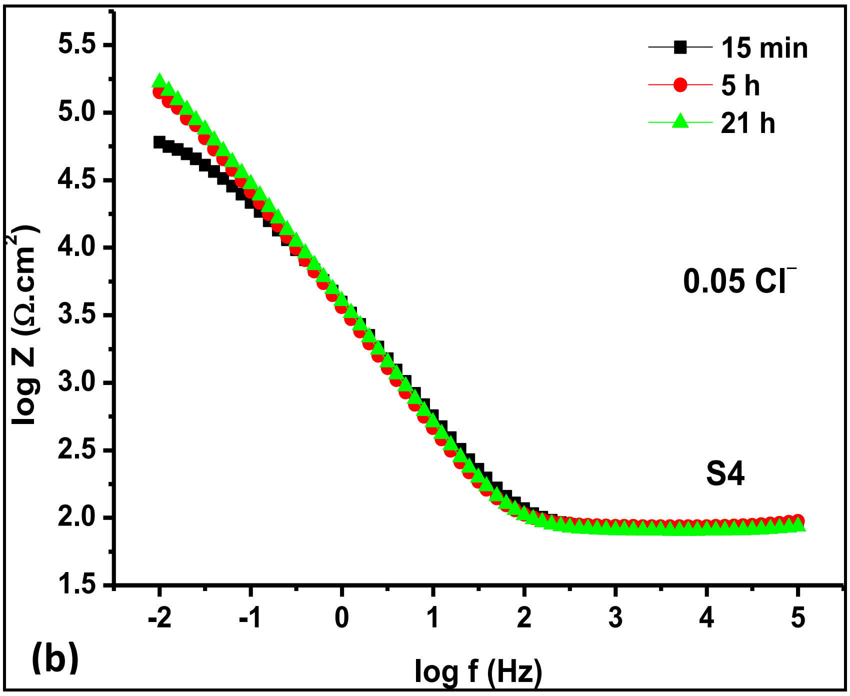

Fig. 4.4.3.8. (b) Bode magnitude plots of S4 steel in saturated $Ca(OH)_2$ solution with 0.05 wt. % Cl^-

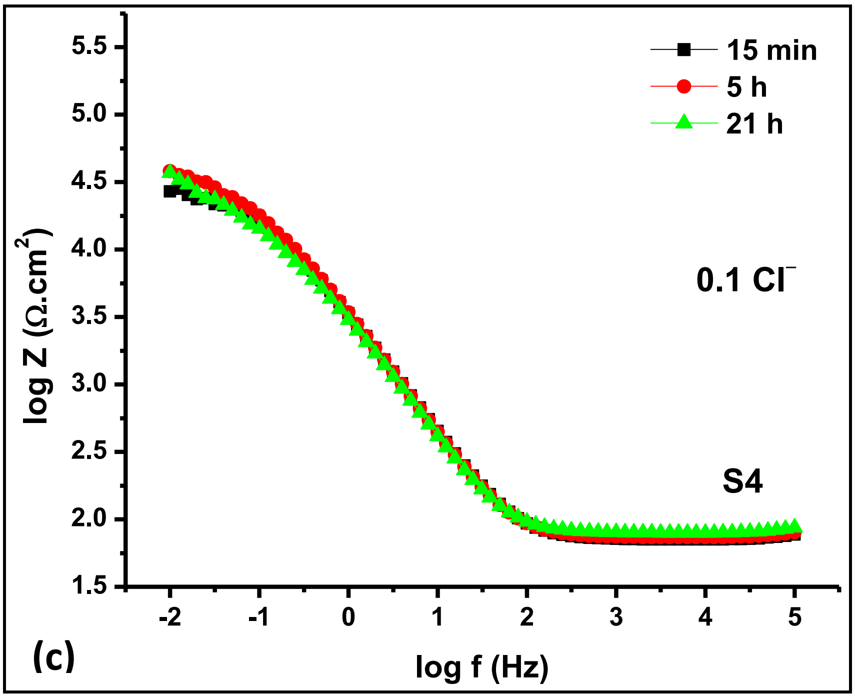

Fig. 4.4.3.8. (c) Bode magnitude plots of S4 steel in saturated $Ca(OH)_2$ solution with 0.1 wt. % Cl^-

For S1, S2 and S3 steels tested in the saturated solution of $Ca(OH)_2$ without Cl^- and with 0.05 wt. % Cl^- and 0.1 wt. % Cl^-, at frequencies less than about 10^2 Hz the Bode magnitude plots exhibited a purely capacitive behaviour (Fig.4.4.3.5 to Fig.4.4.3.7). With increasing immersion time, the straight-line portion with a slope of about −1 (the capacitive part) expanded. Similar response was observed for S4 steel in $Ca(OH)_2$ solution and ($Ca(OH)_2$ + 0.05 wt. % Cl^-) solution, too (Fig.4.4.3.8a and Fig.4.4.3.8b). At the end of 21 h of immersion, the impedance of passive film ranged from 10^4 $\Omega.cm^2$ to $10^{5.5}$ $\Omega.cm^2$ for all the samples. The passive film acts as a capacitor effectively when the impedance is greater than 10^6 $\Omega.cm^2$ (Kelly et al., 2003). The high values of impedance imply that the passive film becomes more protective with time of immersion. For S4 steel in ($Ca(OH)_2$ + 0.1 Cl^-) solution (Fig.4.4.3.8c), the central portion of bode magnitude curve declined with time of immersion, which indicates that the passive film broke down.

The capacitance corresponding to the low frequency (f_l) break point, C_l declined with time indicating enlargement of passive layer for S1, S2 and S3 steels in all the solutions and S4 steel in solutions containing less than 0.1 Cl^- (Fig.4.4.3.5 to Fig.4.4.3.8b). The C_l of S4 steel for the ($Ca(OH)_2$ + 0.1 Cl^-) solution increased with immersion time depicting the breakdown of passive layer and dissolution of iron (Fig.4.4.3.8c). Capacitance is considered to be a good pointer for the initiation of pitting (Kelly et al., 2003) (Mansfeld et al., 1991). Thus, high phosphorous steels are able to resist 0.1 Cl^- unlike mild steel.

The Bode phase plot of S1 steel (Fig. 4.4.3.9.) immersed in saturated $Ca(OH)_2$ solution for various times shows that the frequency, at which the rise in absolute value of θ starts, increased as the concentration of chloride increased from 0 to 0.1 wt. %. Further, as the immersion time increased, the lower frequency break point corresponding to 45° drifted towards higher frequencies. Therefore, the increase in chloride concentration affects the passive film adversely.

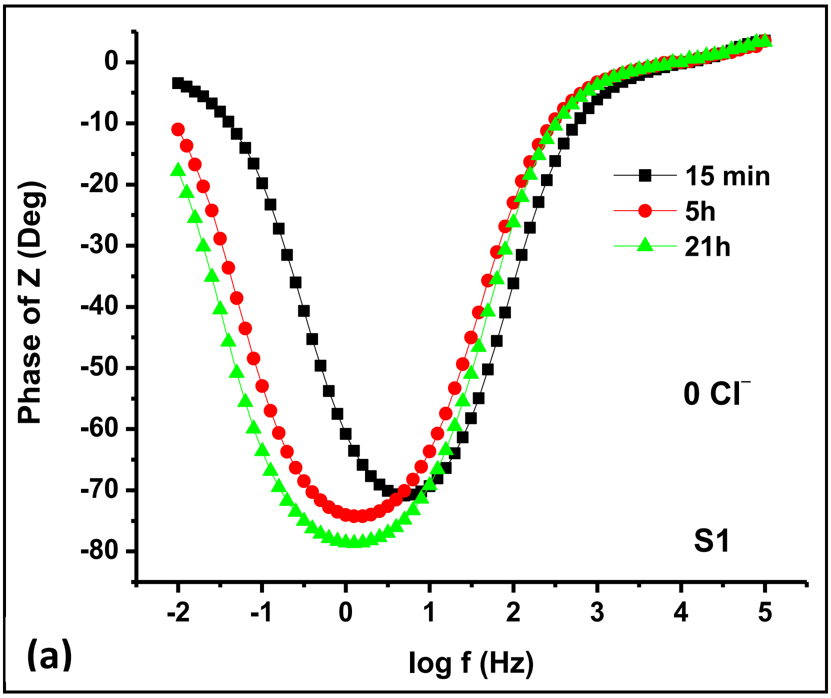

Fig. 4.4.3.9. (a) Bode phase plots of S1 steel in saturated $Ca(OH)_2$ solution without Cl^-

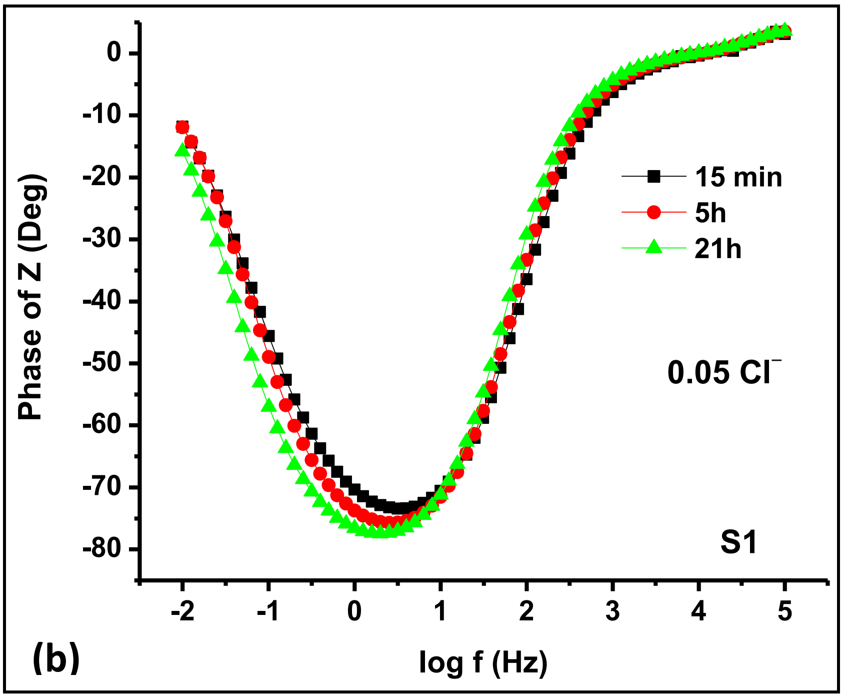

Fig. 4.4.3.9. (b) Bode phase plots of S1 steel in saturated $Ca(OH)_2$ solution with 0.05 wt. % Cl^-

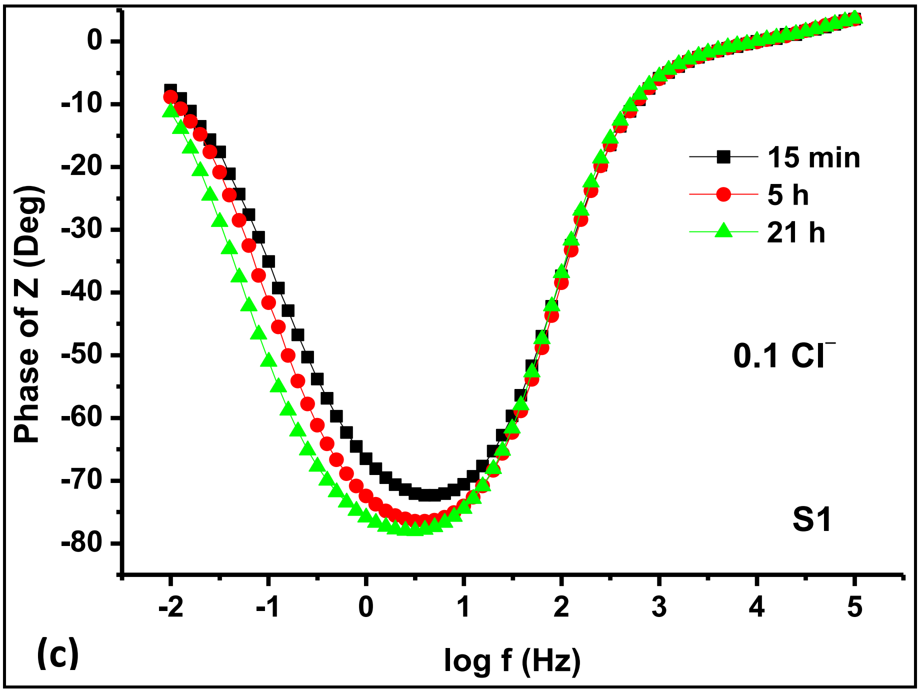

Fig. 4.4.3.9. (c) Bode phase plots of S1 steel in saturated $Ca(OH)_2$ solution with 0.1 wt. % Cl^-

The Bode phase plot of S2 steel (Fig. 4.4.3.10.) immersed in saturated $Ca(OH)_2$ solution for 21h shows that the frequency, at which the rise in absolute value of θ starts, increased as the concentration of chloride increased from 0 to 0.1 wt. %. Further, as the immersion time increased, the lower frequency break point corresponding to 45° drifted towards higher frequencies. Therefore, the increase in chloride concentration reduces the thickness of the passive film.

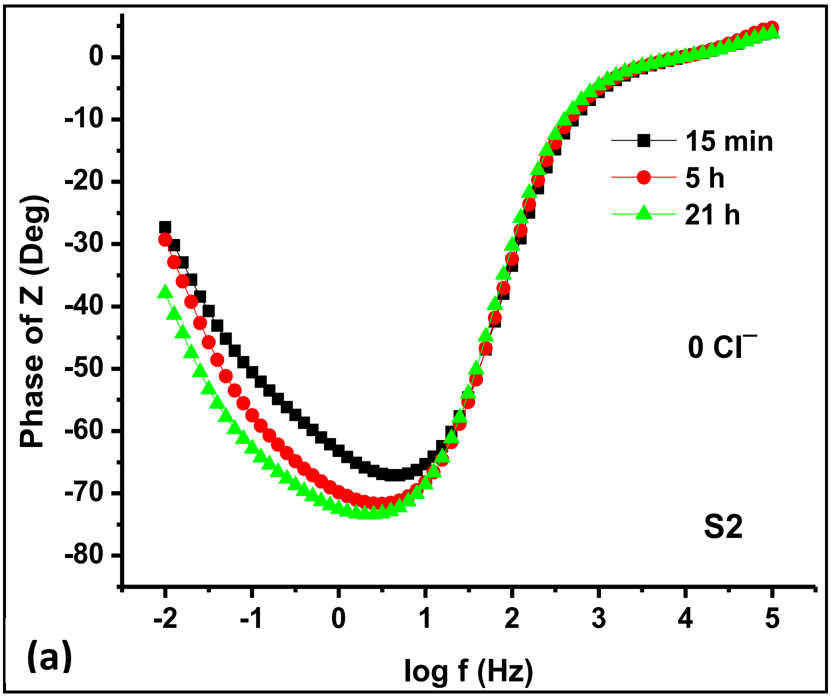

Fig. 4.4.3.10. (a) Bode phase plots of S2 steel in saturated $Ca(OH)_2$ solution without Cl^-

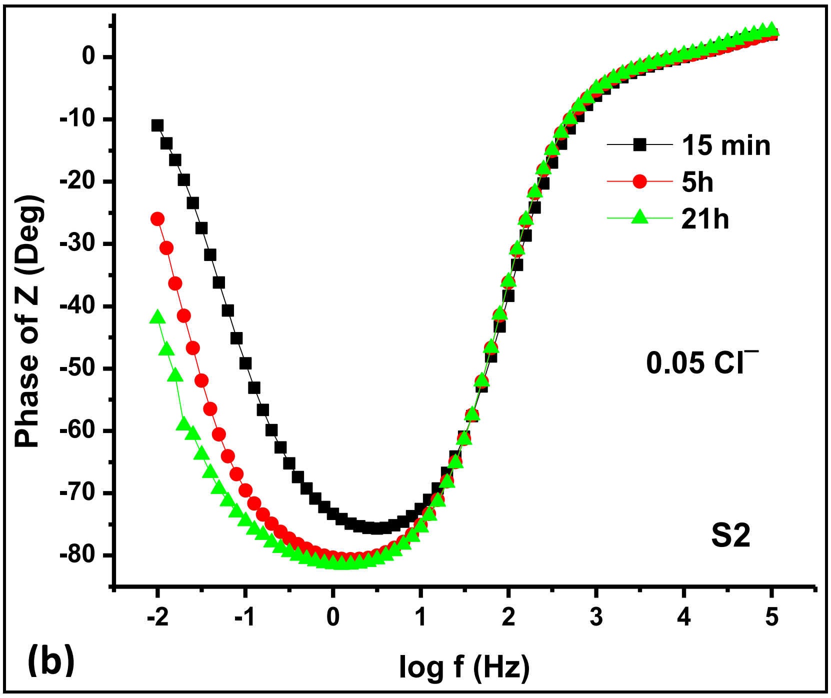

Fig. 4.4.3.10. (b) Bode phase plots of S2 steel in saturated $Ca(OH)_2$ solution with 0.05 wt. % Cl^-

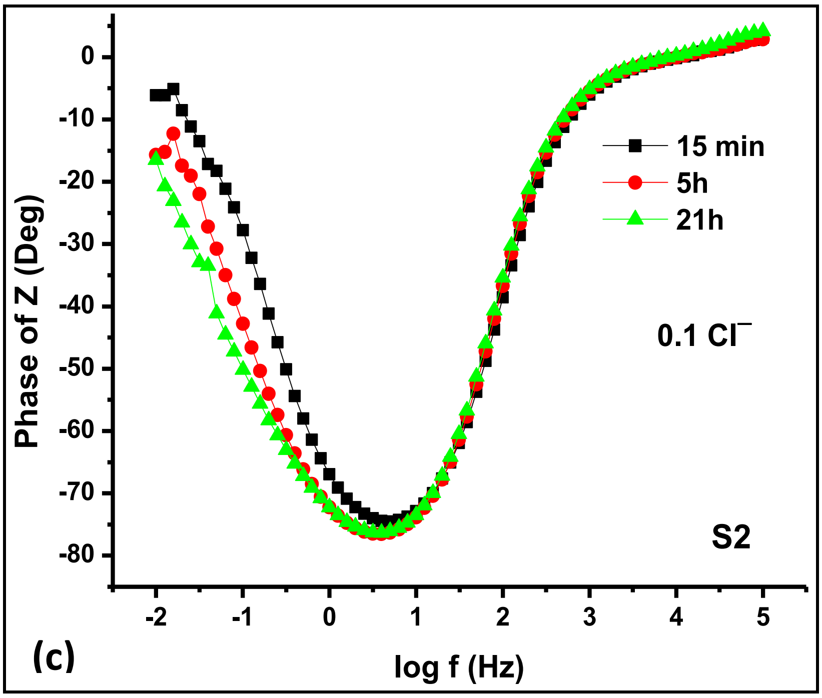

Fig. 4.4.3.10. (c) Bode phase plots of S2 steel in saturated $Ca(OH)_2$ solution with 0.1 wt. % Cl^{-}

The Bode phase plot of S3 steel (Fig. 4.4.3.11.) immersed in saturated $Ca(OH)_2$ solution for 21h shows that the frequency, at which the rise in absolute value of θ starts, increased as the concentration of chloride increased from 0 to 0.1 wt. %. Therefore, the increase in chloride concentration weakens the passive film.

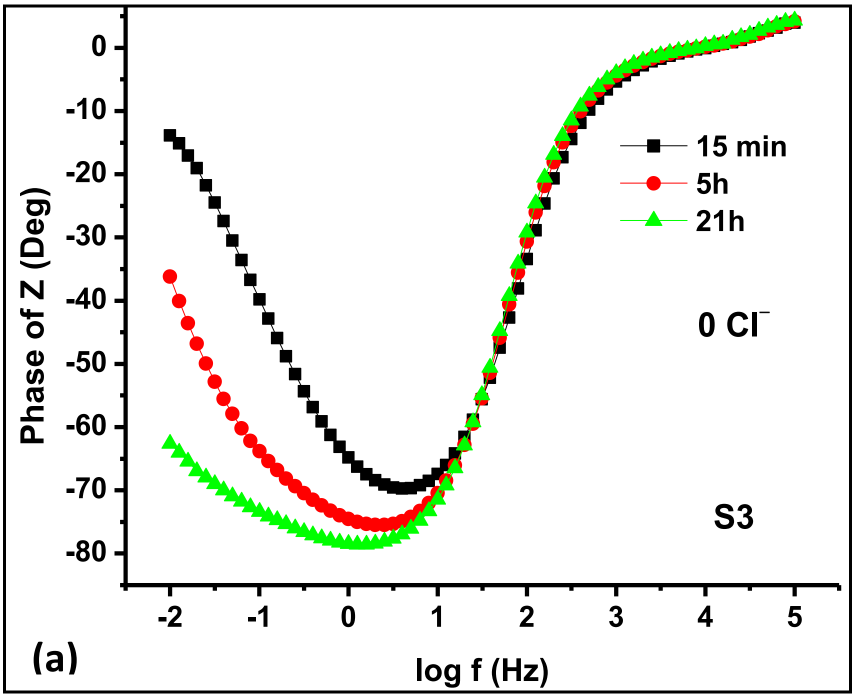

Fig. 4.4.3.11. (a) Bode phase plots of S3 steel in saturated $Ca(OH)_2$ solution without Cl^{-}

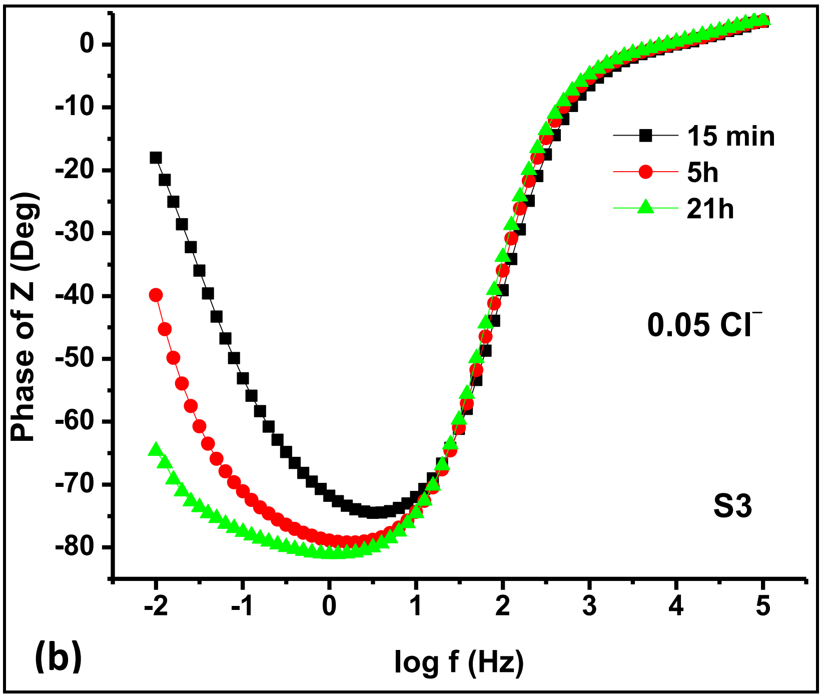

Fig. 4.4.3.11. (b) Bode phase plots of S3 steel in saturated $Ca(OH)_2$ solution with 0.05 wt. % Cl^-

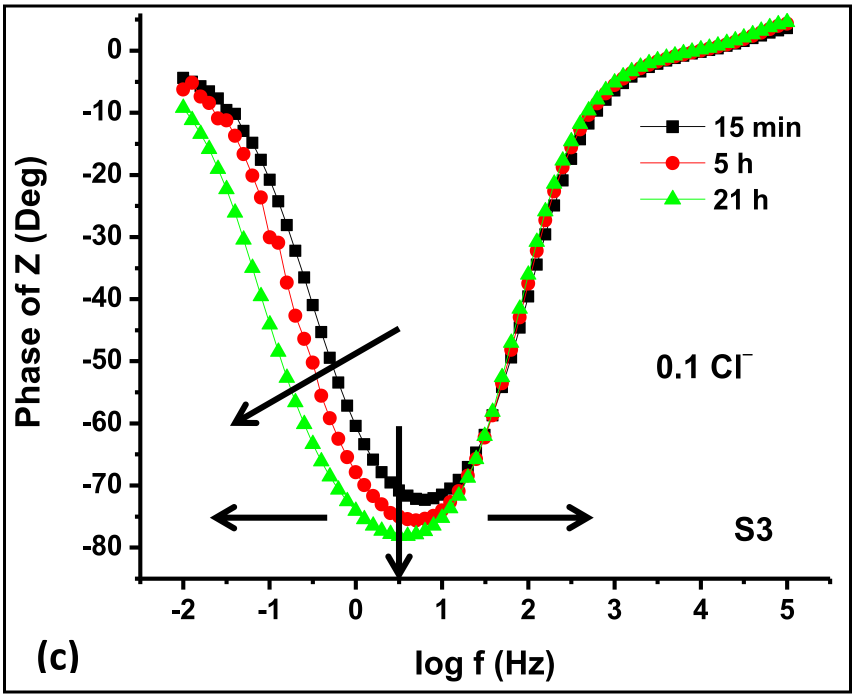

Fig. 4.4.3.11. (c) Bode phase plots of S3 steel in saturated $Ca(OH)_2$ solution with 0.1 wt. % Cl^-

The Bode phase plot of S4 steel (Fig. 4.4.3.12.) immersed in saturated $Ca(OH)_2$ solution for various times shows that the frequency, at which the rise in absolute value of θ starts, increased as the concentration of chloride increased from 0 to 0.1 wt. %. Therefore, the increase in chloride concentration affects the protective character of the passive film adversely.

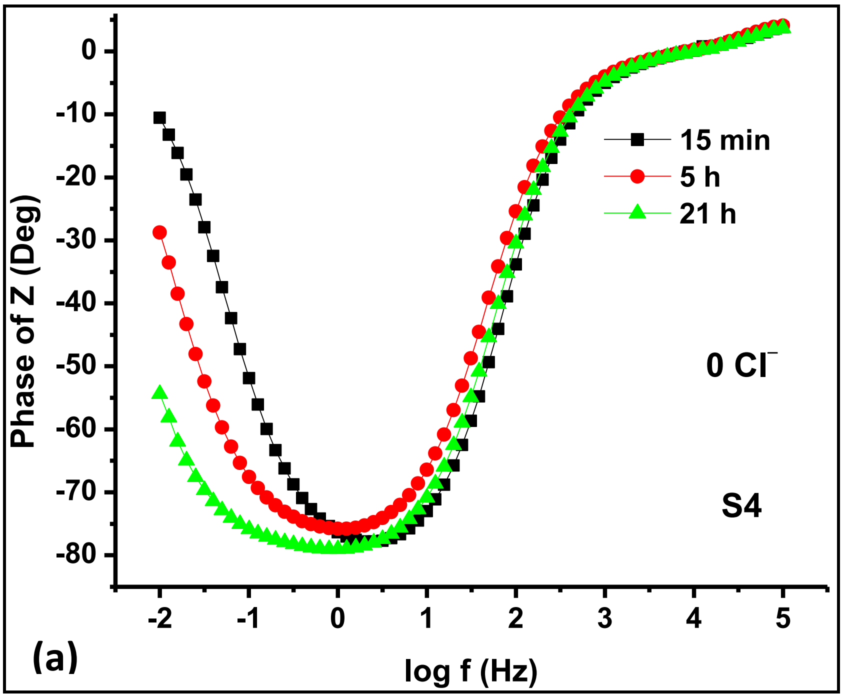

Fig. 4.4.3.12. (a) Bode phase plots of S4 steel in saturated $Ca(OH)_2$ solution without Cl^-

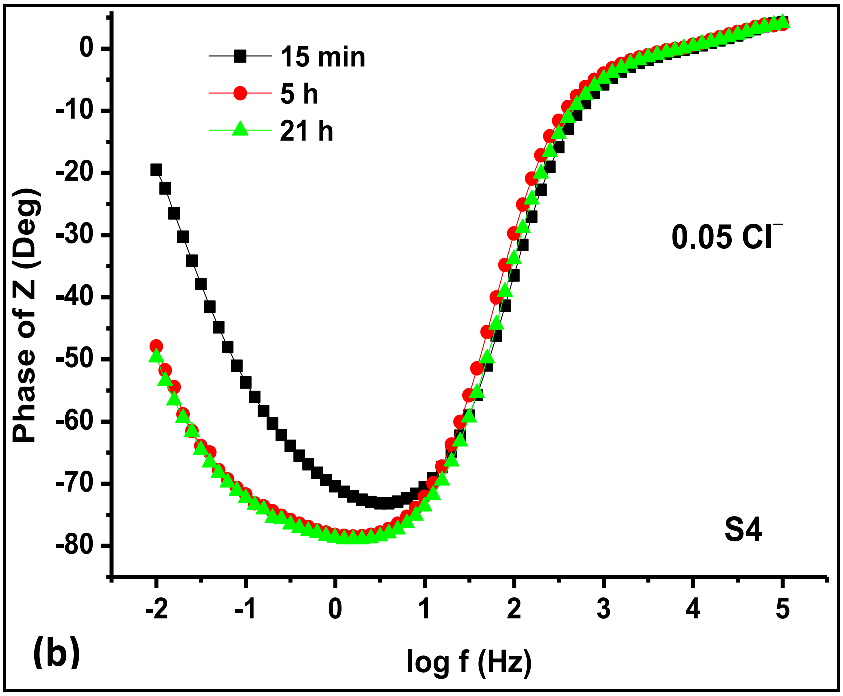

Fig. 4.4.3.12. (b) Bode phase plots of S4 steel in saturated $Ca(OH)_2$ solution with 0.05 wt. % Cl^-

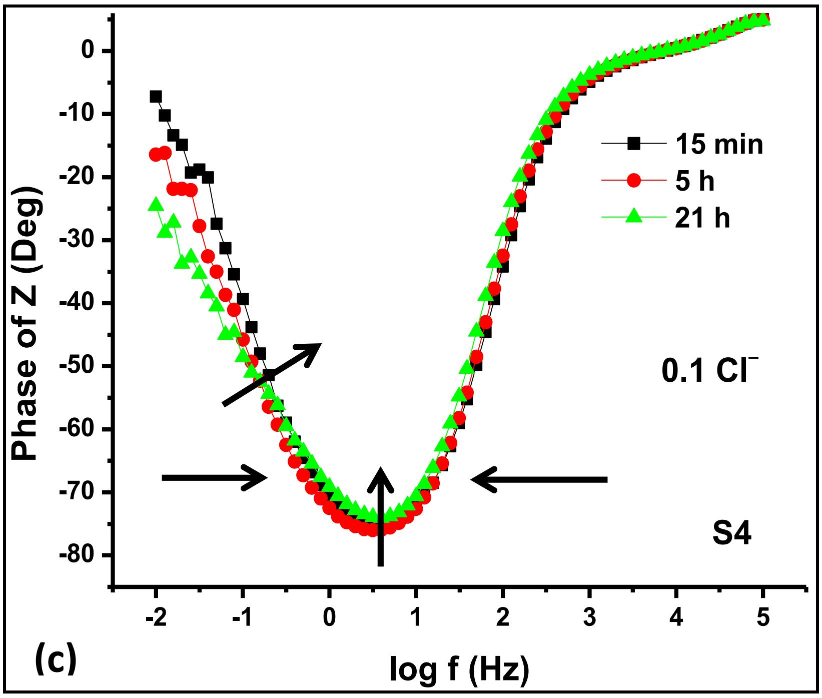

Fig. 4.4.3.12. (c) Bode phase plots of S4 steel in saturated $Ca(OH)_2$ solution with 0.1 wt. % Cl^-

In the Bode phase plots, the phase angle (θ) in S1, S2 and S3 steels in all solutions and S4 steel in solutions containing less than 0.1 Cl^- declined to zero at f_h and f_l. The value of θ at zero correlates with the resistances of R_u and (R_u+R_c+R_p). Capacitive behavior is indicated by the increase of θ towards 90° at intermediate range of frequencies (Walter, 1986).

The trough of Bode phase plots in S1, S2 and S3 steels in all solutions and S4 steel in solutions containing less than 0.1 Cl^- widened with time of immersion (Fig. 4.4.3.9 to Fig. 4.4.3.12b). This considerable phase shift at absolute value of θ (trough of the plot) in the Bode phase angle graph implies broadening of passive layer with immersion time. The frequency, at which the rise in absolute value of θ starts, decreased as the immersion time increased. As the immersion time increased, the lower frequency break point corresponding to 45° drifted towards lower frequencies. Therefore, the phase angle drift at low frequencies increased with immersion time for Bode phase plots in S1, S2 and S3 steels in all solutions and S4 steel in solutions containing less than 0.1 Cl^-. This indicates improvement of protective capabilities of the passive layer with immersion time (Kelly et al., 2003)(Mansfeld et al., 1991)(Sahoo and Balasubramaniam, 2008). The degradation of organic coatings are indicated by a decrease in phase angle shift at low frequency regions (Sahoo and Balasubramaniam, 2008)(Mansfeld et al., 1991). The phase angle drift at low frequencies decreased with immersion time for Bode phase plots in S4 steel in solutions having 0.1 Cl^{-} indicating degradation of passive layer and increasing corrosion with immersion time (Fig.4.4.3.12c).

From the above observations on the Nyquist and Bode plots one can say that the decreasing capacitance and increasing impedance was found in the cases S1, S2 and S3 steels in all solutions and in case of S4 steel in solutions containing less than 0.1 Cl^{-}. This may be due to decrease in the micro-pores and increased protective coverage of the surface by the passive oxide layer with immersion time. The film deteriorated in the case of S4 steel in solutions having 0.1 Cl^{-} and corrosion increased with time. Thus, it can be said that for S1, S2 and S3 steels, the threshold Cl^{-} concentration for degradation of oxide layer is higher than 0.1 wt. %. It is equal to 0.05 wt. % for S4 steel.

The EIS spectra of all samples exhibited two time constants. The Nyquist plot of S3 steel immersed for 5 h in $Ca(OH)_2$ solution with 0.1 wt. % chloride shows the high frequency region as an inset in Fig. 4.4.3.13. The arc in the high frequency region could be associated with the OH^{-} ion adsorption on the surface of the steel (Saremi, M., 2002).

At frequencies lower than 790 Hz, the arc which appears is related to the interfacial reaction. This reaction is composed of two processes viz. the charge transfer reaction and the formation of a passive film (Saremi, M., 2002)(Poupard et al., 2004), which have an identical time constant. In order to fit the experimental data, many equivalent circuits were tried using Gamry Echem Analyst software version 6.04. The best fitting equivalent circuit that approximates the test system is shown in Fig. 4.4.3.14. It can also be written as $R_u\{C_c[R_c(Y_0R_p)]\}$. Here, solution resistance is represented by R_u. The resistance and capacitance of the adsorbed layer are given by R_c and C_c. R_p and Y_0 are the resistance and capacitance associated with the corrosion processes occurring in the micro-pores of the oxide film. The oxide film resistance is composed of the resistance due to the film and charge transfer. Mathematically, the impedance of the circuit can be written as

$$Z = R_u + \frac{A}{Aj\omega C_c + 1} \qquad (4.4.3.1)$$

where ω is the angular frequency and

$$A = R_c + \frac{R_p}{(j\omega)^{\alpha} Y_0 . R_p + 1} \qquad (4.4.3.2)$$

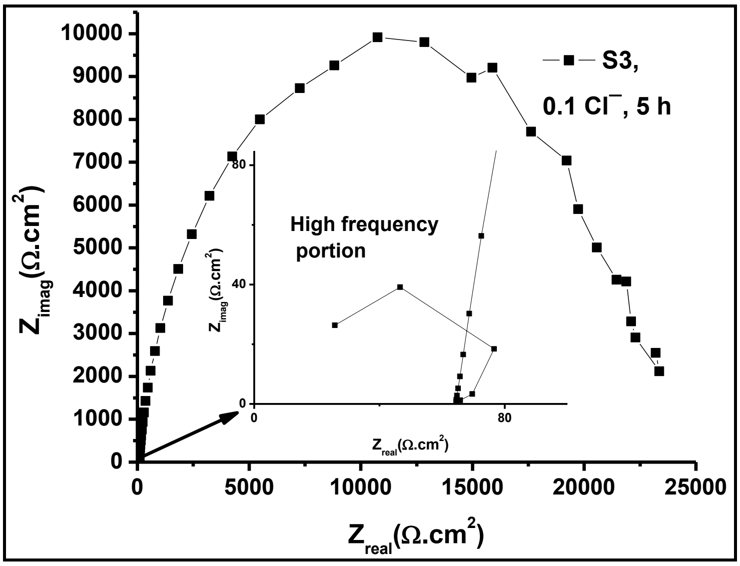

Fig. 4.4.3.13. Nyquist plot showing the second time constant in the high frequency region for S3 steel immersed in saturated $Ca(OH)_2$ solution containing 0.1 wt. % Cl^- for 5 h

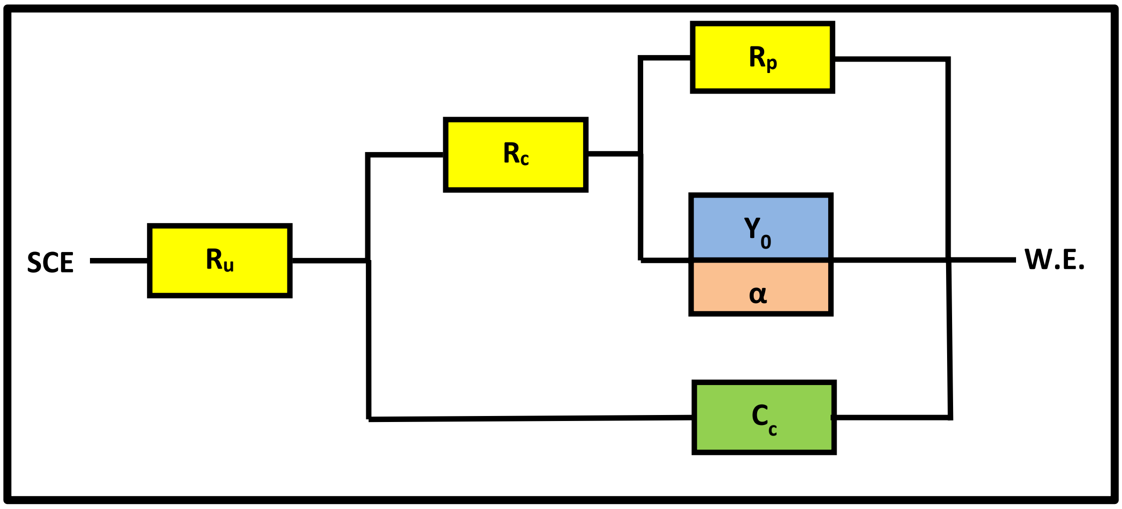

Fig. 4.4.3.14. Equivalent circuit for the steels used in this work (R_p= Polarization resistance)

Very little variation was found in the parameters R_u, R_c and C_c with respect to immersion time and chloride content. In the saturated $Ca(OH)_2$ solution either with or without chloride, mean R_u was about 17 Ω.cm^2, mean R_c was about 80 Ω.cm^2 and mean C_c was about 0.019 μF.cm^{-2} for all the samples (Fig. 4.4.3.13). R_u, R_c and C_c for mild steel and Fe-P alloys in $Ca(OH)_2$ solution with/without Cl^- were approximately 25 Ω.cm^2, 35 Ω.cm^2 and 11 μF.cm^{-2} respectively (Sahoo and Balasubramaniam, 2008). R_s, R_c and mean C_c for mild steel in saturated $Ca(OH)_2$ solution with/without Cl^- were found to be 62 Ω.cm^2 , 31 Ω.cm^2 and 0.02 μF.cm^{-2} respectively (Saremi, M., 2002). Saremi and co-workers attributed the adsorbed layer to OH^- ion on the surface of iron. The miniscule resistance of this adsorbed layer does not help in making the steel corrosion resistant.

The variables concerned with the passive film polarization resistance viz. R_p, CPE exponent α and constant phase element Y_0 showed variation (Tables 4.4.3.1, 4.4.3.2, and 4.4.3.3). The double layer-capacitance impedance can be expressed by a constant phase element (CPE) rather than an ideal capacitor in case the surface is rough and heterogeneous (Sahoo and Balasubramaniam, 2008)(Ye et al., 2013)(Cox and Wong, 1995)(Cai and Park, 1996)(Bardwell and McKubre, 1991). The impedance (Z_{CPE}) and capacitance (C_{CPE}) are defined by equations 4.4.3.3 and 4.4.3.4 (Sahoo and Balasubramaniam, 2008)(Ye et al., 2013)(Zhang et al., 2004).

$$Z_{CPE} = [Y_0(j\omega)^{\alpha}]^{-1} \tag{4.4.3.3}$$

$$C_{CPE} = \frac{Y_0 \omega_m^{\alpha-1}}{\sin(\alpha\pi/2)} \tag{4.4.3.4}$$

Y_0 represents a combination of properties related to electroactive species and the steel surface. It is proportional to the capacitance of pure capacitive electrodes (Sahoo and Balasubramaniam, 2008)(Ye et al., 2013). α is the CPE exponent. It is a phenomenological coefficient which indicates the degree of deviation in the capacitance from the ideal condition (Ye et al., 2013)(Chen et al., 2010)(Cruz et al., 2005). The frequency corresponding to maximum phase angle is ω_m (Ye et al., 2013). Y_0 is called CPE when α lies between 0.5 and 1 and is based on surface heterogeneity and roughness (Sahoo and Balasubramaniam, 2008). Y_0 is pure capacitance when α =1 and pure resistance when α =0 (Feng et al., 2011).

The polarization resistance of S1, S2 and S3 steels immersed in saturated $Ca(OH)_2$ solution with or without chloride increases with immersion time (Table 4.4.3.1). The same behaviour is noted for S4 steel immersed in saturated $Ca(OH)_2$ solution without or with 0.05 wt. % chloride. But the resistance of S4 steel falls when it is immersed in saturated $Ca(OH)_2$ solution with 0.1 wt. % chloride. The resistance of all the steels falls with an increase in chloride concentration.

Table 4.4.3.1: Polarization resistance (R_p) in Ω.cm^2 as a function of time in saturated $Ca(OH)_2$ solution with or without chloride obtained from EIS spectra modelling

Sample	**Cl$^-$**	**15 min**	**5 h**	**21 h**
S1	0	16400	40600	93100
	0.05	49400	52500	73200
	0.1	24500	35200	52500
S2	0	51800	76400	119000
	0.05	51100	152000	292000
	0.1	21100	33500	47800
S3	0	27900	131000	490000
	0.05	72000	239000	777000
	0.1	14600	22700	45500
S4	0	58500	110000	425000
	0.05	62500	235000	285000
	0.1	25300	34800	**32800**

Generally, the constant phase element of S1, S2 and S3 steels immersed in saturated $Ca(OH)_2$ solution with or without chloride and S4 steel without and with 0.05 wt. % chloride decreases with immersion time (Table 4.4.3.2). But, the CPE of S4 steel immersed in saturated $Ca(OH)_2$ solution with 0.1 wt. % chloride increases drastically with immersion time. Thus, S4 steel is unable to withstand the chloride concentration of 0.1 wt. %.

Table 4.4.3.2: Constant phase element (Y_0) in μS·s^a/cm^2 as a function of time in saturated $Ca(OH)_2$ solution with or without chloride obtained from EIS spectra modelling

Sample	**Cl$^-$**	**15 min**	**5 h**	**21 h**
S1	0	38.1	67.7	47.6
	0.05	42.4	43.3	45.0
	0.1	52.5	43.2	42.4
S2	0	77.4	64.5	63.5
	0.05	44.9	42.4	41.1
	0.1	43.1	46.9	52.6
S3	0	59.4	56.4	49.0
	0.05	45.1	43.9	39.5
	0.1	39.2	37.0	36.3
S4	0	43.1	68.2	49.0
	0.05	55.5	56.3	50.1
	0.1	57.8	59.9	**77.4**

Generally, the constant phase element exponent of S1, S2 and S3 steels immersed in saturated $Ca(OH)_2$ solution with or without chloride and S4 steel without and with 0.05 wt. % chloride approaches the value of 1 with immersion time, where CPE is pure capacitance. This implies that the protective film is thickening and improving. But, the CPE exponent of S4 steel immersed in saturated $Ca(OH)_2$ solution with 0.1 wt. % chloride moves away from 1 with immersion time signifying that CPE is moving away from pure capacitance (Table 4.4.3.3).

Table 4.4.3.3: CPE exponent (α) as a function of time in saturated $Ca(OH)_2$ solution with or without chloride obtained from EIS spectra modelling

Sample	**Cl^-**	**15 min**	**5 h**	**21 h**
S1	0	0.88	0.89	0.92
	0.05	0.86	0.89	0.90
	0.1	0.87	0.9	0.91
S2	0	0.78	0.83	0.84
	0.05	0.88	0.92	0.92
	0.1	0.90	0.90	0.88
S3	0	0.83	0.86	0.88
	0.05	0.86	0.90	0.91
	0.1	0.89	0.91	0.91
S4	0	0.91	0.88	0.89
	0.05	0.85	0.89	0.89
	0.1	0.89	0.89	**0.85**

R_p values generally escalated with immersion time for S1, S2 and S3 steels in all solutions and S4 steel in solutions containing less than 0.1 Cl^-. R_p values decreased with time for S4 steel in solutions containing 0.1 Cl^- (Fig. 4.4.3.15. a). R_p values of all the samples vary between 1.4×10^4 to 7.7×10^5 $\Omega.cm^2$. The R_p values obtained for 7 days immersion of Fe-P alloys and mild steel in $Ca(OH)_2$ solution with/without Cl^- varied between 1.5×10^4 and 7.3×10^5 (Sahoo and Balasubramaniam, 2008). The R_p values for plain carbon steel in $Ca(OH)_2$ solution without and with 0.3 Cl^- were between 1.5×10^5 to 1.7×10^5 $\Omega.cm^2$ (Saremi, M., 2002). Reported values for passive layer of steel in borate buffer alkaline solution are 10^4 to 10^6 $\Omega.cm^2$ (Abreu et al., 2004)(Hamadou et al., 2005).

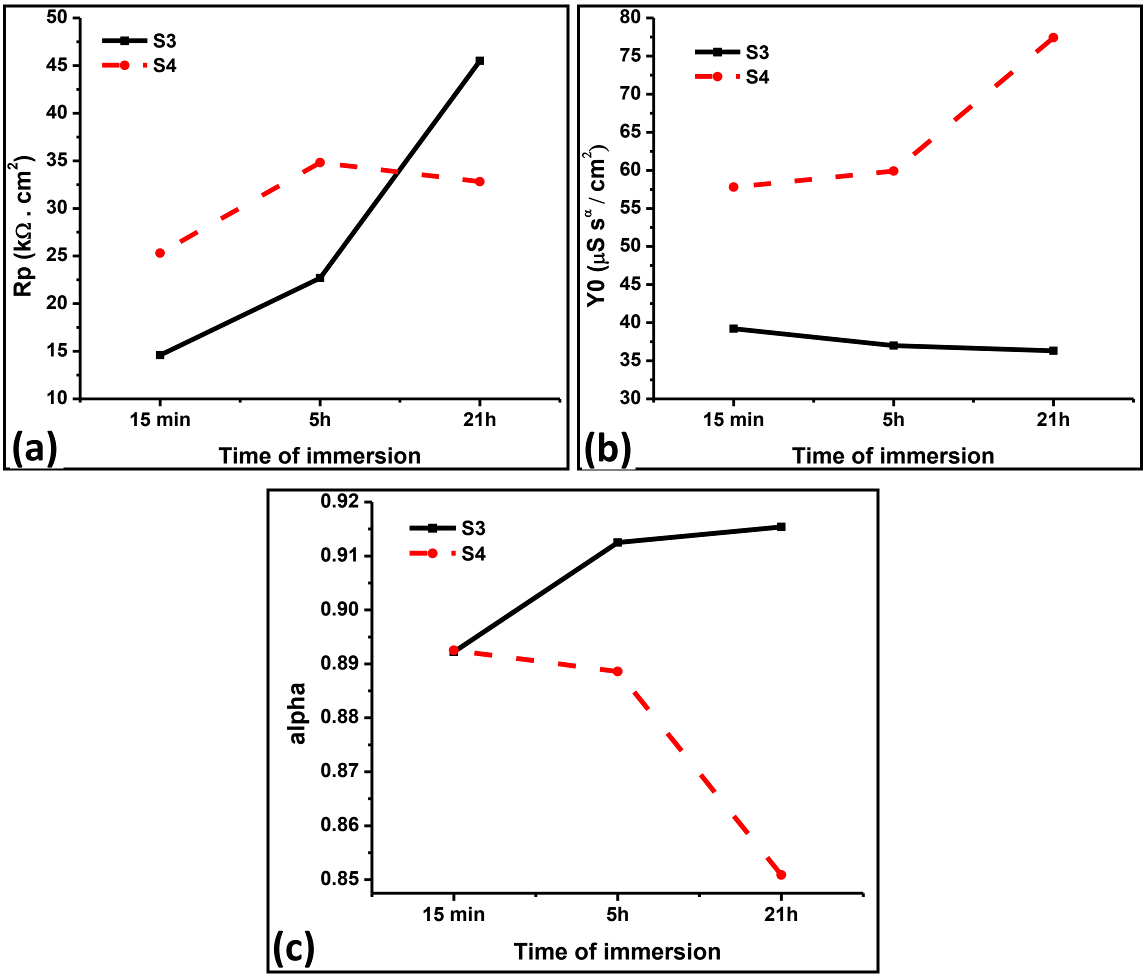

Fig. 4.4.3.15. The variation of (a) R_p, (b) Y_0, and (c) α of the passive film with respect to time of immersion of S3 and S4 steels in saturated $Ca(OH)_2$ solution containing 0.1 wt. % Cl^-

Y_0 values were between 36 to 77 μS s^α/cm^2 which agrees with the values of 14-75 μS s^α/cm^2 for phosphoric irons and mild steel (Sahoo and Balasubramaniam, 2008). An overall decrease in Y_0 was observed with immersion time due to the expansion of passive layer except in the case of S4 steel in $Ca(OH)_2$ solution containing 0.1 wt. % chloride (Fig. 4.4.3.15. b). This is caused due to breakdown of passive film and consequent increase in capacitance (Sahoo and Balasubramaniam, 2008)(Saremi, M., 2002). α values varied between 0.78 to 0.92 which confirms the heterogeneity of the steel surface (Cox and Wong, 1995) (Cai and Park, 1996). The increase in α of S3 steel indicates improvement in passive film and the decrease in α of S4 steel implies that the film became increasingly inhomogeneous and defective with time (Fig. 4.4.3.15. c) (Ye et al., 2013). Thus, the corrosion resistance of the high phosphorous steel is favourably compared with the mild steel sample.

4.4.3.1 Results of the EIS study on S3 steel heat treated at 900°C for 6 h

Out of the three high phosphorous steels, S3X3 offers the best impact toughness out of the lot. Therefore, it was subjected to OCP, LPR and EIS tests in saturated $Ca(OH)_2$ solution with 0.1 wt. % Cl^{-} for a total time period of 65 h to ascertain its corrosion behaviour. The readings were taken at 5, 15, 25, 40, and 65 h. The results are described in the following discussion.

In general, the OCP of the steel specimen increased with time and the i_{corr} decreased on increasing immersion time, showing that the passive film became more and more protective with increase in immersion time. The variation of the OCP and i_{corr} for S3 steel heat treated at 900°C for 6 h exposed to saturated $Ca(OH)_2$ solution containing 0.1 Cl^{-} is shown in Fig. 4.4.3.1.1.

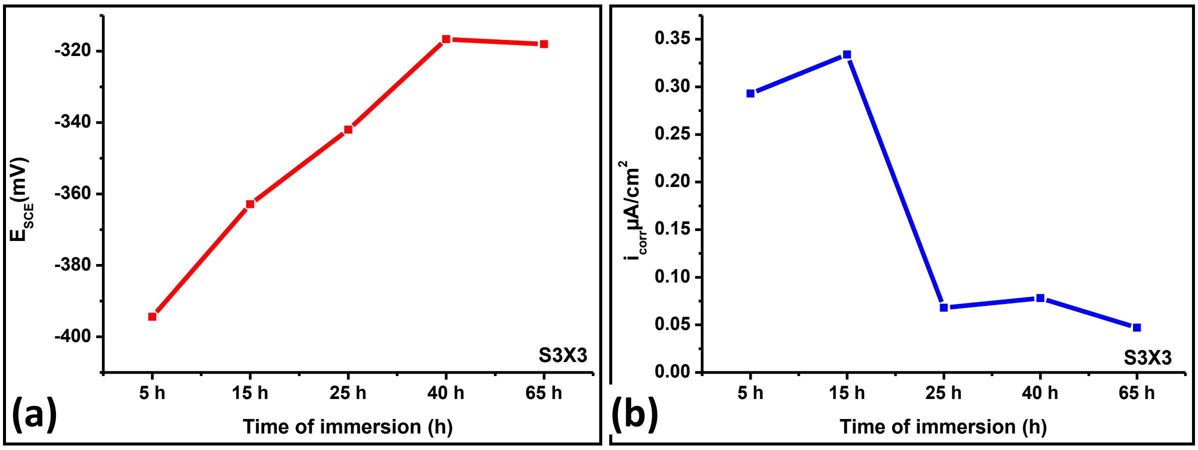

Fig. 4.4.3.1.1. Variation of (a) OCP and (b) i_{corr} for S3 steel heat treated at 900°C for 6 h exposed to saturated $Ca(OH)_2$ solution containing 0.1 wt. % Cl^{-}

The Nyquist plots show that as the time of immersion in the solution increases, both the capacitive part and the real impedance increases. This implies that the passive film became more protective with increasing time of immersion. Nyquist plots of S3 steel heat treated at 900°C for 6 h in saturated concrete pore solution with 0.1 Cl^{-} is shown in Fig. 4.4.3.1.2.

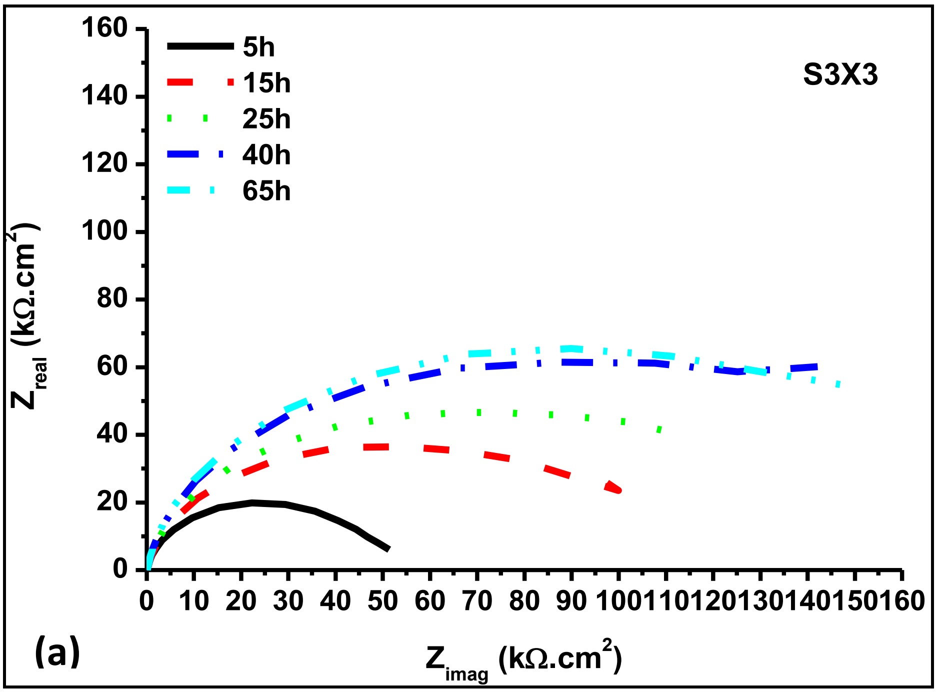

Fig. 4.4.3.1.2. (a) Nyquist plots of S3 steel heat treated at 900°C for 6 h after immersion in saturated $Ca(OH)_2$ solution with 0.1 wt. % Cl^-

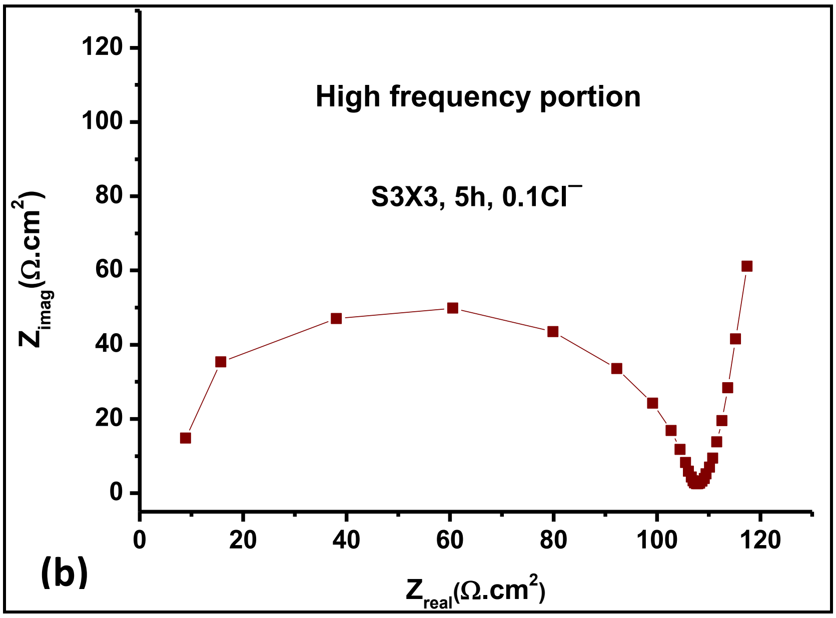

Fig. 4.4.3.1.2. (b) High frequency portion of Nyquist plots of S3 steel heat treated at 900°C for 6 h after immersion in saturated $Ca(OH)_2$ solution with 0.1 wt. % Cl^- for 5 h

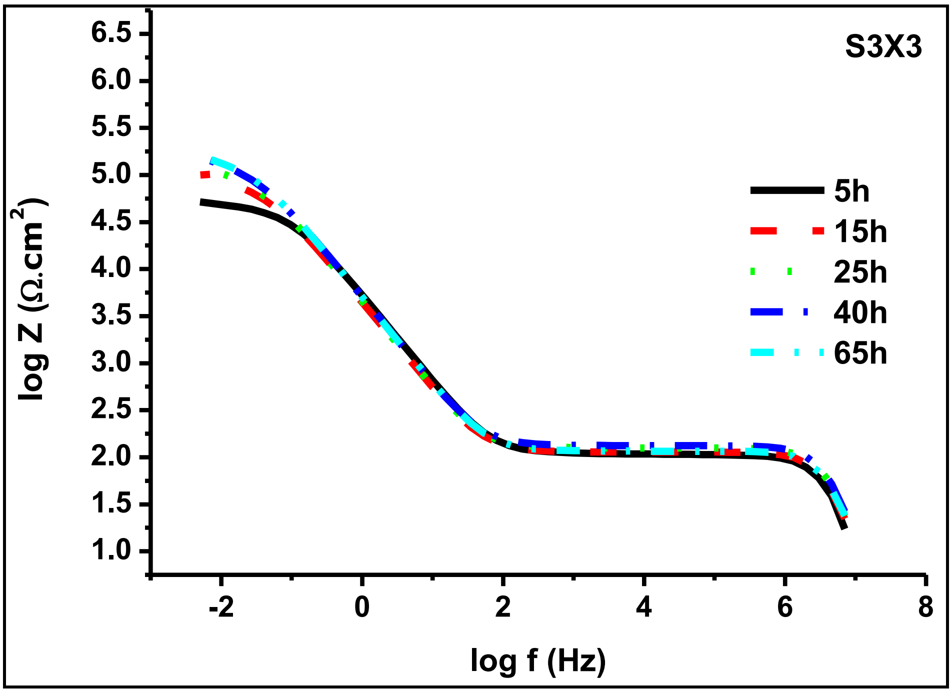

Fig. 4.4.3.1.3. Bode magnitude plots of S3 steel heat treated at 900°C for 6 h in saturated $Ca(OH)_2$ solution with 0.1 wt. % Cl^-

The Bode magnitude showed purely capacitive behaviour below about 100 Hz. The straight line portion with negative slope expanded with the increase in time of immersion. The impedance of the passive film is about $10^{5.2}$ $\Omega.cm^2$ which implies that the film is very close to acting as a pure capacitor and becomes more protective with increasing time of immersion. Bode magnitude plots of S3 steel heat treated at 900°C for 6 h in saturated concrete pore solution with 0.1 Cl^- are shown in Fig. 4.4.3.1.3.

The Bode phase plots show that phase angle decreases to zero at the highest and lowest frequencies of the first loop. The angle increases to 90° at intermediate frequencies indicating capacitive behaviour. The trough of the phase plot widened with increasing time of immersion implying the broadening of the passive film. The frequency, at which the rise in absolute value of phase angle starts, decreases with immersion time indicating an improvement in protective abilities. Bode phase plots of S3 steel heat treated at 900°C for 6 h in saturated concrete pore solution with 0.1 Cl^- are shown in Fig. 4.4.3.1.4.

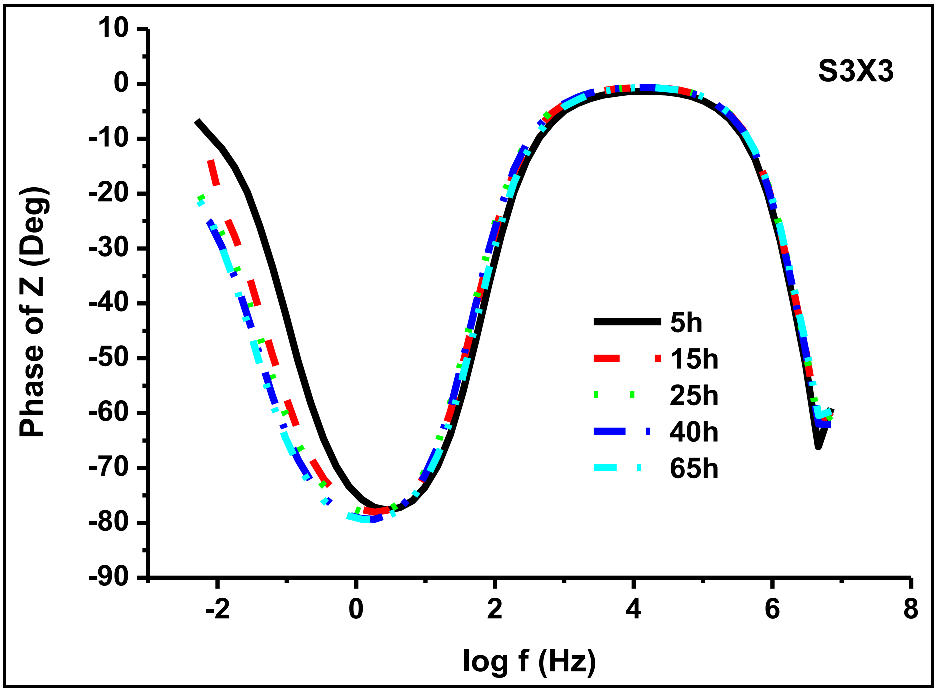

Fig. 4.4.3.1.4. Bode phase plots of S3 steel heat treated at 900°C for 6 h in saturated $Ca(OH)_2$ solution with 0.1 wt. % Cl^-

The Nyquist plots were analysed with Z_{fit} software and the values of R_p, Y_0 and α found out. The values of α varied between 0.907 and 0.914 which confirms the heterogeneity of the surface. The variation of R_p, Y_0, and α of the passive film with respect to time of immersion of S3 steel heat treated at 900°C for 6 h in saturated $Ca(OH)_2$ solution containing 0.1 wt. % Cl^- is shown in Fig. 4.4.3.1.5. R_p, increased and Y_0 decreased with time signifying thickening of passive film. The increase in α towards 1 indicates improvement in passive film, as CPE is pure capacitance at $\alpha = 1$.

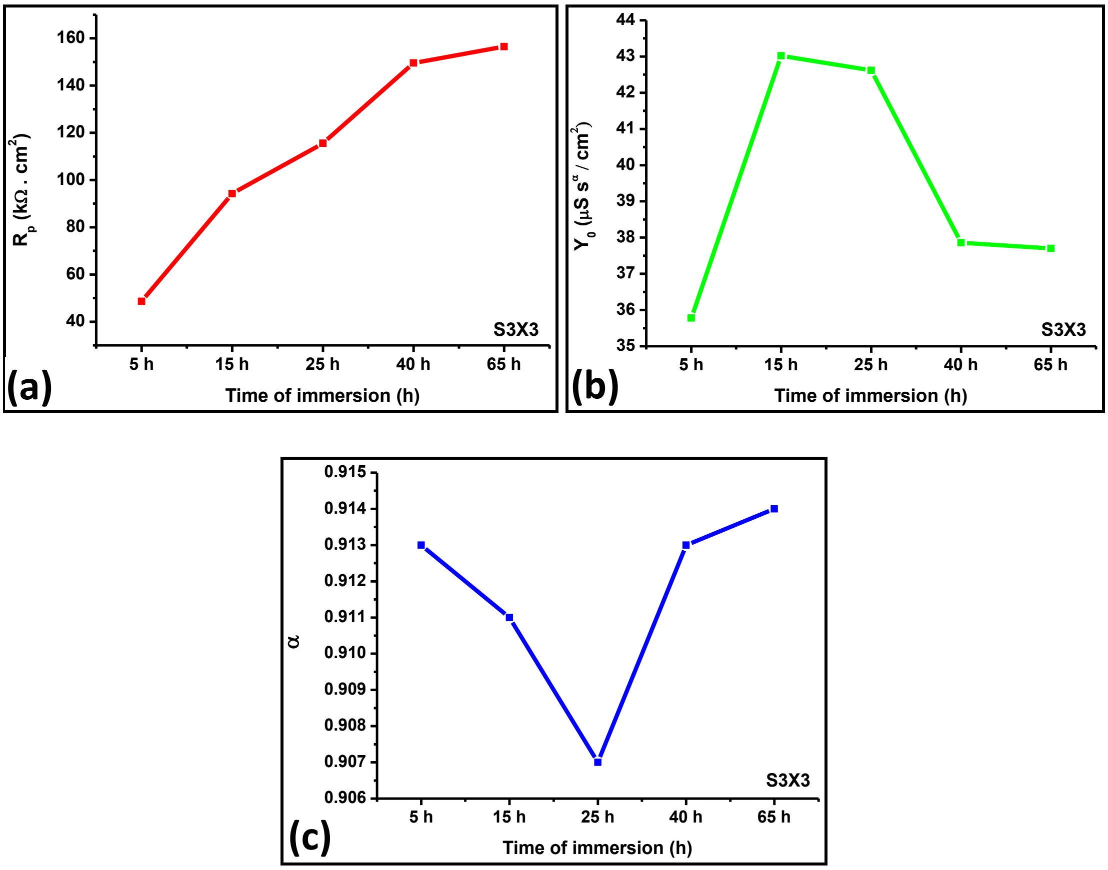

Fig. 4.4.3.1.5. The variation of (a) R_p, (b) Y_0, and (c) α of the passive film with respect to time of immersion of S3 steel heat treated at 900°C for 6 h in saturated $Ca(OH)_2$ solution containing 0.1 wt. % Cl^-

In conclusion, it may be said that S3X3 steel develops a protective passive layer in saturated $Ca(OH)_2$ solution with 0.1 wt. % Cl^- during immersion for 65 h. Hence, it offers a combination of good strength and toughness along with improved corrosion resistance. It can be considered for concrete reinforcement applications in case weldability concerns are suitably addressed.

4.4.3.2 Growth and destruction of the passive layer

Fig. 4.4.3.2.1 shows a schematic diagram of the growth or destruction of the passive layer with time. On immersion in the solution the passive film starts forming and iron ions enter the solution after passing through the micro-pores of the film. Initially the pores are large (Fig. 4.4.3.2.1.a) and later with the growth of the film (Fig. 4.4.3.2.1.b) they become smaller reducing the exposed area and hence the corrosion current. This increase in thickness of double layer causes an increase in R_p and decrease in capacitance (follows decrease in charge per unit area). In the case of S4 steel immersed in saturated $Ca(OH)_2$ solution containing 0.1 wt. % Cl^-, the chloride ions destabilize the passive film by migrating through the micro-pores and probably causing the following reaction on the metal surface exposed inside the pores (Sahoo and Balasubramaniam, 2008).

$$Fe^{2+} + 2H_2O + 2Cl^- \rightarrow Fe(OH)_2 + 2HCl \qquad (4.4.3.2)$$

The Cl^- formed may be used in auto-catalysis of the pitting process, thereby increasing the size of the micro-pores and leading to degradation of passive layer and accelerating the corrosion processes (Fig. 4.4.3.2.1.d).

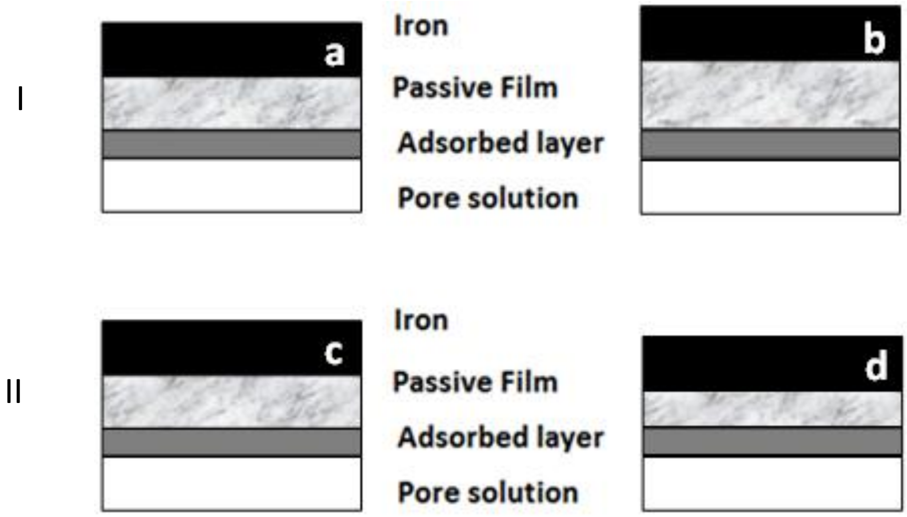

Fig. 4.4.3.2.1. Schematic displaying the formation, growth and degradation of the passive film on the steel surface in saturated $Ca(OH)_2$ solution. In the first condition the solution is without Cl^- or with Cl^- present in amounts lower than the threshold amount; (a) start of immersion; (b) passive layer grows with time. In the second condition the solution contains Cl^- ions more than the threshold amount; (c) same as (a); (d) de-passivated steel

4.4.4. SEM Analysis of the Pit

Surface morphology of S3 steel after potentiodynamic polarization testing in ($Ca(OH)_2$ + 0.14 wt. % Cl^-) solution was observed by SEM to examine its state of corrosion. The surface shows a few pits and sporadic deposits. EDS was employed to understand the mechanism of corrosion of S3 steel from chlorides by recording the elemental distribution at the pitted location (Fig. 4.4.4.). EDS reveals that Mn, S, Cl, Al, O and Si are present in the pit region. This suggests that adsorption of chloride ions followed by the initiation of pits could have been favoured by presence of MnS inclusions associated with oxides of aluminium (Jone, 1992). Literature suggests that chloride is adsorbed preferentially at the MnS inclusions associated with oxides of aluminium causing their dissolution accompanied with a local drop in pH leading to local autocatalysis (Williams et al., 1998). Once a pit nucleates it might grow depending on whether the local chloride concentration exceeds critical limits (Ye et al., 2013). Further, P, Cr and N are found well-distributed outside the pit and deficient in the pit region. It can be stated that they have a positive role in the protection of the pit free surface.

4.4.5 Beneficial Effect of Phosphorous Alloying

The OCP measured vs SCE for all the samples are above −0.5 V. Therefore, according to the Eh-pH diagram of phosphorous-water system, phosphorous in the S1, S2 and S3 steels will remain in equilibrium with PO_4^{3-} in saturated $Ca(OH)_2$ solution having pH 12.5, at and above −0.258 V vs SHE (Muylder and Pourbaix, 1966).

Anodic corrosion inhibitors employed for iron in concrete environments involve phosphates like $CaHPO_4$, Na_3PO_4 and Na_2HPO_4 (Génin et al., 2002)(Awad and Hoar, 1975). The phosphate ions help in the oxidation of ferrous to ferric form. The drift of the ferrous ions away from the metal surface is prevented (Misawa, 1973). The accumulated ferric ions form a protective γ-Fe_2O_3 film in $Ca(OH)_2$ solution (Génin et al., 2002). The film causes a reduction in the intensity of corrosion by reducing active sites. Phosphorous containing steels form a bipolar passive film. The inner iron oxide layer is anion selective while the outer $Fe_3(PO_4)_2$ enriched layer is cation selective and hence blocks the entry of Cl^- ions into the film improving resistance against nucleation and growth of pits (Virtanen et al., 1988)(Nishimura et al., 1984).The inner layer probably converts to gamma Fe_2O_3 leading to the thickening of the passive layer (Sahoo and Balasubramaniam, 2008). This also explains the absence of P in the pit region and presence of P outside the pit region on the surface of the steel in Fig. 4.4.4.

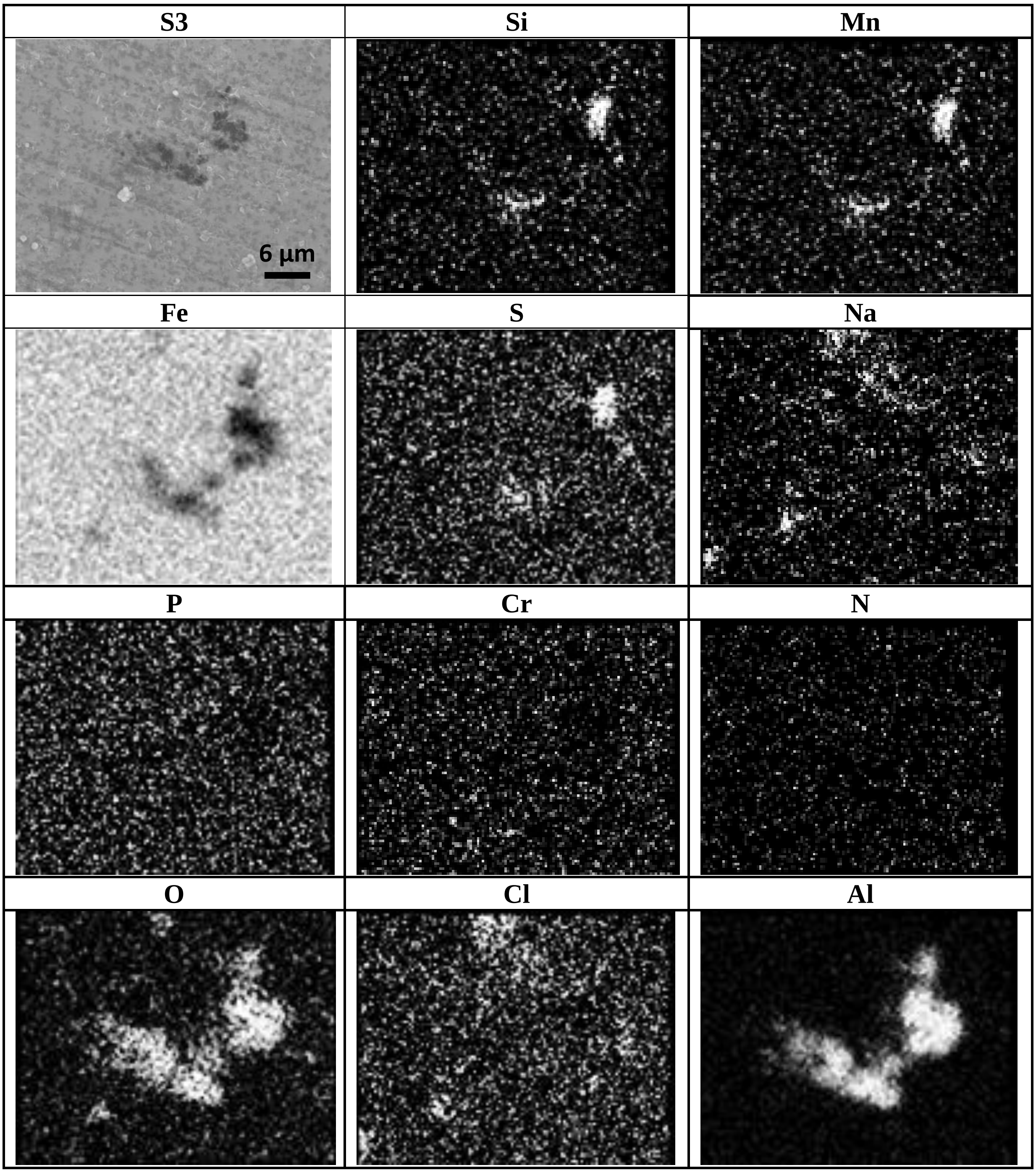

Fig. 4.4.4. The SEM-EDS study of surface morphology of S3 steel after potentiodynamic polarization testing in ($Ca(OH)_2$ + 0.14 wt. % Cl^-) solution, and elemental distribution at the corroded area

4.4.6 Immersion Test in 3.5 wt. % NaCl Solution

Cylindrical samples of S1, S2, S3 and S4 steels were suspended in 3.5 wt. % NaCl solution for a period of 3024 h. The rate of corrosion was found out using Eq. 2.2.3.1. The results are presented in Table 4.4.6.1.

Table 4.4.6.1: Rate of uniform corrosion obtained using immersion test

Specimen	S1	S2	S3	S4
Rate of corrosion (mpy)	4.52	8.5	7.88	6.95

S1 steel shows the best corrosion resistance to chloride ions. The results indicate that S1 steel is better than S4 steel in marine environment. The rate of corrosion of plain carbon steel in 3.5 wt. % NaCl solution was found by other researchers using Tafel extrapolation to be 7 mpy (Gadadhar and Balasubramaniam, 2008). On the basis of the results of the corrosion section, it can be said that the high phosphorous steels are comparable to carbon steel in resisting corrosion due to chloride ion contamination in saturated $Ca(OH)_2$ solution. Hence, they can be considered for concrete reinforcement applications after suitably addressing the weldability concerns. Now, the effect of thermo-mechanical parameters such as strain rate and deformation temperature on grain size shall be investigated.

4.5 GRAIN REFINEMENT

The mechanical properties, especially toughness of the S1, S2 and S3 steels which were designed and prepared in this work have been found to be comparable to those of rebars used in construction work. The corrosion resistance against chloride contamination in saturated $Ca(OH)_2$ solution has been found to be slightly better than plain carbon steel. Since fine grained steel is expected to display better toughness (Kim et al., 2003; Kimura et al., 2008; Sakai et al., 2014) the grain refinement in the high phosphorous steels is studied. The samples are prepared using hot compression. The minimum cooling rate after hot working was 80°Cs^{-1}. The barrelling coefficient B at the end of the tests was about 0.9 ± 0.03. The stress strain curves and microstructural evolution of all the three high phosphorous steel samples prepared using strain rates of 10, 1, 0.1 and 0.01s^{-1} and deformation temperatures of 800-950°C and 1050°C are discussed and the grain sizes calculated. The results are presented in the following discussion.

4.5.1 True Stress, True Strain Curves

4.5.1.1. True stress, true strain curves of S1 steel

Fig. 4.5.1.1 shows the stress strain curves of S1 steel obtained under various deformation temperatures and strain rates. The flow curve for 1050°C shows dynamic recrystallization (DRX) for the strain rates of 1 and 0.1s^{-1}. Almost identical results were reported by Kim *et al.* (Kim et al., 2002). DRX curve showing two peaks is observed at 1050°C and 0.01s^{-1}. This implies that the recrystallized grains are strain hardened before being recrystallized again. The curve for 1050°C and 10s^{-1} exhibits dynamic recovery (DRV) for the larger part with slight evidence of DRX at the end. When the deformation temperature is decreased to 950°C the flow curve indicates work hardening at 10s^{-1}, DRV for the major part and slight DRX at the end for 1s^{-1}, DRX for 0.1s^{-1}, and 0.01s^{-1}. On decreasing the temperature further to 900°C the flow curve shows work hardening ending with DRX at 10s^{-1}, and 1s^{-1}, and DRX at 0.1s^{-1}, and 0.01s^{-1}. At 850°C the flow curves at 10s^{-1}, do not show work hardening beyond a strain of about 0.35, and the flow stress remains more or less constant. This type of non-work hardening behaviour is attributed to DRV. Again, at 850°C the flow curves exhibit DRX at 1s^{-1}, 0.1s^{-1}, and 0.01s^{-1}. At 800°C the flow curves exhibit DRV at 10, and 1 s^{-1}, beyond a strain of 0.35 and DRX at 0.1, and 0.01s^{-1}. The maximum stress is lowest for 1050°C for all the strain rates due to DRX. The maximum stress increases for 900-950°C due to work hardening and decreases at 800-850°C due to the occurrence of DRV.

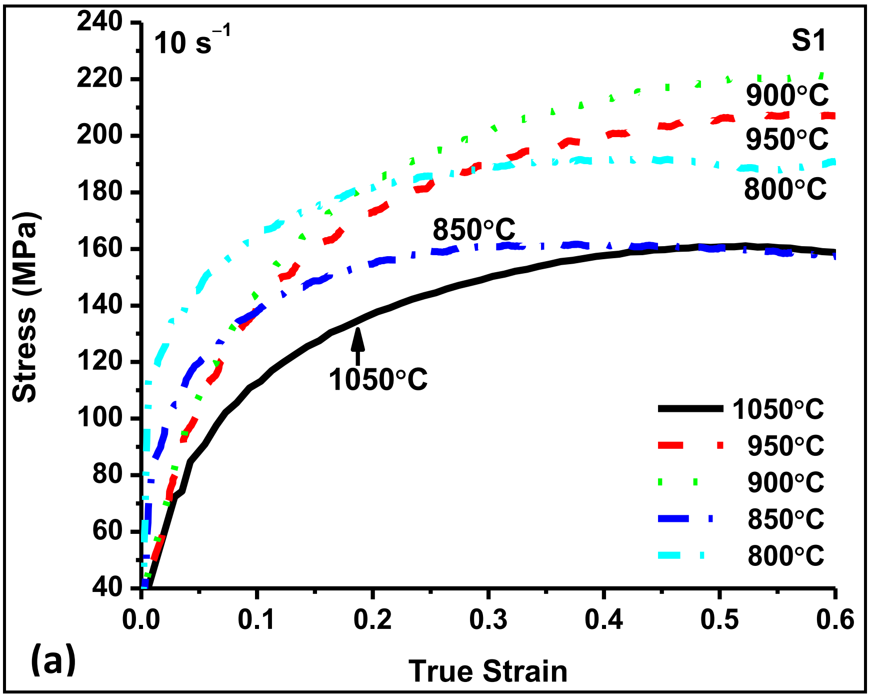

Fig. 4.5.1.1. (a) True stress, true strain curves of S1 steel obtained under various deformation temperatures and strain rate of 10 s^{-1}

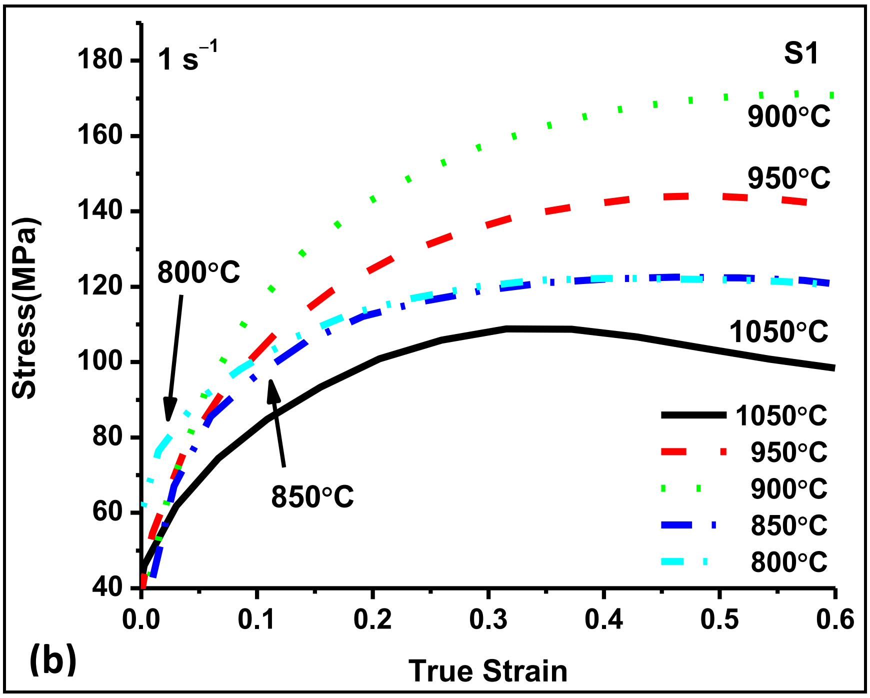

Fig. 4.5.1.1. (b) True stress, true strain curves of S1 steel obtained under various deformation temperatures and strain rate of 1 s^{-1}

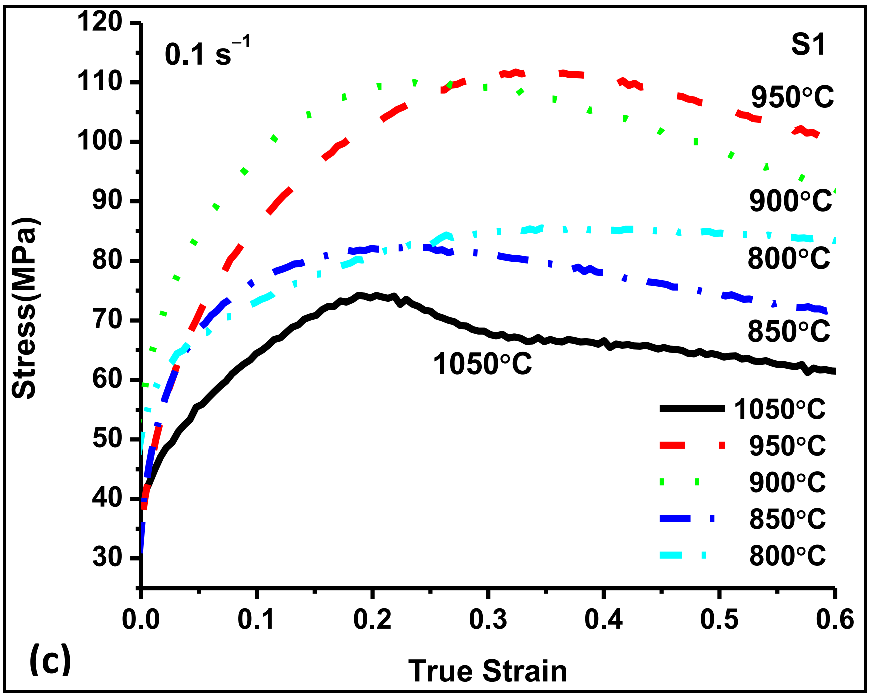

Fig. 4.5.1.1. (c) True stress, true strain curves of S1 steel obtained under various deformation temperatures and strain rate of 0.1 s^{-1}

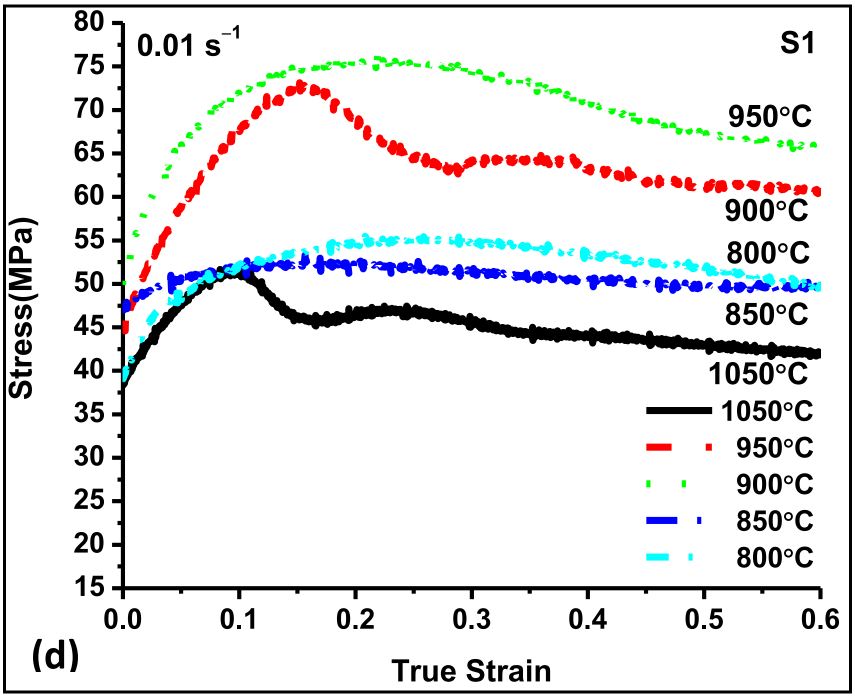

Fig. 4.5.1.1. (d) True stress, true strain curves of S1 steel obtained under various deformation temperatures and strain rate of 0.01 s^{-1}

4.5.1.2. True stress, true strain curves of S2 steel

Fig. 4.5.1.2 shows the stress strain curves of S2 obtained under various deformation temperatures and strain rates. The flow behaviour of S2 steel is comparable to that of S1 steel. The main differences between the curves of S1 steel and S2 steel are discussed in the section 4.5.1.3.

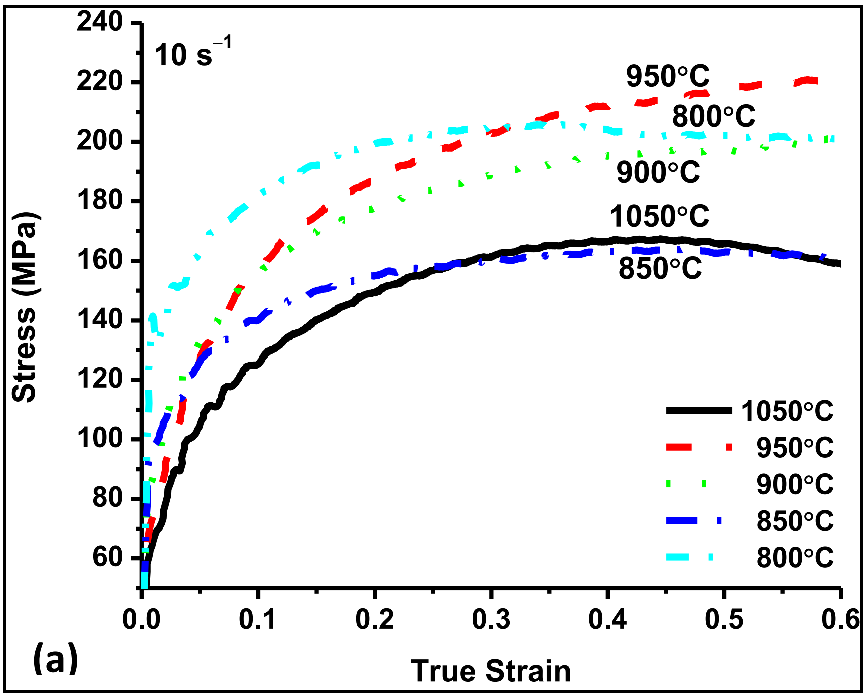

Fig. 4.5.1.2. (a) True stress, true strain curves of S2 steel obtained under various deformation temperatures and strain rate of 10 s^{-1}

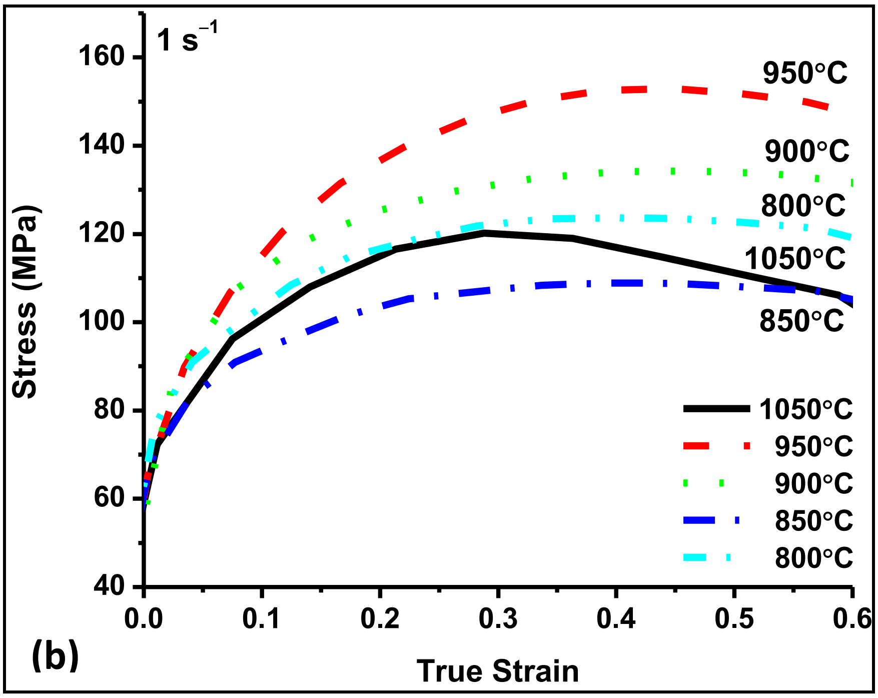

Fig. 4.5.1.2. (b) True stress, true strain curves of S2 steel obtained under various deformation temperatures and strain rate of 1 s^{-1}

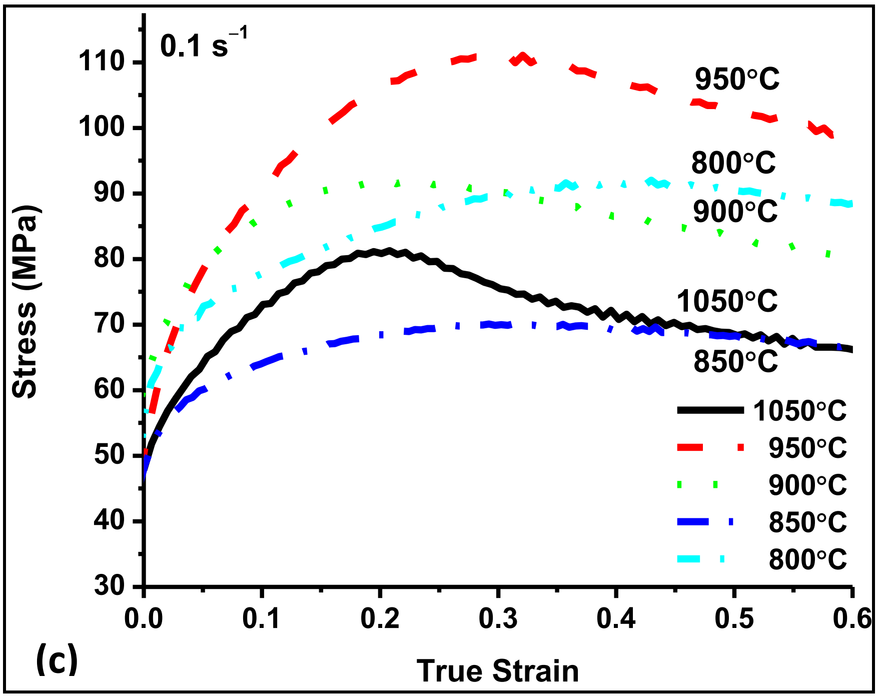

Fig. 4.5.1.2. (c) True stress, true strain curves of S2 steel obtained under various deformation temperatures and strain rate of 0.1 s^{-1}

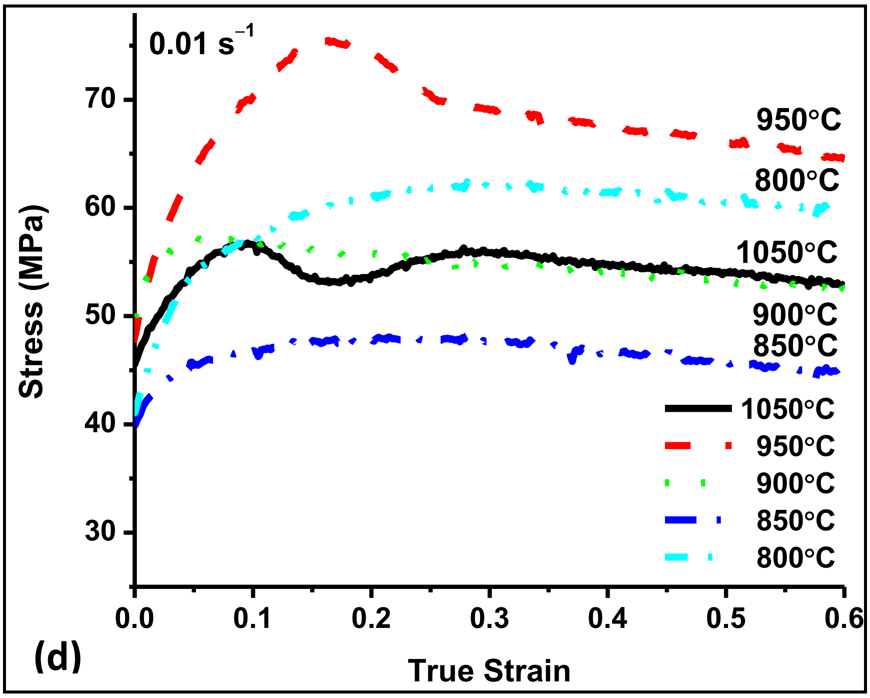

Fig. 4.5.1.2. (d) True stress, true strain curves of S2 steel obtained under various deformation temperatures and strain rate of 0.01 s^{-1}

4.5.1.3. Effect of addition of silicon on flow behaviour of S1 steel

The elements Cr, Mn, Co, Si, C and N tend to lower the stacking fault energy of austenite (Bhadeshia and Honeycombe R W K, 2006). This means that the cross-slip and climb of dislocations will be more difficult. Further, the diffusion of a substitutional element like silicon is difficult as compared to carbon. This leads to an increase in the flow stress of the higher alloying steel. This implies that the addition of silicon to carbon steel should increase the flow stress of the resulting material (compared to the carbon steel) as has been confirmed by Serajzadeh, and Taheri (S. Serajzadeh and Taheri, 2002; S. U. Serajzadeh and Taheri, 2002). At 1050°C and strain rate of 10, 1, 0.1 and 0.01s^{-1} the flow stresses of S2 steel display a higher peak stress than S1 steel. The addition of 0.13 wt. % silicon to S1 steel retards DRX at 1050°C and 0.1 and 0.01s^{-1}. At 950°C and strain rate of 10, 1, and 0.01s^{-1} S2 steel shows a higher peak stress as compared to S1 steel. DRX of S2 steel occurs at lower strain at 1 and 0.1s^{-1} when compared with S1 steel. At 900°C and strain rate of 10, 1, 0.1 and 0.01s^{-1} S2 steel shows lower peak stresses than S1 steel. DRX of S1 steel occurs at lower strain at 0.01s^{-1} when compared with S2 steel. At 850°C and strain rate of 1, 0.1 and 0.01s^{-1} the flow stresses of S1 steel display a higher peak stress than S2 steel. DRX of S1 steel occurs at lower strain at 1, 0.1, and 0.01s^{-1} when compared with S2 steel. At 800°C and strain rate of 10, 1, 0.1 and 0.01s^{-1} the flow stresses of S2 steel display a higher peak stress than S1 steel. DRX of S1 steel occurs at lower strain at 0.1 and 0.01s^{-1} when compared with S2 steel. Generally, S1 steel shows higher peak flow stresses than S2 steel at 850 and 900°C and all the strain rates and lower values as compared to S2 steel at other temperatures and all the strain rates.

When compared with the flow curves of S1 steel the addition of alloying elements could have retarded DRX and increased work hardening behaviour of S2 steel at the strain rates of 0.01s^{-1} and 800°C and 950°C (Fig. 4.5.1.3 a and d). Similar behaviour has been observed by other researchers too (Kim et al., 2005). At the strain rates 10, 1, 0.1 and 0.01s^{-1} and intercritical temperatures of 900°C and 1, 0.1 and 0.01s^{-1} and 850°C; the addition of 0.13 wt. % silicon to S1 steel caused a softening effect, lowering the peak stress (Fig. 4.5.1.3 b and c). Thus, the trend observed at higher temperatures is not followed at intercritical temperatures. Ferrite is softer at higher temperatures than austenite (Gove and Charles, 1974). The proportion of ferrite in the microstructure of S2 steel at the intercritical temperatures of 850°C and 900°C could be higher than S1 steel since silicon which is a ferrite stabilizer (Durand-Charre, 2004) is higher in S2 steel. This could be the cause of the softening behaviour.

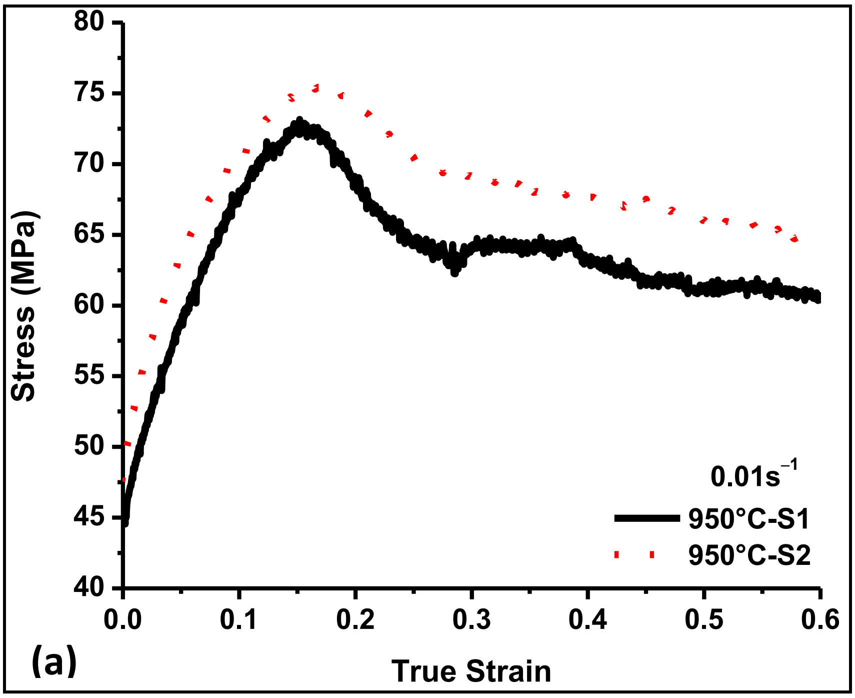

Fig. 4.5.1.3. (a) The effect of alloy chemistry on the true stress, true strain curves of S1 and S2 steels at 950°C and 0.01s^{-1}

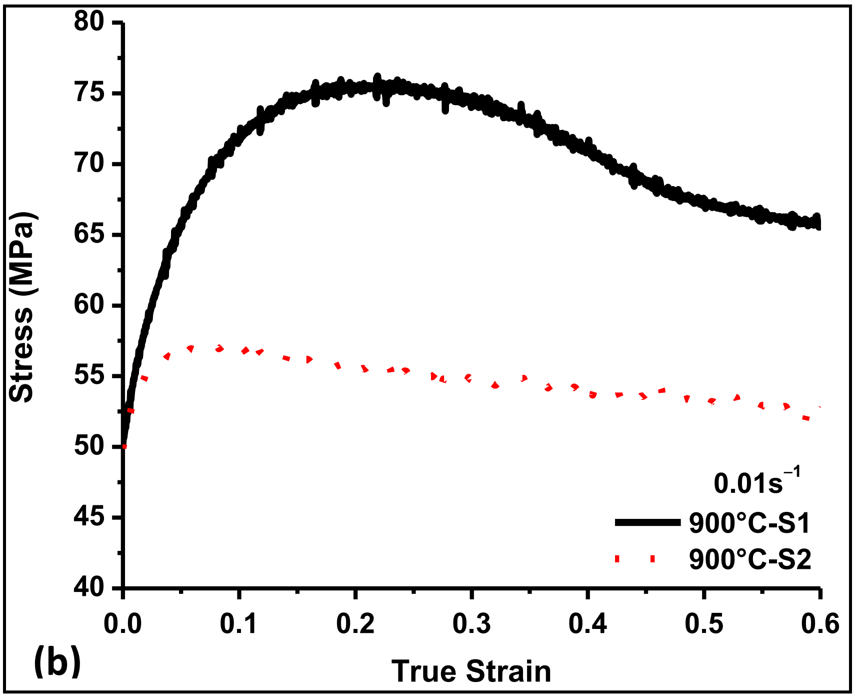

Fig. 4.5.1.3. (b) The effect of alloy chemistry on the true stress, true strain curves of S1 and S2 steels at 900°C and 0.01s^{-1}

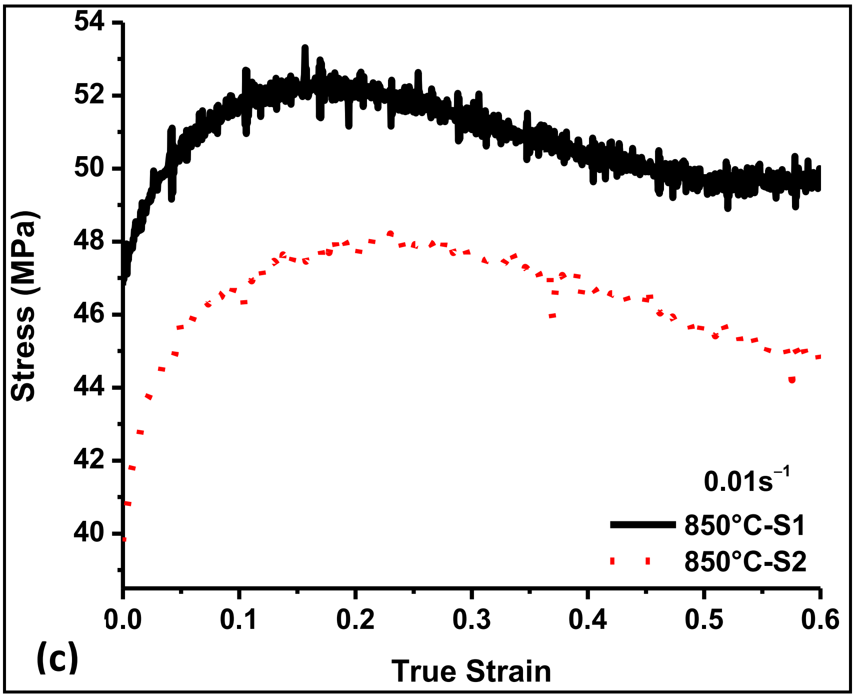

Fig. 4.5.1.3. (c) The effect of alloy chemistry on the true stress, true strain curves of S1 and S2 steels at 850°C and $0.01s^{-1}$

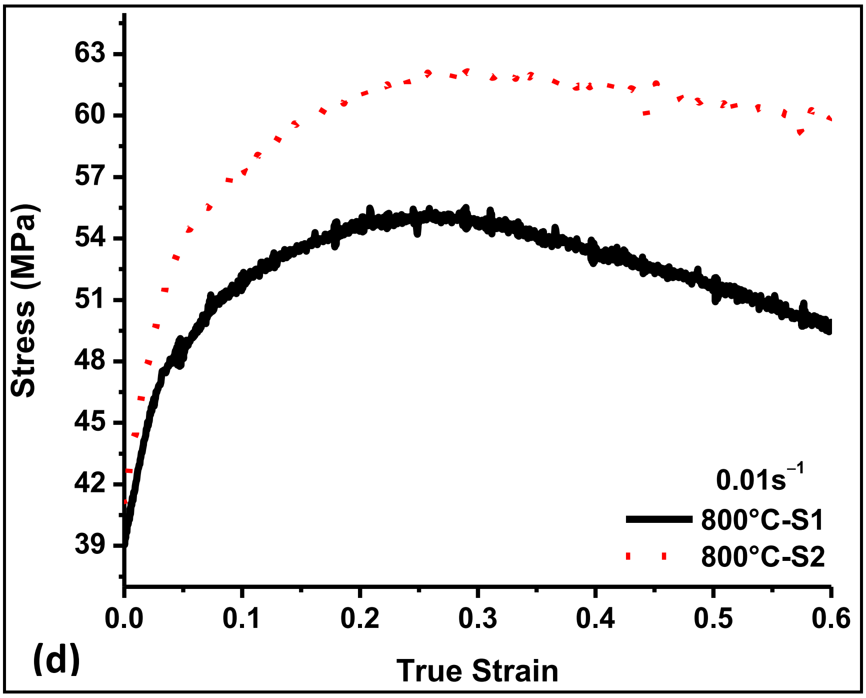

Fig. 4.5.1.3. (d) The effect of alloy chemistry on the true stress, true strain curves of S1 and S2 steels at 800°C and $0.01s^{-1}$

4.5.1.4. True stress, true strain curves of S3 steel

Fig. 4.5.1.4 shows the stress strain curves of S3 steel obtained under various deformation temperatures and strain rates. The flow behaviour of S3 steel is comparable to that of S1 and S2 steel. The main differences between the curves of S1 and S2 steels and S3 steel are discussed in the section 4.5.1.5.

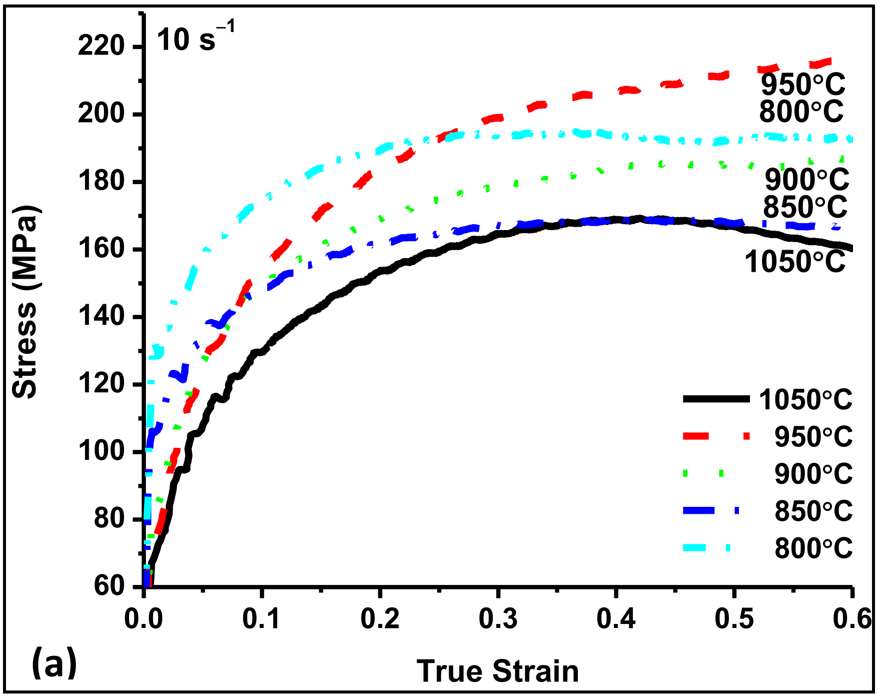

Fig. 4.5.1.4. (a) True stress, true strain curves of S3 steel obtained under various deformation temperatures and strain rates of 10 s^{-1}

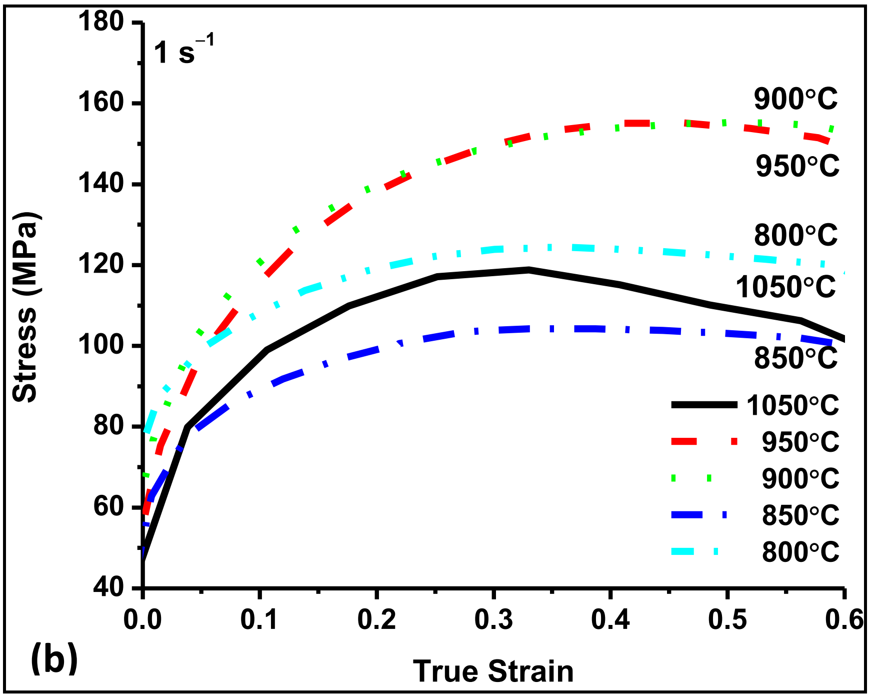

Fig. 4.5.1.4. (b) True stress, true strain curves of S3 steel obtained under various deformation temperatures and strain rates of 1 s^{-1}

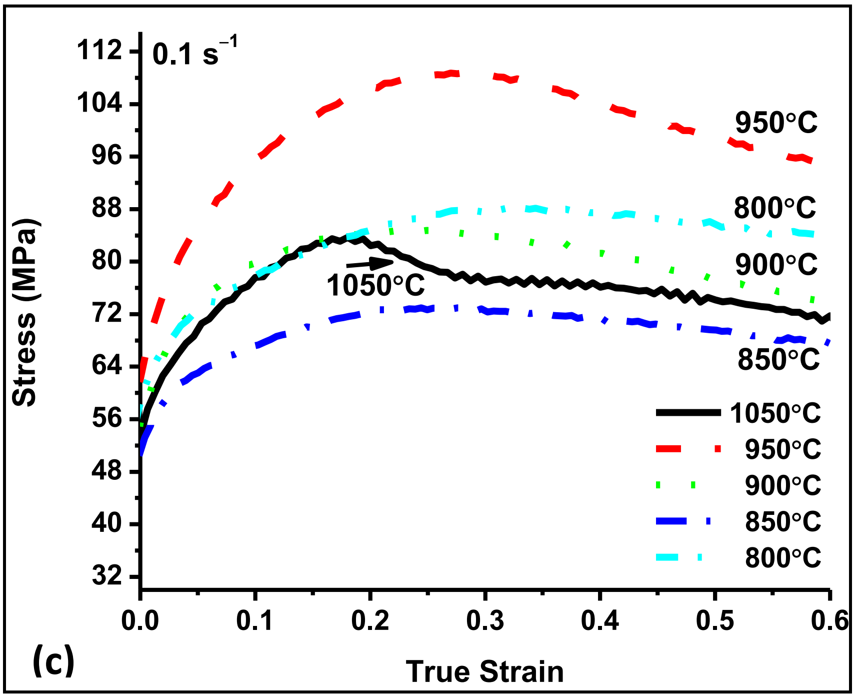

Fig. 4.5.1.4. (c) True stress, true strain curves of S3 steel obtained under various deformation temperatures and strain rates of 0.1 s^{-1}

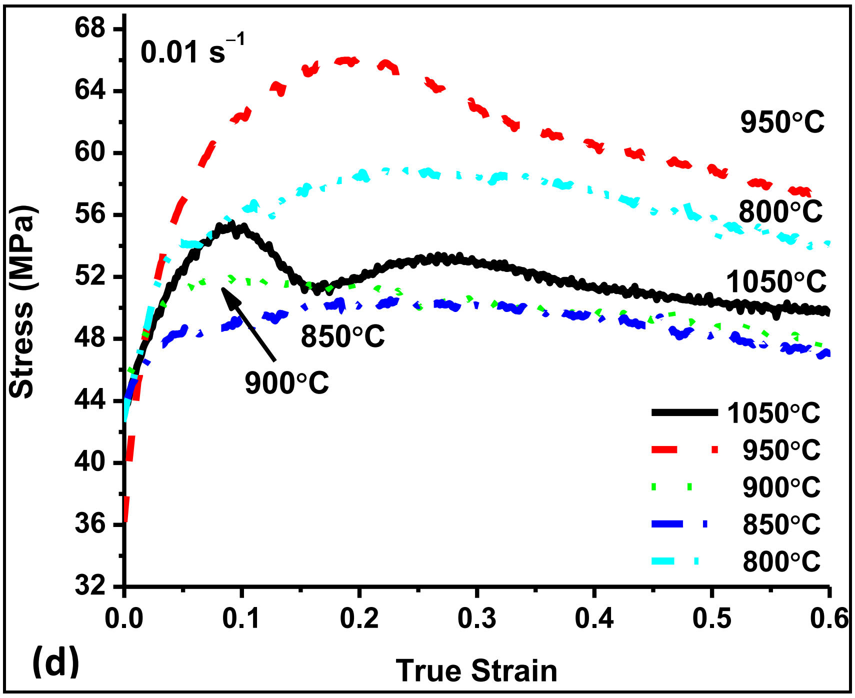

Fig. 4.5.1.4. (d) True stress, true strain curves of S3 steel obtained under various deformation temperatures and strain rates of 0.01 s^{-1}

4.5.1.5. Effect of addition of Si, N, and Mn on flow behaviour of S2 steel

The elements Cr, Mn, Co, Si, C and N tend to lower the stacking fault energy of austenite (Bhadeshia and Honeycombe R W K, 2006). This means that the cross-slip and climb of dislocations will be more difficult. Further, the diffusion of a substitutional element like silicon is more difficult as compared to carbon. This leads to an increase in the flow stress of the higher alloying steel. This implies that the addition of silicon to carbon steel should increase the flow stress of the resulting material (compared to the carbon steel) as has been confirmed by Serajzadeh, and Taheri (S. Serajzadeh and Taheri, 2002; S. U. Serajzadeh and Taheri, 2002). Higher amounts of alloying elements of Si, N and Mn in S3 steel cause higher peak stress in S3 steel at the strain rates of 10, 1, 0.1 and 0.01 s^{-1} at 800°C and 1050°C, at 10, and 1 s^{-1} and 950°C and at 10 s^{-1} and 850°C as compared to the S1 steel. At 1050°C and strain rate of 10 and 0.1s^{-1}, at 750, 800, 900, and 950°C and 1s^{-1}, and at 850°C and 10, 0.1 and 0.01 s^{-1}, S3 steel shows a higher peak stress when compared with S2 steel. At 1050°C and strain rate of 1 and 0.01s^{-1} the flow stresses of S2 steel reach a higher peak stress earlier than S3 steel. At 1050°C and strain rate of 10 and 0.1s^{-1} S3 steel reaches the peak stress earlier than S2 steel. At 950°C, 900°C and 800°C and strain rates of 10, 0.1, and 0.01s^{-1} the flow stresses of S2 steel reach a peak stress earlier than S3 steel whereas S3 steel reaches a peak at 1s^{-1} before S2 steel. At 850°C and strain rates of 10, 0.1, and 0.01s^{-1} the flow stresses of S2 steel reach a peak stress earlier than S3 steel whereas S3 steel reaches the peak stress at 1s^{-1} before S2 steel.

On addition of alloying elements to S2 steel (*i.e.*, S3 steel) the lowering of peak stresses was observed at 900°C and 10, 0.1 and 0.01s^{-1} and 850°C and 1s^{-1} for S3 steel (Fig. 4.5.1.5 a and c). S3 steel shows higher flow stresses at 850°C and 10, 0.1 and 0.01 s^{-1} as compared to S2 steel. This could be due to the higher proportion of austenite in the microstructure of S3 steel at those temperatures and strain rates, where it shows higher peak stresses as compared to S2 steel such as 850°C and 0.1 and 0.01s^{-1} (Fig. 4.5.1.5 b and d). As compared to S2 steel, S3 steel contains higher amount of austenite stabilizing element of nitrogen (Durand-Charre, 2004). Again, the hardness of ferrite is lower than that of austenite at higher temperatures (Gove and Charles, 1974).

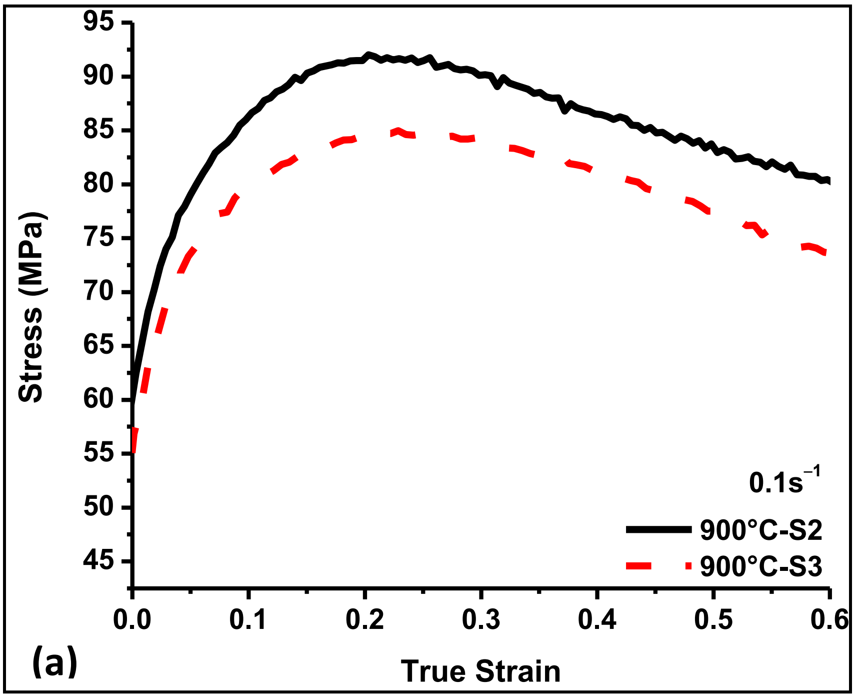

Fig. 4.5.1.5. (a) The effect of alloy chemistry on the true stress, true strain curves of S2 and S3 steels at 900°C and 0.1s^{-1}

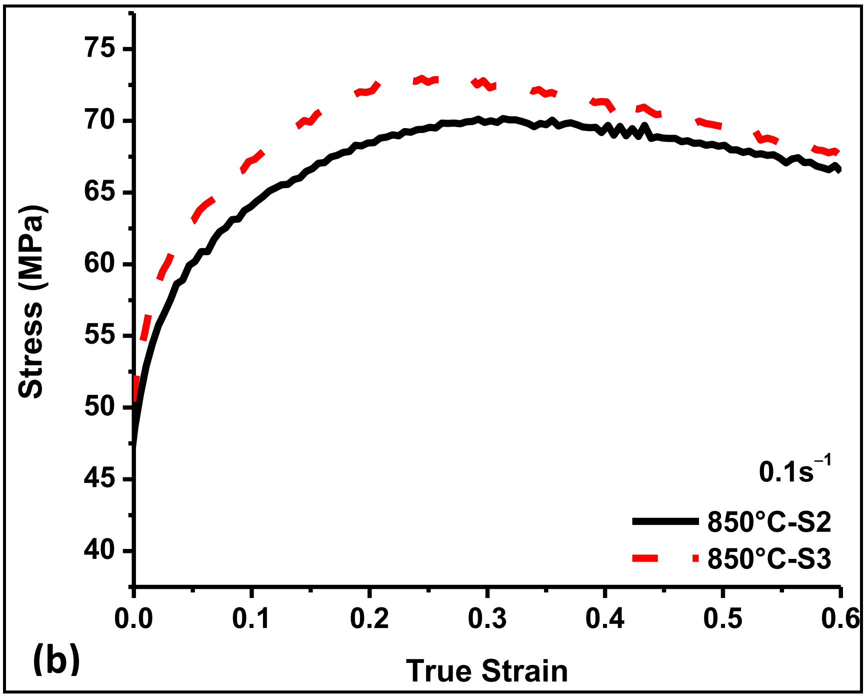

Fig. 4.5.1.5. (b) The effect of alloy chemistry on the true stress, true strain curves of S2 and S3 steels at 850°C and $0.1s^{-1}$

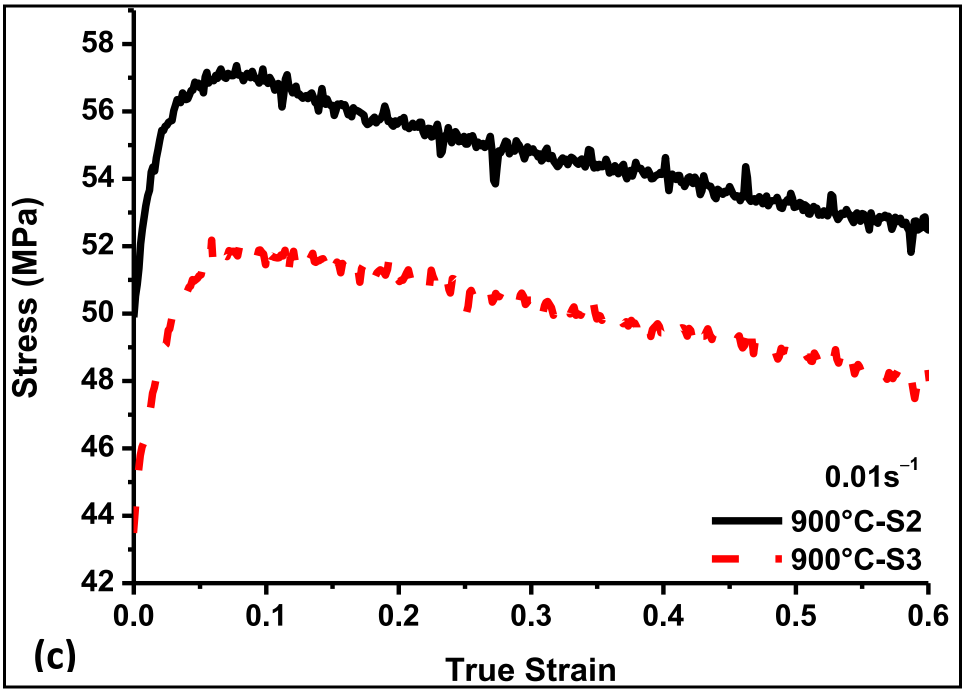

Fig. 4.5.1.5. (c) The effect of alloy chemistry on the true stress, true strain curves of S2 and S3 steels at 900°C and $0.01s^{-1}$

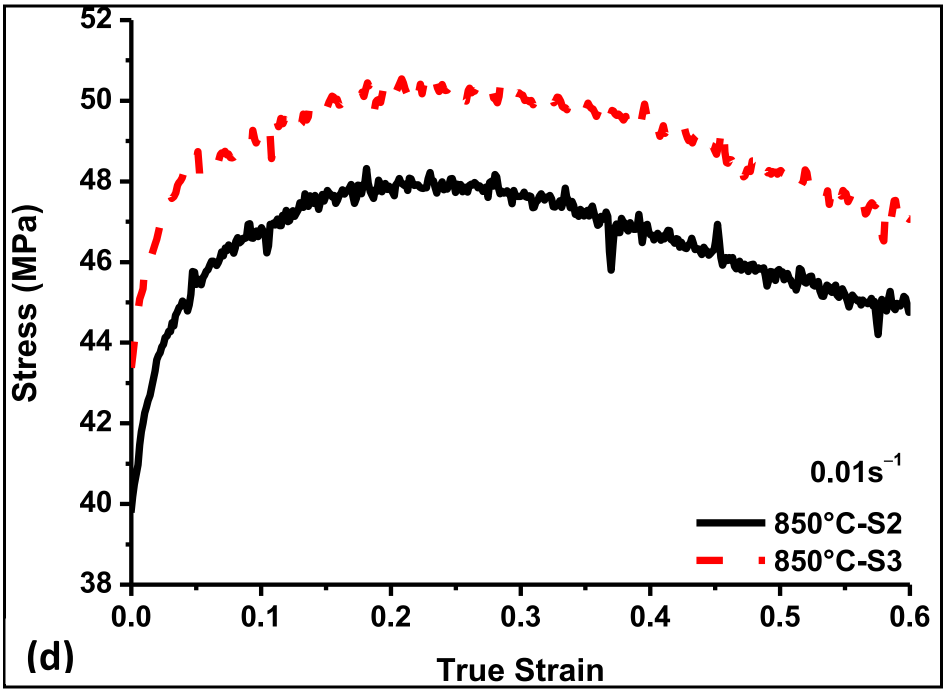

Fig. 4.5.1.5. (d) The effect of alloy chemistry on the true stress, true strain curves of S2 and S3 steels at 850°C and $0.01s^{-1}$

4.5.2 Microstructural Evolution

Fig. 4.5.2.1 represents the evolution of the microstructure and ferrite grain refinement at different deformation temperatures and strain rates of S1 steel. The cylindrical disk of the compressed specimen was sliced across the circular face along the diameter. The section contained the axis of compression. The slice revealed two somewhat rectangular faces with rounded corners. The central portion of one of these faces was studied using optical microscopy to study the microstructures. At 1050°C, 0.1 and 0.01 s^{-1} the microstructure is a mix of polygonal and acicular ferrite. Acicular ferrite is characterized by coarse non-equiaxed, needle shaped ferrite grains having various sizes distributed in a chaotic manner with random orientations. The microstructure obtained at 1050°C and 1 s^{-1} shows thicker needles and polygonal ferrite. Fig. 4.5.1.1 shows that the austenite has experienced DRX in these conditions. Later, grain growth appears to have taken place. The microstructure of ferrite at 1050°C and 10 s^{-1} shows large polygonal grains while Fig. 4.5.1.1 shows that the material has experienced DRX.

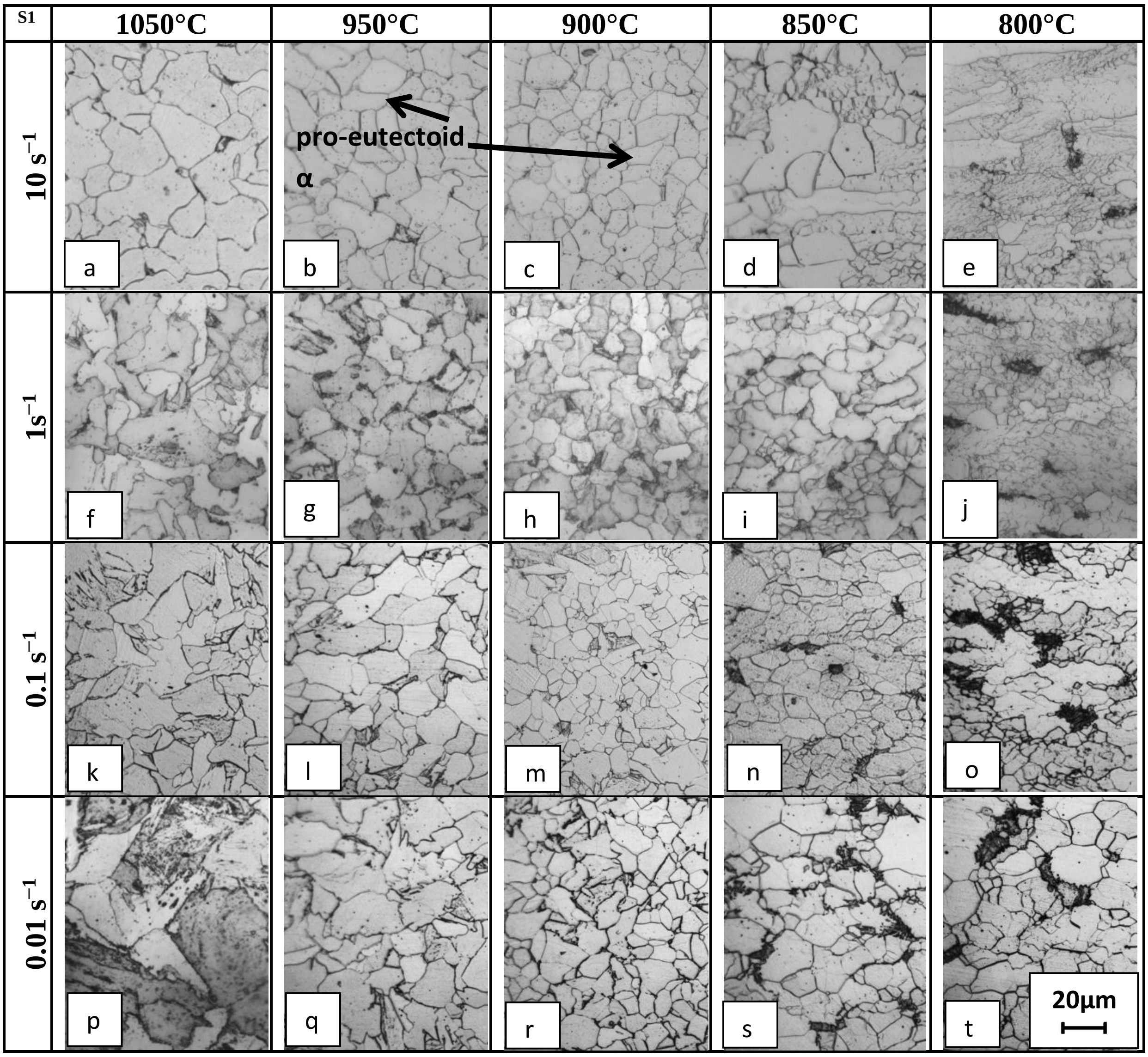

Fig. 4.5.2.1. Evolution of the microstructure and ferrite grain refinement at different deformation temperatures and strain rates of S1 steel

At 950°C, a small amount of pro-eutectoid ferrite is expected at high strain rates. The microstructure at 950°C and 10 s^{-1} and 1 s^{-1} shows equiaxed ferrite. The corresponding stress-strain curve shows work hardening. This implies that the ferrite is formed by transformation of work hardened or deformed austenite. The size of these grains is smaller than those obtained at 1050°C. Some coarse ferrite grains suggest that some grain growth should have occurred although nucleation rates are high at such high temperatures (Eghbali and Abdollah-zadeh, 2005a). Fig. 4.5.1.1 shows that the curves indicate DRX for 950°C and 0.1, and 0.01 s^{-1}. The microstructures for these low strain rate conditions show equiaxed ferrite.

At 900°C finer ferrite grains are obtained as compared to those achieved at 950°C due to the larger amount of undercooling with respect to Ar_3. A miniscule amount of deformed and elongated pro-eutectoid ferrite grains is also observed. The flow curves (Fig. 4.5.1.1) at 900°C show various combinations of hardening, recovery and recrystallization as the strain rate decreases. This implies that the ferrite grains are transformed from deformed and recrystallized austenite grains at 10 and 1 s^{-1}. The microstructures obtained at 0.1 and 0.01 s^{-1} are transformed from recrystallized austenite grains and they have experienced grain growth since the strain rate was low (Eghbali and Abdollah-zadeh, 2005b). The sizes of the grains obtained are smaller than those obtained at higher temperatures due to the larger amount of undercooling and hence a higher nucleation rate (Huang and Froyen, 2002).

At 850°C the microstructures observed are equiaxed ferrite and deformed pro-eutectoid ferrite. The lower maximum stress values as compared to 900°C points towards softening due to the larger proportion of ferrite in the microstructure. Ferrite is softer than austenite at higher temperatures (Gove and Charles, 1974). The flow curves at 10 s^{-1} shows a constant flow stress after a strain of 0.35 due to DRV. The flow curves (Fig. 4.5.1.1) at 1, 0.1 and 0.01 s^{-1} shows dynamic recrystallization. Flow curves at 0.01s^{-1} shows a constant flow stress after a strain of about 0.52 and the microstructure shows equiaxed ferrite with some large grains which signify grain growth. A few small dark coloured grains can be seen at 0.01 s^{-1} strain rate which could not be resolved optically. These were confirmed as pearlite grains by electron microscopy (Fig. 4.5.2.2.). The temperature of 850°C falls in the (α+γ) phase field for S1 steel. The phase transformation temperatures shift to higher values if deformation accompanies cooling as in AISI 1016 discussed elsewhere (Rajput et al., 2013). The aforesaid elevation can be explained by either or all of the following reasons (Rajput et al., 2013):

1) The Gibbs free energy of the austenite phase increases due to plastic deformation.
2) The austenite grains are refined by dynamic recrystallization.

Therefore, the presence of pearlite at 850°C can be explained by this phenomenon.

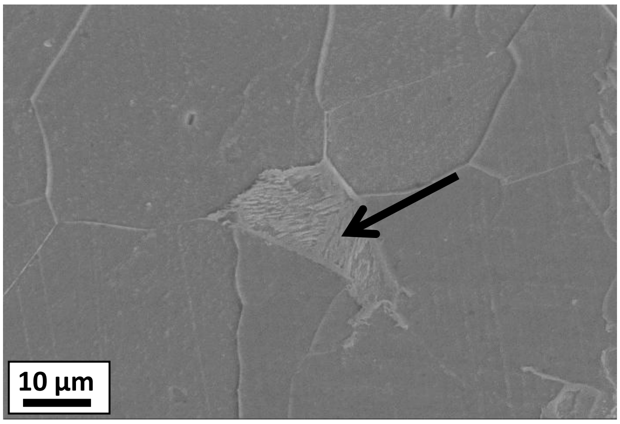

Fig. 4.5.2.2. SEM micrograph showing pearlite grains in S1 steel at 850°C and $0.01s^{-1}$

At 800°C the microstructure consists of deformed pro-eutectoid ferrite and fine equiaxed ferrite. The ferrite grains obtained are by and large the smallest of the lot. The corresponding flow curves (Fig. 4.5.1.1) indicate DRX and DRV. Larger numbers of pearlite grains are observed.

Fig. 4.5.2.3 represents the evolution of the microstructure and ferrite grain refinement at different deformation temperatures and strain rates of S2 steel. The microstructures are similar to those obtained in the case of S1 steel. Fig. 4.5.2.4 represents the evolution of the microstructure and ferrite grain refinement at different deformation temperatures and strain rates of S3. The microstructures are similar to those obtained in the case of S1 and S2 steels.

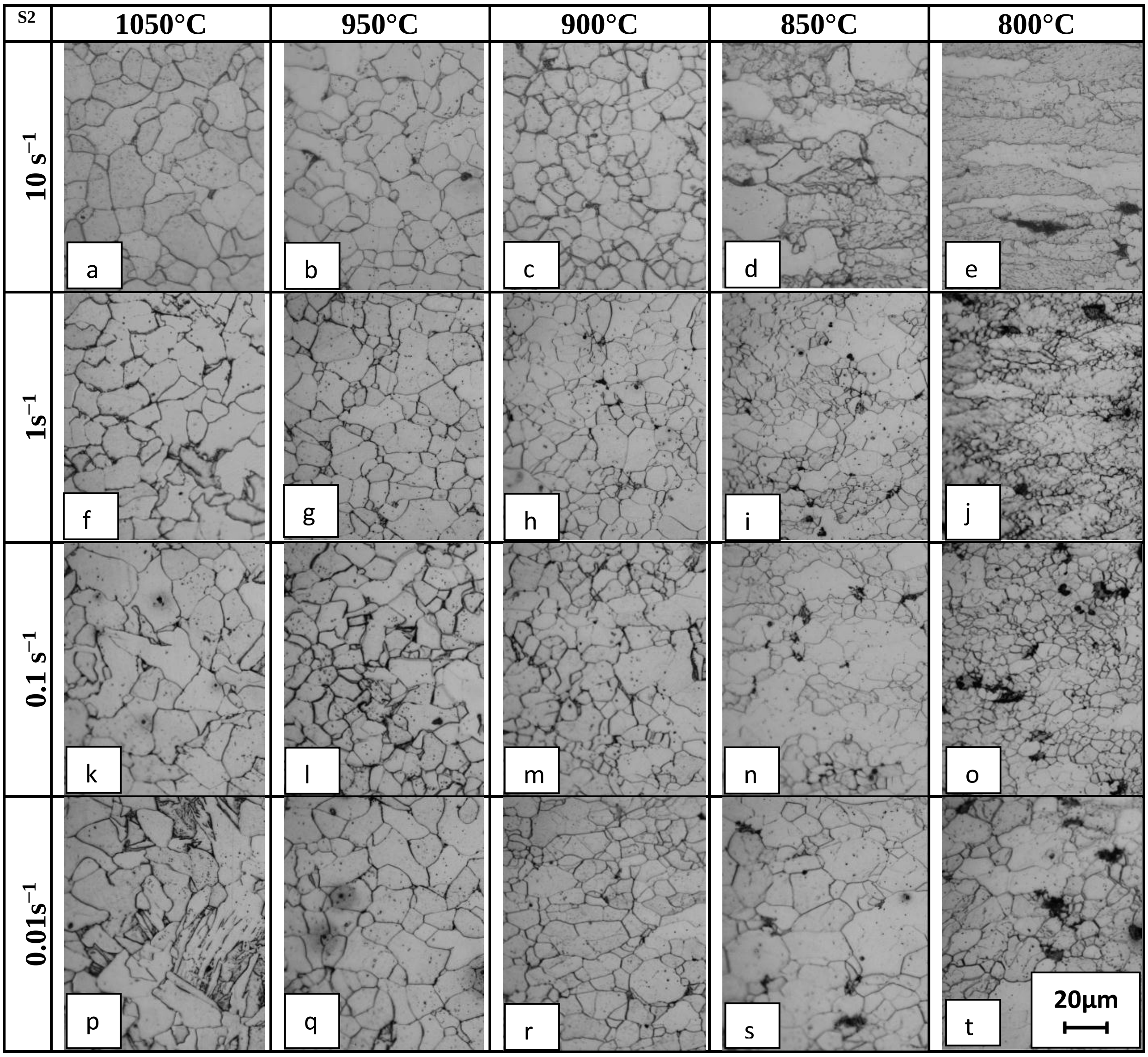

Fig. 4.5.2.3. Evolution of the microstructure and ferrite grain refinement at different deformation temperatures and strain rates of S2 steel

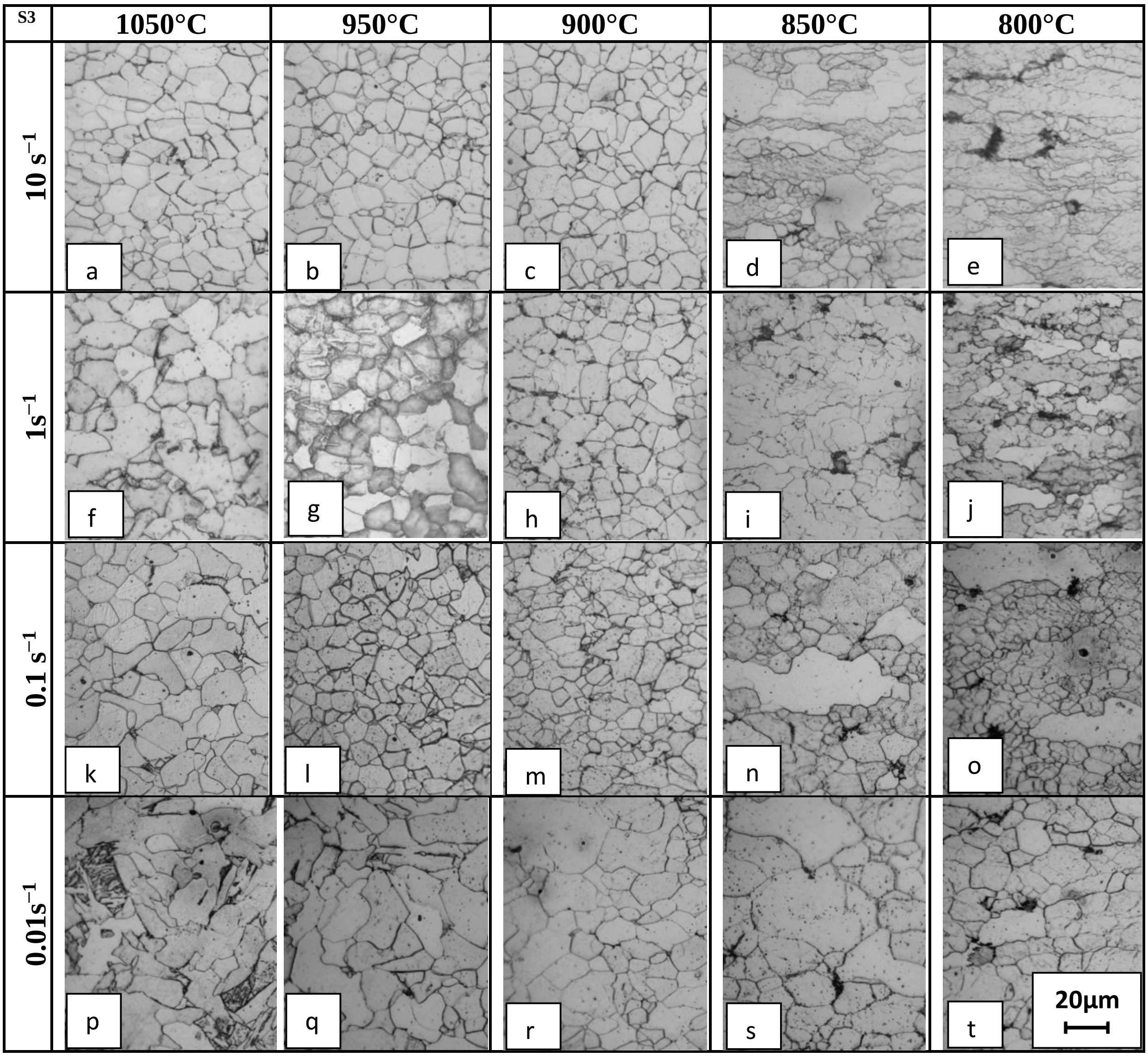

Fig. 4.5.2.4. Evolution of the microstructure and ferrite grain refinement at different deformation temperatures and strain rates of S3 steel

Figures 4.5.2.5. (a), (b) and (c) show the effect of deformation temperature on the ferrite grain size of S1 steel, S2 steel, and S3 steel respectively. The largest grains were obtained at 1050°C. The smallest ferrite grains were obtained at 800°C. The largest grains at 800°C were obtained at a strain rate of $0.01s^{-1}$. This is due to the availability of greater amount of time for grain growth at that strain rate. Largely, the grains obtained at $0.1s^{-1}$ are the smallest for both the steels whereas those obtained at $0.01s^{-1}$ are the largest. The grain sizes obtained at $1s^{-1}$ and different temperatures are generally in between those achieved at 0.1 and $0.01s^{-1}$. The increase in strain rate from 0.01 to $0.1s^{-1}$ causes a decrease in the grain size. The smallest grain size is achieved at 800°C for S1, S2 and S3 steels.

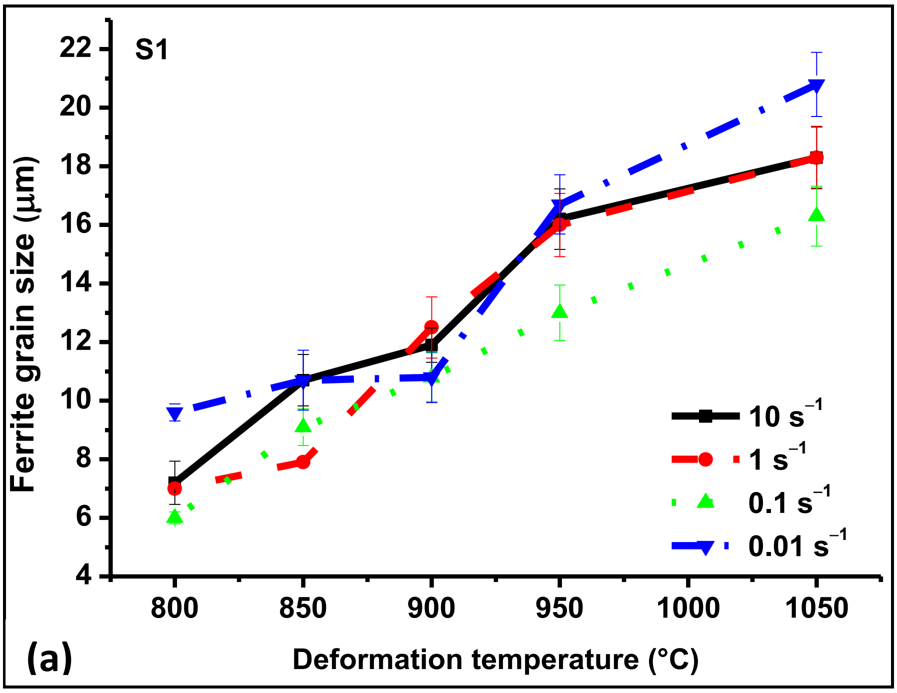

Fig. 4.5.2.5. (a) Effect of various deformation temperatures and strain rates on the ferrite grain size of S1 steel

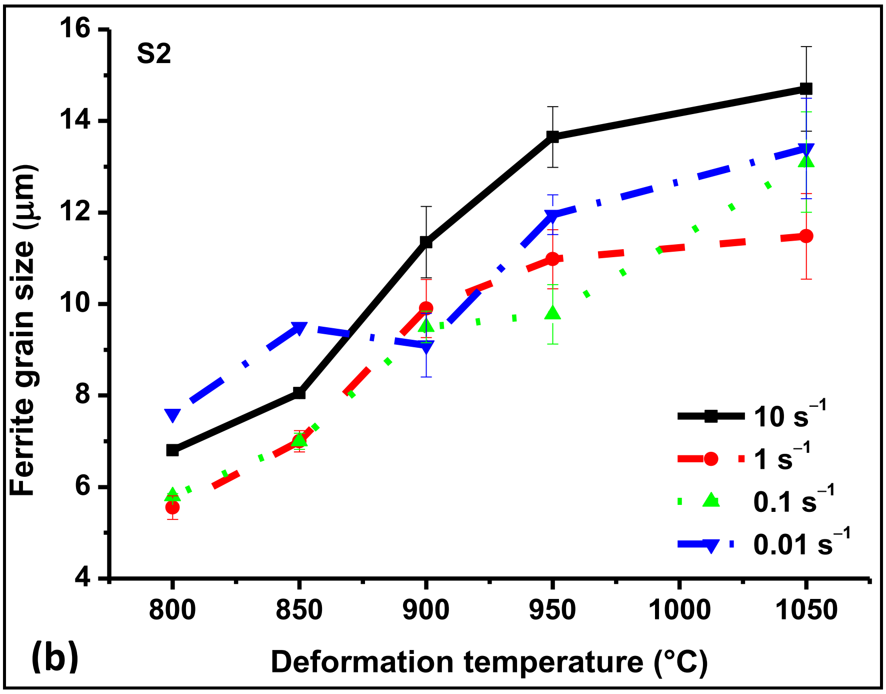

Fig. 4.5.2.5. (b) Effect of various deformation temperatures and strain rates on the ferrite grain size of S2 steel

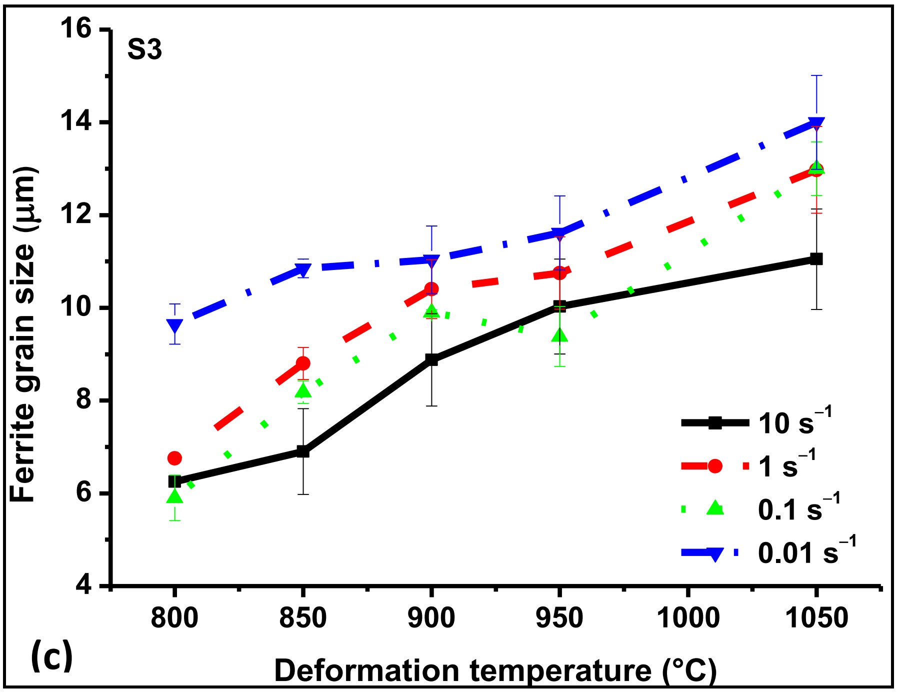

Fig. 4.5.2.5. (c) Effect of various deformation temperatures and strain rates on the ferrite grain size of S3 steel

Subsequently, experiments were also performed to study the effect of strain rates of 0.1 and 1 s^{-1} at the deformation temperature of 750°C for the three steels. A grain size of 3.7 µm at 1 s^{-1} for S2 steel was obtained. The microstructure and the corresponding flow curve are presented in Fig. 4.5.2.6. The mixed type microstructure of S1 steel, hot compressed at 850°C and $10s^{-1}$ can be analysed using ASTM E1181 (ASTM E1181-02, 2015). The report is as follows: "Duplex, Wide-range, 55% ASTM No. 11.5, 45% ASTM No. 6.5".

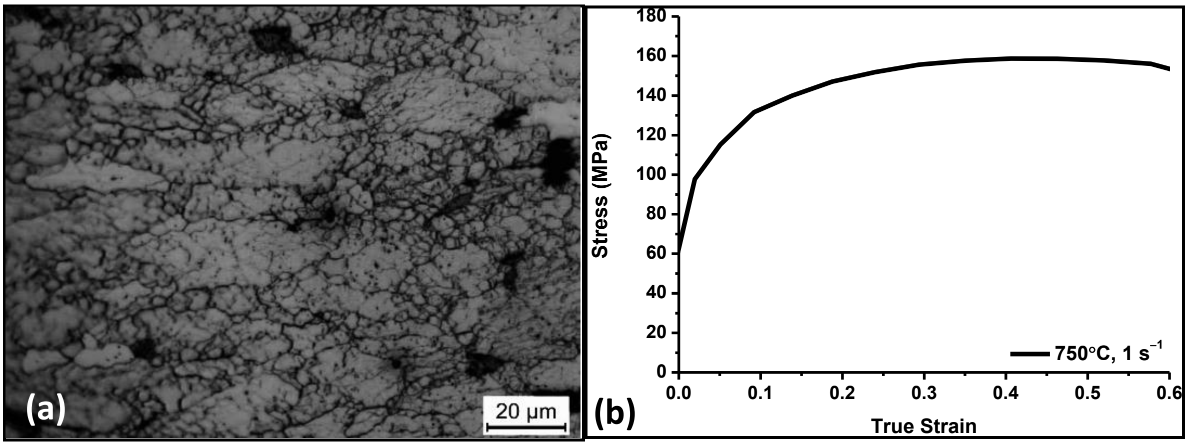

Fig. 4.5.2.6. (a) Microstructure of S2 steel compressed at 750°C and 1 s^{-1};
(b) Corresponding true stress, true strain curve

4.5.3 Adiabatic rise, peak stress and Z values

The adiabatic rise in temperatures is tabulated in Table 4.5.3.1. The maximum rise in temperature is 20.7°C at 900°C and 1 s^{-1} for S1 steel. The highest rise in temperature is 22.1°C at 950°C and 1 s^{-1} for S2 steel. The greatest increment in temperature for S3 steel is 27°C at 750°C and 1 s^{-1}. The peak stresses obtained were corrected for adiabatic rise in temperature during hot compression and are tabulated as Table 4.5.3.2.

Table 4.5.3.1: Maximum increment in temperature during hot compression of S1, S2 and S3 steels

Deformation Temperature (°C)	**S1 steel**			**S2 steel**			**S3 steel**		
	***dT* (°C) at the strain rate of**								
	0.01 s^{-1}	**0.1 s^{-1}**	**1 s^{-1}**	**0.01 s^{-1}**	**0.1 s^{-1}**	**1 s^{-1}**	**0.01 s^{-1}**	**0.1 s^{-1}**	**1 s^{-1}**
750	1.9	12.6	15.7	3.8	5.7	13.2	3.7	8.6	27
800	3.8	6.1	14.3	6.9	5.3	17.7	5.2	3.5	19.2
850	1.2	7.2	16.6	4.2	4.6	18.3	2.6	6.3	17.7
900	2.7	5.4	20.7	4.2	1.9	19.2	3.7	2.9	22.6
950	5.8	4.8	8.5	0.6	4.5	22.1	1.1	4.3	19.4
1000	1.5	2.9	11	2	4.5	11.7	0.9	4.2	18.4
1050	2	4.1	13	1.4	4.2	12.1	1.4	3.9	10.2

Table 4.5.3.2: Peak stress corrected for adiabatic rise in temperature for S1, S2 and S3 steels

Temp.	**Peak stress (MPa) corrected for adiabatic rise in temperature**								
°C	**S1 steel**			**S2 steel**			**S3 steel**		
	1 s^{-1}	**0.1 s^{-1}**	**0.01 s^{-1}**	**1 s^{-1}**	**0.1 s^{-1}**	**0.01 s^{-1}**	**1 s^{-1}**	**0.1 s^{-1}**	**0.01 s^{-1}**
750	156.94	129.07	85.41	164.68	130.67	92.57	208.51	127.48	78.99
800	128.85	88.13	57.26	136.11	95.01	66.29	139.91	95.35	62.16
850	118.04	80.85	53.06	109.18	70.10	48.57	104.16	73.11	50.73
900	164.76	108.38	75.62	123.03	88.67	58.79	139.58	86.62	51.54
950	148.41	112.88	74.77	151.92	110.87	75.48	158.19	107.96	66.08
1000	130.64	90.68	55.03	140.05	98.08	64.45	141.04	100.68	65.36
1050	112.73	75.41	51.74	122.85	84.26	56.19	121.99	85.14	55.92

The peak stresses (Fig. 4.5.3.1) decrease as temperatures increase from 750°C to 850°C since the microstructures are predominantly composed of ferrite phase and ferrite softens at higher temperatures. The amount of austenite phase fraction starts increasing at the expense of ferrite phase fraction between 900°C and 950°C. Since austenite is harder than ferrite at higher temperatures the peak stresses values escalate. Subsequently, at higher temperatures austenite softens and the peak stress values start decreasing upto 1050°C.

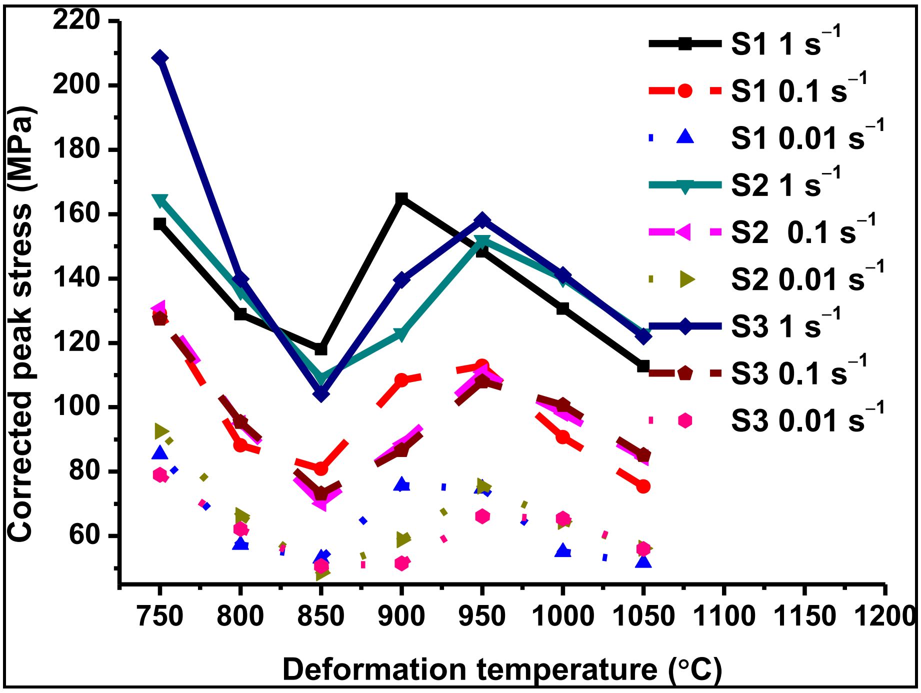

Fig. 4.5.3.1. Peak stress corrected for adiabatic rise in temperature for S1, S2 and S3 steels

The peak stresses obtained are correlated with the reciprocal of the absolute temperature for a large number of combinations of temperatures and strain rates at which hot deformation is carried out for a true strain of 0.69. The peak compressive stresses at the strain rates of 1, 0.1, 0.01s^{-1} and temperatures of 750, 800, 850, 900, 950, 1000, 1050°C were found out.

The corrected peak flow stresses of S1 steel are lower than S2 steel at 750°C, 800°C, and at 950-1050°C. The corrected peak stresses of S1 steel are higher than those of S2 steel at 850°C and 900°C (Fig. 4.5.3.1). This implies that the alloying additions retard DRX and cause an increment in the corrected peak flow stresses at 750°C, 800°C and 950-1050°C. The corrected peak flow stresses of S2 steel are lower than those of S3 steel at 1 s^{-1} and 750, 800, 900, 950, and 1000°C, at 0.1 s^{-1} and 800, 850, 1000, and 1050°C, and at 0.01 s^{-1} and 850, and 1000°C. The addition of alloying elements to S2 steel caused these increments in corrected peak flow stresses by retarding DRX.

High value of *Z* gives rise to grain refinement of steels during hot deformation (Cho et al., 2001), (Kim et al., 2003), (Kim et al., 2005). The Z values of S1 steel are higher than that for S2 steel at 1050°C and lower than that of S1 steel at 800°C. Therefore, addition of 0.13 wt. % Si to S1 steel is detrimental for grain refinement at 1050°C and beneficial at 800°C. The mean grain size decreases from 6.7±0.3 and 10.1±0.5 μm for S1 steel to 5.5±0.5 and 7.6±0.1 μm for S2 steel at 800°C and 1 and 0.01s^{-1} respectively (Table 4.5.3.4). *Z* values for S2 steel are higher than those of S3 steel at 1050°C (Table 4.5.3.4). The opposite is true at 800°C. High values of *Z* also suggest higher flow stresses for S2 steel as compared to S3 steel at 1050°C.

Table 4.5.3.3: Z values for the steels at 1, 0.1 and 0.01 s^{-1} and at 800, and 1050°C

Temperature (°C)	**Strain rate (s^{-1})**	**S1 Steel Z**	**Mean Grain size (μm)**	**S2 Steel Z**	**Mean Grain size (μm)**	**S3 Steel Z**	**Mean Grain size (μm)**
800	1	6.5 x10^{15}	6.7±0.3	7.1 x10^{20}	5.5±0.5	2.9 x10^{21}	6.7±0.1
800	0.1	6.5 x10^{14}	5.6±0.3	7.1 x10^{19}	5.8±0.1	2.9 x10^{20}	6.5±0.8
800	0.01	6.5 x10^{13}	10.1±0.5	7.1 x10^{18}	7.6±0.1	2.9 x10^{19}	9.6±0.7
1050	1	2 x10^{18}	16±2.9	7.2 x10^{15}	11.5±1.6	1.9 x10^{11}	12.9±1.6
1050	0.1	2 x10^{17}	14.7±1.8	7.2 x10^{14}	13.1±1.9	1.9 x10^{10}	13±1
1050	0.01	2 x10^{16}	17.6±3.4	7.2 x10^{13}	13.4±1.9	1.9 x10^{9}	13±2.6

Thus, it has been established that fine grained high phosphorous steels can be made by working in the intercritical region of the phase diagram of high phosphorous steels. This should facilitate the production of tougher high phosphorous steels. Now, the safe processing window for manufacturing such steels shall be identified.

4.6 THERMO-MECHANICAL PROCESSING

The high phosphorous steels namely S1, S2 and S3 steels have been tested and found to be comparable to plain carbon steels in strength, toughness and corrosion resistance. The role of various thermo-mechanical processing parameters like deformation temperature and strain rates has been understood in order to produce fine grained high phosphorous steels. Now, the safe processing window for producing rebars having high phosphorous compositions needs to be identified. The following work is an attempt to identify a processing window for S1 steel using the modified dynamic materials model proposed by Murty and Rao (Murty et al., 2003). Isolated studies have been done on high phosphorous steels (Kim et al., 2005). In order to conduct a comprehensive study on high-phosphorus steels, a large range of strain rates (10-0.001 s^{-1}) and deformation temperatures (750-1050°C) was chosen.

4.6.1 Phase Transformation Characterization

The CCT curve is shown in Fig. 4.1.1 a. The first and second deviation points in the CCT curve during cooling correspond to the Ar_3 and Ar_1 temperatures. They are estimated to be 965°C and 790°C respectively. This indicates that the microstructure is ferrite at 750°C and austenite at 1050°C and a mix of both at 850-900°C.

4.6.2 Flow Behaviour of S1 Steel

Fig. 4.6.2 shows the corrected and uncorrected flow curves corresponding to the 7 test temperatures ranging from 750 to 1050°C and the 6 strain rates ranging from 10 to 0.001 s^{-1}. The true flow stress was found to be a function of strain rate and temperature. At a constant temperature, the flow stress increased as the strain rate was increased (Fig. 4.6.2 a-g). All the stress strain curves showed a peak stress after hardening at low strain rates. DRX is observed at higher temperatures, and DRV is seen at lower temperatures. For a fixed strain rate (10 s^{-1}) as the temperature increased, the values of flow stress first decreased as α is softer at higher temperatures, and then increased as the proportion of γ which is harder than α at high temperatures increased and then finally decreased as γ softened at higher temperatures (Fig. 4.6.2.h). At low strain rates and high temperatures multiple dynamic recrystallization peaks can be seen as new grains grow at the expense of strain hardened old grains. Multiple peaks correspond to grain coarsening (Weiss et al., 1983). As the strain rate is increased while keeping the temperature constant the stress peaks seen at lower strain rates shift towards higher strains. Comparing the flow curve at 850°C and 0.1 s^{-1} with that obtained by Tsuji and co-workers (Tsuji et al., 1997), it can be observed that adding phosphorous to interstitial free steel retards DRX. Again comparing the stress at 750°C and 1 s^{-1} with that obtained by Dong and co-workers (Dong et al., 2010) suggests that adding phosphorous to a very low carbon steel expedites DRX.

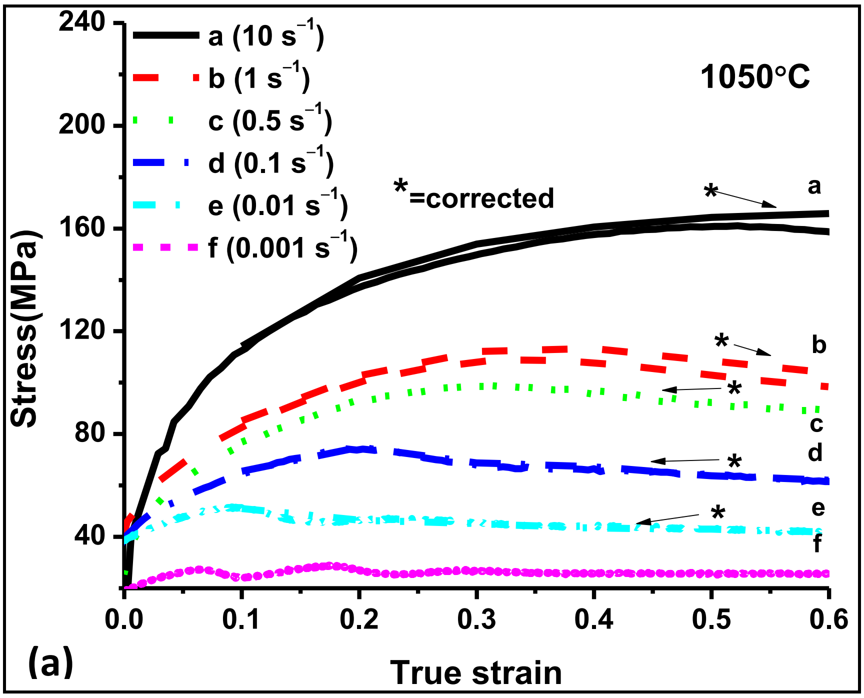

Fig. 4.6.2. (a) True stress, true strain curves of S1 steel corrected and uncorrected for deformation heating at 1050°C, for different strain rates

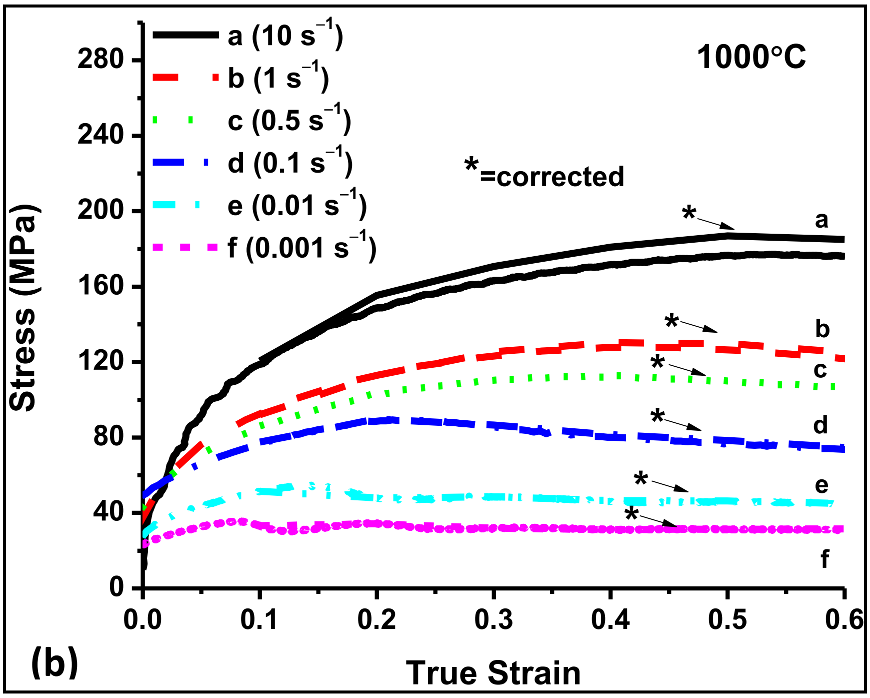

Fig. 4.6.2. (b) True stress, true strain curves of S1 steel corrected and uncorrected for deformation heating at 1000°C, for different strain rates

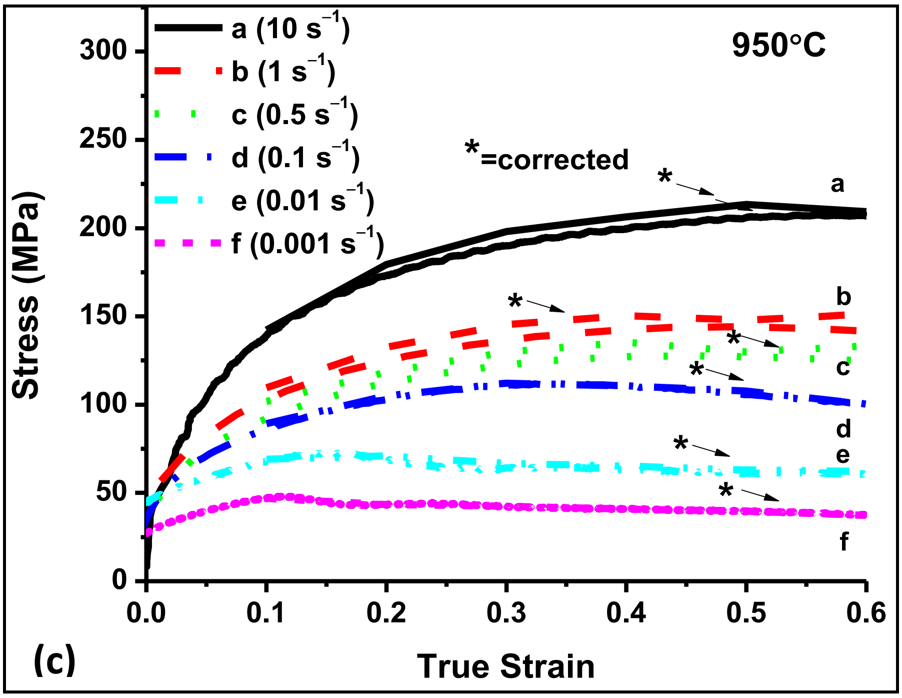

Fig. 4.6.2. (c) True stress, true strain curves of S1 steel corrected and uncorrected for deformation heating at 950°C, for different strain rates

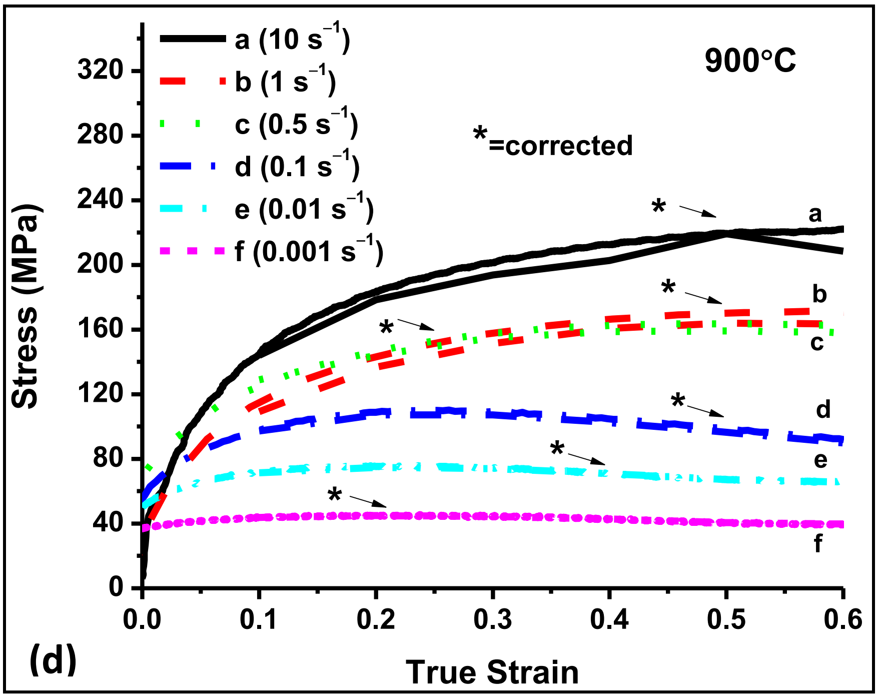

Fig. 4.6.2. (d) True stress, true strain curves of S1 steel corrected and uncorrected for deformation heating at 900°C, for different strain rates

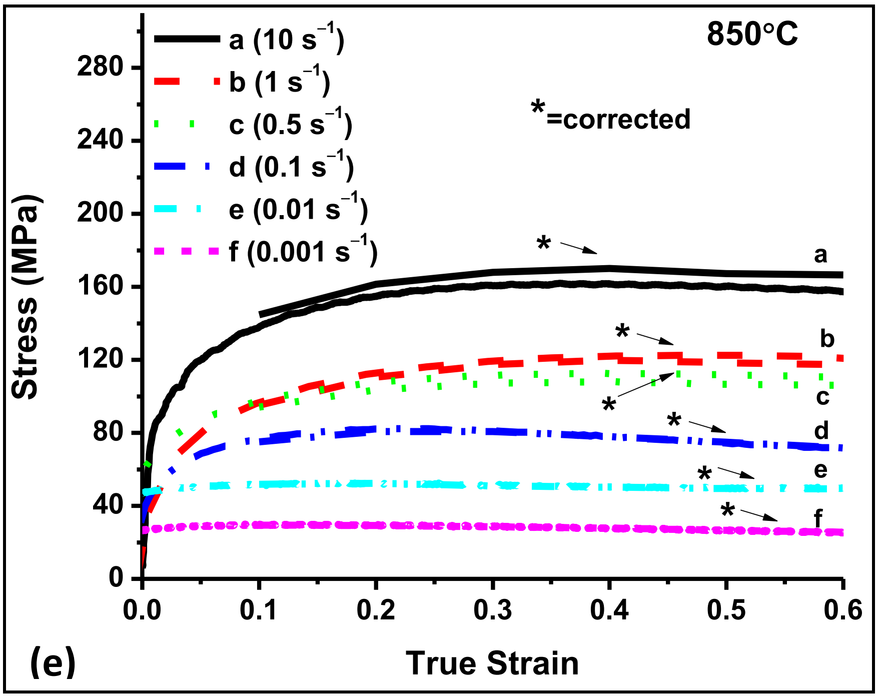

Fig. 4.6.2. (e) True stress, true strain curves of S1 steel corrected and uncorrected for deformation heating at 850°C, for different strain rates

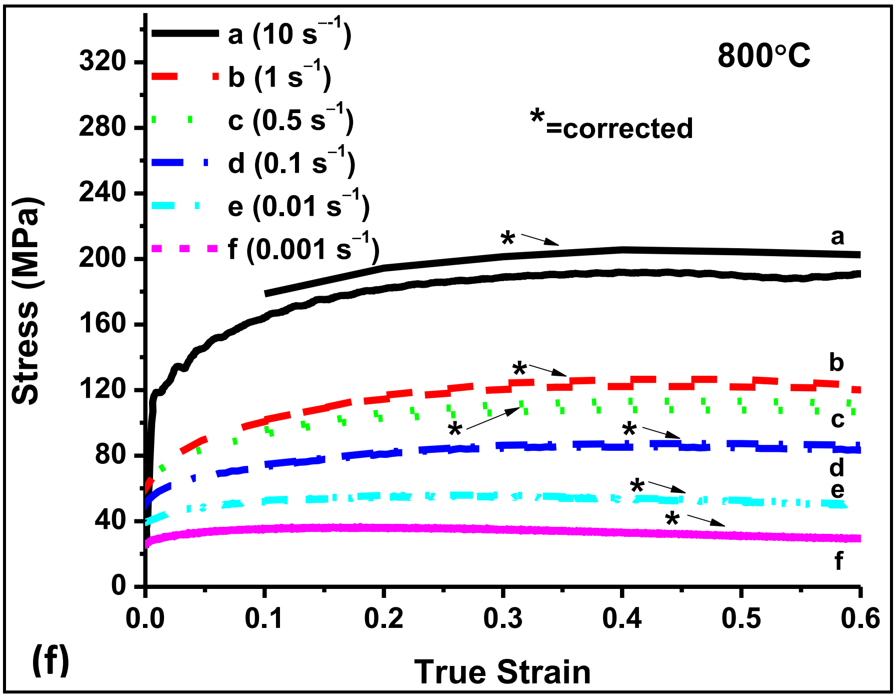

Fig. 4.6.2. (f) True stress, true strain curves of S1 steel corrected and uncorrected for deformation heating at 800°C, for different strain rates

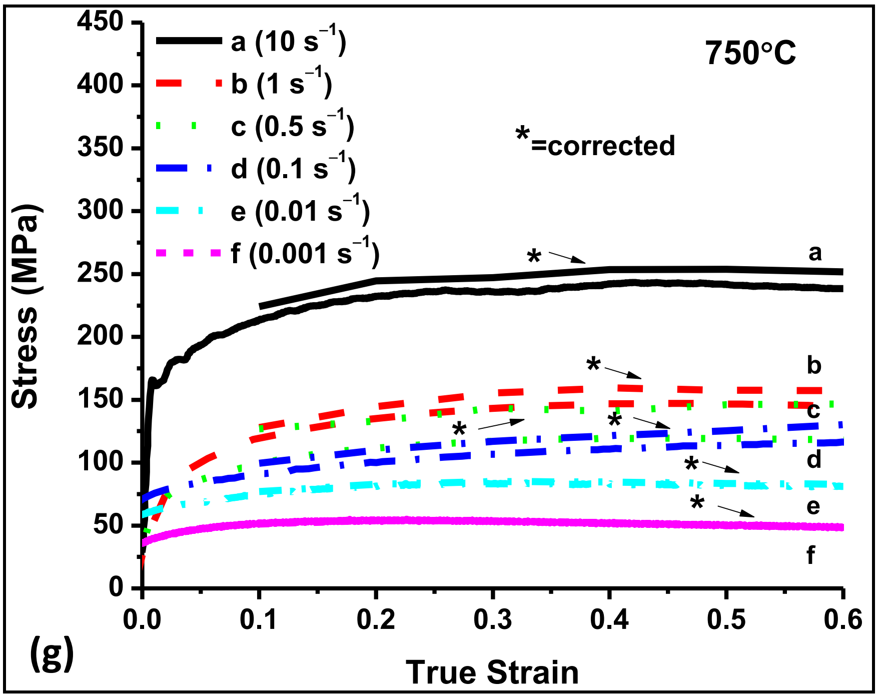

Fig. 4.6.2. (g) True stress, true strain curves of S1 steel corrected and uncorrected for deformation heating at 750°C, for different strain rates

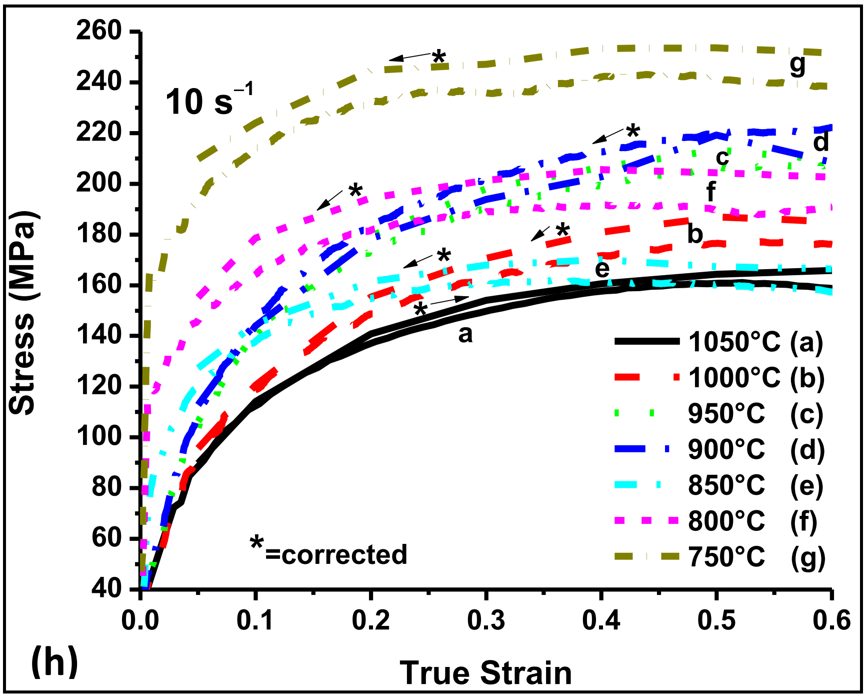

Fig. 4.6.2. (h) True stress, true strain curves of S1 steel corrected and uncorrected for deformation heating at 10 s^{-1} and different temperatures

Table 4.6.1 shows the maximum increment in temperature during compression of S1 steel samples. The lowest temperature increase during hot deformation was observed at the low strain rate of 0.001 s^{-1}. The flow stresses corrected for adiabatic rise in temperature at a true strain of 0.6 for S1 steel are presented in Table 4.6.2.

Table 4.6.1: Maximum increment in temperature during compression of S1 steel

Deformation Temperature (°C)	***dT* (°C) at the strain rate of**					
	0.001 s^{-1}	**0.01 s^{-1}**	**0.1 s^{-1}**	**0.5 s^{-1}**	**1 s^{-1}**	**10 s^{-1}**
750	0.8	1.9	12.6	10.7	15.7	11.5
800	0.9	3.8	6.1	14.3	14.3	16.3
850	0.4	1.2	7.2	14	16.6	14.5
900	0.5	2.7	5.4	9.3	20.7	18.3
950	0.8	5.8	4.8	6.1	8.5	15.8
1000	1.7	1.5	2.9	2.2	11	18.9
1050	1.6	2	4.1	2.4	13	18.6

Table 4.6.2: Flow stress at a true strain of 0.6 corrected for adiabatic rise in temperature for S1 steel

Deformation Temp. (°C)	**Strain rate**					
	0.001 s^{-1}	**0.01 s^{-1}**	**0.1 s^{-1}**	**0.5 s^{-1}**	**1 s^{-1}**	**10 s^{-1}**
750	48.35	82.93	130.19	121.88	157.28	251.64
800	29.61	50.40	86.40	112.06	122.98	202.55
850	25.51	49.4	71.81	106.17	117.33	166.5
900	39.71	65.76	89.93	158.22	163.53	208.51
950	37.32	61.99	100.28	133.22	151.41	209.35
1000	31.61	45.01	74.74	106.7	125.21	185.12
1050	25.91	41.93	62.03	89.3	103.86	165.83

4.6.3 Microstructure of S1 steel

The optical microstructure of the starting specimen is shown in Fig. 4.6.3.1.

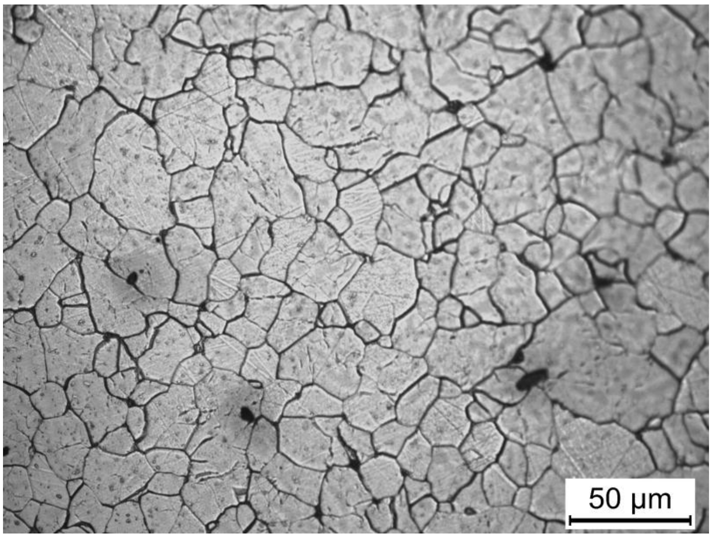

Fig. 4.6.3.1. Light optical micrograph of S1 steel specimen, hot forged at 1150°C, etched with 2% nital solution

Light optical micrographs of specimens water quenched after austenitization at 1050°C for 10 s followed by hot compression to a true strain of 0.69 at different temperatures and strain rates are shown in Fig. 4.6.3.2. All the specimens show a predominantly ferritic microstructure. A few austenite grains containing high amounts of carbon (Ordonez et al., 2010) were converted to martensite on quenching. A few pearlite grains are also observed at and below 850°C (Fig. 4.5.2.2). The ferrite grains may be formed before, during and after deformation. At 750°C, ferrite exists before the onset of deformation because this temperature is lower than $Ar_{1.}$ At 900°C pro-eutectoid ferrite exists before the onset of deformation and ferrite is also formed after deformation. At 1050°C, ferrite is formed after deformation.

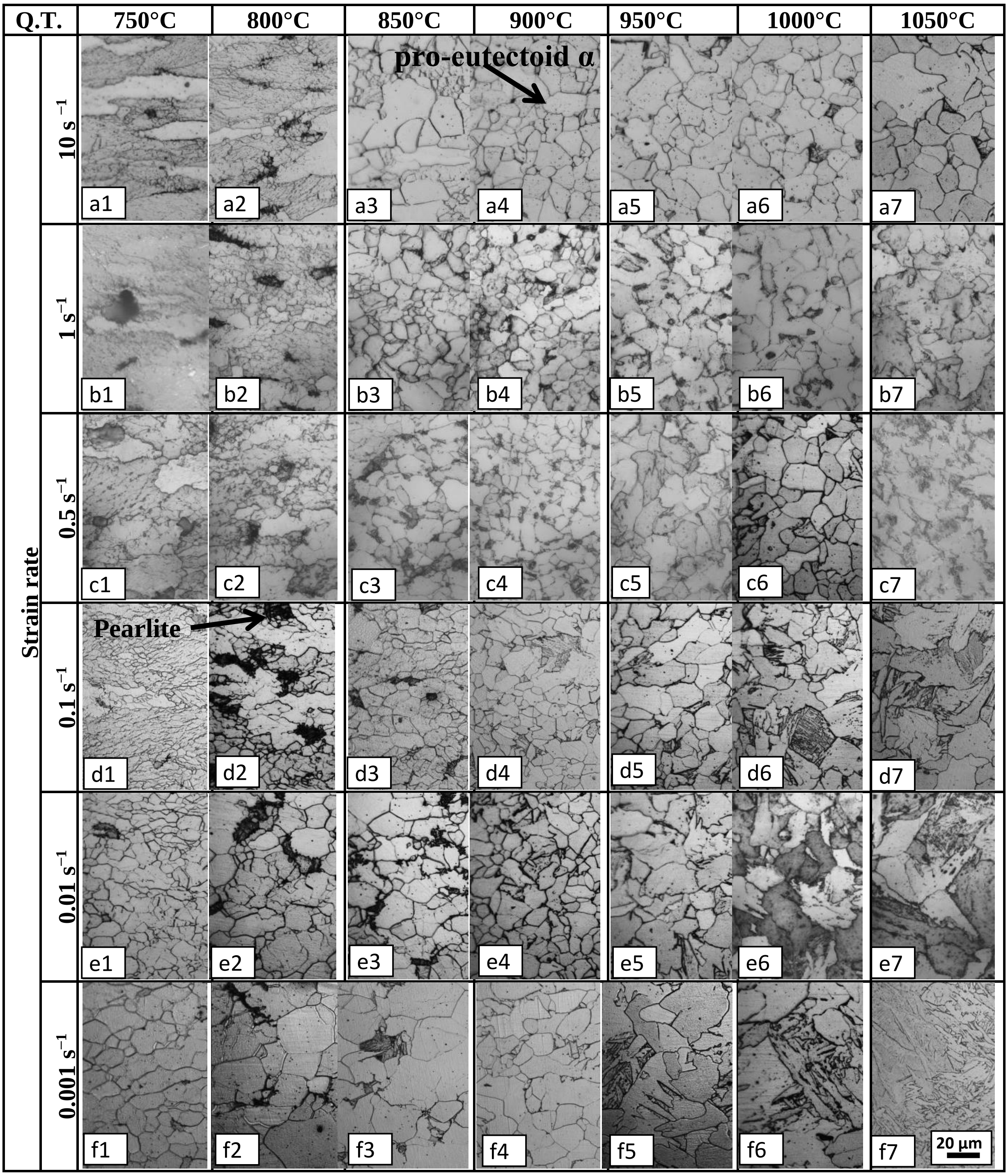

Fig. 4.6.3.2. Microstructures of specimens of S1 steel after hot compression at different temperatures and strain rates; compression axis is vertical

4.6.4 Processing Map

Processing map for 0.6 true strain is shown in Fig. 4.6.5.2. The iso-efficiency (η) lines are shown in the plot of log $\dot{\varepsilon}$ versus T. The instability parameter (κ) domains which are shown as shaded area, is superimposed. The maps show positive values of η in the entire testing zone. Large η values are observed in the region bounded by strain rates between 0.001 s^{-1} and

0.01 s^{-1} and temperatures between 750°C to 850°C. Large η values are also observed at higher strain rates of 0.5 s^{-1} and 900°C. No instability is found at 0.001 s^{-1} and all temperatures.

4.6.5 Discussion

The relation between the microstructures and the deformation mechanisms, and the usability of processing maps is discussed in this section.

4.6.5.1 Microstructure evolution and processing maps

The microstructure is predominantly ferritic with a few grains of martensite or ferrite-carbide mixture. Micro-hardness measurements made on the ferrite-carbide mixture phase found in the specimen compressed at 750°C and 0.001 s^{-1} and quenched (Fig. 4.6.3.2), gave an average value of 490 HV which corresponds to martensite phase of plain carbon steels containing 0.2 wt. % carbon (Callister and Rethwisch, 2014). This means that at Ar_1 *i.e.,* 790°C, the amount of carbon in the austenite grains exceeded the average value of 0.05 wt. % carbon in the bulk due to site competition with phosphorous (H Erhart and Grabke, 1981). An average value of 218 HV was obtained on conducting micro-hardness measurements on the needle like features of the microstructure obtained on compressing at 1050°C and 0.001 s^{-1} (Fig. 4.6.3.2). This corresponds to the hardness of fine pearlite of about 0.5 wt. % carbon steel (Callister and Rethwisch, 2014).

The hot compression experiments have been carried out in ferrite, ferrite-austenite duplex phase and austenite regions. After deformation, ferrite forms during cooling as a function of both the grain size and the stored energy due to hot deformation. This can be observed to occur below 900°C (Fig. 4.6.3.2). Compression in the ferrite region at 10 s^{-1} produces a grain structure which appears elongated and recovered. The microstructures obtained at 850 and 900°C show the results of hot compression in the ferrite-austenite duplex phase region. The amount of ferrite is more than that of austenite phase at 850°C as compared to the situation at 900°C. The hardness of ferrite is lower than that of austenite (Gove and Charles, 1974) at higher temperatures. Therefore, the peak compressive stress values recorded at 850°C are lower than those obtained at 900°C. The microstructures at these temperatures generally reveal recrystallized grains. The microstructures obtained at 1050°C show recrystallized grains at all strain rates. These tests were conducted in the austenite regions.

Microstructural studies suggest that dynamic recrystallization (DRX) takes place at high temperatures and low strain rates. The stress values increase steadily to a peak and then soften to a steady state region during DRX (Fig. 4.6.2). As the strain rate decreases the stress values start decreasing. The trend changes from a high stress value to a peak and further to multiple peaks at low strain rates and high temperatures. The peak of dynamic recrystallization shifts from lower strains to higher values on decreasing the temperature. Hence it can be stated that the tendency for nucleation and growth of new grains is reduced with increasing strain rate and decreasing temperature (Abbasi and Momeni, 2012).

At moderate temperatures *e.g.,* 850 to 950°C, η is moderate and high at low and moderate strain rates. η is low and moderate in this range, at higher strain rates as the time allowed for diffusion is low under these conditions. Both pro-eutectoid ferrite and deformation-induced ferrite are obtained at moderate and lower temperatures. The formation of deformation-induced ferrite causes softening to occur, leading to high values of η. Both these kinds of ferrite can be further deformed by dynamic recovery leading to the formation of sub-grains (Fig. 4.6.5.1).

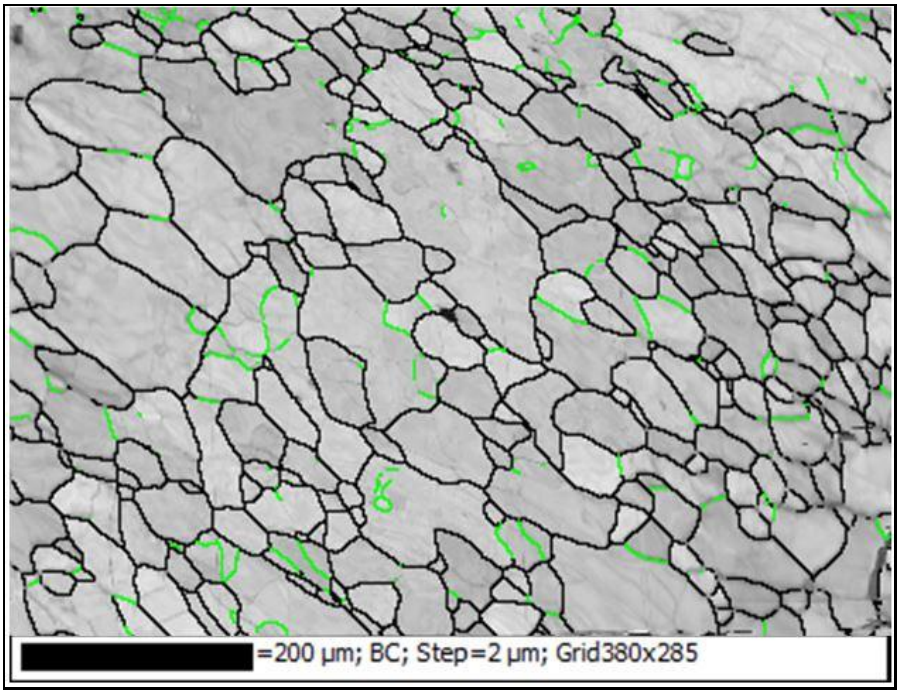

Fig. 4.6.5.1. EBSD grain boundary map of S1 steel specimen, hot forged at 900°C. Grain boundaries are dark (black) and the sub grain boundaries are light (green). Compression axis is horizontal.

As the strain rate increases the value of η decreases (Chakravartty et al., 1995). This can be observed in the processing map (Fig. 4.6.5.2). η parameter is related to workability due to diffusion controlled processes. The values are large at low temperature and low strain rates. The diffusion processes in this range include the formation of ferrite and its dynamic recovery. At higher temperatures higher values of η are due to the dynamic recrystallization of ferrite. In the low strain rate region, no instability can be observed at all temperatures.

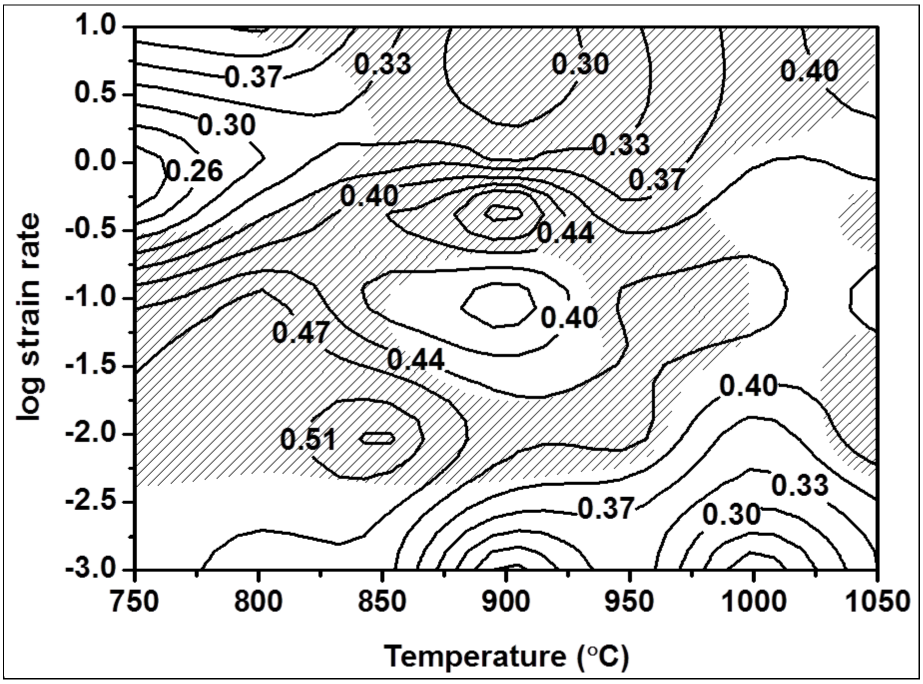

Fig. 4.6.5.2. Processing map of S1 steel as a function of temperature and strain rate for the true strain of 0.6, constructed using modified DMM of Murty and Rao (Murty et al., 2003)

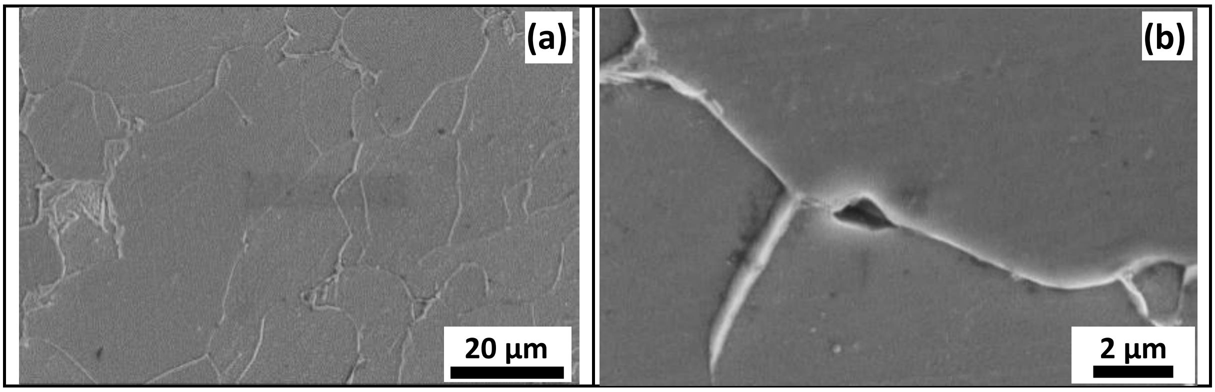

Fig. 4.6.5.3. SEM micrographs of S1 steel after hot compression (a) with strain rate of 0.001 $s^{-1}$and 850°C; (b) with strain rate of 10 $s^{-1}$and 918°C; compression axis is vertical

Representative micrographs of the specimen deformed at 0.001 $s^{-1}$and 850°C, at 10 s^{-1} and 918°C are shown in Fig. 4.6.5.3. The specimen deformed at 0.001 s^{-1} and 850°C does not show any instability. The specimen deformed at 10 s^{-1} and 918°C shows instabilities. Flow softening occurs because of adiabatic heating (Table 4.6.1) during hot working at high strain rates (Murty et al., 2000). Short times of deformation lead to damage due to less restoration of the microstructure (Fig. 4.6.3.2). The low restoration is supported by low values of η parameter. Literature suggests that the tendency for flow localization can be reduced upon the maximization of η (Murty et al., 2000). Therefore, softening produced by adiabatic heating will cause damage if restoration is inadequate *i.e.*, η is small.

Thus, safe processing windows have been identified to facilitate the manufacture of strong and tough high phosphorous steels having improved corrosion resistance for concrete reinforcement applications.

Chapter 5

SUMMARY AND CONCLUSIONS

The salient conclusions based on the experimental results obtained in the present study are summarized in this chapter. Three high phosphorous steels were prepared using the ingot casting route. After forging, rolling and heat treating the prepared steels, different samples were prepared and studied for metallography, mechanical properties, corrosion behaviour and thermo-mechanical processing. The effect of thermo-mechanical parameters on the microstructure and grain size of the prepared high phosphorous steels was understood and the window for safe hot processing of S1 steel was found out using processing maps. Plain carbon steel was used for comparison purposes.

The conclusions are divided into five sub-headings related to the area of investigation, namely phase transformation, mechanical properties, corrosion behaviour, grain refinement during thermo-mechanical processing, and hot formability.

I. Phase transformation studies reveal that:

- The Ar_1 temperatures of S1, S2 and S3 steels were estimated as 790, 813 and 805°C respectively using continuous cooling transformation tests. The Ar_3 temperatures of S1, S2 and S3 steels were estimated as 965, 941 and 925°C respectively.
- The removal of phosphorous from the grain boundaries of S3 steel held at 865°C, within the $(\alpha+\gamma)$ phase field was found to approach completion at 24 h. The variation of contrast within ferrite, attributable to etching with Oberhoffer's reagent was non-existent at 24 h. Thus, the optimum time for complete removal of phosphorous from the grain boundaries to grain interior at 865°C lay between 4h and 24 h.
- In order to achieve the same situation S3 steel specimens held at 900°C would need lesser time. S3 steel specimens should be held at 900°C for a time period between 1.9 to 11.6 h to allow the phosphorous atoms to travel the same diffusion distances and reach similar equilibrium distribution of phosphorous between austenite and ferrite. Since fine grain size is linked with better impact toughness, very long heat treatments were undesirable. Therefore, 1h and 6 h at 900°C were chosen for heat treatment.

II. Mechanical properties and fractography studies reveal that

- The removal of phosphorous from the grain boundaries of S3X3 steel is confirmed by SEM-EDS analysis. This displacement of phosphorous from the grain boundaries ensures better toughness of the steel.
- The Indian standard for steel bars and wires for concrete reinforcement (Indian Standard 1786, 2008) specifies YS as 415 MPa, UTS as 485 MPa, and elongation as 14.5% for Fe-415 (Fe-0.3C-0.06P) rebar. The impact toughness of S4 steel is 222 J. YS of S3 steel in X2 condition is 375 MPa, UTS is 465 MPA and elongation is 30%. The impact toughness is 247 J, although scatter is higher than that recorded for S4 steel. Scatter could also be due to higher amount of inclusions since the steel was made in an induction furnace. Thus, it compares well with Fe-415 rebar. Therefore, S3 steel is a good candidate for development as a concrete reinforcement rebar.
- The S1 steel in X3 condition is close to the 0.09 carbon steel in toughness, with lesser strength and greater ductility. S2 steel in X3 condition shows high impact energy irrespective of the region (gamma/duplex) in which it is worked or heat treated. Again, the S3 steel in X3 condition achieves the highest impact energy (284J). Therefore, heat treatment in intercritical region improves toughness of high phosphorous steels.
- A pattern is observed in the UTS values of the three prepared high phosphorous steels in the X5 condition. The UTS values decrease with an increase in alloying *i.e.*, UTS decreases in the following way S1X5 > S2X5 > S3X5 on hot rolling at 900°C within the ($\alpha+\gamma$) region of the Fe-P phase diagram as the amount of alloying increases. Hence, hot working in the intercritical region is more effective for removal of phosphorous from the grain boundaries of the high phosphorous steels.
- S3X3 steel has the highest impact toughness of 284 J and hence was tested for corrosion resistance in saturated $Ca(OH)_2$ solution with chloride concentration of 0.1 wt. % along with the annealed samples.

III. Corrosion behaviour studies reveal that:

- The potentiodynamic polarization studies of high phosphorous steels in saturated $Ca(OH)_2$ solution containing up to 0.1 wt. % chloride concentration revealed a stable passive behaviour and good pitting corrosion resistance whereas, plain carbon steel could withstand, only up to 0.06 wt. % chloride.

- LPR and OCP measurements also confirmed the improved performance of high phosphorous steels in saturated $Ca(OH)_2$ solution containing upto 0.1 wt. % chloride concentration.
- EIS studies revealed that the polarization resistance of high phosphorous steels increased with immersion time in saturated $Ca(OH)_2$ solution containing 0.1 wt. % chloride concentration indicating improvement in the protective ability of the protective film. On the other hand, the plain carbon steel corroded actively in 0.1 wt. % chloride-containing saturated $Ca(OH)_2$ solution.
- Corroded surface of S3 steel tested in saturated $Ca(OH)_2$ solution with 0.14 wt. % chloride solution suggests that MnS inclusions along with aluminium oxides could be crucial in the initiation of pits since they attract chloride ions. The presence of phosphorous outside the pits indicate that phosphorous could have played a positive role in blocking the entry of chloride ions and thus prevents pitting.
- EIS scan of S3X3 sample immersed in saturated $Ca(OH)_2$ solution with 0.1 wt. % chloride for 65 h revealed that the protective ability of its passive film improved with time of immersion.
- Thus, the S3 steel has a potential to deliver improved corrosion performance in concrete environments provided weldability concerns are suitably addressed.

IV. Grain refinement and microstructural evolution during thermo-mechanical processing. These studies reveal:

- An average grain size of 5-7 μm can be obtained for the high phosphorous steels when worked at lower temperatures of the ($\alpha+\gamma$) region of the phase diagram.
- In general, the grain size decreased with an increase in strain rate and a decrease in the deformation temperature. However, the adiabatic rise in temperature caused deviations from the general trend.
- Generally, higher alloying in the high phosphorous steels increases the activation energy and hence retards the recrystallization of austenite, resulting in the increment of peak flow stress.
- Increased P content in the steels causes the peak stress to first decrease from 750°C to 850°C, then increase from 850°C to 950°C and then decrease again from 950°C to 1050°C, at all strain rates, in general. Hence, it can be hot worked at temperatures near 850°C to achieve fine grain size.

- Fine grained steel is expected to show better impact toughness. Hence toughness can be further improved by producing finer grained high phosphorous steel by thermo-mechanical processing.

V. Hot formability studies reveal that:

- On comparing with the interstitial free steel studied by Tsuji and co-workers (Tsuji et al., 1997) it can be observed that the addition of 0.13 wt. % of phosphorous to pure iron causes the peak flow stress to increase by 33% at 850°C and 10s^{-1} strain rate.
- A processing map for S1 steel is developed over a wide range of deformation temperatures and strain rates by using the modified dynamic materials model.
- High values of η at low strain rates and high temperature result from dynamic recrystallization of austenite. High values of η at low strain rates and low temperatures are the result of ferrite formation and dynamic recovery of ferrite.
- Instability domain is found to occur between 850-1050°C for strain rates between 10-0.5 s^{-1}. Another domain is found at 750-850°C and 0.01-0.5 s^{-1} strain rates. A third domain is located at 900-1000°C between 0.5-0.01 s^{-1} strain rates.
- Stable domains occur at 900°C and 0.1 s^{-1} strain rate, between 1000-1050°C and 0.001-1 s^{-1} strain rates and between 750-1050°C at 0.001 s^{-1} strain rate.

Therefore, fine grained high phosphorous steel rebars, having good impact toughness and improved corrosion resistance can be manufactured. The safe processing window can be utilized for this purpose. The prepared rebars can be used for concrete reinforcement applications after suitably addressing the weldability concerns.

Chapter 6

SUGGESTIONS FOR FUTURE WORK

The following works are suggested for the further investigation of high phosphorous steels.

1. The concentration of phosphorous can be increased and the resulting steel can be studied for the increase in mechanical strength and corrosion resistance.
2. The EIS studies of the steels prepared in this work can be carried out for longer periods of time, *e.g.*, a few months to a few years.
3. Atmospheric exposure study of steels prepared in this work can be conducted over periods of time to understand the long term rusting process.
4. Weldability of the prepared high phosphorous steels can be studied.

PUBLICATIONS

International peer-reviewed journals:

1. Yashwant Mehta, Vikram V. Dabhade, Gajanan P. Chaudhari, Metallography of Fe-P-C and Fe-P-C-Si-N alloys, **Metallography, microstructure and analysis**, Vol. 4, Issue 6, (2015) pp 488-496

2. Yashwant Mehta, Vikram V. Dabhade, Gajanan P. Chaudhari, Effect of silicon and nitrogen on the microstructure and mechanical behaviour of high-phosphorous steels, **Metallography, microstructure and analysis**, Vol. 5, Issue 5, (2016) pp 384-391

3. Yashwant Mehta, S.K. Rajput, V.V. Dabhade, and G.P. Chaudhari, Physical Simulation of Hot Deformation and Microstructural Evolution of Fe-0.05C-0.13P Steel, **Journal of materials engineering and performance**, Vol. 25, Issue 4, (2016) pp 1376-1383

4. Yashwant Mehta, S.K. Rajput, Gajanan P. Chaudhari, Vikram V. Dabhade, Influence of silicon and nitrogen on dynamic recrystallization and grain refinement of high phosphorous steels, under **revision** for **Journal of materials engineering and performance**.

International conference:

1. Yashwant Mehta, Gajanan P. Chaudhari, Vikram V. Dabhade, A study on chloride induced depassivation of Fe-P-C-Si and Fe-P-C-Si-N steels in simulated concrete pore solution, **International Conference on Recent Advances in Materials, Mechanical and Civil Engineering ICRAMMCE-2017**, (June 2017) Hyderabad-Telangana.

2. Yashwant Mehta, S.K. Rajput, G.P. Chaudhari, and V.V. Dabhade, Microstructural evolution in Fe-0.13P-0.05C steel during compression at elevated temperatures, **International Conference on Recent Advances in Materials, Mechanical and Civil Engineering ICRAMMCE-2017**, (June 2017) Hyderabad-Telangana.

BIBLIOGRAPHY

1. Abbasi, S.M., Momeni, A., 2012. Hot working behavior of Fe-29Ni-17Co analyzed by mechanical testing and processing map. Mater. Sci. Eng. A 552, 330–335.
2. Abiko, K., Suzuki, S., Kimura, H., 1982. Effect of carbon on the toughness and fracture mode of Fe-P alloys. Trans. Japan Inst. Met. 23, 43–52.
3. Abreu, C.M., Cristóbal, M.J., Losada, R., Nóvoa, X.R., Pena, G., Pérez, M.C., 2004. Comparative study of passive films of different stainless steels developed on alkaline medium. Electrochim. Acta 49, 3049–3056.
4. Allen, N.P., 1963. Iron and its dilute solid solutions. Wiley Interscience, New York, pp. 271–308.
5. Alonso, C., Andrade, C., Castellote, M., Castro, P., 2000. Chloride threshold values to depassivate reinforcing bars embedded in a standardized OPC mortar. Cem. Concr. Res. 30, 1047–1055.
6. Alvarez, M.G., Galvele, J.R., 1984. The mechanism of pitting of high purity iron in NaCl solutions. Corros. Sci. 24, 27–48.
7. Ameer, M.A., Fekry, A.M., Heakal, F.E.-T., 2004. Electrochemical behaviour of passive films on molybdenum-containing austenitic stainless steels in aqueous solutions. Electrochim. Acta 50, 43–49.
8. Andrade, C., Alonso, C., García, A.M., 1990. Oxygen availability in the corrosion of reinforcements. Adv. Cem. Res. 3, 127–132.
9. Arya, C., Xu, Y., 1995. Effect of cement type on chloride binding and corrosion of steel in concrete. Cem. Concr. Res. 25, 893–902.
10. Ashby, M.F., 1972. A first report on deformation-mechanism maps. Acta Metall. 20, 887–897.
11. Askill, J., 1970. Tracer diffusion data for metals, alloys and simple oxides. IFI/Plenum, New York, p. 47.
12. ASTM A242-04, 2001. High-strength low-alloy structural steel, in: ASTM Standard. p. 1.
13. ASTM A370, 2014. Standard test methods and definitions for mechanical testing of steel products, in: ASTM Standard. pp. 1–50.
14. ASTM A706, 2016. Standard specification for low-alloy steel deformed and plain bars for concrete, in: ASTM Standard. pp. 1–6.

15. ASTM A767, 2015. Standard specification for zinc-coating (galvanized) steel bars for concrete reinforcement, in: ASTM Standard. p. 5.
16. ASTM E1181-02, 2015. Standard test methods for characterizing duplex grain sizes, in: ASTM Standard. pp. 1–15. doi:10.1520/E1181-02R15.2
17. ASTM E 23-12c, 2013. Standard test methods for notched bar impact testing of metallic materials, in: ASTM Standard. pp. 1–25.
18. ASTM G5 14, 2011. Standard reference test method for making potentiostatic and potentiodynamic anodic polarization measurements, in: ASTM Standard. p. 9.
19. Avner, S.H., 1997. Introduction to physical metallurgy. Tata Mcgraw Hill, New Delhi, p. 361.
20. Awad, G.H., Hoar, T.P., 1975. The role of phosphates in inhibiting pitting of commercial mild steel in chloride-containing media. Corros. Sci. 15, 581–588.
21. Awe, S.A., Seifeddine, S., Jarfors, A.E.W., Lee, Y.C., Dahle, A.K., 2017. Development of new Al-Cu-Si alloys for high temperature performance. Adv. Mater. Lett. 8, 695–701.
22. Bain, E.C., 1939. Alloying elements in steel. U.S. Steel Corporation, Pittsburgh, p. 63.
23. Barbé, L., Verbeken, K., Wettinck, E., 2006. Effect of the addition of P on the mechanical properties of low alloyed TRIP steels. ISIJ Int. 46, 1251–1257.
24. Bardwell, J.A., MacDougall, B., Graham, M.J., 1988. Use of 18 O/SIMS and electrochemical techniques to study the reduction and breakdown of passive oxide films on iron. J. Electrochem. Soc. 135, 413–418.
25. Bardwell, J.A., McKubre, M.C.H., 1991. AC impedance spectroscopy of the anodic film on zirconium in neutral solution. Electrochim. Acta 36, 647–653.
26. Baweja, D., Roper, H., Sirivivatnanon, V., 1999. Chloride-induced steel corrosion in concrete : Part 2 - Gravimetric and electrochemical comparisons. Aci Mater. J. 96, 306–313.
27. Bertolini, L., Elsener, B., Pedeferri, P., Redaelli, E., Polder, R., 2004. Corrosion of steel in concrete. Wiley-VCH Verlag GmbH & Co., Weinheim, Germany, p. 22,32,67,90.
28. Bethencourt, M., Botana, F.J., Calvino, J.J., Marcos, M., Rodriguez-Chacon, M.A., 1998. Lanthanide compounds as environmentally-friendly corrosion inhibitors of aluminium alloys: a review. Corros. Sci. 40, 1803–1819.

29. Bethencourt, M., Botana, F.J., Cauqui, M.A., Marcos, M., Rodríguez, M.A., Rodríguez-Izquierdo, J.M., 1997. Protection against corrosion in marine environments of AA5083 Al–Mg alloy by lanthanide chlorides. J. Alloys Compd. 250, 455–460.

30. Betova, I., Bojinov, M., Laitinen, T., Mäkelä, K., Pohjanne, P., Saario, T., 2002. The transpassive dissolution mechanism of highly alloyed stainless steels: II. Effect of pH and solution anion on the kinetics. Corros. Sci. 44, 2699–2723.

31. Bhadeshia, H.K.D.H., Honeycombe R W K, 2006. Steels, microstructure and properties. pp. 246, 283.

32. Bockris, J.O., Drazic, D., Despic, A.R., 1961. The electrode kinetics of the deposition and dissolution of iron. Electrochim. Acta 4, 325–361.

33. Bockris, J.O., Genshaw, M.A., Brusic, V., Wroblowa, H., 1971. The mechanism of the passivation of iron in neutral solutions: An ellipsometric and coulometric investigation. Electrochim. Acta 16, 1859–1894.

34. Bojinov, M., Betova, I., Fabricius, G., Laitinen, T., Raicheff, R., Saario, T., 1999. The stability of the passive state of iron–chromium alloys in sulphuric acid solution. Corros. Sci. 50, 1557–1584.

35. Boyer, H.E., Gall, T.L., 1990. Metals handbook Vol.1. ASM International, Ohio, p. 144.

36. Briant, C.L., 1988. Competitive grain boundary segregation in Fe-P-S and Fe-P-Sb alloys. Acta Metall. 36, 1805–1813.

37. Briant, C.L., Banerji, S.K., 1982. The fracture behavior of quenched and tempered manganese steels. Metall. Trans. A 13, 827–836.

38. Briant, C.L., Banerji, S.K., 1979. Phosphorus induced 350°C embrittlement in an ultra high strength steel. Metall. Trans. A 10, 123–126.

39. Brown, B.F., 1970. The role of the occluded corrosion cell in stress corrosion cracking of high strength steels RT 170, in: Cebelcor. Cebelcor, pp. 1–3.

40. Cai, M., Park, S., 1996. Oxidation of Zinc in alkaline solutions studied by Electrochemical Impedance Spectroscopy. J. Electrochem. Soc. 143, 3895–3902.

41. Callister, W.D., Rethwisch, D.G., 2014. Material science and engineering. WILEY, New Delhi, pp. 285, 390, 261.

42. Capus, J.M., Meyer, G., 1963. Carbide precipitation, impurity elements, and the embrittlement of high-strength martensitic alloy steels. J. Iron Steel Inst. 201, 53–54.

43. Capus, J.M., Meyer, G., 1960. The mechanical properties of some tempered alloy martensites. J. Iron Steel Inst. 196, 149–158.

44. Chakrabarti, D., Patra, S., Haldar, A., Kumar, V., 2013. Refinement of ferrite grain size near to the ultra-fine range by single-pass and multi-pass thermo-mechanical compression. Int. J. Metall. Eng. 2, 52–55.
45. Chakravartty, J.K., Dey, G.K., Banerjee, S., Prasad, Y.V.R.K., 1995. Characterization of hot deformation behaviour of Zr-2.5Nb-0.5Cu using processing maps. J. Nucl. Mater. 218, 247–255.
46. Chen, H.C., Era, H., Shimizu, M., 1989. Effect of phosphorus on the formation of retained austenite and mechanical properties in Si-containing low-carbon steel sheet. Metall. Trans. A 20, 437–445.
47. Chen, W., Du, R., Ye, C., Zhu, Y., Lin, C., 2010. Study on the corrosion behavior of reinforcing steel in simulated concrete pore solutions using in situ Raman spectroscopy assisted by electrochemical techniques. Electrochim. Acta 55, 5677–5682.
48. Chilton, J.M., Roberts, M.J., 1980. Microalloying effects in hot-rolled low-carbon steels finished at high temperatures. Metall. Trans. A 11, 1711–1721.
49. Cho, S., Kang, K., Jonas, J.J., 2001. The dynamic, static and metadynamic recrystallization of a Nb-microalloyed steel. ISIJ Int. 41, 63–69.
50. Choi, J., Seo, D., Lee, J., Um, K., Choo, W., 2003. Formation of ultrafine ferrite by strain-induced dynamic transformation in plain low carbon steel. ISIJ Int. 43, 746–754.
51. Chung, J.H., Park, J.K., Kim, T.H., Kim, K.H., Ok, S.Y., 2010. Study of deformation-induced phase transformation in plain low carbon steel at low strain rate. Mater. Sci. Eng. A 527, 5072–5077.
52. Chunling, Z., Dayong, C., Bo, L., Tianchen, Z., Yunchang, F., 2004. Microstructure and mechanical properties of dual-phase weathering steel 09CuPTiRe. J. Mater. Sci. 39, 4393–4396.
53. Clarke, B.D., McIvor, I.D., 1989. Effect of phosphorus on microstructure and strength of high carbon steel rod. Ironmak. Steelmak. 16, 335–344.
54. Cox, B., Wong, Y.-M., 1995. Simulating porous oxide films on zirconium alloys. J. Nucl. Mater. 218, 324–334.
55. Cramer, S.D., Covino, Jr., B.S., Bullard, S.J., Holcomb, G.R., Russell, J.H., Ziomek-Moroz, M., Virmani, Y.P., Butler, J.T., Nelson, F.J., Thompson, N.G., 2002. Prevention of chloride-induced corrosion damage to bridges. ISIJ Int. 42, 1376–1385.

56. Cruz, J., Pandiyan, T., Garcı, E., 2005. A new inhibitor for mild carbon steel: Electrochemical and DFT studies. J. Electroanal. Chem. 583, 8–16.
57. Dallek, S., Foley, R.T., 1976. Mechanism of pit initiation on aluminum alloy type 7075. J. Electrochem. Soc. 123, 1775–1779.
58. Darwin, A.B., Scantlebury, J.D., 2002. Retarding of corrosion processes on reinforcement bar in concrete with an FBE coating. Cem. Concr. Compos. 24, 73–78.
59. Davies, R.G., 1979. Influence of silicon and phosphorous on the mechanical properties of both ferrite and dual-phase steels. Metall. Trans. A 10, 113–118.
60. De Avillez, R.R., Rios, P.R., 1983. The influence of carbon on the phosphorus segregation in iron alloys. Scr. Mater. 17, 677–680.
61. Dieter, G.E., 1988. Mechanical Metallurgy, 3rd ed. McGraw Hill, London.
62. Dong-sheng, Q., Ya-ya, P., Jia-dong, D., 2017. Hot deformation behavior and constitutive modeling of Q345E alloy steel under hot compression. J. Cent. South Univ. 24, 284–295.
63. Dong, H., Cai, D., Zhao, Z., Wang, Z., Wang, Y., Yang, Q., Liao, B., 2010. Investigation on static softening behaviors of a low carbon steel under ferritic rolling condition. J. Mater. Eng. Perform. 19, 151–154.
64. Dube, C.C., Aaronson, H.I., Mehl, R.F., 1958. la formation de la ferrite proeutectoidedans les aciers au carbon. Rev. Met. 55, 201–210.
65. Durand-Charre, M., 2004. Microstructure of steels and cast irons. Springer-Verlag, Berlin, p. 265.
66. Eghbali, B., Abdollah-zadeh, A., 2006. Influence of deformation temperature on the ferrite grain refinement in a low carbon Nb – Ti microalloyed steel. J. Mater. Process. Technol. 180, 44–48.
67. Eghbali, B., Abdollah-zadeh, A., 2005a. The influence of thermomechanical parameters in ferrite grain refinement in a low carbon Nb-microalloyed steel. Scr. Mater. 53, 41–45.
68. Eghbali, B., Abdollah-zadeh, A., 2005b. Effect of strain rate on the ferrite grain refinement in a low carbon Nb-Ti microalloyed steel during low temperature deformation. J. Mater. Sci. Tech. 21, 851–855.
69. Erhart, H., Grabke, H.J., 1981. Equilibrium segregation of phosphorus at grain boundaries of Fe-P , Fe-C-P , Fe-Cr-P , and Fe-Cr-C-P alloys. Met. Sci. 15, 401–408.
70. Erhart, H., Grabke, H.J., 1981. Site competition in grain boundary segregation of phosphorus and nitrogen in iron. Scr. Metall. 15, 531–534.

71. Feng, X., Tang, Y., Zuo, Y., 2011. Influence of stress on passive behaviour of steel bars in concrete pore solution. Corros. Sci. 53, 1304–1311.

72. Fidler, H., 1907. Influence of phosphorous, in: Notes on Construction in Mild Steel. Longmans, Green, And Co., p. 11.

73. Flitt, H.J., Schweinsberg, D.P., 2005. Evaluation of corrosion rate from polarisation curves not exhibiting a Tafel region. Corros. Sci. 47, 3034–3052.

74. Fontana, M.G., 1987. Corrosion engineering. McGraw Hill, New York, pp. 23-27-503.

75. Foroulis, Z.A., Thubrikar, M.J., 1975. On the kinetics of the breakdown of passivity of preanodized aluminum by chloride ions. J. Electrochem. Soc. 122, 1296–1301.

76. Gadadhar, S., Balasubramaniam, R., 2008. Corrosion of phosphoric irons in acidic environments. J. ASTM Int. 5, 1–7.

77. Garces, P., Andrade, M.C., Saez, A., Alonso, M.C., 2005. Corrosion of reinforcing steel in neutral and acid solutions simulating the electrolytic environments of micropores of concrete in the propagation period. Corros. Sci. 47, 289–306.

78. Génin, J.M.R., Dhouibi, L., Refait, P., Abdelmoula, M., Triki, E., 2002. Influence of phosphate on corrosion products of iron in chloride-polluted-concrete-simulating solutions: Ferrihydrite vs green rust. Corrosion 58, 467–478.

79. Ghasemi, R., Elmquist, L., Svensson, H., König, M., Jarfors, A.E.W., 2016. Mechanical properties of solid solution-strengthened CGI. Int. J. Cast Met. Res. 29, 97–104.

80. Gladman, T., 1997. Physical metallurgy of microalloyed steels. pp. 33–35.

81. Goetz, R.L., Semiatin, S.L., 2001. The adiabatic correction factor for deformation heating during the uniaxial compression test. J. Mater. Eng. Perform. 10, 710–717.

82. Gomez, Mejia, J.A., Antonissen, J., Palacio, C.A., De Grave, E., 2012. Effects of Si as alloying element on corrosion resistance of weathering steel. Corros. Sci. 59, 198–203.

83. Goñi, S., Andrade, C., 1990. Synthetic concrete pore solution chemistry and rebar corrosion rate in the presence of chlorides. Cem. Concr. Res. 20, 525–539.

84. Goodway, M., 1993. Discussion on "Characterization of early and modern wire for an Italian harpsichord’’ by J.H. Underwood et al. J. Test. Eval. 21, 136–137.

85. Goodway, M., Fisher, R.M., 1988. Phosphorus in low carbon iron: Its beneficial properties. Hist. Metall. 22, 21–23.

86. Gouda, V.K., 1970. Corrosion and corrosion inhibition of reinforcing steel: I. immersed in alkaline solutions. Br. Corros. J. 5, 198–203.

87. Gouthama, Balasubramaniam, R., 2003. Alloy design of ductile phosphoric iron: Ideas from archaeometallurgy. Bull. Mater. Sci. 26, 483–491.

88. Gove, K.B., Charles, J.A., 1974. The high temperature hardness of various phases in steel. Met. Technol. 279–283.

89. Grabke, H.J., 1996. The role of nitrogen in the corrosion of iron and steels. ISIJ Int. 36, 777–786.

90. Gruzin, P.L., Mural, V. V., 1969. Mechanism of the effect of molybdenum on the reversible temper brittleness of steel. Met. Sci. Heat Treat. 11, 240–242.

91. Guilbaud, J.P., Chahbazian, G., Derrien, F., Raharinaivo, A., 1994. Electrochemical behaviour of steel under cathodic protection in medium simulating concrete, in: Swamy, R.N. (Ed.), Corrosion and Corrosion Protection of Steel in Concrete. Sheffield academic press Vol.2, pp. 1382–1391.

92. Guttmann, M., 1980. Temper embrittlement and ternary equilibrium segregation. Mater. Sci. Eng. 42, 227–232.

93. Hadfield, R.A., 1889. On alloys of iron and silicon. J. Iron Steel Inst. II, 222–242.

94. Hamadou, L., Kadri, A., Benbrahim, N., 2005. Characterisation of passive films formed on low carbon steel in borate buffer solution (pH 9.2) by electrochemical impedance spectroscopy. Appl. Surf. Sci. 252, 1510–1519.

95. Han, B.Q., Yue, S., 2003. Processing of ultrafine ferrite steels. J. Mater. Process. Technol. 136, 100–104.

96. Hansel, H., Grabke, H.J., 1986. Grain boundary segregation of phosphorus and carbon in ferritic iron. Scr. Metall. 20, 1641–1644.

97. Hara, S., Miura, M., Uchiumi, Y., Fujiwara, T., Yamamoto, M., 2005. Suppression of deicing salt corrosion of weathering steel bridges by washing. Corros. Sci. 47, 2419–2430.

98. Harrison, T.C., 1977. Cold twisting of reinforcing steels. Metallurgia 44, 56–59.

99. Hausmann, D.A., 1967. Steel corrosion in concrete - how does it occur? Mater. Prot. 6, 19–23.

100. Hays, G.F., 2016. Now is the time. World Corros. Organ. 1–2.

101. Hennesen, K., Moller, R., Wei, W., Grabke, H.J., 1987. Effects of manganese on the grain boundary segregation, bulk and grain boundary diffusivity of P in ferrite. Scr. Metall. 21, 1329–1334.

102. Hoar, T.P., 1967. The production and breakdown of the passivity of metals. Corros. Sci. 7, 341–355.

103. Hoar, T.P., 1949. The breakdown and repair of oxide films on iron. Trans. Faraday Soc. 45, 683–693.

104. Hoar, T.P., Jacob, W.R., 1967. Breakdown of passivity of stainless steel by halide ions. Nature 216, 1299–1301.

105. Hoar, T.P., Mears, D.C., Rothwell, G.P., 1965. The relationships between anodic passivity, brightening and pitting. Corros. Sci. 5, 279–289.

106. Hodgson, P.D., Hickson, M.R., Gibbs, R.K., 1999. Ultrafine ferrite in low carbon steel. Scr. Mater. 40, 1179–1184.

107. Hong, S.C., Lee, K.S., 2002. Influence of deformation induced ferrite transformation on grain refinement of dual phase steel. Mater. Sci. Eng. A 323, 148–159.

108. Hong, S.C., Lim, S.H., Lee, K.J., Shin, D.H., Lee, K.S., 2003. Effect of undercooling of austenite on strain induced ferrite transformation behavior. ISIJ Int. 43, 394–399.

109. Hong, T., Walter, G.W., Nagumo, M., 1996. The observation of the early stages of pitting on passivated type 304 stainless steel in a 0.5 M NaCl solution at low potentials in the passive region by using the AC impedance method. Corros. Sci. 38, 1525–1533.

110. Hope, B.B., Ip, A.K.C., 1987. Chloride corrosion threshold in concrete. ACI Mater. J. 84, 306–314.

111. Hopkins, B.E., Tipler, H.R., 1958. The effect of phosphorus on the tensile and notch impact properties of high purity iron and iron carbon alloys. J Iron Steel Inst. 188, 218–237.

112. Horn, R.M., Ritchie, R.O., 1978. Mechanisms of Tempered Martensite Embrittlement in Low Alloy Steels. Metall. Trans. A 9, 1039–1053.

113. Hu, H., 1979. Effect of carbon content on annealing texture, plastic anisotropy, and mechanical properties of 0.07% phosphorous sheet steels. Texture Cryst. Solids 3, 215–230.

114. Hu, H., 1976. Effects of phosphorus on the annealing texture, plastic anisotropy, and mechanical properties of low-carbon steels. Texture Cryst. Solids 2, 113–141.

115. Huang, Y.D., Froyen, L., 2002. Important factors to obtain homogeneous and ultrafine ferrite – pearlite microstructure in low carbon steel. J. Mater. Process. Technol. 124, 216–226.

116. Hudson, J.C., Stanners, J.F., 1955. The corrosion resistance of low alloy steels. J. Iron Steel Inst. 180, 271–284.

117. Hurley, P.J., Hodgson, P.D., 2001. Formation of ultra-fine ferrite in hot rolled strip : potential mechanisms for grain refinement. Mater. Sci. Eng. A 302, 206–214.

118. Hussain, S.E., Rasheeduzzafar, Al-Musallam, A., Al-Gahtani, A.S., 1995. Factors affecting threshold chloride for reinforcement corrosion in concrete. Cem. Concr. Res. 25, 1543–1555.

119. Indian Standard 1786, 2008. High strength deformed steel bars and wires for concrete reinforcement— (Fourth Revision), in: Indian Standard. pp. 1–10.

120. Inman, M.C., Tipler, H.R., 1958. Grain-boundary segregation of phosphorus in an iron-phosphorus alloy and the effect upon mechanical properties. Acta Metall. 6, 73–84.

121. Islam, M.A., Sato, N., Tomota, Y., 2011. Tensile and plane bending fatigue properties of pure iron and iron-phosphorus alloys at room temperature in the air. Trans. Indian Inst. Met. 64, 315–320.

122. ISO 898-1, 2013. Mechanical properties of fasteners made of carbon steel and alloy steel, in: ISO Standard. p. 7.

123. Jae-Hyeok, S., Chang-Seok, O., Dong Nyung, L., 2000. Thermodynamic assessment of the Fe-C-P system. Zeitschrift für Met. 91, 114–120.

124. Jaegermann, C., 1990. Effect of water-cement ratio and curing on chloride penetration into concrete exposed to mediterranean sea climate. Mater. J. 87, 333–339.

125. Jang, J.-W., Hagen, M.G., Engstrom, G.M., Iwasaki, I., 1998. Cl−, SO4 2−, and PO4 3− distribution in concrete slabs ponded by corrosion-inhibitor-added deicing salts. Adv. Cem. Based Mater. 8, 101–107.

126. Janik-Czachor, M., Szummer, A., Szklarska-Smialowska, Z., 1975. Electron microprobe investigation of processes leading to the nucleation of pits on iron. Corros. Sci. 15, 775–778.

127. Jian-wen, F., Xiao-li, D., Rui-ping, X., Wei-xu, Z., Zu-bin, W., 2006. Surface ferrite grain refinement and mechanical properties of low carbon steel plates. J. Iron Steel Res. Int. 13, 35–39.

128. Jone, D.A., 1992. Principles and prevention of corrosion. Macmillan Publishing Company, New York, pp. 145–148.

129. Josefsson, A., 1954. Pearlite-free bessemer steels: its fabrication and properties. J. Iron Steel Inst. 177, 118–128.

130. Katayamaa, T., Tagamia, M., Saraia, Y., Izumib, S., Hirab, T., 2004. Alkali aggregate reaction under the influence of deicing salts in the hokuriku district. Mater. Charact. 53, 105–122.

131. Kayyali, O.A., Haque, M.N., 1995. The C1−/OH− ratio in chloride-contaminated concrete — a most important criterion. Mag. Concr. Res. 47, 235–242.

132. Keddam, M., Krarti, M., Pallotta, C., 1987. Some aspects of the fluctuations of the passive current on stainless steel in presence of chlorides - their relation to the probalistic approach of pitting corrosion. Corrosion 43, 454–458.

133. Kelly, E.J., 1965. The active iron electrode: 1 Iron dissolution and hydrogen evolution reactions in acidic sulfate solutions. J. Electrochem. Soc. 112, 124–131.

134. Kelly, R.G., Scully, J.R., Shoesmith, D.W., Buchheit, R.G., 2003. Electrochemical techniques in corrosion science and engineering. Marcel Dekker, New York, pp. 73–87.

135. Kihira, H., Kimura, M., 2011. Advancements of weathering steel technologies in japan. Corrosion 67, 1–13.

136. Kim, S., Lee, Y., Lee, D., Yoo, Y., 2003. Modeling of AGS and recrystallized fraction of microalloyed medium carbon steel during hot deformation. Mater. Sci. Eng. A 355, 384–393.

137. Kim, S.I., Choi, S.H., Lee, Y., 2005. Influence of phosphorous and boron on dynamic recrystallization and microstructures of hot-rolled interstitial free steel. Mater. Sci. Eng. A 406, 125–133.

138. Kim, Y.M., Kim, S.K., Lim, Y.J., Kim, N.J., 2002. Effect of microstructure on the yield ratio and low temperature toughness of linepipe steels. ISIJ Int. 42, 1571–1577.

139. Kimura, Y., Inoue, T., Yin, F., Tsuzaki, K., 2008. Inverse temperature dependence of toughness in an ultrafine grain-structure steel. Science (80-.). 320, 1057–1060.

140. Kobayashi, K., Shuttoh, K., 1991. Oxygen diffusivity of various cementitious materials. Cem. Concr. Res. 21, 273–284.

141. Kreyser, G., Eckermann, R., 1992. DECHEMA Corrosion Handbook, in: Vol. 11. VCH Publishers, New York, p. 182.

142. Kruger, J., Calvert, J.P., 1967. Ellipsometric-potentiostatic studies of iron passivity I . Anodic film growth in slightly basic solutions. J. Electrochem. Soc. 114, 43–49.

143. Kumar, N., Kumar, S., Rajput, S.K., Nath, S.K., 2017. Modelling of flow stress and prediction of workability by processing map for hot compression of 43CrNi steel. ISIJ Int. 57, 497–505.

144. Kumar, V., 2015. Improving steel processing through thermo-mechanical simulation studies. Mater. Perform. Charact. 4, 421–435.

145. Kundu, S., Mukhopadhyay, A., Chatterjee, S., Chandra, S., 2004. Modeling of microstructure and heat transfer during controlled coolling of low carbon wire rod. ISIJ Int. 44, 1217–1223.

146. Küpper, J., Erhart, H., Grabke, H., 1981. Intergranular corrosion of iron-phosphorus alloys in nitrate solutions. Corros. Sci. 21, 227–238.

147. Lambert, P., Page, C.L., Vassie, P.R.W., 1991. Investigations of reinforcement corrosion. 2. Electrochemical monitoring of steel in chloride-contaminated concrete. Mater. Struct. 24, 351–358.

148. Lee, D.Y., Barrera, E. V, Stark, J.P., Marcus, H.L., 1984. The influence of alloying elements on impurity induced grain boundary embrittlement. Metall. Trans. A 15, 1415–1430.

149. Lee, K., Lee, H., 2010. Grain refinement and mechanical properties of asymmetrically rolled low carbon steel. J. Mater. Process. Technol. 210, 1574–1579.

150. Li, N., Liu, Z., Qiu, Y., Lin, Z., Liu, X., Wang, G., 2006. Solidification structure of low carbon steel strips with different phosphorus contents produced by strip casting. J. Mater. Sci. Technol. 22, 755–758.

151. Lin, Y.C., Liu, G., 2009. Effects of strain on the workability of a high strength low alloy steel in hot compression. Mater. Sci. Eng. A 523, 139–144.

152. Liu, C., Abiko, K., Tanino, M., 1994. Role of chromium in the intergranular fracture of high purity Fe-P-Cr alloys with small amounts of carbon. Mater. Sci. Eng. A 176, 363–369.

153. Liu, C.M., Abiko, K., Kimura, H., 1989. Effect of silicon on the grain boundary segregation of phosphorus and the phosphorus induced intergranular fracture in high purity Fe-Si-P Alloys, in: Kettunen, P.O., Lepistö, T.K., Lehtonen, M.E. (Eds.), Strength of Metals and Alloys (ICSMA 8), Volume 3, Proceedings of the 8th International Conference on the Strength of Metals and Alloys, Tampere, Finland, 22-26 Aug. 1988,. Pergamon Press, Tampere, pp. 1101–1106.

154. Liu, C.M., Nagoya, T., Abiko, K., Kimura, H., 1992. Effect of boron on the grain boundary segregation of phosphorus and intergranular fracture in high-purity Fe-0.2 Pct P-B alloys. Metall. Trans. A 23, 263–269.

155. Liu, Z., Kobayashi, Y., Nagai, K., 2005. Effect of phosphorus on sulfide precipitation in strip casting low carbon steel. Mater. Trans. 46, 26–33.

156. Liu, Z., Zhou, G., Qiu, Y., Wang, G., 2010. Inversed phosphorus segregation in twin roll cast strips for improvement of mechanical properties and weathering resistance. ISIJ Int. 50, 531–539.

157. López, W., González, J.A., Andrade, C., 1993. Influence of temperature on the service life of rebars. Cem. Concr. Res. 23, 1130–1140.

158. Lorbeer, P., Lorenz, W.J., 1980. The kinetics of iron dissolution and passivation in solutions containing oxygen. Corros. Sci. 25, 375–381.

159. MacDougall, B., Graham, M.J., 1995. Growth and stability of passive films, in: Marcus, P. (Ed.), Corrosion Mechanism in Theory and Practice. Marcel Dekker, New York, pp. 199–201.

160. Mammoliti, L.T., Brown, L.C., Hansson, C.M., Hope, B.B., 1996. The influence of surface finish of reinforcing steel and pH of the test solution on the chloride threshold concentration for corrosion initiation in synthetic pore solutions. Cem. Concr. Res. 26, 545–550.

161. Mansfeld, F., 2005. Editorial: Misconceptions and misnomers. Corrosion 61, 1019–1021.

162. Mansfeld, F., 1974. Some errors in linear polarization measurements and their correction. Corrosion 30, 92–96.

163. Mansfeld, F., Wang, V., Shih, H., 1991. Development of stainless Aluminum. J. Electrochem. Soc. 138, L74–L75.

164. Martinez, L., Hernandez, G., Pérez, J.J.C., Arganis, C., 1995. Corrosion and physical properties of microalloyed rebar. Mater. Perform. 34, 14–17.

165. McCafferty, E., 2005. Validation of corrosion rates measured by the Tafel extrapolation method. Corros. Sci. 47, 3202–3215.

166. McDonnell, G., 1989. Iron and its alloys in the fifth to eleventh centuries AD in England. World Archaeol. 20, 373–382.

167. McQueen, H.J., 2002. Elevated-temperature deformation at forming rates of 10−2 to 10 2 s−1. Metall. Mater. Trans. A 33, 345–362.

168. Mcqueen, H.J., Yue, S., Ryan, N.D., Fry, E., 1995. Hot working characteristics of steels in austenitic state. J. Mater. Process. Technol. 53, 293–310.

169. Mehta, Y., Chandra, K., Ambardar, R., Mishra, P.S., 2010. Effect of heat treatment on Fe–0.3 % P – 0.14 % C alloy. J. Miner. Mater. Charact. Eng. 9, 787–794.

170. Mehta, Y., Mishra, P.S., 2011. Thermo-mechanical processing of iron-phosphorous-carbon alloys. J. Miner. Mater. Charact. Eng. 10, 93–100.

171. Menyhard, M., 1992. Phosphorus on the non-brittle grain boundaries of iron. Scr. Metall. Mater. 26, 1695–1700.

172. Menyhard, M., McMahon, C.J., 1989. On the effect of molybdenum in the embrittlement of phosphorus-doped iron. Acta Metall. 37, 2287–2295.

173. Mirzaee, M., Keshmiri, H., Ebrahimi, G.R., Momeni, A., 2012. Dynamic recrystallization and precipitation in low carbon low alloy steel 26NiCrMoV 14-5. Mater. Sci. Eng. A 551, 25–31.

174. Misawa, T., 1973. The thermodynamic consideration for Fe-H2O system at 25°C. Corros. Sci. 13, 659–676.

175. Misra, R.D.K., 1991. Influence of vanadium on grain boundary segregation of phosphorus in iron and iron-carbon alloys. Bull. Mater. Sci. 14, 1309–1322.

176. Modak, P., Ghosh, A., Rarhi, N., Kumar, V., Balamuralikrishnan, R., Chakrabarti, D., 2016. A review on the effect of microstructure, texture and inclusion on Charpy impact transition behaviour of low- carbon ferritic steels. IIM Met. News 19, 21–34.

177. Momeni, A., Arabi, H., Rezaei, A., Badri, H., Abbasi, S.M., 2011. Hot deformation behavior of austenite in HSLA-100 microalloyed steel. Mater. Sci. Eng. A 528, 2158–2163.

178. Montheillet, F., Jonas, J.J., Neale, K.W., 1996. Modeling of dynamic material behavior: A critical evaluation of the dissipator power co-content approach. Metall. Mater. Trans. A 27, 232–235.

179. Moreno, M., Morris, W., Alvarez, M.G., Duffo, G.S., 2004. Corrosion of reinforcing steel in simulated concrete pore solutions effect of carbonation and chloride content. Corros. Sci. 46, 2681–2699.

180. Mulford, R.A., Mcmahon, C.J., Pope, D.P., Feng, H.C., 1976. Temper embrittlement of Ni-Cr steels by phosphorus. Metall. Trans. A 7, 1183–1195.

181. Murty, S.V.S.N., Rao, B.N., 1998. Ziegler 's criterion on the instability regions in processing maps. J. Mater. Sci. Lett. 17, 1203–1205.

182. Murty, S.V.S.N., Rao, B.N., Kashyap, B.P., 2005a. On the hot working characteristics of 2014 Al–20 vol % Al2O3 metal matrix composite. J. Mater. Process. Technol. 166, 279–285.

183. Murty, S.V.S.N., Rao, B.N., Kashyap, B.P., 2003. On the hot working characteristics of 6061Al–SiC and 6061–Al2O3 particulate reinforced metal matrix composites. Compos. Sci. Technol. 63, 119–135.

184. Murty, S.V.S.N., Rao, B.N., Kashyap, B.P., 2002. Development and validation of a processing map for zirconium alloys. Model. Simul. Mater. Eng. 10, 503–520.

185. Murty, S.V.S.N., Rao, B.N., Kashyap, B.P., 2000. Instability criteria for hot deformation of materials. Int. Mater. Rev. 45, 15–26.

186. Murty, S.V.S.N., Torizuka, S., Nagai, K., Kitai, T., Kogo, Y., 2005b. Dynamic recrystallization of ferrite during warm deformation of ultrafine grained ultra-low carbon steel. Scr. Mater. 53, 763–768.

187. Muylder, J. Van, Pourbaix, M., 1966. Establishment and interpretation of potential-pH equilibrium diagram of P, in: Atlas of Electrochemical Equilibria in Aqueous Solutions, Cebelcor. Pergamon Press, Brussels, pp. 504–515.

188. Nagayama, M., Cohen, M., 1962. The anodic oxidation of iron in a neutral solution I . The nature and composition of the passive film. J. Electrochem. Soc. 109, 781–790.

189. Ngala, V.T., Page, C.L., Page, M.M., 2002. Corrosion inhibitor systems for remedial treatment of reinforced concrete . Part 1 : calcium nitrite. Corros. Sci. 44, 2073–2087.

190. Nishimura, R., Araki, M., Kudo, K., 1984. Breakdown of Passive Film on lron. Corrosion 40, 465–470.

191. Nishimura, T., 2008. Rust formation and corrosion performance of Si- and Al-bearing ultrafine grained weathering steel. Corros. Sci. 50, 1306–1312.

192. Nishimura, T., 2008. Corrosion resistance of Si–Al-bearing ultrafine-grained weathering steel. Sci. Technol. Adv. Mater. 9, 1–7.

193. Nmai, C.K., 2004. Multi-functional organic corrosion inhibitor. Cem. Concr. Compos. 26, 199–207.

194. Nmai, C.K., Farrington, S.A., Bobroski, G., 1992. Organic-based corrosion-inhibiting admixture for reinforced concrete. Concr. Int. 14, 45–51.

195. O. Kubaschewski, 1982. Iron—binary phase diagrams. Springer Verlag, Berlin, p. 84.

196. O’Neill, R.C., Hill, R.L., 2008. Guide to durable concrete, in: American Concrete Institute. p. 18.

197. Okamoto, H., 1990. The Fe-P (iron-phosphorus) system. Bull. Alloy Phase Diagrams 11, 404–412.

198. Oldham, K.B., Mansfeld, F., 1971. Technical note on the so-called linear polarization method for measurement of corrosion rates. Corrosion 27, 434–435.

199. Oranowska, H., Szklarska-Smialowska, Z., 1981. An electrochemical and ellipsometric investigation of surface films grown on iron in saturated calcium hydroxide solutions with or without chloride ions. Corros. Sci. 21, 735–747.

200. Ord, J.L., DeSmet, D.J., 1966. Correlation between ellipsometric and electrical measurements on passive iron. J. Electrochem. Soc. 113, 1258–1262.

201. Ordonez, R., Garcia, C.I., DeArdo, A.J., 2010. Effect of thermomechanical processing and cooling rate conditions on the austenite decomposition behavior in hypereutectoid steels, in: Material Science and Technology (MS & T) 2010, October 2010; Austenite Formation and Decomposition IV. pp. 1327–1335.

202. Panigrahi, B.K., 2010a. Microstructure-related properties of some novel reinforcement bar steel. J. Mater. Eng. Perform. 19, 287–293.

203. Panigrahi, B.K., 2010b. Microstructure-mechanical property relationships for a Fe/Mn/Cr rock bolt reinforcing steel. J. Mater. Eng. Perform. 19, 885–893.

204. Panigrahi, B.K., Jain, S.K., 2002. Impact toughness of high strength low alloy TMT reinforcement ribbed bar. Bull. Mater. Sci. 25, 319–324.

205. Panigrahi, B.K., Srikanth, S., Sahoo, G., 2009. Effect of alloying elements on tensile properties, microstructure, and corrosion resistance of reinforcing bar steel. J. Mater. Eng. Perform. 18, 1102–1108.

206. Piccardo, P., Ienco, M.G., Balasubramaniam, R., Dillmann, P., 2004. Detecting non-uniform phosphorus distribution in ancient Indian iron by colour metallography. Curr. Sci. 87, 650–653.

207. Pickering F.B., 1978. Physical metallurgy and the design of steels. Applied Science Publishers, London, pp. 10–11.

208. Poupard, O., Ait-Mokhtar, A., Dumargue, P., 2004. Corrosion by chlorides in reinforced concrete: Determination of chloride concentration threshold by impedance spectroscopy. Cem. Concr. Res. 34, 991–1000.

209. Pourbaix, M., 1974. Applications of electrochemistry in corrosion science and in practice. Corros. Sci. 14, 25–82.

210. Pourbaix, M., Zoubov, N.D., 1966. Establishment and interpretation of potential-pH equilibrium diagram of Fe, in: Atlas of Electrochemical Equilibria in Aqueous Solutions, Cebelcor. Pergamon Press, Brussels, pp. 307–321.

211. Prado, J.M., Catalan, J.J., Marsal, M., 1990. Dilatometric study of isothermal phase tranformation in a C-Mn steel. J. Mater. Sci. 25, 1939–1946.

212. Prasad, Y., 1996. Author's reply: Dynamic materials model: Basis and principles. Metall. Mater. Trans. A 27, 235–236.

213. Prasad, Y.V.R.K., Gegel, H.L., Doraivelu, S.M., Malas, J.C., Morgan, J.T., Lark, K.A., Barker, D.R., 1984. Modeling of dynamic material behavior in hot deformation: Forging of Ti-6242. Metall. Trans. A 15, 1883–1892.

214. R. Vogel, 1929. On the system iron-phosphorus-carbon. Arch Eisenhuttenwes 3, 369–81.

215. Raghavan, V., 2004. C-Fe-P (Carbon-Iron-Phosphorus). J. phase equilibria Diffus. 25, 541–542.

216. Rajput, S.K., Chaudhari, G.P., Nath, S.K., 2014. Physical simulation of hot deformation of low-carbon Ti-Nb microalloyed steel and microstructural studies. J. Mater. Eng. Perform. 23, 2930–2942.

217. Rajput, S.K., Dikovits, M., Chaudhari, G.P., Poletti, C., Warchomicka, F., Pancholi, V., Nath, S.K., 2013. Physical simulation of hot deformation and microstructural evolution of AISI 1016 steel using processing maps. Mater. Sci. Eng. A 587, 291–300.

218. Rao, K.P., Prasad, Y.K.D.V., Hawbolt, E.B., 1996. Hot deformation studies on a low-carbon steel: Part 1 - flow curves and the constitutive relationship. J. Mater. Process. Technol. 56, 897–907.

219. Rasheeduzzafar, S.S., Al-Saadoun, A.S., Al-Gahtani, Dakhil, F.H., 1990. Effect of tricalcium aluminate content of cement on corrosion of reinforcing steel in concrete. Cem. Concr. Res. 20, 723–738.

220. Rastegari, H., Kermanpur, A., Najafizadeh, A., Somani, M.C., Ghassemali, E., Jarfors, A.E.W., 2016. Determination of processing maps for the warm working of vanadium microalloyed eutectoid steels. Mater. Sci. Eng. A 658, 167–175.

221. Rege, J.S., Hua, M., Garcia, C.I., DeArdo, A.J., 2000. The segregation behavior of phosphorus in Ti and Ti + Nb stabilized interstitial-free steels. ISIJ Int. 40, 191–199.

222. Renavikar, M.P., 2003. Small strain deformation behavior of interstitial-free (IF) steels. University of Pittsburgh, p. 2,182.

223. Riecke, E.M., Johnen, B., Moeller, R., 1987. The effect of phosphorus on hydrogen uptake by iron in acidic sulphate and sulphide solutions. Corros. Sci. 27, 1027–1039.

224. Rinebolt, J.A., Harris, W.J., 1951. Effect of alloying elements on notch toughness of pearlitic steels. Trans. ASM 43, 1175–1201.

225. Rocquet, P., Jegaden, G., 1951. Contribution to the study of iron-phosphorus phase diagram. Rev. Met. 48, 712–721.

226. Rosenfeld, I.L., Marshakov, I.K., 1964. Mechanism of crevice corrosion. Corrosion 20, 115t–125t.

227. Sahoo, G., Balasubramaniam, R., 2008. On the corrosion behaviour of phosphoric irons in simulated concrete pore solution. Corros. Sci. 50, 131–143.

228. Sahoo, G., Balasubramaniam, R., 2007a. Mechanical behavior of novel phosphoric irons for concrete reinforcement applications. Scr. Mater. 56, 117–120.

229. Sahoo, G., Balasubramaniam, R., 2007b. On phase distribution and phase transformations in phosphoric irons studied by metallography. Metall. Mater. Trans. A 38, 1692–1697.

230. Sahoo, G., Balasubramaniam, R., Mungole, M.N., 2008. Comparison of thermal expansion behavior of phosphoric irons with conventional concrete reinforcement steel. J. ASTM Int. 5, 1–7.

231. Sahoo, G., Singh, B., Saxena, A., 2015. Characterization of high phosphorous containing hot rolled weather resistant structural steels. Mater. Sci. Eng. A 628, 303–310.

232. Saito, N., Abiko, K., Kimura, H., 1988. Reduction of intergranular fracture in Fe-P alloys by the addition of nickel. Mater. Sci. Eng. A 102, 169–174.

233. Sakai, T., Belyakov, A., Kaibyshev, R., Miura, H., Jonas, J.J., 2014. Dynamic and post-dynamic recrystallization under hot, cold and severe plastic deformation conditions. Prog. Mater. Sci. 60, 130–207.

234. Sankaran, S., Sangal, S., Padmanabhan, K.A., 2005. Microstructural evolution and tensile behaviour of medium carbon microalloyed steel processed through two thermomechanical routes. Mater. Sci. Technol. 21, 1152–1160.

235. Sankaran, S., Sarma, V.S., Kaushik, V., Padmanabhan, K.A., 2003. Thermomechanical processing and characterisation of multi-phase microstructures in a V-bearing medium medium carbon micro-alloyed steel. J. Mater. Process. Technol. 139, 642–647.

236. Santos, D.B., Bruzszek, R.K., Rodriguez, P.C.M., Pereloma, E. V, 2003. Formation of ultra-fine ferrite microstructure in warm rolled and annealed C-Mn steel. Mater. Sci. Eng. A 346, 189–195.

237. Saremi, M., M.E., 2002. A study on chloride-induced depassivation of mild steel in simulated concrete pore solution. Cem. Concr. Res. 32, 1915–1921.

238. Sawhill, J.M., Baker, J.C., 1980. Spot weldability of high strength steel sheets. Weld. J. 59, 19s–30s.

239. Sellars, C.M., McTegart, W.J., 1966. On the mechanism of hot deformation. Acta Metall. 14, 1136–1138.

240. Serajzadeh, S., Taheri, A.K., 2002. An investigation of the silicon role on austenite recrystallization. Mater. Lett. 56, 984–989.

241. Serajzadeh, S.U., Taheri, A.K., 2002. An investigation on the effect of carbon and silicon on flow behavior of steel. Mater. Des. 23, 2–7.

242. Sharma, A., Kumar, A., Tyagi, R., 2015. Erosive wear analysis of medium carbon dual phase steel under dry ambient condition. Wear 334–335, 91–98.

243. Shimada, H., Sakakibara, Y., 1989. Seawater-corrosion-resistant non-magnetic steel materials. US 4844865.

244. Silvermann, D.C., Puyear, R.B., 1987. Effect of environmental variables on aqueous corrosion, in: Davis, J.R., Destetani, D., Frisell, H.J., Crankovic, G.M. (Eds.), ASM Handbook, Corrosion Vol.13. ASM International, Materials Park, Ohio, pp. 37–44.

245. Singh, S., Sribalaji, M., Wasekar, N.P., Joshi, S., Sundararajan, G., Singh, R., Kumar, A., 2016. Microstructural, phase evolution and corrosion properties of silicon carbide reinforced pulse electrodeposited nickel – tungsten composite coatings. Appl. Surf. Sci. 364, 264–272.

246. Song, R., Ponge, D., Raabe, D., 2005. Improvement of the work hardening rate of ultrafine grained steels through second phase particles. Scr. Mater. 52, 1075–1080.

247. Spitzig, W.A., 1974. Mechanical properties of Fe-P and Fe-P-Ti alloys. Mater. Sci. Eng. 16, 169–179.

248. Spitzig, W.A., 1972. Effects of phosphorus on mechanical properties of low-carbon iron. Metall. Trans. 3, 1172–1183.

249. Spitzig, W.A., Hu, H., Sober, R.J., 1978. Effect of dynamic strain aging on the plastic anisotropy and mechanical properties of low-carbon phosphorus steels. Texture Cryst. Solids 3, 37–51.

250. Spitzig, W.A., Sober, R.J., 1977. Effect of phosphorus on the mechanical properties of normalized 0.1 pct C, 1.0 pct Mn steel strip. Metall. Trans. A 8A, 651–655.

251. Spitzig, W.A., Sober, R.J., 1977. Effect of phosphorus on the mechanical properties of hot-rolled 0.1C–1.0Mn steel strip. Metall. Trans. A 8, 1585–1590.

252. Spitzig, W.A., Sober, R.J., 1975. Dynamic strain aging as a strengthening mechanism in iron and iron-phosphorus alloys. Mater. Sci. Eng. A 20, 179–184.

253. Stead, J.E., 1915. Iron, carbon, and phosphorus. J. Iron Steel Inst. 91, 140–181.

254. Stern, M., 1955. The electrochemical behaviour, including hydrogen overvoltage of iron in acid environments. J. Electrochem. Soc. 609–616.

255. Stewart, J.W., Charles, J.A., Wallach, E.R., 2000a. Iron – phosphorus – carbon system Part 3 – Metallography of low carbon iron – phosphorus alloys. Mater. Sci. Technol. 16, 291–303.

256. Stewart, J.W., Charles, J.A., Wallach, E.R., 2000b. Iron-phosphorus-carbon system Part 2 - Metallographic behaviour of Oberhoffer’s reagent. Mater. Sci. Technol. 16, 283–290.

257. Stewart, J.W., Charles, J.A., Wallach, E.R., 2000c. Iron – phosphorus – carbon system Part 1 – Mechanical properties of low carbon iron – phosphorus alloys. Mater. Sci. Technol. 16, 275–282.

258. Stumpf, W., 2004. Hot work modelling of two equivalent low carbon strip steels produced , respectively , by the cold charge route and by the hot charge route. J. South African Inst. Min. Metall. December, 643–652.

259. Stumpf, W., 2003. Grain size modelling of a low carbon strip steel during hot rolling in a compact strip production (CSP) plant using the hot charge route. J. South African Inst. Min. Metall. December, 617–632.

260. Suzuki, S., Obata, M., Abiko, K., Kimura, H., 1985. Role of carbon in preventing alloys the intergranular fracture in iron-phosphorus. Trans. Iron Steel Inst. Japan 25, 62–68.

261. Svidunovich, N.A., Parfenov, L.I., Sorokin, G.A., Garost, A.I., Volkov, V.N., Obiedkov, V.A., Karbanovich, V.A., Vashkevich, V. V, Verbitsky, A.N., 1989. A wear-resistant steel. US 4855105.

262. Szklarska-Smialowska, Z., 2002. Mechanism of pit nucleation by electrical breakdown of the passive film. Corros. Sci. 44, 1143–1149.

263. Thomas, M., 1996. Chloride thresholds in marine concrete. Cem. Concr. Res. 26, 513–519.

264. Tiwari, S.K., Sahu, R.K., Pramanick, A.K., Singh, R., 2011. Development of conversion coating on mild steel prior to sol gel nanostructured Al2O3 coating for enhancement of corrosion resistance. Surf. Coat. Technol. 205, 4960–4967.

265. Tiwari, S.K., Tripathi, M., Singh, R., 2012. Electrochemical behavior of zirconia based coatings on mild steel prepared by sol – gel method. Corros. Sci. 63, 334–341.

266. Trejo, D., Monteiro, P.J., 2005. Corrosion performance of conventional (ASTM A615) and low-alloy (ASTM A706) reinforcing bars embedded in concrete and exposed to chloride environments. Cem. Concr. Res. 35, 562–571.

267. Tsuji, N., Matsubara, Y., Saito, Y., 1997. Dynamic recrystallization of ferrite in interstitial free steel. Scr. Mater. 37, 477–484.

268. Tyagi, R., Nath, S.K., Ray, S., 2004. Development of wear resistant medium carbon dual phase steels and their mechanical properties. Mater. Sci. Technol. 20, 645–652.

269. Verlinden, B., Driver, J., Samajdar, I., Doherty, R.D., 2007. Thermo-Mechanical Processing of Metallic Materials 75, 103.

270. Virtanen, S., Elsener, B., Bohni, H., 1988. Effect of metalloids Fe-Cr alloys. J. less common Met. 145, 581–593.

271. Vrable, J.B., Wilde, B.E., 1980. Electrical-potential requirements for cathodic protection of steel in simulated concrete environments. Corrosion 36, 18–23.

272. Walter, G.W., 1986. A review of impedance plot methods used for corrosion performance analysis of painted metals. Corros. Sci. 26, 681–703.

273. Wang, C.Y., Wang, X.J., Chang, H., Wu, K., Zheng, M.Y., 2007. Processing maps for hot working of ZK60 magnesium alloy. Mater. Sci. Eng. A 464, 52–58.

274. Wang, C.Y., Wu, K., Zheng, M.Y., 2008. Hot deformation and processing maps of Al 18 B 4 O 33 w / ZK60 composite. Mater. Sci. Eng. A 477, 179–184.

275. Wang, X.J., Hu, X.S., Nie, K.B., Deng, K.K., Wu, K., Zheng, M.Y., 2012. Dynamic recrystallization behavior of particle reinforced Mg matrix composites fabricated by stir casting. Mater. Sci. Eng. A 545, 38–43.

276. Weiss, I., Alvarado, P.J., Fitzsimons, G., DeArdo, A.J., 1983. Grain refinement and coarsening during dynamic recrystallization in plain carbon steel. Scr. Mater. 17, 693–697.

277. Weyers, R.E., Cady, P.D., 1987. Deterioration of concrete bridge decks from corrosion of reinforcing steel. Concr. Int. 9, 15–20.

278. Williams, D.E., Mohiuddin, T.F., Zhu, Y.Y., 1998. Elucidation of a trigger mechanism for pitting corrosion of stainless steels using submicron resolution scanning electrochemical and photoelectrochemical microscopy. J. Electrochem. Soc. 145, 2664–2672.

279. Woodfine, B.C., 1953a. Temper-brittleness: A critical review of the literature. J. Iron Steel Inst. 173, 229–239.

280. Woodfine, B.C., 1953b. Some aspects of temper-brittleness. J. Iron Steel Inst. 173, 240–255.

281. Wranglen, G., 1970. The "rustless" iron pillar at Delhi. Corros. Sci. 10, 761–770.

282. Yamashita, M., Miyuki, H., Matsuda, Y., Nagano, H., Misawa, T., 1994. The long term growth of the protective rust layer formed on weathering steel by atmospheric corrosion during a quarter of a century. Corros. Sci. 36, 283–299.

283. Ye, C.Q., Hu, R.G., Dong, S.G., Zhang, X.J., Hou, R.Q., Du, R.G., Lin, C.J., Pan, J.S., 2013. EIS analysis on chloride-induced corrosion behavior of reinforcement steel in simulated carbonated concrete pore solutions. J. Electroanal. Chem. 688, 275–281.

284. Yendrzhievsky, B.Y., Klimkin, P.A., 1994. The role of cementite shape in the fracture surface formation of steels embrittled by phosphorus. Scr. Metall. Mater. 31, 221–224.

285. Yin, F., Hanamura, T., Umezawa, O., Nagai, K., 2003. Phosphorus-induced dislocation structure variation in the warm- rolled ultrafine-grained low-carbon steels. Mater. Sci. Eng. A 354, 31–39.

286. Yoshimura, T., 1991. Corrosion-resistant clad steel and method for producing tne same. EP 0225983 B1.

287. Yu-Qing, W., McMahon, C.J., 1987. Interaction of P, C, Mn, Cr in intergranular embrittlement of iron. Mater. Sci. Technol. 3, 207–216.

288. Zakroczymski, T., Fan, C.-J., Szklarska-Smialowska, Z., 1985. Kinetics and mechanism of passive film formation on iron in 0.05M NaOH. J. Electrochem. Soc. 132, 2862–2867.

289. Zhang, J., Di, H., Mao, K., Wang, X., Han, Z., Ma, T., 2013. Processing maps for hot deformation of a high-Mn TWIP steel: A comparative study of various criteria based on dynamic materials model. Mater. Sci. Eng. A 587, 110–122.

290. Zhang, J., Hu, J., Zhang, J., Cao, C., 2004. Studies of water transport behavior and impedance models of epoxy-coated metals in NaCl solution by EIS. Prog. Org. Coatings 51, 145–151.

291. Zhang, Z., Lin, Q., Yu, Z., 2000. Grain boundary segregation in ultra-low carbon steel. Mater. Sci. Eng. A 291, 22–26.

292. Zhou, G.P., Liu, Z.Y., Qiu, Y.Q., Wang, G.D., 2009. The improvement of weathering resistance by increasing P contents in cast strips of low carbon steels. Mater. Des. 30, 4342–4347.